Some Aspects of Low Scale Seesaw Models

A thesis submitted in partial fulfilment of

the requirements for the degree of

Doctor of Philosophy

by

Vishnudath K. N.

(Roll No. 14330005)

Under the supervision of

Prof. Srubabati Goswami

Professor

Theoretical Physics Division

Physical Research Laboratory, Ahmedabad, India.

DISCIPLINE OF PHYSICS

INDIAN INSTITUTE OF TECHNOLOGY GANDHINAGAR

2019

to

My Family

Declaration

I declare that this written submission represents my ideas in my own words and where others' ideas or words have been included, I have adequately cited and referenced the original sources. I also declare that I have adhered to all principles of academic honesty and integrity and have not misrepresented or fabricated or falsified any idea/data/fact/source in my submission. I understand that any violation of the above will be cause for disciplinary action by the Institute and can also evoke penal action from the sources which have thus not been properly cited or from whom proper permission has not been taken when needed.

Signature

Name: Vishnudath K. N.

(Roll No: 14330005)

Date:

CERTIFICATE

It is certified that the work contained in the thesis titled **" Some Aspects of Low Scale Seesaw Models"** by Mr. Vishnudath K. N. (Roll No. 14330005), has been carried out under my supervision and that this work has not been submitted elsewhere for a degree.

Prof. Srubabati Goswami
Theoretical Physics Division,
Physical Research Laboratory,
Ahmedabad, India.

(Thesis Supervisor)

Date:

Thesis Approval

The thesis entitled

Some Aspects of Low Scale Seesaw Models

by

Vishnudath K. N.
(Roll No. 14330005)

is approved for the degree of

Doctor of Philosophy

Examiner	Examiner
Supervisor	Chairman

Date: ____________________

Place: ____________________

Acknowledgments

The work presented in this thesis would not have been possible without the help and support that I received from many people. I take this opportunity to extend my sincere gratitude and appreciation to all those who made this Ph.D thesis possible.

First and foremost, I would like to extend my sincere gratitude to my supervisor Prof. Srubabati Goswami who introduced me to this exciting field of neutrino physics. I have benefited immensely from her expertise in the subject. She has instilled in me the intellectual curiosity which a researcher should always possess and showed me how one should question any piece of information or idea without taking it for granted. I am extremely grateful for her dedicated help, advice, inspiration, encouragement and the continuous support that she provided during the times of difficulty in both academic and personal life. I am positive that these things will go a long way in my life.

Besides my supervisor, I would like to thank my doctoral committee members Prof. Subhendra Mohanty and Dr. Partha Konar for their insightful comments and encouragement during the last four years, and also for the hard questions from which I learned a lot and which motivated me to widen my research from various perspectives.

I express my immense gratitude to my collaborators Prof. Sandhya Choubey, Dr. Najimuddin Khan, Dr. Arindam Das and Dr. Takaaki Nomura. It has been a very pleasent experience to work with them and I have learned a lot on different aspects of particle physics from them. A special thanks to Dr. Ila Garg, who has been a collaborator, a friend and a sister, for all the support that she has given me during the last six years.

I would also like to express my gratitude to the Director of PRL, the Dean, the Academic Committee members and the area chairman Prof. Hiranmaya Mishra for providing the necessary facilities to carry out the research work. I am also thankful to the head of the academic services Dr. Bhushit G. Vaishnav for his constant help.

I express my sincere gratitude to all the faculty members who had taught me during the course work including Prof. R. Rengarajan, Prof. J. Banerji, Prof. R. P. Singh, Prof. D. Angom, Dr. N. Mahajan, Dr. B. K. Sahoo, Dr. G. K. Samanta, Prof. R. Sekar, Dr. D. Chakrabarty, Dr. L. K. Sahu, Prof. P. Venkatakrishnan, Prof. N. Srivastava, Prof. S. K. Mathew, Dr. R. Bhattacharyya, Dr. B. Sivaraman and Dr. M. K. Srivastava. I would also like to thank Dr. S. Naik from astronomy division with whom I had done my project during the first semster of my coursework. I would also like to thank other professors from the theory division Prof. J. R. Bhatt, Dr. N. Singh and Dr. K. Patel for the useful physics discussions that we had during various seminars. I would also like to express my sincere gratitude to Prof. R. Mohanta and Dr. E. Harikumar from University of Hyderabad and Prof. V. Kodankandath from St. Thomas College, Thrissur, for all the support and motivation.

I am thankful to all the staff members of our division, library, computer center, administration, dispensary, canteen, workshop and maintenance section of PRL for their assistance and support. I also take this moment to express my gratitude to the academic and administrative staff members of IIT Gandhinagar for helping with the registration procedures. Thanks *to Praggya for all those small talks and the useful suggestions that she had given at various occasions.*

I thank my seniors Monojit, Gulab, Newton and Chandan, my juniors Kaustav and Tanmay and the postdoctoral fellows Dr. Lakshmi, Dr. Biswajit and Dr. Ananya for various useful discussions. A special thanks to Dr. K. N. Deepthi for the continuous support that she has been giving in both academic and non-academic matters.

Thanks to Nijil for always being there ever since we boarded our train from Kerala to take admission in PRL. I would also like to thank my friend Aman, with whom I have been sharing my office in the last four years, for all the field theory discussions and for putting up with me all this while. I express my thanks to my friends and batch-mates Bhavesh, Bharti, Soumik, Niharika, Kiran, Anil and Pradeep for all the science discussions and the great times that we had together.

I would like to thank Chithra, Swapna, Jimbalu, Lekshmy, Bivin, Amala, Bhavya, Apoorv, Anju, Jabir, Ali, Hajira, Aravind, Subith, and Deva for making me feel at home and for all the delicious Kerala food.

I am also grateful to all the fellow researchers from PRL for the numerous helps and the support that they have given at various times. Especially, I would like to mention Rukmani, Akanksha, Balbeer, Arpan, Suchismita, Alekha, Tripurari, Ashish, Arvind, Richa, Avdhesh, Tanmoy, Abhaya, Lata, Girish, Chandan, Ikshu, Shradha, Manu, Venkatesh, Nidhi, Soumya, Selva, Arun, Prasanna, Archita, Aarthy, Navpreet, Rupa, Kuldeep, Prahlad, Ashim, Oindrila, Sukanya, Surya, Ayon, Priyank, Anshika, Vishal, Deepak, Sudipta, Pravin and Hrushikesh. Kindly forgive if I have left out anyone's name and please know that I am thankful to all of you.

I would also like to thank my friends Manjula, Vishnu, Jayaram, Alex, Saranya, Sameer, Thasni, Vishnu K., Kartavya and Aditya for all the support and care and for the wonderful times that I had spent with them.

Above all, I am immensely grateful to my parents and brother for everything that they have done for me.

Vishnudath K. N.

Abstract

The Standard Model (SM) of particle physics has been very successful in explaining a wide range of experimental observations and the discovery of the Higgs boson at the Large Hadron Collider has confirmed the mode of generation of the masses of the fundamental particles via the mechanism of electroweak symmetry breaking. This has put the SM on a solid foundation. However, despite its success in explaining most of the experimental data, the SM can not address certain issues, of which two of the most important are non-zero neutrino mass and the existence of dark matter.

The most plausible way to generate small neutrino masses is the seesaw mechanism which implies neutrinos to be lepton number violating Majorana particles. This Majorana nature of the neutrinos can give rise to the neutrino-less double beta decay process in which the total lepton number is violated by two units. It is well known that the canonical high scale seesaw models are not testable in the colliders and there are various low scale seesaw models proposed in the literature motivated by their testability. Such models can have various phenomenological as well as theoretical consequences. For example, the heavy seesaw particles can lead to enhanced rates of various charged lepton flavor violating decays and the new couplings associated with the seesaw can alter the stability/metastability of the electroweak vacuum. In addition, these heavy particles can have interesting signatures in the collider experiments. In this thesis, we study various phenomenological and theoretical implications of massive neutrinos in the context of various low scale seesaw models. We also explore the possibilities of having viable candidates for dark matter in the context of seesaw models.

First, we explore the implications of the Dark-LMA (DLMA) solution to the solar neutrino problem for neutrino-less double beta decay ($0\nu\beta\beta$). The standard Large Mixing Angle (LMA) solution corresponds to standard neutrino oscillations with $\Delta m^2_{21} \simeq 7.5 \times 10^{-5}$ eV^2 and $\sin^2\theta_{12} \simeq 0.3$, and satisfies the solar neutrino data at high significance. The DLMA solution appears as a nearly-degenerate solution to the solar neutrino problem for $\Delta m^2_{21} \simeq 7.5 \times 10^{-5}$ eV^2 and $\sin^2\theta_{12} \simeq 0.7$, once we allow for the existence of large non-standard neutrino interactions in addition to standard oscillations. We show that while the predictions for the effective mass governing $0\nu\beta\beta$ remains unchanged for the inverted hierarchy, that for normal hierarchy becomes higher

for the Dark-LMA parameter space and moves into the "desert region" between the two. This sets a new goal for sensitvity reach for the next generation experiments if no signal is found for the inverted hierarchy by the future search programmes. We also obtain the sensitivity for the DLMA region in the future ^{136}Xe experiments.

In the next part of the thesis, we study the minimal type-III seesaw model in which we extend the SM by adding two $SU(2)_L$ triplet fermions with zero hypercharge to explain the origin of the non-zero neutrino masses. The lightest active neutrino will be massless in this case. We use the Casas-Ibarra parametrization for the neutrino Yukawa coupling matrix and by choosing the two triplets to be degenerate, we have only three independent real parameters, namely the mass of the triplet fermions and a complex angle. The parametrization used allows us to have low masses of the triplet fermions and large Yukawa couplings at the same time. We show that the naturalness conditions and the limits from lepton flavor violating decays provide very stringent bounds on the model parameters along with the constraints from the stability/metastability of the electroweak vacuum. We perform a detailed analysis of the model parameter space including all the constraints for both normal as well as inverted hierarchies of the light neutrino masses. We find that most of the region that is allowed by lepton flavor violating decays and naturalness falls is stable/metastable depending on the values of the SM parameters.

In addition to neutrino masses, the existence of the dark matter is another issue that points towards the need for an extension of the SM. Hence, it is important to study the implications of the models that can simultaneously address these two issues. From this point of view, we consider singlet extensions of the SM, both in the fermion and the scalar sector, to account for the generation of neutrino mass at the TeV scale and the existence of dark matter, respectively. For the neutrino sector we consider models with extra singlet fermions which can generate neutrino masses via the so called inverse or linear seesaw mechanism whereas a singlet scalar is introduced as the candidate for dark matter. The scalar particle is odd under a discrete Z_2 symmetry which ensures its stability. We show that although these two sectors are disconnected at low energy, the coupling constants of both the sectors get correlated at a high energy scale by the constraints coming from the perturbativity and stability/metastability of the electroweak vacuum. The singlet fermions try to destabilize the electroweak vacuum while the singlet scalar aids the stability. As a consequence, the electroweak vacuum may attain absolute stability even up to the Planck scale for suitable values of the parameters. We delineate the parameter space for the singlet fermion and the scalar couplings for which the electroweak vacuum remains stable/metastable and at the same time giving the correct relic density and neutrino masses and mixing angles as observed.

In addition to the simple extensions of the particle content, we also consider a class of gauged $U(1)$ extensions of the SM, where active light neutrino masses are generated by an inverse seesaw mechanism. Along with the three right handed neutrinos needed for the cancellation of gauge anomalies, we add three singlet fermions. This allows us to consider large neutrino Yukawa couplings keeping the $U(1)'$ symmetry breaking scale to be of the order of $\sim\ O(1)$ TeV. Demanding an extra Z_2 symmetry under which, the third generations of both the electrically neutral fermions are odd gives us a stable dark matter candidate. We express the $U(1)$ charges of all the fermions in terms of the $U(1)$ charges of the SM Higgs and the new complex scalar. We perform a comprehensive study to find out the parameter space consistent with the low energy neutrino data, vacuum stability and perturbativity, dark matter bounds and constraints from the collider searches.

Keywords: Neutrino mass, Seesaw mechanism, Majorana neutrinos, Neutrino-less double beta decay, Vacuum stability, Metastability, Low scale seesaw, Dark matter, Naturalness, Lepton flavor violation.

Contents

List of Figures

Chapter 1

Introduction

In nature, we have four fundamental forces which are identified as : the strong interaction, the electromagnetic interaction, the weak interaction and the gravitational interaction. The fundamental interactions are mediated by the exchange of field quanta, i.e. particles, which are called as gauge bosons. The Standard Model (SM) of the particle physics is a mathematical framework that explains how the elementary particles interact among themselves via these fundamental forces except for the gravitational interaction [6–8]. In this chapter, we review the basics of the SM including the Higgs mechanism and the generation of the particle masses. Then we discuss the major motivations towards the search for a theory beyond SM, with special emphasis on the issues of neutrino oscillation (which indicates that the neutrinos are massive) and the existence of the dark matter.

1.1 The Standard Model

The SM is based on the principle of the invariance of the Lagrangian under local gauge transformations and the gauge group corresponding to the SM is $G_{SM} = SU(3)_c \times SU(2)_L \times U(1)_Y$, where c stands for the color quantum number, the subscript L indicates that only the left-handed fermions transform under $SU(2)$ and Y stands for the hypercharge. Corresponding to each generator of the gauge group, there is a gauge boson which act as the mediator of the forces. The SM has been highly successful in explaining a wide range of experimental observations and the discovery of the Higgs boson at the Large Hadron Collider (LHC) experiment has completed the hunt for the last missing piece of the SM [9, 10]. The Higgs boson holds a special status in the SM as it gives mass to all the other particles, with the exception of the neutrino [1].

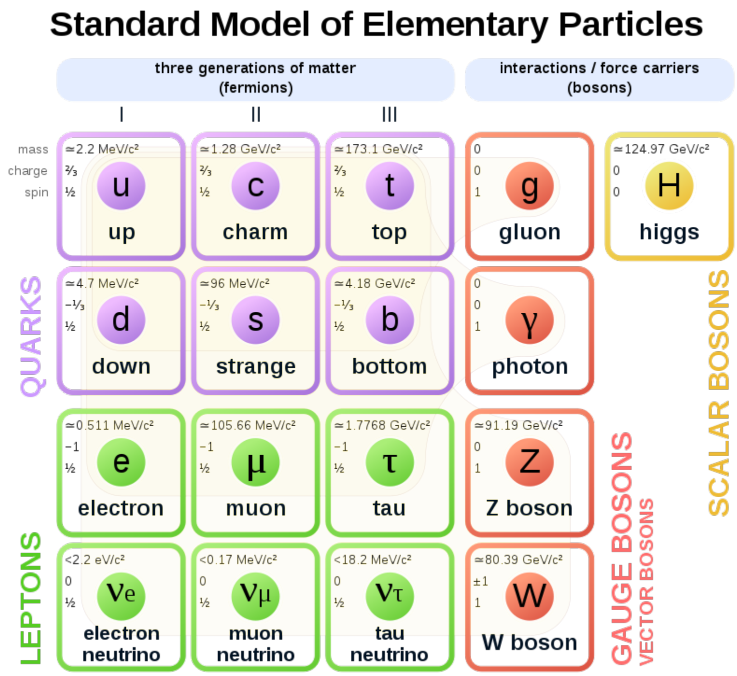

Figure 1.1: The building blocks of the SM. The first three columns correspond to the three generations of fermions (the matter particles) including quarks and leptons. The fourth column corresponds to the gauge bosons, the force carriers. The last column consists of the Higgs boson, which gives masses to all the other particles except neutrinos. The mass, charge and spin are also given for all the particles. Image source : Wikipedia [1]

The SM consists of three generation of fermions (which include both the quarks and the leptons), the Higgs doublet (H) and the gauge bosons corresponding to the strong (gluons) and the electroweak (EW) interactions ($W^{\pm}, Z, \gamma$). Fig. 1.1 shows the particle content of the SM along with the mass, charge and spin of each particle. The transformation properties of the matter and the Higgs field content under $SU(3)_c \times$

[1]The Higgs boson can give rise to a Dirac mass term for the neutrinos once we include right handed neutrinos as well. But this requires the Yukawa couplings to be extremely small ($\sim O(10^{-12})$) to give the sub-eV scale neutrino masses and this is not natural.

$SU(2)_L \times U(1)_Y$ are as given below.

$$Q_L = \begin{bmatrix} u_L \\ d_L \end{bmatrix} \sim (3,\ 2,\ \frac{1}{6}) \ ; \ d_R \sim (3,\ 1,\ -\frac{1}{3}) \ ; \ u_R \sim (3,\ 1,\ \frac{2}{3}), \tag{1.1}$$

$$l_L = \begin{bmatrix} \nu_L \\ e_L \end{bmatrix} \sim (1,\ 2,\ -\frac{1}{2}) \ ; \ e_R \sim (1,\ 1,\ -1) \ , \tag{1.2}$$

$$H = \frac{1}{\sqrt{2}} \begin{pmatrix} G^+ \\ v + h + iG^0 \end{pmatrix} \sim (1,\ 2,\ \frac{1}{2}). \tag{1.3}$$

From the above transformation properties, one can see that the left-handed fermions transform as doublets under $SU(2)_L$ whereas the right-handed fermions transform as singlets. Also, note that there are no right-handed neutrinos in SM and hence one can not have a Dirac mass term for the neutrinos. However, with the above transformation properties, one can not write mass terms for any of the particles that are invariant under the $SU(3)_c \times SU(2)_L \times U(1)_Y$ gauge symmetry. The Higgs mechanism of spontaneous symmetry breaking prescribes a way in which the particle masses can be generated in a gauge invariant way [11–14]. In this mechanism, the $SU(2)_L \times U(1)_Y$ gauge group is broken down to $U(1)_{Q_{em}}$ where Q_{em} stands for the electromagnetic charge. For a particle, Q_{em} is related to the hypercharge and the $SU(2)$ isospin I_3 by the Gell-MannNishijima formula [15, 16] as,

$$Q_{em} = I_3 + Y. \tag{1.4}$$

1.1.1 The Higgs Mechanism and the Generation of the Particle Masses

The SM Higgs doublet can be written as,

$$H = \frac{1}{\sqrt{2}} \begin{pmatrix} G^+ \\ v + h + iG^0 \end{pmatrix} \equiv \frac{1}{\sqrt{2}} \begin{pmatrix} \phi_1 + i\phi_2 \\ \phi_3 + i\phi_4 \end{pmatrix}. \tag{1.5}$$

This is the minimal choice of the Higgs multiplet that one needs to give masses to all the SM particles except neutrinos. The terms in the Lagrangian that involve H are given as,

$$\mathcal{L}_H = (D_\mu H)^\dagger (D^\mu H) - V(H) + \mathcal{L}_{Yukawa} \tag{1.6}$$

where the first term corresponds to the kinetic as well as the gauge interaction terms via the covariant derivative, the second term represents the Higgs potential and the Yukawa terms correspond to the interaction of the Higgs field with the fermions. The most general gauge invariant scalar potential is given by,

$$V(H) = -\mu^2 H^\dagger H + \lambda (H^\dagger H)^2. \tag{1.7}$$

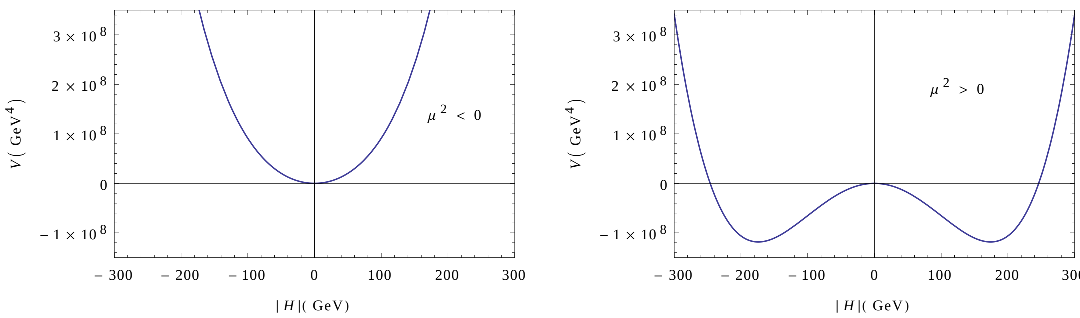

Figure 1.2: Plots of $V(H)$ as a function of $|H| = \sqrt{H^\dagger H}$. The left panel is for $\mu^2 < 0$ and the right panel is for $\mu^2 > 0$. We have taken $|\mu^2| = 88.4$ (GeV)^2 and $\lambda = 0.129$ from the measured values of $m_h \sim 125$ GeV and $v \sim 246$ GeV.

Let us examine the possible signs of the coefficients of the two terms in the above equation :

- Case - 1 : $\lambda < 0$: In this case, the potential is unbounded from below and the vacuum will be unstable.
- Case-2 : $\mu^2 < 0, \lambda > 0$: The potential has a minimum at $|H| = \sqrt{H^\dagger H} = 0$ (as shown in the left panel of Fig. 1.2). Here, the action of a gauge transformation on the vacuum state $H = 0$ does not alter the vacuum state and as result, the EW symmetry is unbroken in the vacuum.
- Case - 3 : $\mu^2 > 0, \lambda > 0$: Here, the potential has a minimum at $H^\dagger H = \dfrac{\mu^2}{2\lambda}$, which is away from $|H| = 0$. In this case, the vacuum is not invariant under $SU(2)_L \times U(1)_Y$ transformations and hence, the gauge symmetry is broken spontaneously.

Coming to the symmetry breaking scale, the potential is a function of,

$$H^\dagger H = \frac{1}{2}(\phi_1^2 + \phi_2^2 + \phi_3^2 + \phi_4^2), \tag{1.8}$$

which is the square of the length of a vector in the four dimensional space. The minimization of the potential fixes the length of the vector as,

$$H^\dagger H = \frac{\mu^2}{2\lambda}, \tag{1.9}$$

which is positive for $\mu^2 > 0$. This projects out a spherical surface from the four dimensional space when the potential is minimized. In fact, the $SU(2)_L \times U(1)_Y$ gauge transformations on H is equivalent to the rotations in this four dimensional space. Under such a rotation, the potential is invariant since it depends only on the length of the vector from the origin, but the vacuum is not. Thus, there is an infinite number of equivalent vacuum states (all the vectors of length $\sqrt{\mu^2/2\lambda}$), each of which transform to a new vacuum (another vector of length $\sqrt{\mu^2/2\lambda}$) under the $SU(2)_L \times U(1)_Y$ gauge transformation.

Now, let us consider the excitations around this vacuum state. Since the potential is flat along the three rotational directions, excitations in these directions cost zero energy. Hence, these correspond to the massless Goldstone bosons [17–20]. But, an excitation along the radial direction is like climbing the wall and corresponds to a massive particle.

For convenience, H can be written in another form as,

$$H = \frac{1}{\sqrt{2}} \exp\left(\frac{i\zeta^a\sigma^a}{v}\right) \begin{pmatrix} 0 \\ v+h \end{pmatrix}. \tag{1.10}$$

Here, σ^a are the Pauli matrices, h and ζ^a are the fields and a is summed over 1,2,3. This representation is equivalent to the one in Eq.1.5 and the fields ζ^a correspond to ϕ_1, ϕ_2 and ϕ_4. Now, the $SU(2)_L \times U(1)_Y$ gauge transformations on H are given by,

$$U(1)_Y \quad : \quad H \to \exp\left(\frac{i\lambda_Y(x)}{2}\right), \tag{1.11}$$

$$SU(2)_L \quad : \quad H \to \exp\left(\frac{i\lambda_L^a(x)\sigma^a}{2}\right). \tag{1.12}$$

Choosing $\lambda^a_L(x) = -2\zeta^a/v$ at every point in space-time brings us to a gauge in which,

$$H = \frac{1}{\sqrt{2}} \begin{pmatrix} 0 \\ v+h \end{pmatrix}. \tag{1.13}$$

Thus, the unphysical Goldstone degrees of freedom have been gauged away. This is known as the unitary gauge. In fact, the Goldstone modes will appear as the longitudinal degrees of freedom of the three gauge bosons $W^{\pm}_{\mu}$ and Z_{μ}. These gauge bosons get mass through their interaction with the Higgs field via the covariant derivative in the kinetic term,

$$D_{\mu} = \partial_{\mu} - i\frac{g^{'}}{2}B_{\mu} - i\frac{g}{2}W^a_{\mu}\sigma^a. \tag{1.14}$$

${W_{\mu}}^{\pm}$ correspond to $\dfrac{{W_{\mu}}^1 \mp i{W_{\mu}}^2}{\sqrt{2}}$ and one of the two linear combinations of B_{μ} and ${W_{\mu}}^3$ gives Z_{μ}, the other one being A_{μ}, the massless photon.

Also, the charged leptons and the quarks get mass from the Yukawa interactions,

$$-\mathcal{L}_{Yukawa} = Y_e\overline{e_R}H^{\dagger}l_L + Y_d\overline{d_R}H^{\dagger}Q_L + Y_u\overline{u_R}\tilde{H}^{\dagger}Q_L \quad + \quad \text{H. c.}, \tag{1.15}$$

where, $\tilde{H} = i\sigma^2 H^*$ and σ_2 is the second Pauli matrix.

Note that the neutrinos are massless tn the SM due to absence of right handed neutrinos. This is to incorporate parity violation which was observed in 1956 by Madam Wu and her collaborators by observing angular distribution of electrons in the the β-decay of ^{60}Co nuclei [21]. In addition, the left handed and the right handed charged fermions are also not treated on equal footing in the SM since only the left handed fermions participate in the charged current (CC) weak interactions.

As already mentioned, the SM is a very successful model and is in very good agreement with most of the observed phenomena. Still, there are several compelling reasons that motivate us to look for theories beyond the Standard Model (BSM). Some of the theoretical drawbacks of the SM which motivate us to consider a new theory are,

- The SM contains a large number (19) of free parameters which have to be determined from various experiments and this is certainly not a desirable characteristic of a minimal theory of nature.

- The masses of the fermions in the SM vary over a wide range, all the way from the sub-eV scale neutrinos to the top quark of mass $\sim$ 170 GeV. There is no explanation to why such a large hierarchy among fermion masses exists.

- The Higgs mass gets large corrections from the higher order loop diagrams due to its self-interaction as well as the couplings with gauge bosons and fermions. The theory is perceived unnatural if a severe fine-tuning between the quadratic radiative corrections and the bare mass is needed to bring down Higgs mass to the observed scale. This is known as fine-tuning or naturalness problem.

- The ultimate goal of particle physicists has been to have one unified field theory that describes all the interactions in a single framework. The three gauge couplings are not unified at any scale in the SM and this motivates studies of grand Unified theories in which SM can be embedded in some larger groups like $SO(10)$ or $SU(5)$. Also, gravity, the fourth fundamental force is not included in the SM.

- It is observed that the present universe contain mostly matter and no antimatter other than the rare antiparticles produced from cosmic rays. The SM can not explain this observed matter-antimatter asymmetry of the Universe.

In addition, the two most important motivations for going beyond the SM come from experiments which are the observation of neutrino oscillations which has shown that the neutrinos are massive and the existence of dark matter. In the next two sections, we will discuss the phenomena of neutrino oscillation and the issue of dark matter in some detail.

1.2 Neutrino Oscillation

Neutrino oscillation is a quantum mechanical interference phenomenon in which a neutrino created with a particular flavor can be measured to have a different flavor after propagating for some distance in space [22–24]. The transition probability varies as a periodic function, which depends on the distance of propagation, the energy of the neutrinos as well as the neutrino-mass squared differences. This phenomenon was predicted for the first time by Bruno Pontecorvo in 1957 [22, 23]. The observation of this phenomenon implies that the neutrino has a non-zero mass unlike as predicted by the SM and hence, this serves as the first direct experimental indication of the existence of a theory beyond SM.

In the case of the massive neutrinos, the three flavor eigenstates (ν_α) are superpositions of the mass eigenstates (ν_i), i.e.,

$$\nu_\alpha = \sum_{i=1}^{3} U_{\alpha i}\nu_i, \tag{1.16}$$

where it is assumed that there are three different mass eigenstates and U is the Pontecorvo-Maki-Nakagawa-Sakata (PMNS) neutrino mixing matrix relating the mass and the flavor eigenstates. In the standard three neutrino mixing, U is a 3×3 unitary matrix. If the neutrinos are Majorana particles, U will have three mixing angles and three physical phases (two Majorana phases and one Dirac CP phase) and if the neutrinos are Dirac particles, U is parametrized by three mixing angles and only one phase (the Dirac CP phase). In the standard parametrization, U is given as,

$$U = \begin{pmatrix} c_{12}c_{13} & s_{12}c_{13} & s_{13}e^{-i\delta} \\ -c_{23}s_{12} - s_{23}s_{13}c_{12}e^{i\delta} & c_{23}c_{12} - s_{23}s_{13}s_{12}e^{i\delta} & s_{23}c_{13} \\ s_{23}s_{12} - c_{23}s_{13}c_{12}e^{i\delta} & -s_{23}c_{12} - c_{23}s_{13}s_{12}e^{i\delta} & c_{23}c_{13} \end{pmatrix} P, \tag{1.17}$$

where $c_{ij} = cos\theta_{ij}$, $s_{ij} = sin\theta_{ij}$ and the phase matrix $P = \text{diag}\,(1,\, e^{i\alpha_2},\, e^{i(\alpha_3+\delta)})$ contains the Majorana phases.

In vacuum, the probability of transition from one flavor (ν_α) to another flavor (ν_β) is given by,

$$\begin{aligned} P(\nu_\alpha \to \nu_\beta) =& \delta_{\alpha\beta} - 4\sum_{i>j} Re\ (U^*_{\alpha i}U_{\beta i}U_{\alpha j}U^*_{\beta i})\ \sin^2(\Delta m^2_{ij}\frac{L}{4E}) \\ &+ 2\sum_{i>j} Im\ (U^*_{\alpha i}U_{\beta i}U_{\alpha j}U^*_{\beta i})\ \sin(\Delta m^2_{ij}\frac{L}{2E}) \end{aligned}, \tag{1.18}$$

where E is the energy of the neutrino and L is the distance between the source and the detector. From this equation, one can see that the neutrino oscillation probabilities are sensitive only to the mass squared differences and the mixing angles, but not to the absolute masses. Also, the probabilities are independent of the Majorana phases and hence the oscillation experiments can not provide any bound on these. The propagation of the neutrinos can be modified considerably when they travel through a dense medium like in the sun or the core of the earth. Hence, the probability for oscillation will be different than that in the vacuum. This mechanism of flavor changing is known as Mikhaev-Smirnov-Wolfenstein (MSW) effect [25–27], named after the ones who pointed out for the first time that there is an interplay between neutrino mixing and the flavor non changing neutrino-matter interactions. We will discuss more on this in chapter 3.

The first indication of neutrino oscillation came from the observed shortfall of solar neutrinos in the Homestake radio-chemical experiment using ^{37}Cl [28]. This was corroborated by Ga based experiments Gallex [29], SAGE [30] and GNO [31] and also the real time Kamiokande neutrino electron scattering experiments [32]. High statistics Super-Kamiokande (SK) experiment [33, 34], a successor of Kamiokande also supported this. Finally the smoking gun signature came from the Sudbury Neutrino Observatory (SNO) experiment [35, 36] which could measure the ratio of the CC events that are sensitive only to ν_e to the neutral current (NC) events that are sensitive to all three neutrino flavors. The observed value for CC/NC ratio was less than 1 and this unambiguously affirmed the presence of a ν_μ/ν_τ component in solar ν_e flux. This established neutrino flavor conversion as the solution to the solar neutrino problem. Another major importance of the SNO experiment was that the NC events matched with the flux of ^8B neutrinos as predicted by the standard solar model (SSM) [37]. This showed that the SSM does a great job in describing the physical processes that occur in the sun's core. Subsequently, the KamLAND experiment confirmed the oscillation parameters responsible for solar neutrino problem using man made reactor neutrinos [38, 39].

Indication of neutrino oscillation also came from the disappearance of the atmospheric ν_μ and $\bar{\nu}_\mu$ in the Kamiokande and IMB [40, 41] experiments. This came to be known as the atmospheric neutrino anomaly. SK experiment later confirmed this and also measured the zenith angle distribution of the atmospheric neutrinos. The departure of the observed zenith angle distribution from expectations conclusively established $\nu_\mu - \nu_\tau$ oscillation as the solution to the atmospheric anomaly. Also, the long-baseline accelerator neutrino experiment K2K [42] provided strong evidences for ν_μ disappearance due to oscillations, which was later confirmed by the MINOS [43–45] and the T2K [46, 47] long baseline experiments. These experiments lend independent support to atmospheric neutrino oscillations using beam neutrinos. All these experiments established the existence of neutrino oscillations which confirmed the existence of nonzero neutrino masses and mixing.

Assuming there are three mass eigenstates of the active light neutrinos, there are two independent mass squared differences. From the matter effect of the solar neutrinos in the sun, it has been inferred that the sign of $\Delta m^2_{21}(\Delta m^2_{sol})$ is positive. But the sign of the other mass squared difference, $\Delta m^2_{3l}(\Delta m^2_{atm})$ is not yet known from the experiments. This implies the possibility of two different hierarchies for the light neutrino masses : Normal hierarchy (NH) : $m_1 < m_2 << m_3$ with

$$m_1 \;\; ; \;\; m_2 = \sqrt{m_1^2 + \Delta m^2_{sol}} \;\; ; \;\; m_3 = \sqrt{m_1^2 + \Delta m^2_{sol} + \Delta m^2_{atm}}, \tag{1.19}$$

Inverted hierarchy (IH) : $m_3 << m_1 \approx m_2$ with

$$m_1 = \sqrt{m_3^2 + \Delta m^2_{atm}} \;\; ; \;\; m_2 = \sqrt{m_3^2 + \Delta m^2_{sol} + \Delta m^2_{atm}} \;\; ; \;\; m_3. \tag{1.20}$$

Fig. 1.3 displays the two possible hierarchies of the active neutrino masses and the colors in the mass eigenstates indicates the amount of different flavor eigenstate present. In addition to these two hierarchies, the neutrino masses can also have a quasi-degenerate spectrum in which $m_1 \sim m_2 \sim m_3 >> \sqrt{\Delta m^2_{atm}}$.

The 3σ ranges of the mixing angles and the mass squared difference given by the global analysis of neutrino oscillation data with three light active neutrinos [48] are given below. Similar analysis can also be found in references [49, 50].

⋆ **Mass squared differences**

$$\Delta m^2_{21}/10^{-5}\text{eV}^2 = (6.79 \to 8.01) \;\; ; \;\; \Delta m^2_{3l}/10^{-3}\text{eV}^2 = \begin{cases} (+2.431 \to +2.622) & \text{NH} \\ (-2.606 \to -2.413) & \text{IH} \end{cases} \tag{1.21}$$

⋆ **Mixing angles**

$$\sin^2\theta_{12} = (0.275 \to 0.350) \;\; ; \tag{1.22}$$

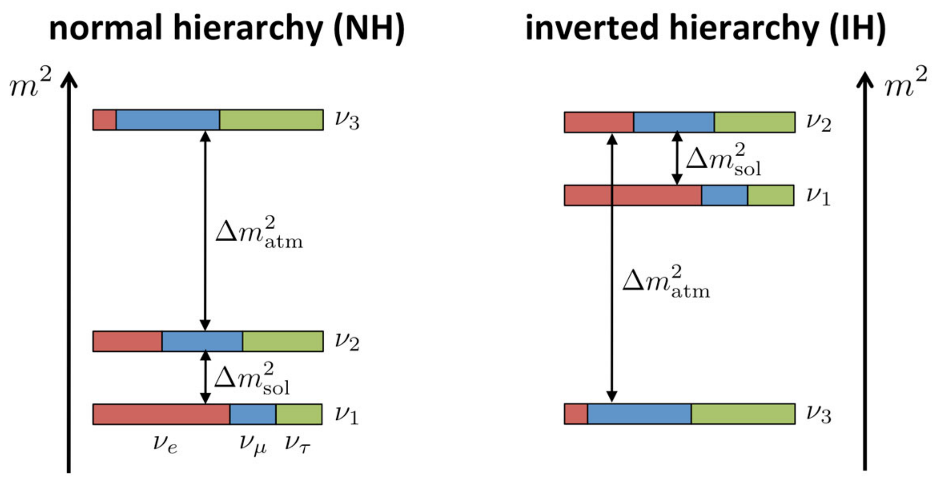

Figure 1.3: Neutrino mass hierarchies.

$$\sin^2\theta_{23} = \begin{cases} (0.428 \to 0.624) & \text{NH} \\ (0.433 \to 0.623) & \text{IH} \end{cases} ; \quad \sin^2\theta_{13} = \begin{cases} (0.02044 \to 0.02437) & \text{NH} \\ (0.02067 \to 0.02461) & \text{IH} \end{cases} \tag{1.23}$$

⋆ **Dirac CP Phase**

$$\delta = \begin{cases} (0.75\pi \to 2.03\pi) & \text{NH} \\ (1.09\pi \to 1.95\pi) & \text{IH} \end{cases} \tag{1.24}$$

Here, $\Delta m^2_{3l} = \Delta m^2_{31} > 0$ for NH and $\Delta m^2_{3l} = \Delta m^2_{32} < 0$ for IH and one can see that the value of $r = |\frac{\Delta m^2_{sol}}{\Delta m^2_{atm}}|$ is very small. Also, out of the three mixing angles, two are large (θ_{12} and θ_{23}) and one is small (θ_{13}) unlike in the case of quark mixing where all the mixing angles are small and the largest on is $\theta_C \sim 13°$, the Cabibbo angle [51]. The Majorana phases are allowed in the range $0 - \pi$. It has been found that the best fit of the data is for the NH and IH is disfavoured with a $\Delta\chi^2 = 4.7(9.3)$ without (with) Super-Kamiokande atmospheric neutrino data [48].

As already mentioned, the neutrino oscillation experiments are not sensitive to the absolute neutrino masses. But, the neutrino-less double beta decay process ($0\nu\beta\beta$) [52] is sensitive to the absolute neutrino masses through the effective Majorana mass

$m_{\beta\beta}$, given by,

$$|m_{\beta\beta}| \;=\; |\Sigma\, U_{ei}^2\, m_i|. \tag{1.25}$$

We will discuss more about $0\nu\beta\beta$ later. In addition to $\beta\beta_{0\nu}$ decay, the non-oscillation data from single β-decay add an independent constraint on the absolute neutrino masses through its sensitivity to the observable,

$$m_\beta = [\, c_{13}^2 c_{12}^2 m_1^2 \,+\, c_{13}^2 s_{12}^2 m_2^2 \,+\, s_{13}^2 m_3^2 \,]^{\frac{1}{2}} \tag{1.26}$$

The Troitsk nu-mass experiment [53] and the Mainz experiment [54] put constraints on the electron neutrino mass as $m_\beta < 2.05$ eV and $m_\beta < 2.3$ eV respectively. KATRIN is an ongoing experiment at the Karlsruhe Institute of Technology and has a sensitivity of $m_\beta \sim 0.2$ eV at 90% confidence level and has a 3σ discovery potential of 0.3 eV [55, 56]. Also, the cosmological constraint on the sum of light neutrino masses as given by the Planck 2018 results [57] puts an upper limit on the sum of the active light neutrino masses as, $\Sigma = m_1 + m_2 + m_3 < 0.12\,\mathrm{eV}$

1.3 Dark Matter

There are several astrophysical evidences that have established that there is more matter in the universe than the luminous matter and this unknown matter is called as dark matter (For review, see references [58–61]). Even though there are several evidences for the existence of dark matter, we still do not know much about its nature. A successful theory of particle physics should provide some suitable candidate for dark matter. One thing that we know for sure is that dark matter can not be baryonic, since in that case, the cosmic microwave background (CMB) structure that is being seen today would have been different. The information on the abundance of the light elements during the big bang nucleosynthesis (BBN) era also gives similar constraints on the baryonic content. Other important properties of any dark matter candidate is that it should be electrically neutral, weakly interacting and massive. In this section, after reviewing some of the astrophysical evidences for the existence of dark matter, we will briefly discuss the particle physics properties of the dark matter. We will also discus the principles behind the direct and the indirect detections as well as the collider searches of dark matter.

1.3.1 Evidences

The studies of the galactic clusters, gravitational lensing and CMB provide very compelling evidences for the existence of dark matter. We briefly review them here.

Galactic clusters

In 1932, the Dutch astronomer Jan Oort observed stellar motions in the galactic neighborhood and calculated the velocities of the stars from Doppler Shift [62]. It was found that in order to prevent the stars from escaping, the galaxies should be three times more massive than as indicated by the luminous matter, which implied the presence of some unknown, missing matter.

Around the same time when Oort made his discovery, Fritz Zwicky conducted an independent study of the Coma cluster [63]. Zwicky found that the average mass of one Nebula in this cluster is $M_{Nebula} = 4.5 \times 10^{10} M_{\odot}$ ($M_{\odot}$ is the solar mass) and hence, the entire mass of the cluster with around thousand nebula should be $4.5 \times 10^{13} M_{\odot}$. This was very surprising since this value was only about 10% of the mass measured from the luminosity indicating that the majority of the mass on the coma cluster is non-luminous.

Galactic rotation curve

Almost 40 years later, Vera Rubin along with her collaborators studied the rotational curve of around 60 isolated galaxies [64]. According to Newtons law of gravity, the rotational velocity of the stars as a function of the distance from the center (R) of the galaxy is given by the relation,

$$v(R) = \sqrt{\frac{GM(R)}{R}}. \tag{1.27}$$

Here, $M(R)$ is the total mass contained within a radius R. If one assumes that the majority of the mass is concentrated in the galactic nucleus as indicated by the luminosity profile, then $V(R)$ should decrease as $1/\sqrt{R}$ for stars that are far from the galactic center as indicated by the dotted line in Fig. 1.4. But it was found from the galactic rotation curves that the stellar velocity remains constant with increasing distance as shown by the solid line in Fig. 1.4. This indicates the presence of some non-luminous

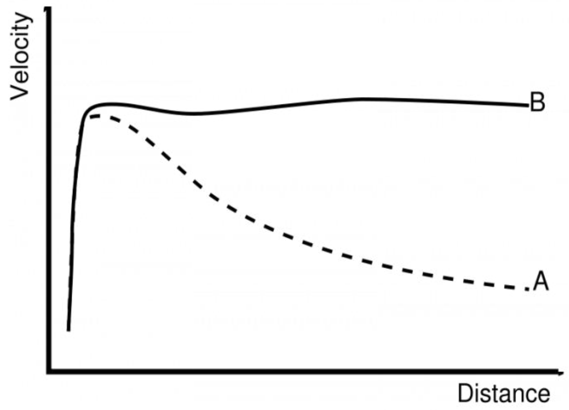

Figure 1.4: Rotation curve of a typical spiral galaxy. Line A represents the prediction from observed luminous mass distribution combined with the Newtonian gravity and line B corresponds to the actual observation. Image source : Wikipedia [2]

mass contributing to $M(R)$, extending out to a great distance beyond the central luminous region of the galaxy.

Gravitational lensing

The Bullet cluster (IE0657-56) contains two colliding clusters of galaxies. The speed and shape of the 'Bullet' combined with the other information from different telescopes indicate that about 150 million years ago, the smaller cluster passed through the core of the larger cluster. These two huge objects collided at very high speed of several million miles per hour. Due to the gravity of the mass in the cluster, light from the background galaxies will be distorted and this is known as gravitational lensing. Because of lensing, two distorted images of the same background galaxy can be seen above and below the real location of the galaxy. By observing several background galaxies like this, it is possible to make a map indicating where the majority of the mass in the cluster is located. It was found that the largest lensing is in the region that is not luminous, which is attributed to the presence of dark matter in this region [65]. It has been found that out of the total mass of the Bullet cluster, $\sim 2\%$ is due to the galaxies , $\sim 10\%$ is due to the intergalactic plasma and $\sim 88\%$ is because of the dark matter.

Cosmic microwave background

Even though the observations that we have discussed above give compelling evidence of localized dark matter, they do not say anything about the total amount of dark matter in the universe. This information can be extracted by studying the CMB radiation, which was emitted 13.7 billion years ago, just a few thousand years after the big bang. As the Universe got cooled, the neutral hydrogen atoms were formed and the photons got decoupled from the matter. These CMB photons can travel very long distances ($\sim$ Mpc) in straight lines without getting scattered. The Planck 2018 measurements of the CMB [57] give the following constraints on the baryonic and the total matter content of universe :

$$\Omega_m h^2 = 0.1430 \pm 0.0011 \quad ; \quad \Omega_b h^2 = 0.02237 \pm 0.00015 \tag{1.28}$$

The baryon density can be subtracted from the total matter density to find the global dark matter density as,

$$\Omega_{DM} h^2 = 0.1200 \pm 0.0012. \tag{1.29}$$

During the period of Big-bang nucleosynthesis (BBN) (i.e., a few seconds to a few minutes after the Big Bang), protons and neutrons fused together to form deuterium, helium and also, trace amounts of lithium and some other light elements. The other heavy elements were produced later inside the stars. The BBN limits the average baryonic content of the universe. The largest source of deuterium in the universe is BBN since any deuterium found or produced in stars will immediately get fused to helium. From the deuterium to hydrogen ratio (D/H) of regions with low levels of elements heavier than lithium, the D/H abundance directly after BBN can be determined. D/H ratio is heavily dependent on the overall density of baryons in the universe and hence, measuring the D/H abundance gives the overall baryon abundance and this is also consistent with the CMB observations.

1.3.2 Properties and Possible Candidates

Since the ordinary matter is made of particles, it is very natural to assume that the dark matter is also composed of some sort of elementary particles. There are several particle physics models in the literature with fermionic/scalar/vector dark matter. Any prospective dark matter candidate has to fulfill the following criteria :

- Massive, in order to explain the gravitational effects.
- Neutral since the dark matter is non-luminous.
- Stable and long-lived since they have not decayed until today.
- No strong interaction and at most weak interaction.
- Either cold or warm, but not hot. (A cold DM candidate is non-relativistic at the time of freeze-out, with a number density of $n \sim T^{3/2}e^{m/T}$, where T and m are the temperature and the mass of the DM species. Hot DM is relativistic at the time of freeze-out, with $n \sim T^3$ and a warm particle belongs somewhere in between these two cases.)

The SM contains left handed neutrinos which are stable and neutral. But as we already discussed, the Planck data constrains the sum of the neutrino masses to be ≤ 0.12 eV [57]. This indicates a very small relic density and hence can not account for the whole dark matter content. This points towards the need for a theory beyond SM.

The weakly interacting massive particles (WIMPs) are popular candidates since they can have the right relic abundance to account for dark matter. The WIMPs were in equilibrium with the thermal plasma in the early universe when the temperature was high. As the universe expands, the temperature decreases along with which, the number density of WIMPs also decreases. Finally, it reaches a point where this number density remains constant, a stage called freeze out. This depends on the thermal average of the effective annihilation cross section times the relative velocity, $\langle \sigma_{eff} v \rangle$. The evolution of the number density (n) of a particle in the early universe is governed by the Boltzmann equation,

$$\frac{dn}{dt} + 3Hn = -\langle \sigma_{eff} v \rangle (n^2 - n_{eq^2}), \tag{1.30}$$

where H is the Hubble parameter and n_{eq} is the number density at equilibrium. One can get the correct dark matter relic density as given in Eqn.1.29 for particle masses of $\sim 0.1 - 1$ TeV having interactions with typical strength of that of weak interaction. This remarkable coincidence is often referred to as WIMP miracle. Among the various WIMP models of dark matter studied in literature, the so called Higgs portal models [66–68] are the simplest ones. Here, the SM is extended by an additional singlet scalar with a Z_2 symmetry. This scalar is odd under the Z_2 symmetry ensuring its stability, which is necessary for a dark matter candidate. In chapter 5, we have studied this model in detail in the context of TeV scale seesaw models. In addition, one of the right handed neutrinos added for neutrino mass generation via seesaw mechanism (see chapter 2) can be made a dark matter candidate by adding an extra Z_2 symmetry. We have explored such a scenario in the context of a class of general $U(1)$ extensions of the SM in chapter 6. Also, there are several particles like neutralinos, sneutrinos and gravitinos which can be possible dark matter candidates in the context of various supersymmetric models [69–72]. In addition to WIMPs, several other candidates for dark matter such as strongly interacting massive particles (SIMPs) [73], axionic dark matter [74], Massive Compact Halo Objects (MACHOs) [75], the Kaluza-Klein particle [76], etc. have been proposed in the literature. However, in this thesis, we have limited our studies to just WIMPs where we have considered scalar as well as fermionic singlets as dark matter candidates.

1.3.3 Detection

Detection of the dark matter is very important in determining its properties and also in understanding their role in the structure formation of the universe. Many experiments have searched and are currently searching for a WIMP like dark matter and they use different detection methods. Here, we briefly discuss the basic principles of the direct and indirect detection schemes as well as the collider searches for dark matter particles (See [77] for a recent review).

Direct Detection

The direct detection experiments [78, 79] try to measure the energy deposited due to the recoil of the nuclei in a detector resulting from the elastic scattering with the WIMP. The detectors are located far underground in order to reduce the effect of the background cosmic rays and are sensitive to the WIMPs streaming across the earth. The recoiling nucleus in the detector deposits energy in the form of ionization, heat and light, which can be detected. The energy with which a nucleus of mass M recoils after an elastic collision with a dark matter particle of mass m is given as,

$$E = \left(\frac{\mu^2 v^2}{M}\right)(1 - \cos\theta). \tag{1.31}$$

Here, $\mu = \dfrac{Mm}{M+m}$ is the reduced mass, v is the relative velocity of the dark matter particle with respect to the nucleus and θ is the angle of scattering in the center of mass frame. Sensitivity to a wide range of WIMP masses can be achieved using liquid noble gases such as Xenon and Argon. The Large Underground Xenon (LUX) experiment located 1,510 meters underground at the Sanford Underground Laboratory in the Homestake Mine of South Dakota aims to detect the WIMP dark matter interactions with the ordinary matter on Earth [80]. The Particle and Astrophysical Xenon Detector (PandaX), the XENON experiment, COSINE, DAMA etc are some of the other direct detection experiments. No positive signal for the detection of dark matter has been observed in any direct detection experiment so far and this has put some bounds on the nucleon dark matter scattering cross section [2].

Indirect Detection

The indirect detection experiments are based on the detection of particles produced due to the annihilation or decay of dark matter [82]. These can include gamma rays, neutrinos as well as antimatter (positrons). The gamma rays from the annihilation of WIMPs are more readily produced in the galactic center. There are two processes by which these can be produced: First is the one in which the WIMPs annihilate into a quark-antiquark pair, which can further produce a particle jet from which a stream of gamma rays is emitted. The second one is the direct annihilation of WIMPs into gamma rays. WIMPs can have typical masses of $\sim O(100)$ GeV and can produce very high energy gamma rays. Even though such a gamma ray line will be a direct indication of the dark matter, the detection is not very easy because the production of

[2] The DAMA experiment has claimed an observation of the annual modulation in the dark matter signal because of the relative motion of the earth through the dark matter halo [81]. However, this has not been confirmed by other experiments.

gamma rays from other sources is not understood well. The Fermi Gamma Ray Space Telescope of NASA is designed to capture the gamma rays from the center of our own galaxy [83].

Similarly, the annihilation of WIMPs may produce highly energetic neutrinos, which can travel very long distances and can be detected by the neutrino detectors on earth. The IceCube Neutrino Observatory at the AmundsenScott South Pole Station in Antarctica which is designed to look for point sources of neutrinos in the TeV range to explore the high energy astrophysical processes is an example [84]. In addition, antimatter can be an excellent signal of dark matter because of the relatively lower cosmic abundance. For instance, the WIMP annihilation can produce positrons through secondary products of annihilation such as W^+W^-, where $W^+ \rightarrow e + \nu_e$. One has to study the flux of the antimatter particles over the entire galactic halo rather than the flux in particular areas. This is because the products are charged and hence will be affected by the magnetic fields within the space and might lose their energy very soon. So we might not be able to say where the annihilation was exactly taken place, unlike gamma rays and neutrinos.

The EDGES experiment, that has been designed to observe the signatures of the Hydrogen from the epoch of reionization after the formation of the stars in the early universe, observed an absorption profile in the radio background at the frequency of 78 MHz. This has been interpreted as a redshifted 21 cm line and it is highly improbable that the radiation from stars and stellar remnants account for this [85]. It is possible that the observed amplitude can be due to the cooling of gas as a result of interactions between dark matter and baryons.

Searches at the LHC

The dark matter searches have been carried out by the ATLAS and the CMS experiments as well [86]. The presence of a dark matter particle will be seen as a large missing momentum E_T^{miss} in the colliders (See [87] for a review.). The advantage of the collider searches of dark matter is that there is no background signal from other astrophysical sources and hence can compliment the other direct and indirect detection experiments. If the mass of the mediator is much higher than that of the dark matter particle, then the WIMP pair will be boosted in a direction opposite to that of the visible hadronic particle(s) which will give the mono-X signature. Here X can be photon, gluon, quarks, W, Z, H, etc. In the case of WIMPs heavier than the mediators, the constraints coming from the collider searches will be weak since the WIMP production cross section is kinematically suppressed.

1.4 Thesis Overview

In this thesis, we have studied various phenomenological and theoretical implications of massive neutrinos, assuming neutrinos are Majorana particles and they get a small non-zero mass via the seesaw mechanism. We have explored a few models that simultaneously explain the origin of neutrino masses and the existence of dark matter and how these two sectors are related by various theoretical constraints like vacuum stability and perturbative unitarity using the renormalization group running of the couplings.

In the next chapter, we have reviewed various seesaw models including a few TeV scale extensions. We have also discussed their phenomenological as well as theoretical implications like $0\nu\beta\beta$ decay, lepton flavor violation, vacuum stability etc.

Chapter 3 discusses one of the major implications of the Majorana nature of the neutrinos in detail : the lepton number violating $0\nu\beta\beta$ decay. In particular, we have studied the impact of the so-called Dark-LMA solution to the solar neutrino problem in the presence of large non-standard interactions (NSI) for the future $0\nu\beta\beta$ experiments.

In chapter 4, we have studied the minimal type-III seesaw model in which we have extended the SM by adding two $SU(2)_L$ triplet fermions with zero hypercharge. We show that the naturalness conditions and the limits from lepton flavor violating decays provide very stringent bounds on the model parameters along with the constraints from the stability/metastability of the electroweak vacuum.

In chapter 5, we consider singlet extensions of the SM, both in the fermion and the scalar sector, to account for the generation of neutrino mass at the TeV scale and the existence of dark matter respectively. We show that the coupling constants of these two seemingly disconnected sectors at low energy get correlated at high energy scale by the constraints coming from the perturbativity and stability/metastability of the electroweak vacuum.

In chapter 6, we study a class of gauged $U(1)$ extensions of the SM, where active light neutrino masses are generated by a minimal inverse seesaw mechanism. The model also has a stable fermionic dark matter candidate. We express the $U(1)$ charges of all the fermions in terms of the $U(1)$ charges of the SM Higgs and the new complex scalar. We perform a comprehensive study to chart out the parameter space consistent with the low energy neutrino data, vacuum stability and perturbative unitarity constraints, dark matter bounds and constraints from the collider searches.

Finally, we summarize and present the impact of our results in chapter 7.

Chapter 2

Massive Neutrinos in Physics Beyond the Standard Model : Seesaw Mechanism

2.1 Introduction

As discussed in the previous chapter, it is now well established that the neutrinos have small, non-zero masses and this serves as one of the major motivations for going beyond the SM. One can generate small neutrino masses either by extending just the particle content or by extending the gauge group and consequently the particle content. Among the various models proposed for understanding the sub-eV scale neutrino masses, the so-called seesaw mechanism is considered as the most natural approach. Here, the tree level exchange of some heavy particle present at a higher energy scale will give rise to an effective dimension-five Weinberg operator $\kappa l_L l_L HH$[88] at low scale. This operator generates tiny lepton number violating Majorana neutrino masses once the EW symmetry is broken. Here, κ is a proportionality constant with negative mass dimension and is inversely proportional to the energy scale at which the new physics enters.

There are three ways to form a gauge singlet with the SM doublets l_L and H such that neutrino mass can be generated. Thus depending on the type of the heavy states added for the ultraviolet completion, three different types of seesaw mechanisms are possible :

(i) Type-I seesaw mechanism : l_L and H form an $SU(2)$ singlet $[2 \otimes 2 = 3 \oplus 1]$ and this singlet forms a singlet term with a heavy singlet right-handed neutrino [89–92],

(ii) Type-II seesaw mechanism : l_L and l_L (as well as H and H) form an $SU(2)$ triplet $[2 \otimes 2 = 3 \oplus 1]$ and this triplet forms a singlet with a scalar triplet $[3 \otimes 3 = 5 \oplus 3 \oplus 1]$ [93–96] and

(iii) Type-III seesaw mechanism : l_L and H form an $SU(2)$ triplet $[2 \otimes 2 = 3 \oplus 1]$ and this triplet forms a singlet with a heavy fermionic triplet $[3 \otimes 3 = 5 \oplus 3 \oplus 1]$ [97].

The different seesaw mechanisms can be implemented in various models like the left-right symmetric models, $SO(10)$ grand unified models, etc. (See [98] for a review.)

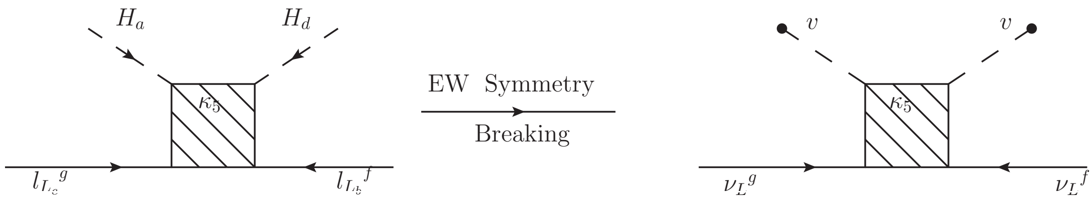

Figure 2.1: The effective dimension-five operator giving rise to a small neutrino mass

2.2 The effective Lagrangian for the seesaw model of neutrino mass

In this section, we review how one can generate the effective dimension-five operator giving rise to the Majorana neutrino masses in the case of seesaw models using the effective action and the classical equations of motion [99]. We will discuss the case of the type-I seesaw model. Similar procedure can also be applicable for the type-II and type-III seesaw models as well.

In the case of type-I seesaw mechanism, one can, in general, introduce n heavy right handed Majorana neutrinos (N_R) into the SM , keeping the EW Lagrangian invariant under $SU(2)_L \times U(1)_Y$.Then the most general gauge invariant renormalizable Lagrangian is given by, $\mathcal{L} = \mathcal{L}_{SM} + \mathcal{L}_{N_R}$, where,

$$\mathcal{L}_{N_R} = i\bar{N}_R\gamma_\mu\partial^\mu N_R \; - \; \bar{l}_L Y_\nu \tilde{H} N_R \; + \; \frac{1}{2}\bar{N}_R^c M_N N_R \; + \; \text{h.c.}. \tag{2.1}$$

Here, Y_ν is the Yukawa coupling matrix of dimension $3 \times n$ and M_N is the $n \times n$ complex symmetric Majorana mass matrix for N_R. Note that the lepton number violating Majorana mass terms are allowed by the gauge symmetries. M_N can have n complex eigenvalues, $M_i = e^{i\theta_i}|M_i| = \eta_i |M_i|$. We will work in a basis in which M_N is real and diagonal. Then, the Majorana neutrino eigenstates with $N_i = N_i^c$ are given by,

$$N_i = \sqrt{\eta_i}\, N_{Ri} + \sqrt{\eta_i^*}\, N_{Ri}^c, \tag{2.2}$$

and the Lagrangian for heavy neutrinos becomes,

$$\mathcal{L}_{N_R} = \frac{1}{2}\bar{N}_i(i\gamma_\mu\partial^\mu \,-\, M_i)N_i \,-\, (\,\frac{1}{2}\,[\bar{l_L}\tilde{H}Y_\nu\sqrt{\eta^*} \,+\, \bar{l_L^c}\tilde{H}^*Y_\nu^*\sqrt{\eta}]_i N_i \,+\, \text{h.c.}). \tag{2.3}$$

An effective Lagrangian, $\mathcal{L}_{eff}$ valid at energies less than $O(M_N) \sim \Lambda$ can be constructed by integrating out the heavy Majorana neutrinos N_i. $\mathcal{L}_{eff}$ has a power series expansion in $1/M$,

$$\mathcal{L}_{eff} \,=\, \mathcal{L}_{SM} \,+\, \frac{1}{M}\mathcal{L}^{d=5} \,+\, \frac{1}{M^2}\mathcal{L}^{d=6} \,+\, ... \tag{2.4}$$

$\mathcal{L}_{SM}$ contains all $SU(3) \times SU(2) \times U(1)$ invariant operators of $d \leq 4$ and the gauge invariant operators of $d > 4$ accounts for the physics effects of heavy N_i at energies $<< M \sim \Lambda$. The effective Lagrangian is defined through the effective action as,

$$e^{iS_{eff}} \,=\, exp\,[\,i\int d^4x\,\mathcal{L}_{eff}(x)\,] \,=\, e^{iS_{SM}}\int DN\,D\bar{N}\,e^{iS_N}. \tag{2.5}$$

Here,

$$S_{SM} = \int d^4x\,\mathcal{L}_{SM}(x). \tag{2.6}$$

The classical equations of motion for the N field with solution N_0 are obtained from

$$\frac{\delta S}{\delta N_i(x)}|_{N_{0i}} \,=\, 0\;\;;\;\;\frac{\delta S}{\delta \bar{N}_i(x)}|_{\bar{N}_{0i}} \,=\, 0. \tag{2.7}$$

Using the solutions for N_{0i} and $\bar{N}_{0i}$, the effective action is given by,

$$S_{eff} \,=\, S_{SM} \,+\, S_N(N_0), \tag{2.8}$$

where,

$$S_N(N_0) = \frac{1}{2}\int d^4x(\bar{l_L}\tilde{H}Y_\nu\sqrt{\eta^*}+\bar{l_L^c}\tilde{H}^*Y_\nu^*\sqrt{\eta})_i\frac{\delta_{ij}}{i\partial\!\!\!/ - M_i}(\sqrt{\eta}Y_\nu^\dagger\tilde{H}^\dagger l_L+\sqrt{\eta^*}Y_\nu^T\tilde{H}^T l_L^c)_j. \tag{2.9}$$

The contributions to the $\mathcal{L}_{eff}$ can be obtained by substituting,

$$\frac{1}{i\partial\!\!\!/ - M} = -\frac{1}{M} - \frac{i\partial\!\!\!/}{M^2} + \ldots \tag{2.10}$$

in Eqn.2.9. This yields us the terms of dimension $d \leq 6$, in which, the $d = 5$ operator of the effective Lagrangian for the seesaw model is obtained as,

$$\delta\mathcal{L}^{d=5} = \frac{1}{2}(\kappa_{\alpha\beta})(\bar{l}^c_{L\alpha}\,\tilde{H}^*)(\tilde{H}^\dagger\, l_{L\beta}) + \text{h.c.}, \tag{2.11}$$

where,

$$\kappa_{\alpha\beta} = (Y^*_\nu \frac{\eta}{M} Y^\dagger_\nu\,)_{\alpha\beta}. \tag{2.12}$$

Eqn.2.11 gives the well known dimension-five Weinberg operator which gives rise to small Majorana neutrino masses once the EW symmetry is broken and the Higgs doublet, H acquires a vev, $v/\sqrt{2} \approx 174$ GeV. The Majorana mass matrix of the light neutrinos is given by,

$$m_{\alpha\beta} = -\kappa_{\alpha\beta}\frac{v^2}{2}. \tag{2.13}$$

Alternately, one can also evaluate the tree level diagram in Fig. 2.2 using the Majorana fermion Feynman rules and do a matching to derive Eqn.2.13.

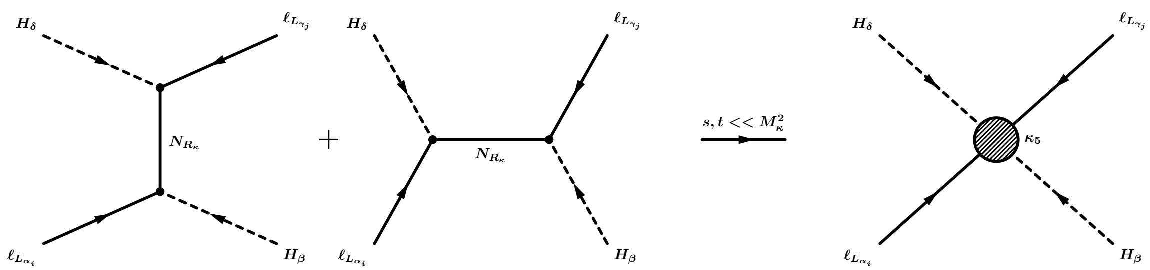

Figure 2.2: The tree diagrams giving rise to the effective dimension-five Weinberg operator in the type-I seesaw model.

2.3 Seesaw Mass Matrix and Diagonalization

We have discussed the origin of seesaw and the generation of the dimension-five Weinberg operator in the last section. In this section, we describe the mass matrices arising in different types of seesaw mechanism and explain the diagonalization procedure.

2.3.1 Type-I Seesaw Mechanism

From Eqn.2.1, after spontaneous symmetry breaking, the terms relevant for the neutrino mass are,

$$-\mathcal{L}_{mass} = \bar{\nu}_L M_D N_R + \frac{1}{2}\bar{N}_R^c M_N N_R + \text{h.c.}, \tag{2.14}$$

where, $M_D = Y_\nu v/\sqrt{2}$. Noting that $\bar{\nu}_L M_D N_R = \bar{N}_R^c M_D^T \nu_L^c$, the above equation can be written as,

$$-L_{mass} = \frac{1}{2}(\bar{\nu}_L \;\; \bar{N}_R^c)\begin{pmatrix} 0 & M_D \\ M_D^T & M_N \end{pmatrix}\begin{pmatrix} \nu_L^c \\ N_R \end{pmatrix} + \text{h.c.} \tag{2.15}$$

The scale of M_N can naturally be chosen to be much higher than the EW scale v since N_R and the corresponding Majorana mass terms are not related to the EW symmetry breaking. Without loss of generality, we will be working in a flavor basis in which M_l is diagonal, and also real and positive. To diagonalize the $(3+n)\times(3+n)$ neutrino mass matrix, one can use a unitary matrix as [100, 101],

$$U_0^T\, M_\nu\, U_0 = M_\nu^{diag} \tag{2.16}$$

where, $M_\nu^{diag} = \text{diag}\,(m_1,\, m_2,\, m_3,\, M_1,\, M_2, .., n)$ with mass eigenvalues $m_i\,(i = 1,\, 2,\, 3)$ and $M_j\,(j = 1,\, ..., n)$ for three light neutrinos and n heavy neutrinos respectively. Following a two-step diagonalization procedure, U_0 can be expressed as (by keeping terms up to order $\mathcal{O}(M_D^2/M_N^2)$) [101],

$$U_0 = W\,T = \begin{pmatrix} U_L & V \\ S & U_H \end{pmatrix} = \begin{pmatrix} (1-\frac{1}{2}\epsilon)U_\nu & M_D^*(M_N^{-1})^* U_R \\ -M_N^{-1}M_D^T\, U_\nu & (1-\frac{1}{2}\epsilon')U_R \end{pmatrix}. \tag{2.17}$$

Here, $U_L,\, V,\, S$ and U_H are 3×3, $3\times n$, $n\times 3$ and $n\times n$ matrices respectively, which are not unitary. W is the matrix which brings the full $(3+n)\times(3+n)$ neutrino matrix, in the block diagonal form,

$$W^T\begin{pmatrix} 0 & M_D \\ M_D^T & M_N \end{pmatrix} W = \begin{pmatrix} M_{light} & 0 \\ 0 & M_{heavy} \end{pmatrix}, \tag{2.18}$$

$T = \text{diag}\,(U_\nu, U_R)$ diagonalizes the mass matrices in the light and heavy sectors appearing in the upper and lower block of the block diagonal matrix respectively. The parameters ϵ and ϵ' characterize the non-unitarity and are given by,

$$\epsilon = M_D^* M_N^{-1*} M_N^{-1} M_D^T\,, \tag{2.19}$$

$$\epsilon' = M_N^{-1} M_D^T M_D^* M_N^{-1*}. \tag{2.20}$$

In the limit $O(M_N) >> O(M_D)$, one can derive the seesaw formula for the light neutrino mass matrix as,

$$M_\nu \approx -M_D M_N^{-1} M_D^T. \tag{2.21}$$

Also, the heavy Majorana maass matrix will be

$$M_{heavy} \approx M_N \tag{2.22}$$

Now, assuming $O(M_D) \approx 100GeV$ (the EW scale, assuming order of Yukawa couplings to be 1) , to get the observed sub-eV scale light neutrinos, it can be seen from Eqn.2.21 that $M_0 \approx 10^{14}GeV$, which is close to the grand unification scale. The above seesaw formula is very general and can be used whenever the condition $O(M_N) >> O(M_D)$ is met. Here, the unitarity violation of the PMNS matrix is negligibly small, which need not be the case when one consider TeV scale seesaw mechanisms. Also note that the minimum number of right handed neutrinos required to explain the observed oscillation data is two, in which case, the lightest active neutrino is massless.

2.3.2 Type-II Seesaw Mechanism

In the case of the type-II seesaw mechanism, the SM is extended with a $SU(2)$ triplet Higgs field, Δ. In the adjoint representation,

$$\Delta = \begin{bmatrix} \Delta^+/\sqrt{2} & \Delta^{++} \\ \Delta^0 & -\Delta^+/\sqrt{2} \end{bmatrix}. \tag{2.23}$$

The Yukawa part of the Lagrangian relevant for the neutrino masses is given by,

$$L_\Delta = -Y_\Delta \overline{l^c_{L\beta}} \epsilon_{\beta\gamma} \Delta_{\gamma\alpha} P_L l_{L\alpha} + \mu_\Delta H_\beta \epsilon \beta\gamma \Delta_{\gamma\alpha} H_\alpha - (M_\Delta)^2 \, \mathrm{Tr}\, [\Delta^\dagger \Delta] \;+\; \text{h.c.}. \tag{2.24}$$

Here, α, β, γ are the $SU(2)$ indices and the flavor indices have been suppressed. After symmetry breaking, the neutral component of Δ gets a vev,

$$v_\Delta = (\mu_\Delta)^* v^2/(M_\Delta)^2. \tag{2.25}$$

The light neutrino mass matrix is then given by,

$$m_\nu = 2(Y_\Delta v_\Delta). \tag{2.26}$$

For $\mu_\Delta \sim M_\Delta \sim 10^{12} - 10^{14}$ GeV, one gets, $v_\Delta \sim v^2/M_\Delta$, which is suppressed by the mass scale M_Δ. For $Y_\Delta \approx O(1)$, light neutrino masses of the sub-eV scale can be generated . In the case of type-II seesaw model, one can also have a TeV scale seesaw assuming that the lepton number is explicitly violated at a low energy scale such that $\mu_\Delta << v << M_\Delta$ [102]. In this case, small neutrino mass can be generated by taking $\mu_\Delta \sim O(1)$ keV, $v_\Delta \sim O(10)$ eV, $M_\Delta \sim O(1)$ TeV and $Y_\Delta \sim O(0.1)$.

2.3.3 Type-III Seesaw Mechanism

In type-III seesaw, the SM is extended with n fermionic triplets Σ_{R_i}, $i = 1, 2, ..n$ with zero hypercharge. These triplets can be represented as,

$$\Sigma_R = \begin{bmatrix} \Sigma_R^0/\sqrt{2} & \Sigma_R^+ \\ \Sigma_R^- & -\Sigma_R^0/\sqrt{2} \end{bmatrix} \equiv \frac{\Sigma_R^i \sigma^i}{\sqrt{2}}. \tag{2.27}$$

Here, $\Sigma_R^\pm = (\Sigma_R^1 \mp i\Sigma_R^2)/\sqrt{2}$. The terms of the Lagrangian that are responsible for the neutrino mass generation are,

$$-\mathcal{L}_\Sigma = \tilde{H}^\dagger \overline{\Sigma}_R \sqrt{2} Y_\Sigma l_L + \frac{1}{2}\,\mathrm{Tr}\,[\overline{\Sigma}_R M \Sigma_R^c] \;+\; \text{h.c.}, \tag{2.28}$$

where the generation indices have been suppressed and M is the Majorana mass of the triplet fermions. Once the Higgs field H acquires the vev, the neutral fermion mass matrix can be written as,

$$M_\nu = \begin{pmatrix} 0 & M_D^T \\ M_D & M \end{pmatrix}. \tag{2.29}$$

In this case, $M_D = Y_\Sigma v/\sqrt{2}$. This mass matrix can be diagonalized in the same way as we had discussed for the type-I seesaw and in the limit $M >> M_D$, the light neutrino mass matrix can be written as,

$$m_{\text{light}} = -M_D^T M^{-1} M_D. \tag{2.30}$$

The minimal model corresponds to $n = 2$ as in the case of type-I seesaw model. The charged components of the triplet fermions mix with the charged leptons of SM and this is governed by the Lagrangian [103],

$$\mathcal{L} = -\begin{pmatrix} \bar{l}_R & \bar{\Psi}_R \end{pmatrix} \begin{pmatrix} m_l & 0 \\ \sqrt{2}M_D & M \end{pmatrix} \begin{pmatrix} l_L \\ \Psi_L \end{pmatrix} \;+\; \text{h.c.}. \tag{2.31}$$

Here we have defined,

$$\Psi = \Sigma_R^{+c} \; + \; \Sigma_R^{-}. \tag{2.32}$$

The above charged fermion mass matrix can be diagonalized by a bi-unitary transformation. We will discuss in more detail about the type-III seesaw in Chapter 4.

2.4 TeV Scale Extensions of the Type-I Seesaw

In the last section, we have seen that in the case of simple type-I seesaw mechanism, one has to either go for extremely small Yukawa couplings or one has to resort to very large seesaw scale. Thus, the canonical type-I seesaw model has no direct experimental testability. A way out is to lower the seesaw scale, and different variants to the type-I seesaw have been proposed in literature. By decoupling the new physics scale from the scale of the lepton number violation, one can reduce the scale of new physics to TeV. Then, the smallness of the neutrino mass can be attributed to small lepton number violating terms. As per the t Hooft's criteria [104], a tiny value of the lepton number violating parameter is deemed natural, since when this is zero, the global $U(1)$ lepton number symmetry is restored and neutrinos are massless.

One can get the most general low scale extension of the canonical type-I seesaw scenario by adding m right handed neutrinos N_R and n gauge-singlet sterile neutrinos ν_s to the SM. ν_s and N_R are assigned with lepton numbers -1 and $+1$ respectively. The most general Yukawa Lagrangian responsible for neutrino masses before SSB is,

$$-\mathcal{L}_\nu = \bar{l}_L Y_\nu \, H^c N_R \, + \, \bar{l}_L Y_s \, H^c \nu_s \, + \overline{N_R^c} \, M_R \, \nu_s \, + \, \frac{1}{2} \, \overline{\nu_s^c} M_\mu \nu_s \; + \; \frac{1}{2} \, \overline{N_R^c} M_N N_R \; + \text{h.c.}. \tag{2.33}$$

Here, Y_ν and Y_s are the Yukawa coupling matrices and M_N and M_μ are the Majorana mass matrices for N_R and ν_s respectively. Y_ν, Y_s, M_N and M_μ are of dimensions $3 \times m$, $3 \times n$, $m \times m$ and $n \times n$ respectively.

Now, after SSB, the mass terms for the neutral fermions can be written as,

$$-\mathcal{L}_{mass} = \overline{\nu}_L M_D N_R \, + \, \overline{\nu}_L M_s \nu_s \, + \overline{N_R^c} \, M_R \nu_s \, + \, \frac{1}{2} \, \overline{\nu_s^c} M_\mu \nu_s \, + \, \frac{1}{2} \, \overline{N_R^c} M_N N_R \; + \; \text{h.c.} \tag{2.34}$$

where, $M_D = Y_\nu \langle H \rangle$ and $M_s = Y_s \langle H \rangle$. The neutral fermion mass matrix M can be defined as,

$$-\mathcal{L}_{mass} = \frac{1}{2}(\overline{\nu}_L \ \overline{N_R^c} \ \overline{\nu_s^c}) \begin{pmatrix} 0 & M_D & M_s \\ M_D^T & M_N & M_R \\ M_s^T & M_R^T & M_\mu \end{pmatrix} \begin{pmatrix} \nu_L^c \\ N_R \\ \nu_s \end{pmatrix} + \text{h.c.} \tag{2.35}$$

One can get the variants of the singlet seesaw scenarios from this equation by setting certain terms to be zero. Another significant feature of the TeV scale seesaw models is that they can have appreciably large values of light-heavy mixing.

2.4.1 Inverse Seesaw Mechanism

M_s and M_N are taken to be zero [105] in the inverse seesaw model. Since the mass term M_R is not subject to the $SU(2)_L$ symmetry breaking and the mass term M_μ violates the lepton number, the scales corresponding to the three sub-matrices of the neutral fermion mass matrix may naturally have a hierarchy $M_R >> M_D >> M_\mu$. Assuming $m = n = 3$, which is motivated by the grand unified theories based on superstring inspired E_6 models[105], the 9×9 inverse seesaw mass matrix can be rewritten as,

$$M_\nu = \begin{pmatrix} 0 & \hat{M}_D \\ \hat{M}_D^T & \hat{M}_R \end{pmatrix} \tag{2.36}$$

where,

$$\hat{M}_D = (M_D \ \ 0) \text{ and } \hat{M}_R = \begin{pmatrix} 0 & M_R \\ M_R^T & M_\mu \end{pmatrix}. \tag{2.37}$$

In this case, the effective light neutrino mass matrix in the seesaw approximation is given by,

$$M_{light} \approx -\hat{M}_D \hat{M}_R^{-1} \hat{M}_D^T = M_D (M_R^T)^{-1} M_\mu M_R^{-1} M_D^T \tag{2.38}$$

where we have used,

$$\begin{pmatrix} 0 & M_R \\ M_R^T & M_\mu \end{pmatrix}^{-1} = \begin{pmatrix} -(M_R^T)^{-1} M_\mu M_R^{-1} & (M_R^T)^{-1} \\ M_R^{-1} & 0 \end{pmatrix}. \tag{2.39}$$

In the heavy sector, there will be three pairs of degenerate pseudo-Dirac neutrinos of masses of the order $\sim M_R \pm M_\mu$. Note that the smallness of M_{light} is naturally attributed to the smallness of both M_μ and $\dfrac{M_D}{M_R}$. For instance, $M_{light} \sim \mathcal{O}\,(0.1)$ eV can easily be achieved for $\dfrac{M_D}{M_R} \sim 10^{-2}$ and $M_\mu \sim \mathcal{O}\,(1)$ keV. Thus, the seesaw scale can be lowered down considerably assuming $Y_\nu \sim \mathcal{O}(0.1)$, such that $M_D \sim 10$ GeV and $M_R \sim 1$ TeV. Here, the minimal model corresponds to $m = n = 2$ in which case, the lightest active neutrino is massless.

The same procedure that was discussed in section 2.2 to can be extended to this case also where we use a 9×9 unitary matrix, U_0, to diagonalize the mass matrix,

$$U_0^T\, M_\nu\, U \;=\; M_\nu^{diag} \tag{2.40}$$

where, $M_\nu^{diag} = \text{diag}\,(m_1,\, m_2,\, m_3,\, M_1,\, ...,\, M_6)$ with mass eigenvalues $m_i\,(i = 1,\, 2,\, 3)$ and $M_j\,(j = 1,\, ...,6)$ for three light neutrinos and 6 heavy neutrinos respectively. In this case, the parameter ϵ characterizing the non-unitary correction to the PMNS matrix is given by,

$$\epsilon \;=\; \hat{M}_D^* \hat{M}_R^{-1*} \hat{M}_R^{-1} \hat{M}_D^T\,, \tag{2.41}$$

which is $\sim O\Big(\dfrac{M_D^2}{M_R^2}\Big)$ to the leading order.

2.4.2 Linear Seesaw Mechanism

In linear seesaw model, the Yukawa coupling terms of ν_L to the singlet fields ν_s are also introduced, keeping the Majorana mass terms to be 0 [106–108]. Thus neutral fermion mass matrix will be,

$$\begin{pmatrix} 0 & M_D & M_s \\ M_D^T & 0 & M_R \\ M_s^T & M_R^T & 0 \end{pmatrix}. \tag{2.42}$$

where $M_s >> M_D, M_R$. Using the same method outlined in the case of the inverse seesaw model, the effective light neutrino mass matrix becomes,

$$M_\nu \;=\; M_D^T M_s^{-1} M_R \,+\, M_T^T M_s^{-1} M_D. \tag{2.43}$$

Note that this contains only one power of the Dirac mass term and hence known as linear seesaw. To get the conditions required to have $M_\nu \approx 0.1\,eV$, one can make an order of magnitude estimate as it was done in the earlier cases. Assuming typical values $M_D \approx 100\,GeV$ and $M_s \approx 1TeV$, one needs $Y_s \approx 10^{-11}$ to get the correct order of the light neutrino masses. The minimal linear seesaw model corresponds to $m = n = 1$.

2.4.3 Double Seesaw Mechanism

The double seesaw model is almost similar to the inverse seesaw scenario [105, 109], but unlike in the case of the inverse seesaw mechanism where the order of the sub-matrix M_μ is very small, in double seesaw mechanism, M_μ is taken to be very large. The form of the neutral fermion mass matrix and hence the expression for the low energy mass matrix is the same as for the inverse seesaw, but now obeys the condition, $M_D, M_R << M_\mu$ and $M_D << \frac{M_R^2}{M_\mu}$. Thus, the expression for the light neutrino masses is given by Eqn. 6.11 whereas the heavy neutrinos will have masses of the order M_μ and M_R^2/M_μ. Here, one will again have to resort to a large seesaw scale. The correct order of magnitude of neutrino masses can be obtained by taking $M_D \approx 100$ GeV, $M_\mu \approx M_{pl}$ and $M_R \approx M_{GUT} \approx 10^{16}$ GeV.

2.4.4 Extended Double Seesaw Mechanism

In this case, the neutral fermion mass matrix is given by [110, 111],

$$-L_{mass} = \frac{1}{2}(\overline{\nu}_L \;\; \overline{N_R^c} \;\; \overline{\nu_s^c}) \begin{pmatrix} 0 & M_D & 0 \\ M_D^T & M_N & M_R \\ 0 & M_R^T & M_\mu \end{pmatrix} \begin{pmatrix} \nu_L^c \\ N_R \\ \nu_s \end{pmatrix} + \text{h.c.}, \tag{2.44}$$

where only the Yukawa coupling term of ν_L to ν_s is kept as 0. Following the same procedure as earlier, the neutral fermion mass matrix in the extended double seesaw mechanism (EDSM) can be rewritten as

$$\begin{pmatrix} 0 & \hat{M}_D \\ \hat{M}_D^T & \hat{M}_R \end{pmatrix}, \tag{2.45}$$

where, $\hat{M}_D = (M_D \;\; 0)$ and $\hat{M}_R = \begin{pmatrix} M_N & M_R \\ M_R^T & M_\mu \end{pmatrix}$. Then, assuming $O(\hat{M}_D) << O(\hat{M}_R)$, the effective light neutrino mass matrix M_ν can be approximately written as,

$$M_\nu \;\approx\; -\hat{M}_D \hat{M}_R^{-1} \hat{M}_D^T = M_D(M_R M_\mu^{-1} M_R^T - M_N)^{-1} M_D^T, \tag{2.46}$$

provided $M_N \neq M_R M_\mu^{-1} M_R^T$.

Now, consider the following two cases :

(1) Mass scale of $M_N <<$ the mass scale of $M_R M_\mu^{-1} M_R^T$: Then, the formula can be approximated as

$$M_\nu \;\approx\; M_D (M_R^T)^{-1} M_\mu M_R^{-1} M_D^T \tag{2.47}$$

which is the same as that for Inverse seesaw mechanism.

(2) Mass scale of $M_N >>$ the mass scale of $M_R M_\mu^{-1} M_R^T$: In this case,

$$M_\nu \;\approx\; -M_D M_R^{-1} M_D^T \tag{2.48}$$

Thus, it can be seen that the EDSM will degenerate into either the conventional type-I seesaw or the inverse seesaw depending on whether $M_N >> M_R M_\mu^{-1} M_R^T$ or $M_N << M_R M_\mu^{-1} M_R^T$. Also, one can verify that the EDSM boils down to the canonical type-I seesaw when $M_N = M_R M_\mu^{-1} M_R^T$ exactly holds [111].

2.4.5 Radiative neutrino mass mechanism for the Inverse Seesaw Models

In Eqn. 6.10, if both M_s and M_μ are kept as 0, the neutral fermion mas matrix becomes [112],

$$\begin{pmatrix} 0 & M_D & 0 \\ M_D^T & M_N & M_R \\ 0 & M_R^T & 0 \end{pmatrix}. \tag{2.49}$$

In this case, it can be seen that the effective light neutrino mass matrix will turn out to be 0 at the tree level, but it acquires a small, non-zero value at the one-loop level due to the Majorana mass term for N_R (M_N).

2.5 Implications of Seesaw

We have already seen that the seesaw mechanism is one of the most popular models for explaining the generation of tiny neutrino masses and according to this, the neutrinos are lepton number violating Majorana particles. This can have various phenomenological as well as theoretical consequences, especially in the case of TeV scale seesaw models. For example, the lepton number violating couplings can give rise to the neutrino-less double beta decay ($0\nu\beta\beta$) process and the heavy seesaw particles can lead to enhanced rates of various lepton flavor violating (LFV) decays. The seesaw models can naturally incorporate leptogenesis which can explain the observed baryon asymmetry of the universe. Also, the new couplings associated with the seesaw can alter the stability of the EW vacuum. In addition, these heavy particles can have interesting signatures in collider experiments. In this section, we discuss in some detail the implications that have been considered in this thesis.

2.5.1 Neutrino-less Double Beta Decay

The question of whether the neutrinos are Dirac particles or lepton number violating Majorana particles for which the particle and the antiparticle are the same is one of the major puzzles in neutrino physics. Oscillation experiments do not help us to determine the Majorana nature of neutrinos and hence, one needs to study processes in which the total lepton number is violated.

The $0\nu\beta\beta$ process [52] ($X_Z^A \rightarrow X_{Z+2}^A + 2e^-$), in which the lepton number is violated by 2 units can establish the Majorana nature of the neutrinos. There is another process, two-neutrino double beta decay ($2\nu\beta\beta$), first proposed by Maria Goeppert-Mayer in 1935 [113] and is allowed in SM for some even-even nuclei for which, pairing forces make the nucleons more bound than in its $(Z+1, A)$ neighbor, but less than that

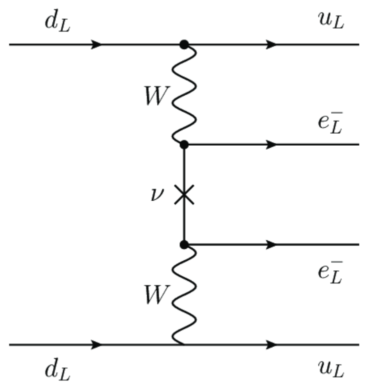

Figure 2.3: Feynman diagram showing $0\nu\beta\beta$ decay by active light neutrino exchange.

in the $(Z+2, A)$ nuclide. It is an extremely rare process of the second order in G_F, where G_F is the Fermi's constant. $2\nu\beta\beta$ was first observed in a laboratory in 1987 by the group of Michael Moe at UC Irvine for Se^{82} nucleus [114] :

$$Se^{82} \rightarrow Kr^{82} + 2e^- + 2\hat{\nu}$$

with a half life of 1.1×10^{20} years. This conserves the lepton number and hence provides a confirmation of the SM. $0\nu\beta\beta$ decay is further suppressed by the proportionality of the transition amplitude to the effective Majorana mass. $0\nu\beta\beta$ decay has not been observed so far and there are several ongoing and upcoming experiments search for $0\nu\beta\beta$.

Considering the standard 3 generation picture, it can be shown that the rate of the $0\nu\beta\beta$ decay is given as [115, 116],

$$\frac{\Gamma_{0\nu\beta\beta}}{\ln 2} = G^{0\nu}(Q,Z)\,|M_\nu|^2\frac{|m_{\beta\beta}|^2}{m_e^2} \tag{2.50}$$

$G^{0\nu}$ contains the phase space factors and $Q = M_i - M_f - 2m_e$, where M_i and M_f are the masses of the initial and the final nuclei respectively, $m_{\beta\beta}$ is the effective Majorana mass given by Eqn.1.25 and m_e is the electron mass. M_ν is the nuclear matrix element whose calculation is highly challenging. The best limit on the half life of $\beta\beta_{0\nu}$ decay is $T_{1/2} > 1.07 \times 10^{26}$ years coming from the KamLAND-Zen experiment using ^{136}Xe [117]. This gives a bound on the effective mass,

$$m_{\beta\beta} \leq 0.061 - 0.165\text{eV}.$$

The range corresponds to the uncertainty in nuclear matrix elements.

What we have discussed so far is the long-range mechanism of $0\nu\beta\beta$ process due to the three active light neutrinos. In addition to this, the $\beta\beta_{0\nu}$ process can also get contributions from the short-range mechanism due to the heavy particles associated with the seesaw, especially when these particles are at the TeV scale [118–123]. In such cases, the different diagrams may interfere, and as a result, there can be an enhancement or suppression of the rate of $0\nu\beta\beta$. Such contributions to $0\nu\beta\beta$ in the context of left-right symmetric models have been discussed in [124–129].

2.5.2 Lepton Flavor Violation

The phenomenon of neutrino oscillation already indicates that the lepton flavor is violated in the neutral lepton sector. Now, the question is whether this happens in the charged lepton sector as well. Search for charged LFV decays has been carried out for processes involving leptons, mesons, Z bosons etc,. [130, 131]. For the seesaw models considered in this thesis, the most relevant processes are the decays $\mu \to e\gamma$ and $\mu \to 3e$ and $\mu \to e$ conversion in the atomic nucleus. Lot of ongoing experiments are looking for these LFV decays. The current upper bound on the branching ratio (Br) of $\mu \to e\gamma$ is [132],

$$\text{Br}(\mu \to e\,\gamma) \;<\; 4.2 \times 10^{-13}. \tag{2.51}$$

In the case of SM modified with neutrino mass terms and mixing, the prediction for Br($\mu \to e\gamma$) is very small,

$$\text{Br}(\mu \to e\,\gamma)_{SM} \;\leq\; 10^{-50}, \tag{2.52}$$

and hence, this process can not be observed. But in the case of the seesaw models, the new heavy particles can give rise to additional diagrams contributing to this process. For example, in the case of type-I seesaw model, the heavy neutrino contribution to Br($\mu \to e\gamma$) is,

$$\text{Br}(\mu \to e\,\gamma)_{type-I} \;=\; \frac{3\alpha}{8\pi}|V_{ei}V_{i\mu^\dagger}f(x)|^2, \tag{2.53}$$

where

$$x = \left(\frac{M_i^2}{m_W^2}\right), \qquad f(x) = \frac{x(1-6x+3x^2+2x^3-6x^2\ln x)}{2(1-x)^4}. \tag{2.54}$$

Here, $f(x)$ is a slowly varying function of x ranging from 0 to infinity. V is the light heavy mixing matrix and M_i are the masses of the heavy neutrinos. In the case of TeV scale seesaw models where the light-heavy mixing is large, the Br($\mu \to e\gamma$) can be enhanced considerably.

The upper bounds on the branching ratio for the decay $\mu \to 3e$ and $\mu \to e$ conversion in the nucleus also put very strong constraints on the masses of the heavy particles in low scale seesaw models and are given as[133–135],

$$\text{Br}(\mu \to 3e) \;<\; 1.0 \times 10^{-12}, \tag{2.55}$$

$$\text{R}(\mu\, Ti \to e\, Ti) \;<\; 4.3 \times 10^{-12} \tag{2.56}$$

and

$$\text{R}(\mu\, Au \to e\, Au) \;<\; 7 \times 10^{-13}. \tag{2.57}$$

Here, R($\mu\, N \to e\, N$) is the ratio of μ to e conversion rate to the total nucleon muon capture rate for the nucleus N.

2.5.3 Vacuum Stability

The tree level Higgs potential in the SM is given by,

$$V(H) \;=\; -m^2 H^\dagger H \;+\; \lambda (H^\dagger H)^2. \tag{2.58}$$

This will get corrections from higher order loop diagrams of SM particles. Thus, we have the one-loop effective Higgs potential $(V_1(h))$ in standard model as [136, 137],

$$V_1^{SM}(h) \;=\; \sum_i \frac{n_i}{64\pi^2} M_i^4(h) \left[\ln \frac{M_i^2(h)}{\mu^2(t)} \;-\; c_i \right]. \tag{2.59}$$

Here, the index i is summed over all SM particles and $c_{H,G,f} \;=\; 3/2$ and $c_{W,Z} \;=\; 5/6$, where H, G, f, W and Z stand for the Higgs boson, the Goldstone boson, fermions and W and Z bosons respectively ; $M_i(h)$ can be expressed as,

$$M_i^2(h) \;=\; \kappa_i(t)\, h^2(t) \;-\; \kappa_i'(t).$$

The values of n_i, κ_i and κ_i' are given as [136],

$$n_W = 6 \;;\; \kappa_W = \frac{1}{4} g^2(t) \;;\; \kappa_W' = 0$$
$$n_Z = 3 \;;\; \kappa_Z = \frac{1}{4}(g^2(t) + g'^2(t)) \;;\; \kappa_Z' = 0$$

$$n_f = -12 \; ; \; \kappa_f = \frac{1}{2}y_f^2(t) \; ; \; \kappa'_f = 0$$
$$n_H = 1 \; ; \; \kappa_H = \frac{3}{4}\lambda(t) \; ; \; \kappa'_H = m^2(t)$$
$$n_G = 3 \; ; \; \kappa_G = \frac{1}{4}\lambda(t) \; ; \; \kappa'_G = m^2(t) \tag{2.60}$$

Here $h = h(t)$ denotes the classical value of the Higgs field, t being the dimensionless parameter related to the running energy scale μ as $t = log(\mu/M_Z)$. For $h(t) >> v$, the effective potential could be approximated as,

$$V_{eff}^{SM} = \lambda_{eff}(h)\frac{h^4}{4} \tag{2.61}$$

with

$$\lambda_{eff}^{SM}(h) = e^{4\Gamma(h)}\,[\lambda(\mu = h) + \lambda_{eff}^{(1)}(\mu = h) + \lambda_{eff}^{(2)}(\mu = h)\,]. \tag{2.62}$$

$\lambda_{eff}^{(1)}$ and $\lambda_{eff}^{(2)}$ are the one- and two- loop contributions respectively and their expressions are given in appendix-B.

In addition to the correction to the potential, it is well known that the couplings in any quantum field theory get corrections from higher-order loop diagrams because of which, the couplings run with the renormalization scale. For a coupling C, we have the renormalization group equation (RGE),

$$\mu\frac{dC}{d\mu} = \sum_i \beta_C^{(i)} \tag{2.63}$$

where i stands for the i^{th} loop. In the case of the SM, the Higgs quartic coupling λ is pulled down to negative values by renormalization group running, at an energy of about $10^9 - 10^{10}$ GeV. The exact scale at which λ becomes negative depends on the value of α_s and the top quark mass M_t, as the dominant contribution comes from the top-Yukawa coupling, y_t [138, 139]. If the quartic coupling $\lambda(\mu)$ becomes negative at large renormalization scale μ, it means that the Higgs potential would be unbounded from below in the early universe and the vacuum would be unstable in that era. This implies the existence of another low lying vacuum and the EW vacuum can decay to this vacuum via quantum tunneling. But it does not pose any threat to the SM as it has been shown that the decay time is greater than the age of the universe [140], in which case, it is said that the EW vacuum is metastable.

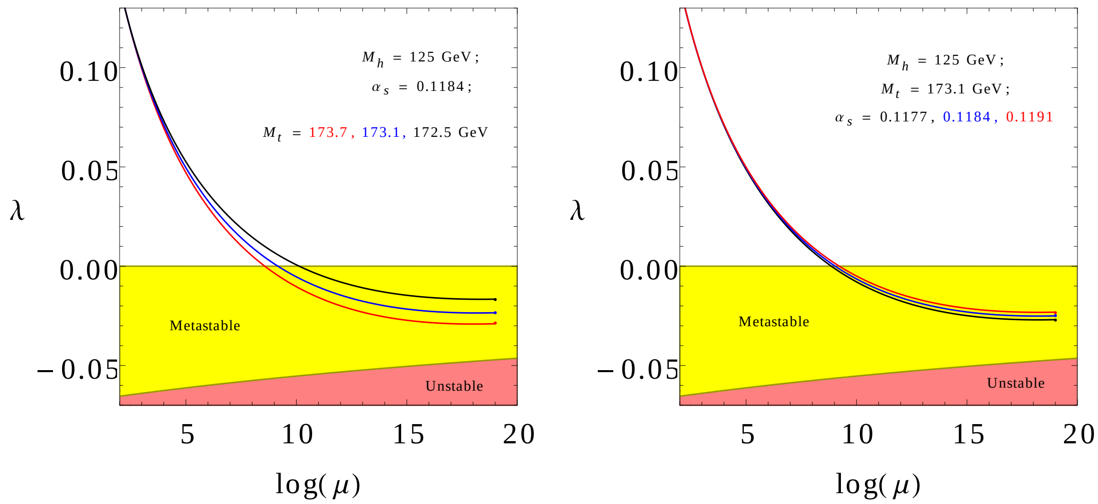

(a) Running of λ for different values of M_t keeping α_S and M_h fixed.

(b) Running of λ for different values of α_s keeping M_t and M_h fixed.

Figure 2.4: Running of λ with the renormalization scale for different values of the SM parameters.

In Fig. 2.4, we have plotted the running of the λ for different values of the SM parameters. In the left panel, we have shown the running for different values of M_t keeping all the other parameters fixed whereas in the right panel, it is shown for different values α_S. From these plots, one can see that an increase in M_t (or equivalently, an increase in y_t) pulls the EW vacuum towards the unstable region whereas an increase in α_s pushes it towards stability. The SM RGEs used are given in appendix-B.

The present central values of the SM parameters, especially the top Yukawa coupling y_t and strong coupling constant α_s with Higgs mass $M_h \approx 125.7$ GeV suggest that the beta function of the Higgs quartic coupling $\beta_\lambda (\equiv dV(h)/dh)$ goes from negative to positive around 10^{15} GeV [138, 139] and this is the scale at which the aforementioned extra deeper minima is situated. The expression for the probability with which the EW vacuum tunnel into that true (deeper) vacuum at zero temperature is given by [140, 141],

$$\mathcal{P}_0 = V_U \, \Lambda_B^4 \exp\Big(- \frac{8\pi^2}{3\,|\lambda(\Lambda_B)|} \Big) \tag{2.64}$$

where Λ_B is the energy scale at which the action of the Higgs potential is minimum. V_U is the volume of the past light cone taken as τ_U^4, where τ_U is the age of the universe

($\tau_U = 4.35 \times 10^{17}$ sec)[142]. [1]. For the vacuum to be metastable, one should have $\mathcal{P}_0 < 1$ which implies that [144],

$$0 > \lambda(\mu) > \lambda_{min}(\Lambda_B) = \frac{-0.06488}{1 - 0.00986 \ln\left(v/\Lambda_B\right)}, \tag{2.65}$$

whereas the situation $\lambda(\mu) < \lambda_{min}(\Lambda_B)$ leads to an unstable vacuum.

In the presence of new physics, the new particles can affect the running of λ and also, alter the effective potential. In fact, the presence of additional Yukawa couplings can destabilize the vacuum whereas the presence of extra scalar quartic couplings can stabilize it. For example, in the context of the SM extended with neutrino masses via type-I seesaw mechanism, the RGE for the SM quartic coupling is modified as,

$$\beta_\lambda = \beta_{\lambda_{SM}} + 4\lambda \mathrm{Tr}(Y_\nu^\dagger Y_\nu) - 4\mathrm{Tr}[(Y_\nu^\dagger Y_\nu)^2]. \tag{2.66}$$

From the above equation, it can be seen that the neutrino Yukawa coupling is giving additional negative contribution. In addition, the contribution of the extra neutrino Yukawa coupling to the one loop effective potential can be written as [145, 146],

$$V_1^\nu(h) = -\frac{((M'^\dagger M')_{ii})^2}{32\pi^2}\left[\ln\frac{(M'^\dagger M')_{ii}}{\mu^2(t)} - \frac{3}{2}\right] - \frac{((M' M'^\dagger)_{jj})^2}{32\pi^2}\left[\ln\frac{(M' M'^\dagger)_{jj}}{\mu^2(t)} - \frac{3}{2}\right]. \tag{2.67}$$

Here $M' = \frac{Y_\nu}{\sqrt{2}}h$ and j and i run over the light and the heavy neutrinos respectively. Also, the above equation is in the diagonal basis for $Y_\nu^\dagger Y_\nu$. In this case, the effective quartic coupling will get modified as,

$$\lambda_{eff}(h) = \lambda_{eff}^{SM}(h) + \lambda_{eff}^{\nu}(h), \tag{2.68}$$

where,

$$\begin{aligned}\lambda_{eff}^{\nu}(h) = -\frac{e^{4\Gamma(h)}}{32\pi^2}\Bigg[&((Y'^\dagger_\nu Y'_\nu)_{ii})^2\left(\ln\frac{(Y'^\dagger_\nu Y'_\nu)_{ii}}{2} - \frac{3}{2}\right) + \\ &((Y'_\nu Y'^\dagger_\nu)_{jj})^2\left(\ln\frac{(Y'_\nu Y'^\dagger_\nu)_{jj}}{2} - \frac{3}{2}\right)\Bigg].\end{aligned} \tag{2.69}$$

Demanding the EW vacuum to be stable in this case can give additional constraints on the masses of the heavy neutrinos as well as the Yukawa couplings. Particularly, in

[1] In this work, we have neglected the loop corrections and gravitational correction to the action of the Higgs potential [143]

the case of the TeV scale seesaw models with sizable Yukawa couplings, the stability of the vacuum can be altered considerably by the contribution from the neutrinos since here, the effect of the neutrino Yukawa couplings enter at a lower scale due to low mass thresholds [146–155]. In this thesis, we have studied the stability of the EW vacuum in the presence of various low scale seesaw models in great detail.

2.5.4 Collider Signatures

One of the major motivations for considering low scale seesaw models is that they can be tested in the collider experiments. The heavy particles of masses of the order of $\sim O(\text{TeV})$ associated with the low scale seesaw models can have interesting signatures in the colliders (See [156] for a recent review.). For example, a Majorana heavy neutrino can give the smoking gun lepton number violating signature of same-sign dilepton plus jets with a very less SM background and no missing transverse energy in the context of hadron colliders [157–165],

$$pp(p\overline{p}) \to W^* \to Nl^{\pm} \to l^{\pm}l^{\pm}jj. \tag{2.70}$$

Similarly, the charged fermions and scalars in the context of type-II and type-III seesaw models can have interesting signatures in the colliders. Since the scalar and the fermionic triplets have direct interactions with the gauge bosons unlike in the case of type-I seesaw model, these states can be directly produced at the colliders via their gauge interactions. For the type-II seesaw, the most important signal will be the detection of a doubly charged scalar which has lepton number violating interactions [166–177]. The most important production channels in this case are,

$$\begin{gathered} pp \to Z^*\gamma^* \to \Delta^{++}\Delta^{--}, \Delta^{+}\Delta^{-} \ \ ; \ \ pp \to W^{\pm *}W^{\pm *} \to \Delta^{\pm}\Delta^{\pm} \ \ ; \\ pp \to W^* \to \Delta^{\pm\pm}\Delta^{\mp}, \Delta^{\pm\pm}W^{\mp} \end{gathered} \tag{2.71}$$

The doubly charged Higgs can decay to $l^{\pm}l^{\pm}$, $W^{\pm}W^{\pm}$, $W^{\pm}\Delta^{\pm}$ or $\Delta^{\pm}\Delta^{\pm}$. The triplet fermions in the type-III seesaw model can be produced and detected in the collider experiments through the process(es) [166, 178–185],

$$pp \to \Sigma^{+}\Sigma^{-} \to m\,j + n\,l + \not{E}_T \tag{2.72}$$

where m, n are integers. In the case of inverse seesaw model where the heavy neutrinos are pseudo-Dirac neutrinos, the golden signature is the trilepton signal [166, 186–194] :

$$pp(p\bar{p}) \to W^* \to Nl^\pm \to l^\pm l^\pm l^\pm + \not{E}_T. \tag{2.73}$$

The presence of the extra gauge bosons and additional scalars in the gauge extensions with Majorana neutrinos provide more ways of testing the models in the colliders. In this thesis, we have studied an inverse seesaw model in the context of a class of $U(1)$ extensions of the SM in Chapter 6, where we have constrained the mass and the coupling of the extra gauge boson from collider bounds.

Chapter 3

Implications of the Dark-LMA Solution for Neutrino-less Double Beta Decay

3.1 Introduction

:

The question whether neutrinos are Dirac or Majorana particle is one of the most fundamental issues in physics which is still unanswered. The most straightforward way to probe the Majorana nature of neutrinos is through $0\nu\beta\beta$ experiments [52][1]. They measure the half-life, which in the standard mechanism can be expressed in terms of the effective mass $m_{\beta\beta}$, which in turn depends on the oscillation parameters as well as the neutrino mass ordering, as discussed in section 2.5.1. A positive signal of $0\nu\beta\beta$ will be a definite confirmation of the existence of lepton number violating Majorana mass term for the neutrinos [93]. Such a term requires the existence of some theory beyond the Standard Model of particle physics. This could also be related to the observed dominance of matter over antimatter which is essential for our existence. The searches for $0\nu\beta\beta$ have been on-going for the past several decades [195].

In this chapter, we discuss the implications of the so-called Dark-LMA (DLMA)

[1]The heavy Majorana neutrinos can also be probed via the lepton number violating dilepton signal at the hadron colliders [157–165].

[196–198] solution to the solar neutrino problem for $0\nu\beta\beta$. The standard LMA solution corresponds to standard neutrino oscillations with $\Delta m^2_{21} \simeq 7.5 \times 10^{-5}$ eV^2 and $\sin^2\theta_{12} \simeq 0.3$, and satisfies the solar neutrino data at high significance. The DLMA solution appears as a nearly-degenerate solution to the solar neutrino problem for $\Delta m^2_{21} \simeq 7.5 \times 10^{-5}$ eV^2 and $\sin^2\theta_{12} \simeq 0.7$, once we allow for the existence of non-standard neutrino interactions (NSIs) in addition to standard oscillations. The KamLAND experiment is unable to break this degeneracy since it observes neutrino oscillations in vacuum which depends on $\sin^2 2\theta_{12}$ which is the same for both LMA and DLMA solutions. The occurrence of the DLMA solution can also adversely affect the determination of mass ordering in beam based neutrino oscillation experiments in presence of NSI [199–201]. In this chapter, we will see that while the IH band for the effective mass in $0\nu\beta\beta$ experiments remains nearly same for LMA and DLMA solutions, the NH band gets shifted upwards for the DLMA solution. As a result this may make it possible for the next-generation experiments to start probing $0\nu\beta\beta$ for NH as well. Along with opening up new regions of the effective neutrino mass to be probed by future $0\nu\beta\beta$ experiments, this also provides a way of testing the long-standing DLMA solution to the solar neutrino problem, irrespective of the value of the NSI parameters.

In the next section, we discuss the matter effect in solar neutrinos and the DLMA solution in the presence of large NSI. In section 3.3, we briefly discuss the various experiments looking for $0\nu\beta\beta$ and their current status. Then we analyze the implications of the DLMA solution to $0\nu\beta\beta$ in section 3.4. After examining the sensitivity of the new parameter space for $0\nu\beta\beta$ due to the DLMA solution in the future ^{136}Xe experiments in section 3.5, we summarize in section 3.6.

3.2 Large NSI and the DLMA Solution

The presence of NSI will modify the neutrino flavor evolution equation resulting in a degeneracy which leads to the DLMA solution. This requires a solar mixing angle greater than $\pi/4$ and indicates an uncertainty in the neutrino mass hierarchy. We need non-oscillation experiments to lift this degeneracy. In this section, after reviewing the two flavor neutrino evolution equation in matter and the MSW effect, we discuss how the presence of NSI will lead to the DLMA solution for θ_{12}.

3.2.1 Two Flavor Neutrino Evolution Equation in Matter

Assuming there are only two flavors and two mass eigenstates corresponding to them, the time evolution equation in vacuum for neutrinos in the mass eigenstate basis can be written as,

$$i \begin{bmatrix} \dot{\nu_1} \\ \dot{\nu_2} \end{bmatrix} = \begin{bmatrix} E_1 & 0 \\ 0 & E_2 \end{bmatrix} \begin{bmatrix} \nu_1 \\ \nu_2 \end{bmatrix}. \tag{3.1}$$

This can be converted to the flavor basis using a unitary transformation,

$$iU \begin{bmatrix} \dot{\nu_1} \\ \dot{\nu_2} \end{bmatrix} = U \begin{bmatrix} E_1 & 0 \\ 0 & E_2 \end{bmatrix} U^T U \begin{bmatrix} \nu_1 \\ \nu_2 \end{bmatrix}$$

or,

$$i \begin{bmatrix} \dot{\nu_e} \\ \dot{\nu_\mu} \end{bmatrix} = U \begin{bmatrix} E_1 & 0 \\ 0 & E_2 \end{bmatrix} U^T \begin{bmatrix} \nu_e \\ \nu_\mu \end{bmatrix} \tag{3.2}$$

Where U is the 2×2 orthogonal neutrino mixing matrix given by,

$$U = \begin{bmatrix} \cos\theta & \sin\theta \\ -\sin\theta & \cos\theta \end{bmatrix}. \tag{3.3}$$

Taking $E_i = p + \dfrac{m_i^2}{2E}$ and defining $\Delta_i = \dfrac{m_i^2}{2E}$ and $\Delta_{21} = \Delta_2 - \Delta_1 = \dfrac{\Delta m^2}{2E}$, the evolution equation becomes,

$$i \begin{bmatrix} \dot{\nu_e} \\ \dot{\nu_\mu} \end{bmatrix} = \frac{\Delta_{21}}{2} \begin{bmatrix} -\cos 2\theta & \sin 2\theta \\ \sin 2\theta & \cos 2\theta \end{bmatrix} \begin{bmatrix} \nu_e \\ \nu_\mu \end{bmatrix}. \tag{3.4}$$

Here, we have ignored the constant phase part that has no contribution to the transition probability. Thus, the Hamiltonian for neutrino propagation in vacuum is obtained as,

$$H_{vac} = \frac{\Delta_{21}}{2} \begin{bmatrix} -\cos 2\theta & \sin 2\theta \\ \sin 2\theta & \cos 2\theta \end{bmatrix}. \tag{3.5}$$

When the active neutrino flavors propagate through matter, their evolution equation is modified by the potentials due to their interactions with the medium via the coherent forward elastic weak charged current (CC) and the neutral current (NC) scatterings [25–27]. Since normal matter consists of electron, proton and neutron, the CC interactions affect only ν_e whereas the NC interactions affect all the three active neutrinos. The potential due to NC scattering modifies the propagation equation for all the neutrinos in the same way and hence it does not affect the final expressions of neutrino oscillation probabilities. The CC interaction affects only ν_e and it modifies the probability expression significantly. The interaction potential is given by the average of the effective Hamiltonian over the electron background and is given by,

$$H_{CC} = \sqrt{2} G_F N_e. \tag{3.6}$$

Thus, in the presence of matter the total Hamiltonian becomes,

$$H_{vac+mat} = \begin{bmatrix} -\frac{\Delta_{21}}{2}\cos 2\theta + \sqrt{2}G_F N_e & \frac{\Delta_{21}}{2}\sin 2\theta \\ \frac{\Delta_{21}}{2}\sin 2\theta & \frac{\Delta_{21}}{2}\cos 2\theta \end{bmatrix}, \tag{3.7}$$

and the evolution equation in matter becomes,

$$i \begin{bmatrix} \dot{\nu_e} \\ \dot{\nu_\mu} \end{bmatrix} = \begin{bmatrix} -\frac{\Delta_{21}}{2}\cos 2\theta + \sqrt{2}G_F N_e & \frac{\Delta_{21}}{2}\sin 2\theta \\ \frac{\Delta_{21}}{2}\sin 2\theta & \frac{\Delta_{21}}{2}\cos 2\theta \end{bmatrix} \begin{bmatrix} \nu_e \\ \nu_\mu \end{bmatrix}. \tag{3.8}$$

This evolution equation describes the $\nu_e \leftrightarrow \nu_\mu$ oscillation in matter. Now, we can apply a unitary transformation to convert the above equation into the mass basis using the matrix,

$$U_M = \begin{bmatrix} \cos\theta_M & \sin\theta_M \\ -\sin\theta_M & \cos\theta_M \end{bmatrix}, \tag{3.9}$$

where θ_M is the mixing angle in matter and it can be expressed as,

$$\tan 2\theta_M = \frac{\frac{\Delta m^2_{21}}{2E}\sin 2\theta}{\frac{\Delta m^2_{21}}{2E}\cos 2\theta - \sqrt{2}G_F N_e}. \tag{3.10}$$

Here, θ is the mixing angle in vacuum. Now if the condition,

$$\frac{\Delta m^2_{21}}{2E}\cos 2\theta = \sqrt{2}G_F N_e \tag{3.11}$$

is satisfied, $\tan 2\theta_M$ becomes infinite. i.e., $\theta_M = \pi/4$, which corresponds to maximum mixing even if the vacuum mixing angle θ is small. This is called MSW resonance and the above condition is called the MSW resonance condition [25–27]. The MSW resonance condition is sensitive to the sign of Δm^2_{21}. Since the sign of the perturbing potential is positive for neutrinos, resonance can occur only if $\Delta_{21} > 0$ and $\theta < \pi/4$ or $\Delta_{21} < 0$ and $\theta > \pi/4$. Similarly, for antineutrinos, the resonance condition is given by $\Delta_{21} > 0$ and $\theta > \pi/4$ or $\Delta_{21} < 0$ and $\theta < \pi/4$. Thus the enhancement of the oscillation probabilities depends on the sign of Δ_{21} and the octant of θ and the experimental measurement of this resonance can help in determining the same.

Now, the difference of neutrino eigenenergies in matter is (eigenvalues of $H_{vac+mat}$),

$$E_1 - E_2 = \sqrt{\left(\frac{\Delta m^2}{2E}\cos 2\theta - \sqrt{2}G_F N_e\right)^2 + \left(\frac{\Delta m^2}{2E}\right)^2 \sin^2\theta}. \tag{3.12}$$

Noting that $E_2 - E_1 = (m_2^2 - m_1^2)/2E$ in vacuum, we can see from the above equation how the mass squared difference is modified in the presence of matter.

3.2.2 Three Flavors neutrino evolution equation in the presence of NSI

In the three flavor scenario, the Hamiltonians for the neutrino and the antineutrino flavor states are given as,

$$H^{\nu} = H_{vac} + H_{mat} \quad \text{and} \quad H^{\bar{\nu}} = (H_{vac} - H_{mat})^* \tag{3.13}$$

respectively. Here,

$$H_{vac} = U_{vac} D_{vac} U^{\dagger}_{vac}, \tag{3.14}$$

with

$$D_{vac} = \frac{1}{2E_\nu}\,\text{diag}\,(0, \Delta m^2_{21}, \Delta m^2_{31}), \tag{3.15}$$

and $\Delta m^2_{ij} = m_i^2 - m_j^2$. In the following discussion, we have assumed that the active neutrino masses follow NH. Including NSI, the most general matter potential can be parametrized as,

$$H_{mat} = H_m + H_{NSI} = \sqrt{2}G_F N_e(r)\begin{bmatrix}1 & 0 & 0\\ 0 & 0 & 0\\ 0 & 0 & 0\end{bmatrix} + \sqrt{2}G_F \sum_{f=e,u,d} N_f(r)\begin{bmatrix}\epsilon^f_{ee} & \epsilon^f_{e\mu} & \epsilon^f_{e\tau}\\ \epsilon^{f*}_{e\mu} & \epsilon^f_{\mu\mu} & \epsilon^f_{\mu\tau}\\ \epsilon^{f*}_{e\tau} & \epsilon^{f*}_{\mu\tau} & \epsilon^f_{\tau\tau}\end{bmatrix}. \tag{3.16}$$

The Lagrangian for NSI in matter is given by the effective four fermion operator as,

$$\mathcal{L}_{NSI} = -2\sqrt{2}G_F\epsilon_{\alpha\beta}^{fP}(\bar{\nu_\alpha}\gamma^\mu\nu_\beta)(\bar{f}\gamma_\mu Pf), \tag{3.17}$$

where f is the charged fermion, P is the projection operator (left and right) and $\epsilon_{\alpha\beta}^{fP}$ are the NSI parameters which govern the deviation from the standard interactions. NSI affects the neutrino propagation in matter through vector couplings and hence in the matter Hamiltonian, we can write $\epsilon_{\alpha\beta}^{f} = \epsilon_{\alpha\beta}^{fL} + \epsilon_{\alpha\beta}^{fR}$.

3.2.3 Earth Matter potential for the solar and KamLAND neutrinos

Following the discussion in [202], for this case, we can work in the limit $\Delta m_{31}^2 \to \infty$ which effectively means,

$$G_F\sum_f N_f(r)\epsilon_{\alpha\beta}^{f} \ll \frac{\Delta m_{31}^2}{E_\nu}. \tag{3.18}$$

The survival probability P_{ee} can be written in this approximation as,

$$P_{ee} = c_{13}^4 P_{eff} + s_{13}^4. \tag{3.19}$$

We can calculate the probability, P_{eff} in an effective 2×2 model with the Hamiltonian $H_{eff} = H_{vac}^{eff} + H_{mat}^{eff}$ where,

$$H_{vac}^{eff} = \frac{\Delta m_{21}^2}{4E_\nu}\begin{bmatrix} -\cos 2\theta_{12} & \sin 2\theta_{12} \\ \sin 2\theta_{12} & \cos 2\theta_{12}\end{bmatrix} \quad \text{and} \tag{3.20}$$

$$H_{mat}^{eff} = \sqrt{2}G_F N_e(r)\begin{bmatrix} c_{13}^2 & 0 \\ 0 & 0\end{bmatrix} + \sqrt{2}G_F\sum_f N_f(r)\begin{bmatrix} -\epsilon_D^f & \epsilon_N^f \\ \epsilon_N^{f*} & \epsilon_D^f\end{bmatrix}. \tag{3.21}$$

The new parameters ϵ_D^f and ϵ_N^f are related to $\epsilon_{\alpha\beta}^f$ as,

$$\begin{aligned}\epsilon_D^f =& c_{13}s_{13}Re[e^{i\delta_{CP}}(s_{23}\epsilon_{e\mu}^f + c_{23}\epsilon_{e\tau}^f)] - (1+s_{13}^2)c_{23}s_{23}Re(\epsilon_{\mu\tau}^f) - \frac{c_{13}^2}{2}(\epsilon_{ee}^f \\ &- \epsilon_{\mu\mu}^f) + \frac{s_{23}^2 - s_{13}^2c_{23}^2}{2}(\epsilon_{\tau\tau}^f - \epsilon_{\mu\mu}^f),\end{aligned} \tag{3.22}$$

$$\epsilon_N^f = c_{13}(c_{23}\epsilon_{e\mu}^f - s_{23}\epsilon_{e\tau}^f) + s_{13}e^{-i\delta_{CP}}[s_{23}^2\epsilon_{\mu\tau}^f - c_{23}^2\epsilon_{\mu\tau}^{f*} + c_{23}s_{23}(\epsilon_{\tau\tau}^f - \epsilon_{\mu\mu}^f)] \tag{3.23}$$

Thus, the oscillation probabilities depend on $\Delta m_{21}^2, \theta_{12}, \theta_{13}$, one real matter parameter ϵ_D^f and one complex matter parameter ϵ_N^f for each f. In the analysis of solar data, one considers a particular choice of f ($f = e, u$ or d) at a time. Since the angle θ_{13} appears only through Eqn.3.19, it is enough to consider $0 \leq \theta_{13} \leq \pi/2$. The effective Hamiltonian H_{eff} is invariant under $\Delta m^2_{21} \rightarrow -\Delta m^2_{21}$ and $\theta_{12} \rightarrow \theta_{12} + \pi/2$ and hence without loss of generality, one can take $\Delta m^2_{21} > 0$. Also from H^{vac}_{eff} we can write $-\pi \leq 2\theta_{12} \leq \pi$ or $-\pi/2 \leq \theta_{12} \leq \pi/2$. The probabilities are insensitive to the non-diagonal entries of Eqn.3.21 which gives the symmetry $\theta_{12} \rightarrow -\theta_{12}$ and $\epsilon^f_N \rightarrow -\epsilon^f_N$ and this further restricts θ_{12} to $0 \leq \theta_{12} \leq \pi/2$. Thus in the most general case, we have, $\Delta m^2_{21} > 0, 0 \leq \theta_{ij} \leq \pi/2$, ϵ^f_D as real and ϵ^f_N as complex. In the NSI, if we take the fermion as electron ($f = e$), there is another exact symmetry. In this case,

$$H^{eff}_{mat} = \sqrt{2} G_F N_e(r) \begin{bmatrix} -\epsilon^e_D + \dfrac{c^2_{13}}{2} & \epsilon^e_N \\ \epsilon^{e*}_N & \epsilon^e_D - \dfrac{c^2_{13}}{2} \end{bmatrix}. \tag{3.24}$$

The probabilities are invariant under $H \rightarrow -H^*$ which corresponds to the symmetry transformations $\Delta m^2_{21} \rightarrow -\Delta m^2_{21}, \epsilon^e_D - \dfrac{c^2_{13}}{2} \rightarrow -(\epsilon^e_D - \dfrac{c^2_{13}}{2}), \epsilon^e_N \rightarrow -\epsilon^{e*}_N$. Combining this we can reabsorb the sign flip of both Δm^2_{21} and ϵ^{e*}_N into θ_{12}, resulting in the transformation $\theta_{12} \rightarrow \pi/2 - \theta_{12}, \epsilon^e_D \rightarrow c^2_{13} - \epsilon^e_D, \epsilon^e_N \rightarrow \epsilon^{e*}_N$. This invariance implies that for each point in the light side of the parameter space (region with $\theta_{12} < \pi/4$) there is a point in the dark side (region with $\theta_{12} > \pi/4$), which cannot be distinguished experimentally by oscillation alone and this is the origin of the DLMA solution [196–198, 202]. Note that such a symmetry is no longer exact for $f = u/d$, but it is still realized with considerable accuracy.

The scattering experiments can resolve the degeneracy associated with the DLMA solution by measuring the NSI parameters. For instance, in [203], combined constraints from neutrino oscillation and CHARM and NuTeV measurements were used to demonstrate that the degeneracy between the two LMA solutions can be resolved if NSI is only with the down quarks. Subsequently, the study performed in [204] included the COHERENT neutrino-nucleus scattering data and showed that the DLMA solution can be disfavored at the 3.1σ and 3.6σ C.L. for NSI with up and down quarks, respectively. However, it is worth stressing that these bounds depend on the mass of the light mediator and it has been shown in [205] that the COHERENT data excludes the DLMA solution at 95% C.L. for light mediator mass > 48 MeV only. The global analysis including oscillation and COHERENT data performed in [206] shows that the DLMA solution is still allowed at 3σ, albeit for a smaller range of values of NSI parameters and for light mediators of mass ≥ 10 MeV. It has been found that by including COHERENT constraints, the DLMA solution is valid at 2σ confidence level for values of NSI parameters in the range [206],

$$-0.41 < \epsilon^u_{ee} - \epsilon^u_{\mu\mu} < 0.729 \quad \text{and} \quad -0.373 < \epsilon^d_{ee} - \epsilon^d_{\mu\mu} < 0.668. \tag{3.25}$$

Also, from now onwards, we denote the DLMA solution for θ_{12} in the presence of NSI as θ_{D12} and the standard LMA solution as θ_{12}. The 3σ ranges of these two parameters are given in Table 3.1 [48, 206].

3.3 $0\nu\beta\beta$ Experiments

The search for $0\nu\beta\beta$ is of great importance since it will tell us if neutrinos are Dirac particles or lepton number violating Majorana particles. A lot of experiments searching for this rare decay have been performed in the past and there are several ongoing and future experiments that search for $0\nu\beta\beta$ using different techniques and isotopes (See [207] for a recent review.). As mentioned before, these experiments measure the half-life which is given by,

$$T^{0\nu}_{1/2} = a\epsilon\sqrt{\frac{MT}{BdE}}\,, \tag{3.26}$$

where M is the mass of the isotope, T is the observation time scale, B is the background in counts/(keV kg yr), dE is the energy resolution and ϵ is the efficiency. This half life is then related to the effective mass $m_{\beta\beta}$ through Eqn.2.50. There are various parameters that one should take into account like the Q value and natural abundance of the isotope, cost effectiveness of the isotopic enrichment, resolution, efficiency, background etc. while planning a $0\nu\beta\beta$ experiment using a particular isotope. The most commonly used isotopes are ^{136}Xe, ^{76}Ge and ^{130}Te.

In general, the experiments follow two main approaches where main difference is only how the electrons are detected :

- Indirect methods : The unnatural concentrations of the daughter nuclei in selected samples are measured after very long exposures. Eg. : KamLAND-Zen

[117], GERDA [208], nEXO [209], CUORE [210].

- Direct methods : The properties of the two electrons emitted in real time in the $\beta\beta$ decay are measured. Here, the $0\nu\beta\beta$ decay isotope is separate from the detector. Eg. : SuperNEMO [211, 212].

As mentioned in chapter 2, the best limit on the half life of $\beta\beta_{0\nu}$ decay is $T_{1/2} < 1.5 \times 10^{25}$ years coming from the KamLAND-Zen experiment using ^{136}Xe [117]. This gives a bound on the effective mass,

$$m_{\beta\beta} \ \leq \ 0.061 - 0.165\text{eV}.$$

The range corresponds to the uncertainty in nuclear matrix elements. Also, the GERDA experiment using ^{76}Ge gives a bound on $T_{1/2}$ as $T_{1/2}(^{76}Ge) > 8 \times 10^{25}$ years [208] and the combined results of Cuoricino and CUORE experiments using ^{130}Te give a bound of $T_{1/2}(^{130}Te) > 1.5 \times 10^{25}$ years [210]. The corresponding bounds on $m_{\beta\beta}$ are less stringent compared to the one coming from the KamLAND-Zen. Among the various next generation experiments, the ^{136}Xe experiment - nEXO has the best sensitivity with a 3σ discovery sensitivity of $T_{1/2} = 5.7 \times 10^{27}$ years [209]. This corresponds to $m_{\beta\beta}$ sensitivity of $\sim 0.007 - 0.020$ eV.

3.4 Predictions of the DLMA solution for $0\nu\beta\beta$

The half-life for $0\nu\beta\beta$ process in the standard three generation picture is given by Eqn.2.50 as,

$$\frac{\Gamma_{0\nu\beta\beta}}{\ln 2} = G\left|\frac{M_\nu}{m_e}\right|^2 m_{\beta\beta}^2$$

Here, $m_{\beta\beta}$ is the effective neutrino mass, which, in the standard parametrization given in Eqn.1.17 is given by,

$$m_{\beta\beta} \ = \ |m_1\, c_{12}^2 c_{13}^2 + m_2\, s_{12}^2 c_{13}^2 e^{2i\alpha_2} + m_3\, s_{13}^2 e^{2i\alpha_3}|. \tag{3.27}$$

Clearly, $|m_{\beta\beta}|$ depends on whether the neutrino mass states follow normal or inverted hierarchy or if they are quasi-degenerate in addition to the mixing parameters.

Fig. 3.1 shows $m_{\beta\beta}$ as a function of the lightest neutrino mass for both NH and IH. The pink region is for NH with the standard solution for θ_{12} and the red band

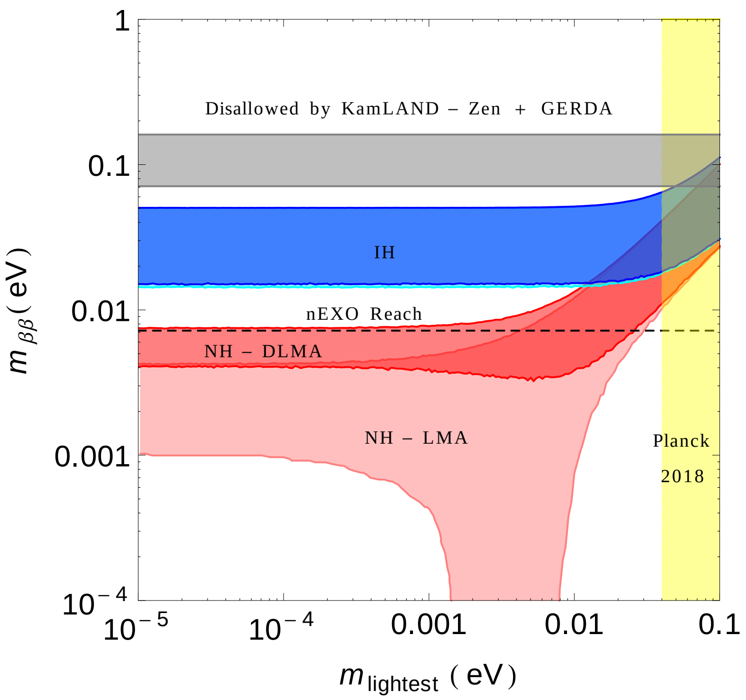

Figure 3.1: The effective neutrino mass $m_{\beta\beta}$ for $0\nu\beta\beta$ as a function of the lightest neutrino mass for both NH and IH. The pink region is for NH with the standard solution for θ_{12} and the red band is for NH with θ_{D12}. For the IH case(the blue band), $m_{\beta\beta}$ remains the same for the DLMA solution. See text for details.

is for NH with θ_{D12}, corresponding to the DLMA solution [2]. The dark blue band is for IH with the standard θ_{12} value and the cyan band (which overlaps with the blue band) is for IH with θ_{D12}. The gray band $(0.071 - 0.161$ eV) corresponds to the current upper limit from combined results of GERDA and KamLAND-Zen experiments [213]. The region above this is disallowed. The range corresponds to the NME uncertainty [208, 214, 215]. The black dashed line represents the future 3σ sensitivity of the nEXO experiment : $T_{1/2} = 5.7 \times 10^{27}$ years [209], which, for the highest value of NME, translates to $m_{\beta\beta} = 0.007$ eV. This can probe a small part of the NH region with the LMA solution for $m_{lightest} \geq 0.005$ eV, whereas the upper edge of the DLMA region can be probed even for small values of $m_{lightest}$. The yellow region is disfavored by the

[2]Note that the effective dimension-6 operator that gives rise to NSI and the dark-LMA solution is a lepton flavor violating operator whereas it conserves the lepton number. On the other hand, $0\nu\beta\beta$ violates lepton number by two units. Hence the NSI operators can not contribute directly to $0\nu\beta\beta$.

cosmological constraints on the sum of the light neutrino masses [57]. In obtaining this plot, all the oscillation parameters are varied in their 3σ ranges [48] and the Majorana phases are varied from 0 to π.

From the figure, we can see that for NH, $m_{\beta\beta}$ for the DLMA solution is higher than that for the standard LMA solution, shifting into the gap between IH and NH. The effect is more pronounced for lower values of $m_{lightest}$. There is some overlap in the predictions between the maximum value of $m_{\beta\beta}$ for the LMA with the minimum value of this for the DLMA solution, which increases as $m_{lightest}$ increases. One noteworthy feature is the absence of the cancellation region for the DLMA solution. For IO, the predicted values of $m_{\beta\beta}$ remain the same for LMA and DLMA solutions. Since the predictions of $m_{\beta\beta}$ for NH with LMA and IH with DLMA are well separated, the generalized hierarchy degeneracy [200] is not present.

The behavior of $m_{\beta\beta}$ can be understood by considering the limiting cases for different mass schemes.

Inverted Hierarchy : In this case, for very small values of m_3 such that $m_3 << \sqrt{\Delta m^2_{atm}}$, $m_2 \approx m_1 \approx \sqrt{\Delta m^2_{atm}}$, the effective mass is given as,

$$m_{\beta\beta_{IH}} \approx \sqrt{\Delta m^2_{atm}}(|\, c^2_{12}c^2_{13} + s^2_{12}c^2_{13}e^{2i\alpha_2}|).$$

In this region, $m_{\beta\beta}$ is independent of m_3 and is bounded from above and below by a maximum and minimum value given by [216],

$$m_{\beta\beta_{IHmax}} = |c^2_{13}\sqrt{\Delta m^2_{atm}}\,| \qquad (\alpha_2 = 0, \pi),$$

$$m_{\beta\beta_{IHmin}} = |c^2_{13}\cos 2\theta_{12}\sqrt{\Delta m^2_{atm}}\,| \qquad (\alpha_2 = \pi/2).$$

The maximum value is independent of θ_{12} while for the minimum value, we can see from Table 3.1, that the 3σ range for $|\cos 2\theta_{12}|$ is the same for both LMA and DLMA solutions. This explains why the prediction for $m_{\beta\beta}$ is the same for both the cases in this region.

Now, as m_3 approaches $\sim \sqrt{\Delta m^2_{atm}}$, the other masses can be approximated as, $m_1 \approx m_2 \approx \sqrt{2\Delta m^2_{atm}}$ and the effective mass becomes,

$$m_{\beta\beta_{IH}} = \sqrt{\Delta m^2_{atm}}\; |(\sqrt{2}c^2_{13}(c^2_{12} + s^2_{12}e^{2i\alpha_2}) + s^2_{13}e^{2i\alpha_3})|.$$

	$\sin^2\theta_{12}$	$\sin^2\theta_{D12}$	$\cos2\theta_{12}$	$\cos2\theta_{D12}$	$\sin^2\theta_{13}$
$Maximum$	0.350	0.725	0.45	-0.30	0.024
$Minimum$	0.275	0.650	0.30	-0.45	0.020

Table 3.1: The 3σ ranges of the oscillation parameters relevant for understanding the behavior of the effective mass in different limits.

This is maximum for $\alpha_2 = \alpha_3 = 0$ and is again independent of θ_{12}. Also, $m_{\beta\beta_{IH}}$ is minimum for $\alpha_2 = \pi/2$ and $\alpha_3 = 0$ or $\pi/2$ depending on whether we take θ_{12} or θ_{D12}. But since, s^2_{13} is very small, this is almost independent of what we choose for α_3 and effectively, the minimum of $m_{\beta\beta_{IH}}$ in this regime is approximated as,

$$m_{\beta\beta_{IHmin}} = \sqrt{\Delta m^2_{atm}}\ |\sqrt{2}c^2_{13}\cos2\theta_{12}|,$$

which is independent of the solution for θ_{12}.

Normal Hierarchy: Unlike in IO, the behavior of $m_{\beta\beta}$ is different for the LMA as well as the DLMA solutions of θ_{12}. For very small values of m_1 such that $m_1 << m_2 \approx \sqrt{\Delta m^2_{sol}} << m_3 \approx \sqrt{\Delta m^2_{atm}}$, $m_{\beta\beta}$ can be written as,

$$m_{\beta\beta_{NH}} = \sqrt{\Delta m^2_{atm}}|\sqrt{r}\, s^2_{12}c^2_{13}e^{2i\alpha_2} + s^2_{13}e^{2i\alpha_3}|,$$

where, $r = |\dfrac{\Delta m^2_{sol}}{\Delta m^2_{atm}}|$. The maximum value of this corresponds to $\alpha_2 = \alpha_3 = 0, \pi$ and the minimum value corresponds to $\alpha_2 = 0$ and $\alpha_3 = \pi/2$. These will be higher for higher values of $\sin^2\theta_{12}$. This explains why the prediction for $m_{\beta\beta}$ for the DLMA solution in this region is higher.

Moving on to the cancellation region, the typical values of masses are $m_1 \sim 0.005$ eV, $m_2 \sim 0.01$ eV and $m_3 \sim 0.05$ eV. Then, the minimum of $m_{\beta\beta}$ $(\alpha_2 = \alpha_3 = \pi/2)$ can be approximated as,

$$m_{\beta\beta_{min}} \approx m_1|(1 - 3s^2_{12}c^2_{13} - 11s^2_{13})|.$$

For the values of s^2_{12} and s^2_{13} as listed in the Table 3.1, complete cancellation is possible in the LMA region. However, for s^2_{12} in the DLMA region, such a cancellation is not possible because of higher values of s^2_{12}.

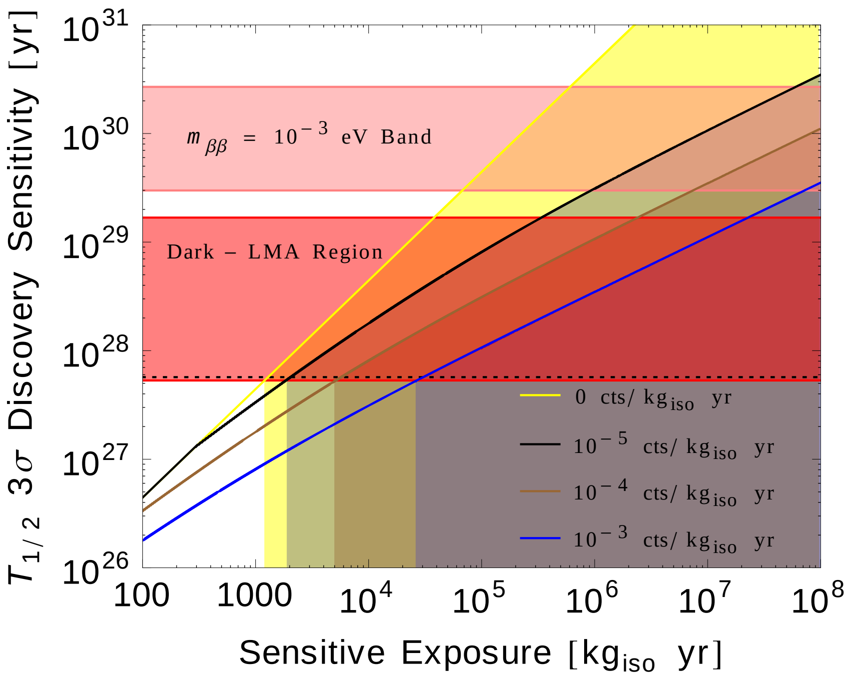

Figure 3.2: ^{136}Xe discovery sensitivity as a function of sensitive exposure for a selection of sensitive background levels. The yellow, black, brown and blue lines correspond to different values of the sensitive background levels of 0, 10^{-5}, 10^{-4} and 10^{-3} cts/(kg$_{\rm iso}$ yr) respectively.

As we increase the value of m_1 and reach the limit of partial hierarchy where $m_1 \approx m_2 \approx \sqrt{\Delta m^2_{sol}} << m_3 \approx \sqrt{\Delta m^2_{atm}}$, the maximum value of $m_{\beta\beta}$ is given by,

$$m_{\beta\beta_{NHmax}} \approx \sqrt{\Delta m^2_{atm} r} c^2_{13} \qquad (\alpha_2 = \alpha_3 = 0),$$

which is independent of θ_{12}. Hence the maximum values of $m_{\beta\beta}$ for the two LMA solutions tend to overlap. In QD limit, $m_{\beta\beta}$ varies linearly with the common mass scale m_0 and both maximum and minimum values are independent of θ_{12}.

At this point it is worthwhile to note that if we assume the existence of a fourth sterile neutrino as suggested by the LSND/MiniBooNE results, even with the standard LMA solution, the predicted $m_{\beta\beta}$ for NH can be in the desert region [217, 218]. In fact, depending on the value of the mass squared difference governing the LSND/MiniBooNE oscillations, the prediction can even overlap with the IH prediction for three generation and hence, can be probed by the near future experiments.

Isotope	NME (M_ν)	$G(10^{-15}\text{year}^{-1})$	$T_{1/2}$ range (years)
^{136}Xe	$1.6 - 4.8$	14.58	$5.3 \times 10^{27} - 1.7 \times 10^{29}$
^{76}Ge	$2.8 - 6.1$	2.363	$2.0 \times 10^{28} - 3.4 \times 10^{29}$
^{130}Te	$1.4 - 6.4$	14.22	$4.9 \times 10^{28} - 2.2 \times 10^{29}$

Table 3.2: The $T_{1/2}$ ranges corresponding to the DLMA region $m_{\beta\beta} = 0.004 - 0.0075$ eV for different isotopes. The NME values [208, 214] and the phase space factors [215] used in the calculation are also given.

3.5 Sensitivity in the future experiments

Here, we discuss a simple method to obtain the sensitivity of the DLMA region in the future ^{136}Xe experiments following the discussion in reference [213]. The discovery sensitivity is prescribed as the value of $T_{1/2}$ for which an experiment has a 50% probability of measuring a 3σ signal above the background. It is defined as,

$$T_{1/2} = \ln 2 \frac{N_A \epsilon}{m_a S_{3\sigma}(B)}. \tag{3.28}$$

Here, N_A is the Avogadro number, m_a is the atomic mass of the isotope, $B = \beta\epsilon$ is the expected background where ϵ and β denote the sensitive exposure and background respectively ; $S_{3\sigma}$ is the value for which half of the measurements would give a signal above B assuming a Poisson signal and is calculated from the relation

$$1 - CDF_{Poisson}(C_{3\sigma}|S_{3\sigma} + B) = 50\%.$$

$C_{3\sigma}$ denotes the number of counts for which the cumulative Poisson distribution with mean B follows $CDF_{Poisson}(C_{3\sigma}|B) = 3\sigma$. To avoid the discrete variations that would arise in the discovery sensitivity if $C_{3\sigma}$ is restricted to be integer valued, we use the following definition of $CDF_{Poisson}$ as a continuous distribution in C using the normalized upper incomplete gamma function,

$$CDF_{Poisson}(C|\mu) = \frac{\Gamma(C+1, \mu)}{\Gamma(C+1)}.$$

Using the above equations, the $T_{1/2}$ discovery sensitivities of ^{136}Xe as a function of ϵ for various values of β are shown in Fig. 3.2. In this plot, the red shaded band corresponds to the new allowed region of $m_{\beta\beta} \sim 0.004 - 0.0075$ eV for the DLMA solution. This band in $m_{\beta\beta}$ which is due to the variation of the parameters in the PMNS matrix, is converted to a band in $T_{1/2}$ using Eqn.2.50, by taking into account the NME uncertainty as given in Table 3.2. The pink band corresponds to $m_{\beta\beta} = 10^{-3}$ eV, which is the minimum of the NH regime for lower values of $m_{lightest}$ with the LMA solution. In Fig. 3.2, the dotted black line corresponds to the future 3σ sensitivity of nEXO, which is $T_{1/2} = 5.7 \times 10^{27}$ years [209]. The yellow, black, brown and blue lines correspond to different values of the sensitive background levels of 0, 10^{-5}, 10^{-4} and 10^{-3} $\text{cts}/(\text{kg}_{\text{iso}}\text{yr})$ respectively. From the figure, we can see that for a sensitive background level of 10^{-4} $\text{cts}/(\text{kg}_{\text{iso}}\text{yr})$, the DLMA region could be probed with a sensitive exposure greater than $\sim$ 5000 $\text{kg}_{\text{iso}}\text{yr}$. To probe the 10^{-3} regime shown by the dashed lines requires lower background levels and/or higher sensitive exposure. In Table 3.2, we have given the $T_{1/2}$ ranges corresponding to the DLMA region, $m_{\beta\beta} = 0.004 - 0.0075$ eV for three different isotopes.

3.6 Summary

Searching for $0\nu\beta\beta$ process is of utmost importance since it can establish the Majorana nature of the neutrinos which implies they are their own antiparticles. This will in-turn signify a lepton number violating Majorana mass term for the neutrinos, which may hold the key in explaining why neutrino masses are much smaller than the other fermion masses. This can have profound implications for a deeper understanding of physics beyond the Standard Model of particle physics. So far these searches have yielded negative results and have put an upper bound on the effective mass governing $0\nu\beta\beta$. Assuming light Majorana neutrino exchange as the sole mechanism for $0\nu\beta\beta$, the predictions of effective mass for IH and NH are separated by a "desert region". The current upper bound is just above the IH region ($\sim$ 0.1 eV) and several future experiments with sensitivity reach ~ 0.015 eV are expected to probe the IH parameter space completely. However if no positive signal is found in these searches then the projected sensitivity reach of these experiments are in the ballpark of 0.005 eV which can explore only a small part of the NH region for lightest neutrino mass $\geq$ 0.005 eV

[209]. The next frontier that is envisaged is $\sim 10^{-3}$ eV [219]. In this chapter, we have seen that if the Dark-LMA solution to the solar neutrino problem is true, then the effective mass for NH shifts into the intermediate "desert zone" between NH and IH. Therefore, in an incremental advancement, a new goal for the $0\nu\beta\beta$ experiments can be to first explore this region $\sim 0.004 - 0.0075$ eV, which is possible even for very low values of the lightest neutrino mass. This not only defines a newer sensitivity goal of future $0\nu\beta\beta$ experimental program for the NH scenario, but can also provide an independent confirmation/refutal of the Dark-LMA solution to the solar neutrino problem in presence of non-standard interactions.

Chapter 4

Naturalness, Vacuum Stability and Lepton Flavor Violation in Minimal Type-III Seesaw Model

4.1 Introduction

As discussed earlier, the most elegant way to give mass to neutrinos is the seesaw mechanism. This relates new physics at a high scale to the smallness of neutrino mass. The fact that the GUT scale seesaw models have no testability at the colliders gave rise to intense research in TeV scale seesaw models.

Another important aspect to be considered while studying the seesaw models is the issue of naturalness. It is well known that the Higgs mass gets large corrections from the higher order loop diagrams due to its self-interaction as well as the couplings with gauge bosons and fermions. The theory is perceived unnatural if a severe fine-tuning between the quadratic radiative corrections and the bare mass is needed to bring down Higgs mass to the observed scale. Although the dimensional regularization can throw away the quadratic divergences, the presence of other dangerous logarithmic and finite contributions can cause similar naturalness problem. In the case of seesaw models in which the new particles couple to the SM Higgs, this naturalness problem is enhanced [153, 220–229]. Reducing the seesaw scale to TeV will in turn bring down the correction to the Higgs mass to be of the order of TeV.

Thus, while testability at the colliders serves as an experimental motivation for considering low scale seesaw models, the naturalness problem acts as a theoretical motivation. At the same time, the TeV scale seesaw models alter the stability of the EW vacuum considerably and demanding the EW vacuum to be stable/metastable up to the M_{Planck} puts further constraints on the masses and the couplings. The stability/metastability of the EW vacuum in the context of various seesaw models have been studied in references [146–152, 154, 155, 230–234]. In particular, in reference [235], the authors have discussed the implications of vacuum stability and gauge-Higgs unification in the context of the type-III seesaw model and reference [155] has discussed the EW vacuum metastability in the context of type-I as well as type-III seesaw models. In reference [153], the authors have studied the implications of naturalness and vacuum stability in a minimal type-I seesaw model. Similarly, the naturalness and vacuum stability in the case of the type-II seesaw model have been studied in reference [228].

This chapter is based on the work done in [236] and here we study the consequences of naturalness and vacuum stability in the minimal type-III seesaw model, in which we extend the SM by adding two $SU(2)_L$ triplet fermions with zero hypercharge to explain the origin of the non-zero neutrino masses and mixing. Here, the lightest active neutrino will be massless. We use the Casas-Ibarra (CI) parametrization for the neutrino Yukawa coupling matrix [237, 238] and by choosing the two triplets to be degenerate, we have only three independent real parameters, namely the mass of the triplet fermions and a complex angle in the CI parametrization. We study and constrain these parameters using the bounds from naturalness, EW vacuum stability as well as LFV decays.

This chapter is organized as follows: In section 4.2, we review the minimal type-III seesaw model and the parametrization used for our studies. In section 4.3, we discuss the implications of naturalness in the minimal type-III seesaw model and in section 4.4, we have discussed the constraints from the LFV decays. After this, we discuss the effective Higgs potential in the presence of the extra fermion triplets and the renormalization group (RG) evolution of the different couplings, and present a detailed discussion of the results. Finally, we summarize in section 4.7.

4.2 The Minimal Type-III Seesaw Model

We extend the standard model with two fermionic triplets Σ_{R_i}, $i = 1, 2$ having zero hypercharge as given in Eqn.2.27. For simplicity, we consider the scenario in which the Majorana mass matrix M is proportional to the identity matrix so that the heavy fermions have degenerate masses, each of which is now denoted by M_Σ. The seesaw Lagrangian and the diagonalization procedure have been discussed in section 2.3.3 and the light neutrino mass matrix is given by,

$$m_{\text{light}} = -M_D^T M^{-1} M_D. \tag{4.1}$$

Note that here, the lightest active neutrino is massless. We use the Casas-Ibarra parametrization [237, 238] for the Yukawa coupling matrix Y_Σ, such that the constraints on the light neutrino mixing angles as well as the mass squared differences as predicted from the oscillation data are automatically satisfied. In this parametrization,

$$Y_\Sigma = \frac{\sqrt{2}}{v}\sqrt{D_\Sigma} R \sqrt{D_\nu} U^\dagger, \tag{4.2}$$

where $D_\Sigma = \text{diag}(M_\Sigma, M_\Sigma)$, $D_\nu = \text{diag}(m_1, m_2, m_3)$, and R is an arbitrary complex 2×3 orthogonal matrix which parametrizes the information that is lost in the decoupling of the triplet fermions. The light neutrino masses for the normal and inverted hierarchies are given by,

$$m_1 = 0\,,\;\; m_2 = \sqrt{\Delta m^2_{sol}}\,,\;\; m_3 = \sqrt{\Delta m^2_{atm}} \quad \text{(NH)}$$

$$m_1 = \sqrt{\Delta m^2_{atm}}\,,\;\; m_2 = \sqrt{\Delta m^2_{sol} + \Delta m^2_{atm}}\,,\;\; m_3 = 0 \quad \text{(IH)}. \tag{4.3}$$

We use the standard parametrization of the PMNS matrix U as given in Eqn.1.17. But now, the phase matrix P is given as $P = \text{diag}\,(e^{-i\alpha}, e^{+i\alpha}, 1)$ where α is the Majorana phase. In our numerical analysis, we have used the values of mass squared differences and mixing angles in the 3σ ranges as shown in section 1.2 and varied the phases δ and α between 0 to 2π. It has been shown in reference [238] that the matrix R can be parametrized as,

$$R = \begin{cases} \begin{pmatrix} 0 & \cos z & \zeta \sin z \\ 0 & -\sin z & \zeta \cos z \end{pmatrix} & \text{(NH)} \\ \begin{pmatrix} \cos z & \zeta \sin z & 0 \\ -\sin z & \zeta \cos z & 0 \end{pmatrix} & \text{(IH)}, \end{cases} \tag{4.4}$$

where z is a complex parameter and $\zeta = \pm 1$. We fix the value of ζ to be $+1$ for all our analysis and this does not change any of our results. Thus the only free parameters in the model are the mass of the triplet fermions, M_Σ and the complex number, z. z can take any value in the complex plane.

Note that the experimental searches performed by the CMS and the ATLAS have put lower bounds on the triplet masses. CMS [239] has set a lower limit of 430 GeV on the triplet mass with the data from $\sqrt{s} = 13$ TeV run whereas depending on the various scenarios studied, the ATLAS results rule out masses in the range below $325-540$ GeV [240].

4.3 Naturalness

One of the problems associated with the high-scale seesaw models is that the associated heavy particles give very large corrections to the Higgs mass making the theory unnatural. Here, we shall see the implications of naturalness in the context of the type-III seesaw scenario. The tree level SM Higgs potential is given by,

$$V = -\mu^2(H^\dagger H) + \lambda(H^\dagger H)^2, \tag{4.5}$$

where,

$$H = \frac{1}{\sqrt{2}} \begin{pmatrix} G^+ \\ v + h + iG^0 \end{pmatrix}. \tag{4.6}$$

As discussed in Chapter 1, the vev, $v = 246$ GeV and this will give the physical Higgs particle with tree level mass as $m_h^2 = 2\lambda v^2$. For the naturalness of the Higgs mass, the heavy right handed neutrino loop corrections to the mass parameter μ should be smaller than $O(\text{TeV}^2)$. In the $\overline{\text{MS}}$ scheme, the correction is given by,

$$\delta\mu^2 \approx \frac{3}{4\pi^2} \text{Tr}[Y_\Sigma^\dagger D_\Sigma^2 Y_\Sigma]. \tag{4.7}$$

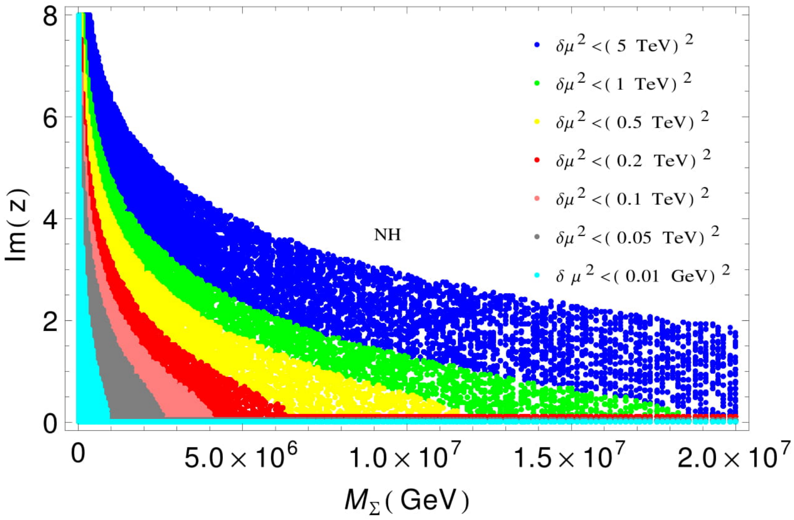

(a) Naturalness contour for NH.

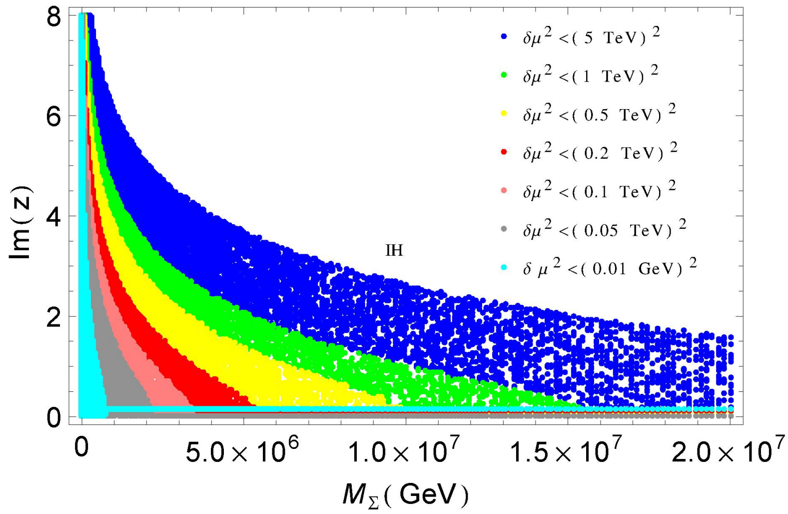

(b) Naturalness contour for IH.

Figure 4.1: Naturalness contours in the Im$[z]$-M_Σ plane. The figure in the upper (lower) panel is for NH (IH). In the shaded regions, $\delta\mu^2$ is less than $p\%$ of 1TeV^2 where $p = 500, 100, 50, 20, 10, 5, 1$ (from top to bottom). The unshaded regions are disfavored by naturalness.

Note that we have taken the quantity $(\ln[\frac{M_\Sigma}{\mu_R}] - \frac{1}{2})$ to be unity (where μ_R is the renormalization scale). Now, using the parametrization in Eqn.4.2, we get,

$$\begin{aligned}\delta\mu^2 \approx & \frac{3}{4\pi^2}\frac{2}{v^2}\,\mathrm{Tr}[D_\nu R^\dagger D_\Sigma^3 R] \\ = & \frac{3M_\Sigma^3}{2\pi^2 v^2}\cosh(2\mathrm{Im}[z]) \times \begin{cases}\sqrt{\Delta m_{sol}^2} + \sqrt{\Delta m_{atm}^2} & (NH) \\ \sqrt{\Delta m_{atm}^2} + \sqrt{\Delta m_{sol}^2 + \Delta m_{atm}^2} & (IH).\end{cases}\end{aligned} \tag{4.8}$$

From the above expressions, we can see that the only unknown parameters are M_Σ and Im$[z]$.

In Fig. 4.1, we have presented the naturalness contours in the Im$[z]$-M_Σ plane for both NH and IH. In the shaded rgions, $\delta\mu^2$ is demanded to be less than $p\%$ of $1\mathrm{TeV}^2$ where $p = 500, 100, 50, 20, 10, 5, 1$ (from top to bottom). The unshaded regions are disfavored by naturalness. From these plots, we can see that higher the mass of the triplet, smaller the allowed values of the Im $[z]$. For instance, demanding $\delta\mu^2 <$ $(1\ \mathrm{TeV})^2$ implies that $M_\Sigma \leq 1.84 \times 10^7$ GeV for Im$[z] = 0$ and $M_\Sigma \leq 3 \times 10^5$ GeV for Im$[z] = 6$. These bounds become even more stringent as we demand $\delta\mu^2$ to be smaller as could be seen from the plots. Also, from Eqn.4.8, we can see that the $\delta\mu^2$ values for NH and IH differ roughly by a factor of half ($\Delta m_{atm}^2 >> \Delta m_{sol}^2$). This effect can be seen from the fact that for a given value of Im(z), the maximum allowed value of M_Σ for NH is slightly higher than that for IH.

4.4 Constraints from Lepton Flavor Violation

The decay widths and the branching ratios (BR) for the various LFV decays in the context of type-III seesaw model have been worked out in the reference [103]. This model can have the decays $\mu \to e\gamma$ and $\tau \to l\gamma$ at the one loop level and $\mu \to 3e$ as well as $\tau \to 3l$ processes in the tree level due to the charged lepton mixing. However, among all the LFV decays, the most stringent bound is the one coming from μ to e conversion in the nuclei. The $\mu \to e$ conversion rate to the total nucleon muon capture rate ratio ($R^{\mu\to e}$) puts a bound on $\epsilon_{e\mu}$. For the $^{48}_{22}$Ti nuclei, the bound given by Eqn.2.56

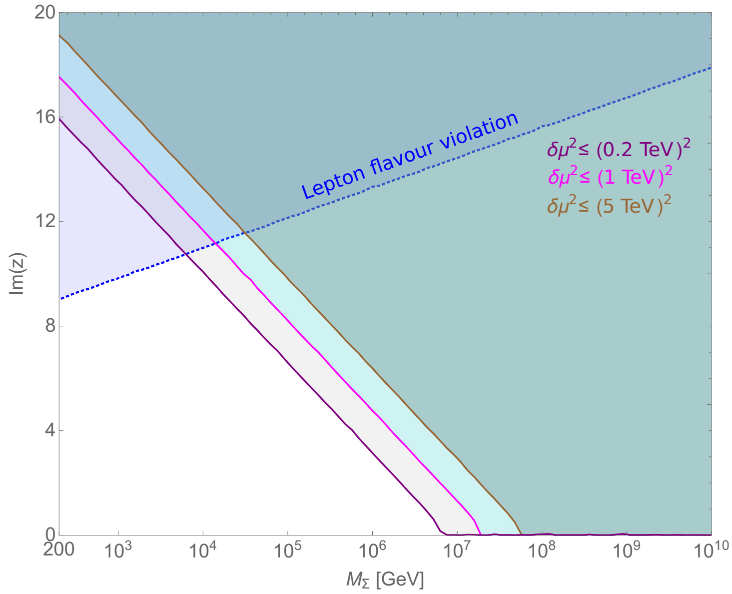

(a) NH

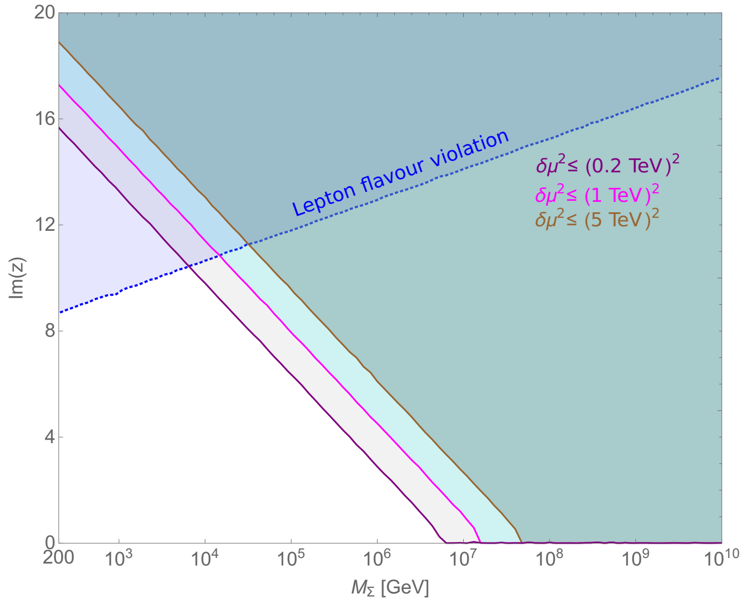

(b) IH

Figure 4.2: Bounds on z from LFV (blue dotted line) and naturalness (purple, magenta and brown solid lines). The figure in the top (bottom) is for NH (IH). The unshaded region is allowed by both LFV as well as naturalness bounds.

gives an upper bound $\epsilon_{e\mu}$ in the triplet fermion model as [103] [1],

$$\epsilon_{e\mu} < 1.7 \times 10^{-7}. \tag{4.9}$$

We present the constraints on z and M_Σ from this bound in Fig. 4.2 for both NH and IH. The region above the blue dotted line are disallowed by the LFV bounds whereas the regions to the right of the purple, magenta and brown solid lines are disallowed by the naturalness bounds depending on the naturalness condition used. We can clearly see that the naturalness bounds restrict larger values of M_Σ whereas the LFV bound constrains the larger values of Im(z) corresponding to the smaller values of M_Σ. The unshaded region is the one that is allowed by both LFV as well as the naturalness bounds. One can notice from these plots that for both NH and IH, the maximum allowed value of Im(z) is ~ 10 which corresponds to a triplet mass of $\sim 10^4$ GeV. In generating these plots, we have varied the light neutrino mass squared differences and mixing angles in their 3σ ranges and the Dirac and Majorana phases are varied in the range 0 to 2π and we have presented the most stringent bounds.

4.5 Vacuum Stability

In this section, we discuss how the stability of the EW vacuum is modified in the presence of the extra fermionic triplets if we assume that there is no other new physics up to the Planck scale (M_{Planck}). It is well known that if we have extra fermions, they tend to destabilize the EW vacuum. We aim to quantify this effect and obtain constraints in the context of the model outlined.

Following the method outlined in [145, 146, 234], the additional contribution to the one-loop effective potential from the fermionic triplet is given as,

$$\begin{aligned} V_1^\Sigma(h) = &-\frac{3(M_D^\dagger(h)M_D(h))^2_{ii}}{32\pi^2}\left[\ln\frac{(M_D^\dagger(h)M_D(h))_{ii}}{\mu^2(t)}-\frac{3}{2}\right] \\ &-\frac{3(M_D(h)M_D^\dagger(h))^2_{jj}}{32\pi^2}\left[\ln\frac{(M_D(h)M_D^\dagger(h))_{jj}}{\mu^2(t)}-\frac{3}{2}\right], \end{aligned} \tag{4.10}$$

[1] Note that this process can occur in tree level in the type-III seesaw model due to the charged lepton mixing. There is only one way to induce a $\mu - e$ transition along the same fermionic line, including two Yukawa couplings and two inverse mass matrices M_Σ.This is through the combination $\epsilon_{e\mu}$.

where $M_D(h) = \dfrac{Y_\Sigma}{\sqrt{2}} h$ and j, i run over the three light neutrinos and the two triplet fermions respectively. In this analysis, we use the two-loop contributions to the effective potential for the SM particles whereas the contribution due to the extra fermion triplet is considered up to one-loop only. For high field value $h(t) >> v$, the effective potential can be approximated as, $V_{eff}^{SM+\Sigma} = \lambda_{eff}(h)\dfrac{h^4}{4}$. The one- and two- loop SM expressions for $\lambda_{eff}(h)$ can be found in reference [139]. The contribution due to the extra fermionic triplet is obtained as,

$$\lambda_{eff}^{\Sigma}(h) = -\frac{3\,e^{4\Gamma(h)}}{32\pi^2}\left((Y_\Sigma^\dagger Y_\Sigma)_{ii}^2\left(\ln\frac{(Y_\Sigma^\dagger Y_\Sigma)_{ii}}{2} - \frac{3}{2}\right) + (Y_\Sigma Y_\Sigma^\dagger)_{jj}^2\left(\ln\frac{(Y_\Sigma Y_\Sigma^\dagger)_{jj}}{2} - \frac{3}{2}\right)\right) \tag{4.11}$$

where, the factor $\Gamma(h) = \int_{M_t}^{h} \gamma(\mu)\, d\ln\mu$ indicates the wave function renormalization of the Higgs field. Here $\gamma(\mu)$ is the anomalous dimension of the Higgs [136, 137, 241–243], the contribution to which from the fermion triplet at one loop is $\dfrac{3}{2}\mathrm{Tr}\left(Y_\Sigma Y_\Sigma^\dagger\right)$. We also assume that $\mu = h$. In this choice, all the running coupling constants ensure faster convergence of the perturbation series of the potential [244].

We compute the RG evolution of all the couplings to analyse the Higgs potential up to M_{Planck}. We first calculate all the SM couplings at the top mass scale M_t, taking care of the threshold corrections [144, 245–247]. We use one-loop RGEs to calculate $SU(2)$ and $U(1)$ gauge couplings $g_2(M_t)$ and $g_1(M_t)$ [2]. For the $SU(3)$ gauge coupling $g_3(M_t)$, we use three-loop RGEs considering contributions from the five quarks and the effect of the sixth, i.e., the top quark has been taken using an effective field theory approach. We also include the leading term in the four-loop RGE for α_s. The mismatch between the top pole mass and the $\overline{MS}$ renormalized coupling has been taken care by using the threshold correction $y_t(M_t) = \dfrac{\sqrt{2}M_t}{v}(1 + \delta_t(M_t))$, where $\delta_t(M_t)$ is the matching correction for y_t at the top pole mass. We use $\lambda(M_t) = \dfrac{M_H^2}{2v^2}(1 + \delta_H(M_t))$ for the Higgs quartic coupling λ. To calculate this at the scale M_t, we have included the QCD corrections up to three loops [248], electroweak corrections up to one-loop [249, 250] and the $O(\alpha\alpha_s)$ corrections to the matching of top Yukawa and top pole mass [246, 251]. The matching conditions we have used are given in appendix-B We have reproduced the SM couplings at M_t as in references [139, 144] by using these

[2]Our result will not change significantly even if we use the two-loop RGEs for g_1 and g_2.

threshold corrections. We evolve them up to the heavy fermionic mass scale using the SM RGEs [252–255]. The extra contributions due to the femionic triplets are included after the threshold heavy fermionic mass scale [256]. The one-loop RGEs for λ, y_t, g_2 and Y_Σ after the scale M_Σ are as given below :

$$\begin{aligned}\beta_\lambda = \frac{1}{16\pi^2}\Big(&\frac{3}{8}g_1^4 + \frac{3}{4}g_1^2 g_2^2 + \frac{9}{8}g_2^4 - 3g_1^2\lambda - 9g_2^2\lambda + 24\lambda^2 + 12\lambda y_t^2 - 6y_t^4 \\ &+ 12\lambda \mathrm{Tr}(Y_\Sigma Y_\Sigma^\dagger) - 10\mathrm{Tr}(Y_\Sigma Y_\Sigma^\dagger Y_\Sigma Y_\Sigma^\dagger)\Big)\end{aligned} \tag{4.12}$$

$$\beta_{y_t} = \frac{1}{16\pi^2}\Big(y_t\Big(\frac{9}{2}yt^2 - 8g_3^2 - \frac{17}{12}g_1^2 - \frac{9}{4}g_2^2 + 3\mathrm{Tr}(Y_\Sigma Y_\Sigma^\dagger)\Big)\Big) \tag{4.13}$$

$$\beta_{g_2} = \frac{1}{16\pi^2}\Big(-\frac{1}{2}g_2^3\Big) \tag{4.14}$$

$$\beta_{Y_\Sigma} = \frac{1}{16\pi^2}\Big(Y_\Sigma\Big(\frac{5}{2}Y_\Sigma Y_\Sigma^\dagger + 3y_t^2 - \frac{33}{4}g_2^2 - \frac{3}{4}g_1^2 + 3\mathrm{Tr}(Y_\Sigma Y_\Sigma^\dagger)\Big)\Big) \tag{4.15}$$

Then we evolve all the couplings up to M_{Planck} to find the position and depth of the new minima at the high scale.

In Fig. 4.3, we show the running of the Higgs quartic coupling for four different sets of benchmark points for the minimal type-III seesaw model. In the first figure, the purple and gray lines correspond to $M_t = 171.3$ and 174.9 GeV respectively with the value of $\mathrm{Tr}[Y_\Sigma^\dagger Y_\Sigma]^{\frac{1}{2}}$ fixed as 0.283 and $M_\Sigma = 10^7$ GeV. For the first case, we can see that the Higgs quartic coupling λ remains positive up to M_{Planck}, i.e., the EW vacuum is absolutely stable up to the M_{Planck}. For $M_t = 174.9$ GeV, we can see that $\lambda \sim \lambda_{eff}$ becomes negative at the energy scale $\sim 10^9$ GeV, the so called instability scale Λ_I, and remains negative upto M_{Planck}. However, we find that the beta function of the Higgs quartic coupling $\beta_\lambda (\equiv dV(h)/dh)$ becomes zero around the energy scale $\sim 10^{17}$ GeV, which implies that there is an extra deeper minima at that scale and we have checked that the EW vacuum corresponding to this point is metastable. Similarly in the second figure, we have given the running of the quartic coupling for two different values of $\mathrm{Tr}[Y_\Sigma^\dagger Y_\Sigma]^{\frac{1}{2}}$ with fixed M_t and M_Σ. We notice that as the value of the $\mathrm{Tr}[Y_\Sigma^\dagger Y_\Sigma]$ is increased from 0.283 to 0.636, the EW vacuum shifts from the metastable to the unstable region. In this way, the conditions of stability and metastability can put constraints on the allowed values of $\mathrm{Tr}[Y_\Sigma^\dagger Y_\Sigma]^{\frac{1}{2}}$.

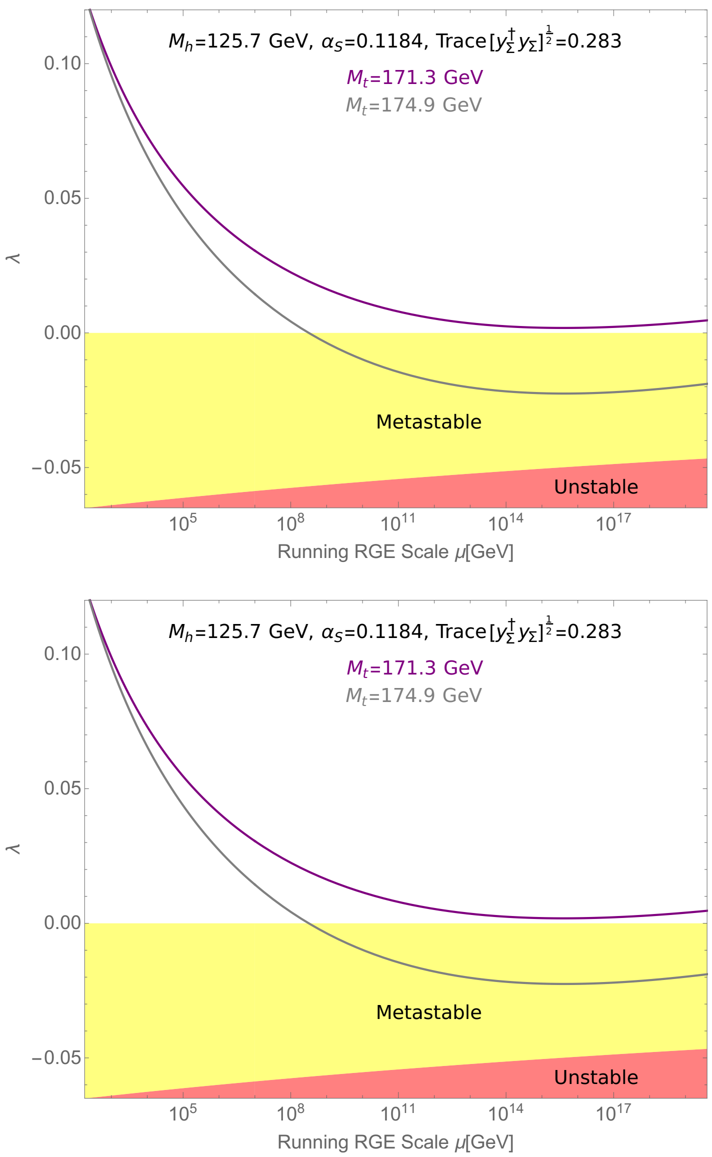

Figure 4.3: RG evolution of the Higgs quartic coupling . The figure in the top shows the running of λ for different values of M_t with fixed M_Σ and Tr$[Y_\Sigma^\dagger Y_\Sigma]^{\frac{1}{2}}$ whereas the figure in the bottom shows the running of λ for different values of Tr$[Y_\Sigma^\dagger Y_\Sigma]^{\frac{1}{2}}$ with M_Σ and M_t fixed. For both the plots, we have taken $M_{\Sigma 1} = M_{\Sigma 2} = M_\Sigma = 10^7$ GeV.

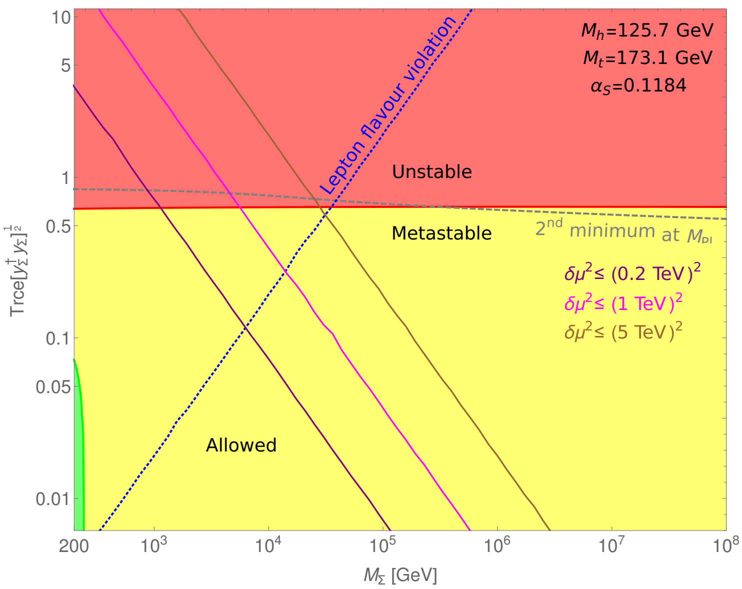

Figure 4.4: The phase diagram in the Tr $[Y_\Sigma^\dagger Y_\Sigma]^{\frac{1}{2}} - M_\Sigma$ plane for NH. Here, we have used the central values of M_t, M_h and α_s. The color coding of the lines (blue, purple, magenta and brown) are the same as in Fig. 4.2. The horizontal red solid line separates the unstable and the metastable regions of the EW vacuum.

4.5.1 Phase diagram of Vacuum stability

As we have already discussed in section 2.5.3, the present central values of the SM parameters imply that an extra deeper minima exists near M_{Planck}. Hence, there is a possibility that the EW vacuum might tunnel into that true (deeper) vacuum. In the type-III seesaw model, depending upon the new physics parameter space, the stability of the EW vacuum is modified compared to that in the SM and there are two effects contributing to this. The first one is the negative contribution to the running of λ as well as to the effective Higgs potential due to the triplet fermion Yukawa coupling (see the Eqns. 5.10 and 4.12). The second one is through the modified RGE for the SU(2) gauge coupling, g_2 (Eqn.4.14), which in turn gives a positive contribution to the running of λ. These effects have also been discussed in reference ([155]).

In Fig. 4.4, we have given the phase diagram in the Tr $[Y_\Sigma^\dagger Y_\Sigma]^{\frac{1}{2}} - M_\Sigma$ plane for the central values of the SM parameters, $M_t = 173.1$, $M_h = 125.7$ and $\alpha_s = 0.1184$. Note that since the bounds from vacuum stability put constraints on the values of Tr $[Y_\Sigma^\dagger Y_\Sigma]$

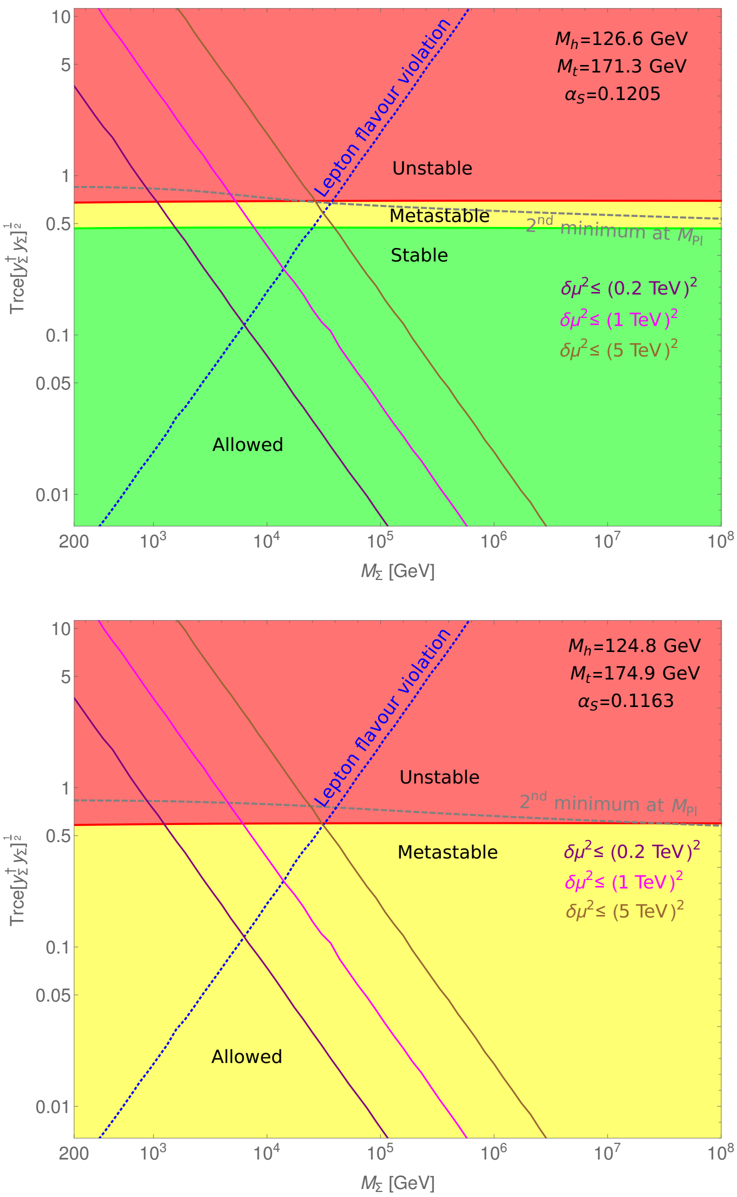

Figure 4.5: The phase diagram in the $\mathrm{Tr}\,[Y_\Sigma^\dagger Y_\Sigma]^{\frac{1}{2}} - M_\Sigma$ plane for NH. The figure in the top (bottom) gives the most liberal (stringent) bound from vacuum stability with minimum (maximum) value of M_t and maximum (minimum) values of M_h and α_s. The color coding of the lines (blue, purple, magenta and brown) are the same as in Fig. 4.2. The horizontal red solid line separates the unstable and the metastable regions of the EW vacuum.

and M_Σ, and Tr$[Y_\Sigma^\dagger Y_\Sigma]$ depends only on Im(z) and M_Σ as given by the equation,

$$\text{Tr}\,[Y_\Sigma^\dagger Y_\Sigma] = \frac{2}{v^2} M_N \cosh(2\,\text{Im}\,(z)) \times \sum_i m_i, \tag{4.16}$$

one can choose either (Tr $[Y_\Sigma^\dagger Y_\Sigma]$, M_Σ) or (Im (z), M_Σ) as the two independent parameters. Hence, from here onwards, all the plots are given in the Tr $[Y_\Sigma^\dagger Y_\Sigma]^{\frac{1}{2}} - M_\Sigma$ plane. In Fig. 4.4, the horizontal red solid line separating the unstable region (red) and the metastable (yellow) region is obtained when $\beta_\lambda(\mu) = 0$ along with $\lambda(\mu) = \lambda_{min}(\Lambda_B)$. From this plot, we can see that the parameter space with Tr $[Y_\Sigma^\dagger Y_\Sigma]^{\frac{1}{2}} \gtrsim 0.64$ with the heavy fermion mass scale $200 - 10^8$ GeV are excluded by instability of the EW vacuum. The gray dashed line corresponds to the points for which the beta function of the quartic coupling λ is zero at M_{Planck}, i.e., the second minima is situated at that scale. Also, we can see a very small green region for lower values of masses and couplings for which the EW vacuum is absolutely stable. However, this region is disfavored from the LFV constraints as shown by the blue dotted line. The region to the right of this line is allowed by the current bounds from LFV as given in Eqn.4.9. We have also given the bounds from naturalness in these figures as shown by the slanted solid lines corresponding to three different values of $\delta\mu^2$. Thus, one can see that the area that are allowed both by naturalness as well as LFV falls in the stability/metastability region.

In Fig. 4.5, we have again plotted the phase diagram in the Tr $[Y_\Sigma^\dagger Y_\Sigma]^{\frac{1}{2}} - M_\Sigma$ plane for NH, but with different values of the SM parameters. The figure in the top (bottom) gives the most liberal (stringent) bound from vacuum stability with minimum (maximum) value of M_t and maximum (minimum) values of M_h and α_s from their allowed 3σ ranges. Clearly, with the smallest value of M_t and the largest values of M_h and α_s, the stability region increases as is shown by the green region in the figure in the top panel. On the other hand, in the bottom panel with the highest value of M_t and lowest values of M_h and α_s, no region of stability is found. In this case, the parameter space with Tr $[Y_\Sigma^\dagger Y_\Sigma]^{\frac{1}{2}} > 0.68$ (0.58) is disfavored from the instability condition in the top(bottom) panels.

Fig. 4.6 gives the phase diagram in the M_t – Tr $[Y_\Sigma^\dagger Y_\Sigma]^{\frac{1}{2}}$ plane for NH with the central values of M_h and α_s. The dashed lines separate the metastable and the unstable regions whereas the solid lines separate the stable and the metastable regions. The red,

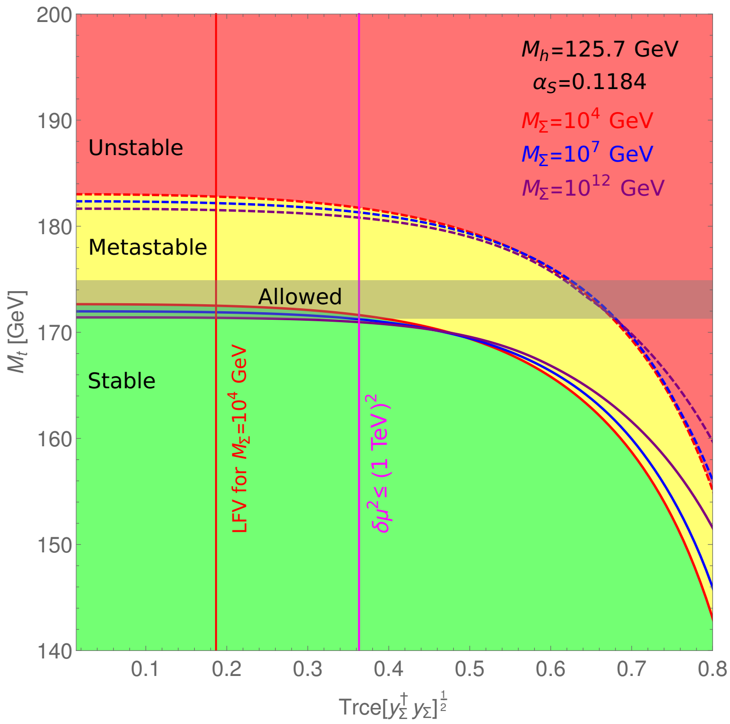

Figure 4.6: The phase diagram in the M_t − Tr $[Y_\Sigma^\dagger Y_\Sigma]^{\frac{1}{2}}$ plane for NH for the central values of M_h and α_s. The dashed lines separate the metastable and the unstable regions whereas the solid lines separate the stable and the metastable regions. The three colors are for for three different values of M_Σ. The two vertical lines give the LFV and naturalness bounds for $M_\Sigma = 10^4$ GeV and the region in the left of the LFV line (red) is allowed by both.

blue and purple colored lines correspond to the representative values of M_Σ as 10^4, 10^7 and 10^{12} GeV respectively. The two vertical lines give the LFV and the naturalness ($\delta\mu^2 < 1$ TeV^2) bounds for $M_\Sigma = 10^4$ GeV and the allowed region is to the left of the red vertical line. The horizontal shaded gray region denote the 3σ allowed range of M_t. It is seen that in this region, the vacuum is metastable for lower values of Tr $[Y_\Sigma^\dagger Y_\Sigma]^{\frac{1}{2}}$, while for higher values, the vacuum is unstable. Once we consider the bounds from LFV, Tr $[Y_\Sigma^\dagger Y_\Sigma]^{\frac{1}{2}}$ is less than 0.18 and the vacuum is in the metastable region.

In Fig. 4.7, we have shown the phase diagram in the $M_t - M_h$ plane for $M_\Sigma = 10^4$ GeV. The red dashed lines correspond to the 3σ variation in α_s. The figures in the top and bottom correspond to Tr $[Y_\Sigma^\dagger Y_\Sigma]^{\frac{1}{2}} = 0.20$ and 0.40 respectively. The ellipses correspond to the allowed values of M_t and M_h at 1σ, 2σ and 3σ. From this figure, we can clearly see that higher values of M_t and Y_Σ affect the stability of the EW vacuum negatively whereas higher value of M_h has a positive effect on the stability. For Tr $[Y_\Sigma^\dagger Y_\Sigma]^{\frac{1}{2}} = 0.20$, some areas of the parameter space fall in the stable region when M_t and M_h are taken in the 3σ ranges, whereas for Tr $[Y_\Sigma^\dagger Y_\Sigma]^{\frac{1}{2}} = 0.40$, all the allowed parameter space is in the metastable region.

It is also important to look at the change in the confidence level at which the (meta)stability is excluded or allowed [144, 257, 258] in the context of the minimal type-III seesaw model. The confidence level plot(s) will provide a quantitative measurement of the (meta)stability for the new physics parameter space. In Fig. 4.8, we show how the confidence level at which EW vacuum is allowed(excluded) from the metastability(instability) depends on new Yukawa couplings of the heavy fermions for the type-III seesaw model for different values of M_Σ and α_s. To plot these, we have considered the variation of M_t (from 160 to 180 GeV) and M_h (from 120 to 132 GeV) in the $M_t - M_h$ plane for fixed values of α_s. We draw the metastability line and an ellipse to which the metastability line is the tangent and the point corresponding to the central values of M_t and M_h ($M_t = 173.1$ GeV, $M_h = 125.7$ GeV) as the center (See Fig. 4.7 for instance). Then we calculate the confidence level as,

$$\text{Confidence level} = \frac{a \text{ of the ellipse}}{1\sigma \text{ error of } M_t} = \frac{b \text{ of the ellipse}}{1\sigma \text{ error of } M_h}, \tag{4.17}$$

where a and b are the lengths of the major and minor axes of the ellipse. Figures in the top and the bottom panels are plotted with the triplet masses as $M_\Sigma = 10^4$ GeV and 10^{12} GeV respectively. In both cases the EW vacuum is metastable for smaller values of the new Yukawa coupling. We can see that the confidence level at which the EW vacuum is metastable (yellow region) increases with the increase of Tr $[Y_\Sigma^\dagger Y_\Sigma]^{\frac{1}{2}}$. Also, one can see that the confidence level at which the EW vacuum is metastable increases with the increase in the mass of the fermion triplets. We can also see the effect of α_s on the confidence level. The dashed, solid and dotted red lines correspond to the values of α_s as 0.1177, 0.1184 and 0.1191 respectively. Clearly, the confidence level at which the EW vacuum is metastable decreases with the increase in α_s. This is because, α_s has a positive effect on the stability of the EW vacuum and the increase in α_s increases the confidence level at which the vacuum is stable and thereby decreasing the confidence level at which it is unstable. The EW vacuum becomes metastable

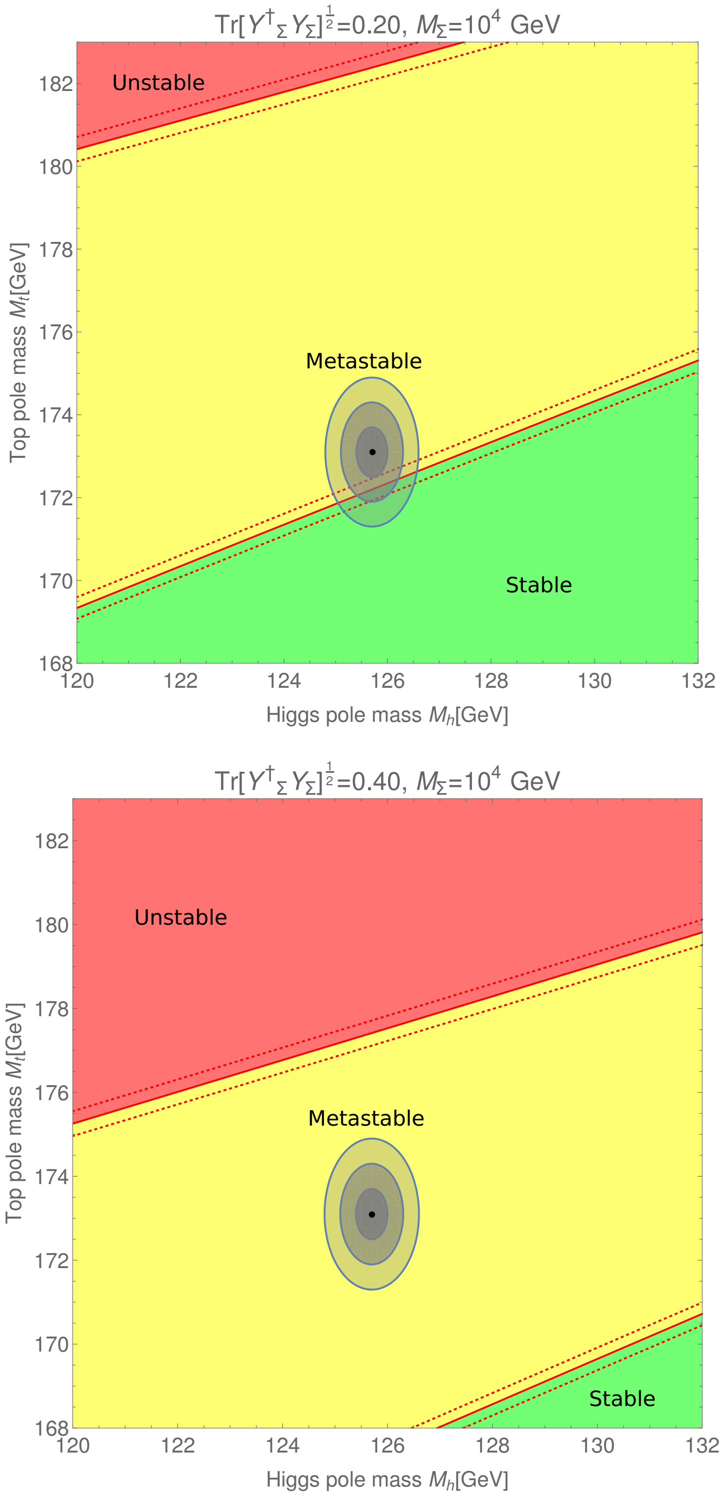

Figure 4.7: The phase diagram in the $M_t - M_h$ plane for two different values of $\mathrm{Tr}\,[Y_\Sigma^\dagger Y_\Sigma]^{\frac{1}{2}}$ and $M_\Sigma = 10^4$ GeV. The ellipses correspond to the allowed values of M_t and M_h at 1σ, 2σ and 3σ.

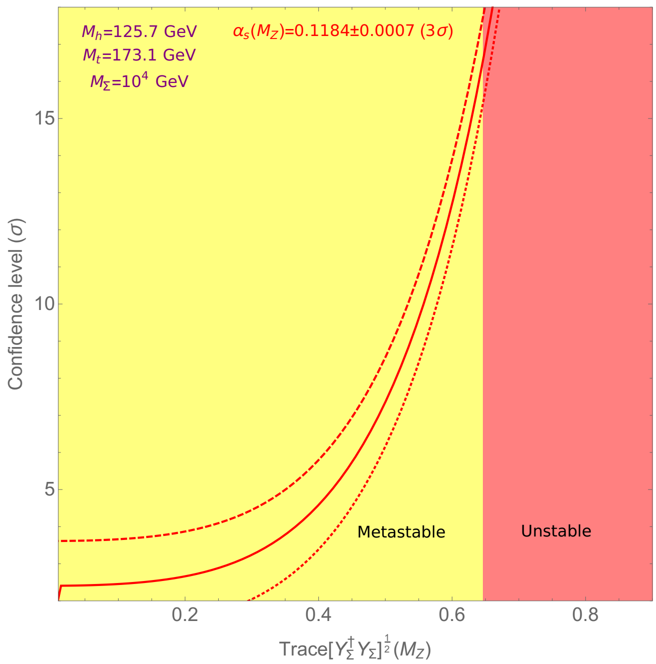

(a)

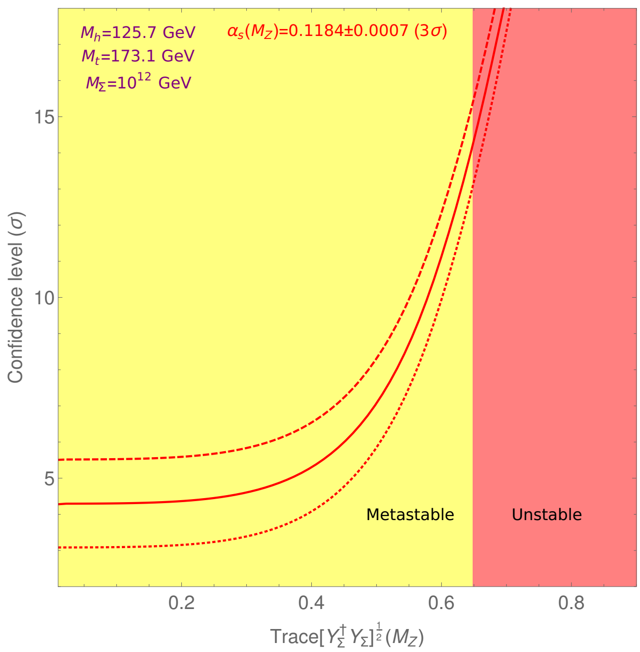

(b)

Figure 4.8: Dependence of confidence level at which the EW vacuum stability is excluded/allowed on Tr $[Y_\Sigma^\dagger Y_\Sigma]^{\frac{1}{2}}$ for different values of α_s and M_Σ.

for Tr $[Y_\Sigma^\dagger Y_\Sigma]^{\frac{1}{2}} = 0.646 \pm 0.008$ and Tr $[Y_\Sigma^\dagger Y_\Sigma]^{\frac{1}{2}} = 0.648 \pm 0.011$ corresponding to $\alpha_s = 0.1184 \pm 0.0007$ for $M_\Sigma = 10^4$ and 10^{12} GeV respectively. The demarcations between the stable and the metastable regions in the plots are only for the central values of α_s

4.6 Neutrino-less Double Beta Decay

The neutral components of the triplet fermions may give rise to additional contributions to $0\nu\beta\beta$ through their mixing with the light neutrinos. The half life for $0\nu\beta\beta$ in this case is given by,

$$\frac{\Gamma_{0\nu\beta\beta}}{\ln 2} = G^{0\nu}(Q,Z)\,\frac{|{M_\nu}^2|}{m_e^2}\left|\Sigma\,U_{ei}^2\,m_i + \langle p^2\rangle\frac{V_{ei}^2}{M_\Sigma}\right|^2. \tag{4.18}$$

Here, V is the light heavy mixing matrix and $\langle p^2\rangle$ is given by,

$$\langle p^2\rangle = -m_e m_p \frac{M_N}{M_\nu}, \tag{4.19}$$

where m_e and m_p are the masses of the electron and proton respectively and the magnitude of $\langle p^2\rangle$ is around $(100\,\text{MeV})^2$. M_ν and M_N represent the nuclear matrix elements corresponding to the light neutrino and the neutral component of the triplet fermion exchange respectively. Using the expression for V from Eqn.2.17, i.e., $V = M_D^*(M^{-1})^* U_R$, and the expression for Y_Σ from Eqn.4.2, we get,

$$\frac{V_{ei}^2}{M_\Sigma} = \frac{\Sigma\,U_{ei}^2\,m_i}{M_\Sigma^2}. \tag{4.20}$$

Thus the contribution due to the triplet is suppressed by a factor of $\langle p^2\rangle/M_\Sigma^2$ as compared to the light neutrino contribution. Thus, the triplet fermions in type-III seesaw mechanism has no significant contribution to $0\nu\beta\beta$ even for the values of M_Σ as low as 100 GeV.

4.7 Summary

In this chapter, we have analyzed the implications of naturalness and the stability of the electroweak vacuum in the context of the minimal type-III seesaw model. We have also studied the constraints from LFV decays. We have found that the lighter masses of the fermionic triplets, $M_\Sigma \simeq 400$ GeV are disallowed for all values of Y_Σ by the constraints from the $\mu \to e$ conversion in the nucleus. At the same time, the heavier triplet masses are disfavored by naturalness. For instance, if we demand the correction to the Higgs mass to be less than 200 GeV, it will put an upper bound of $\sim 10^5$ GeV on the masses of the triplets. Also, the maximum value of Tr$[Y_\Sigma^\dagger Y_\Sigma]^{\frac{1}{2}}$ that is allowed is 0.1, corresponding to $M_\Sigma \sim 10^4$ GeV. Another important result is that in the parameter space which is allowed by both the LFV as well as naturalness constraints, the EW vacuum is stable/metastable depending on the values of Tr$[Y_\Sigma^\dagger Y_\Sigma]^{\frac{1}{2}}$ and the standard model parameters used. Hence, one does not really have to worry about the instability of the vacuum in this model. The major part of the allowed parameter space lies in a region that could be tested in the future collider experiments.

Chapter 5

TeV Scale Singlet Seesaw, Scalar Dark Matter and Vacuum Stability

5.1 Introduction

As discussed in the introduction, two major experimental motivations entailing scenarios beyond SM are neutrino mass and dark matter. For neutrino mass, most natural approach is the seesaw mechanism and from the point of view of testability at the colliders, the TeV seesaw mechaninsm have become an extensive topic of research of late. On the other hand among the various models of dark matter that are proposed in the literature, the most minimal renormalizable extension of the SM are the so called Higgs portal models [66–68]. These models include a scalar singlet that couples only to the SM Higgs. An additional Z_2 symmetry is imposed to prevent the decay of the DM and safe-guard its stability. The coupling of the singlet with the Higgs provides the only portal for its interaction with the SM. Nevertheless there can be testable consequences of this scenario which can put constraints on its coupling and mass. These include constraints from searches of invisible decay of Higgs at the LHC [259–261], direct and indirect detections of dark matter as well as compliance with the observed relic density [233, 262–266]. Implications of such an extra scalar for the LHC [267–271] and ILC [272] have also been studied. Combined constraints from all these have been discussed in [273–277] and most recently in [278].

In addition, the singlet Higgs can also affect the stability of the EW vacuum and this has been discussed in [144, 279–283]. It is seen from these studies that the singlet scalar can help in stabilizing the EW vacuum by adding a positive contribution which prevents the Higgs quartic coupling from becoming negative. On the other hand, as also seen in the previous chapter, the extra fermions can affect the stability adversely and for TeV seesaw models the effect can be appreciable because of low mass thresholds and large Yukawa couplings. The implications of TeV seesaw models with sizable Yukawa couplings to the stability of the vacuum have been discussed in [146–155].

In this chapter, we extent the SM by adding extra fermion as well as scalar singlets and see to what extend the additional scalar singlet can ameliorate the stability problem introduced by fermionic singlets and at the same time explaining the origin of neutrino mass as well as the existence of dark matter. This is based on the work done in [234]. Here, the real singlet scalar is the dark matter candidate where we have imposed an additional Z_2 symmetry which ensures its stability. For generation of neutrino mass at TeV scale we consider two models : (1) The general inverse seesaw model with three right handed neutrinos and three additional singlets and (2) The minimal linear seesaw model. These two sectors are disconnected at the low energy. However, the consideration of the stability of the electroweak vacuum and perturbativity induces a correlation between the two sectors. We study the stability of the electroweak vacuum in this model and explore the effect of the two opposing trends - singlet fermions trying to destabilize the vacuum further and singlet Higgs trying to oppose this. We find the parameter space, which is consistent with the constraints of relic density and neutrino oscillation data and at the same time can cure the instability of the electroweak vacuum. We present some benchmark points for which the electroweak vacuum is stable up to the Planck's scale (M_{Planck}). In addition to absolute stability, we also explore the parameter region which gives metastability in the context of this model. We investigate the combined effect of these two sectors and obtain the allowed parameter space consistent with observations and vacuum stability/metastability and perturbativity. Some studies including neutrino mass, dark matter and/or vacuum stability analysis using scalar singlets can be found in [284–287].

This chapter is organized as follows. In the next section we discuss the fermionic and the scalar sectors of the models that we have studied including the scalar potential in the presence of a singlet scalar. Section 5.3 presents the effective Higgs potential and the renormalization group (RG) evolution of the different couplings. In particular we include the contribution from both fermion and scalar singlets in the effective potential. In section 5.4, we discuss the existing constraints on the fermion and the scalar sector couplings from experimental observations and also from perturbativity. Then we discuss our results a in detail and finally, summarize in section 5.7. .

5.2 Fermionic and the Scalar Sectors of the Model

Here, we briefly discuss the fermionic and the scalar sectors of the models that we are studying.

5.2.1 Fermionic Sector

Out of the various models we had discussed in chapter 2, we will be considering two models :

- **Inverse Seesaw Model (ISM) :** Here, we consider a (3+3+3) scenario for the inverse seesaw model. The Lagrangian and the diagonalization procedure are discussed in detail in section 2.4.

- **Minimal Linear Seesaw Model (MLSM) :** In the case of the MLSM, we add only one right handed neutrino N_R and one gauge-singlet sterile neutrino ν_s [146, 186, 288]. In such a case, the lightest neutrino mass is zero. The source of the lepton number violation is through the coupling Y_s which is assumed to be very small. Here, Y_ν and Y_s are the (3×1) Yukawa coupling matrices and the overall neutrino mass matrix is a symmetric matrix of dimensions 5×5. The light neutrino mass matrix to the leading order is given by Eqn.2.43. The heavy neutrino sector will consist of a pair of degenerate neutrinos.

5.2.2 Scalar Sector

As mentioned earlier, in addition to the extra fermions, we also add an extra real scalar singlet S to the SM. The potential for the scalar sector with an extra Z_2 symmetry under $S \to -S$ is given by,

$$V(S,H) \;=\; -m^2 H^\dagger H \;+\; \lambda(H^\dagger H)^2 + \frac{\kappa}{2} H^\dagger H\, S^2 + \frac{m_S^2}{2} S^2 + \frac{\lambda_S}{24} S^4 \,. \tag{5.1}$$

In this model, we take the vacuum expectation value (vev) of S as 0, so that Z_2 symmetry is not broken. The SM scalar doublet H is given as,

$$H = \frac{1}{\sqrt{2}} \begin{pmatrix} G^+ \\ v + h + iG^0 \end{pmatrix} \tag{5.2}$$

where the vev $v = 246$ GeV.

Thus, the scalar sector consists of two particles h and S, where h is the SM Higgs boson with a mass of $\sim 126\, GeV$, and the mass of the extra scalar is given by,

$$M_{DM}^2 \;=\; {m_S}^2 \,+\, \frac{\kappa}{2} v^2. \tag{5.3}$$

As the Z_2 symmetry is unbroken up to the Planck scale, $M_{Planck} \;=\; 1.22 \times 10^{19}$ GeV, the potential can have minima only along the Higgs field direction and also this symmetry prevents the extra scalar from acquiring a vacuum expectation value. This extra scalar field does not mix with the SM Higgs. Also an *odd* number of this extra scalar does not couple to the SM particles and the new fermions. As a result, this scalar is stable and serve as a viable weakly interacting massive dark matter particle. The scalar field S can annihilate to the SM particles as well as to the new fermions only via the Higgs exchange. So it is called a Higgs portal dark matter.

5.3 Effective Higgs Potential and RG evolution of the Couplings

The effective Higgs potential and the renormalization group equations are the same for both the linear and the inverse seesaw models. The two models differ only by the way in which a small lepton number violation is introduced in them, whose effect could be neglected in the RG evolution. So, effectively, the RGEs are the same in both the models, the only difference being the dimensions of the Yukawa coupling matrices and the number of heavy neutrinos present in the model.

5.3.1 Effective Higgs Potential

In the presence of the extra singlets, the effective potential will get additional contributions from the extra scalar and the fermions. Thus, we have the one-loop effective Higgs potential $(V_1(h))$ in our model as,

$$V_1^{SM+S+\nu}(h) \;=\; V_1^{SM}(h) \;+\; V_1^{S}(h) \;+\; V_1^{\nu}(h), \tag{5.4}$$

where $V_1^{SM}(h)$ is the SM contribution discussed in chapter 2. The one loop contribution due to the extra scalar is given by [289, 290]

$$V_1^{S}(h) \;=\; \frac{1}{64\pi^2} M_S^4(h)\left[\ln\frac{M_S^2(h)}{\mu^2(t)} - \frac{3}{2}\right]. \tag{5.5}$$

where

$$M_S^2(h) \;=\; m_S^2(t) \;+\; \kappa(t)h^2(t)/2$$

The contribution of the extra neutrino Yukawa coupling to the one loop effective potential can be written as [145, 146],

$$V_1^{\nu}(h) = -\frac{((M'^{\dagger}M')_{ii})^2}{32\pi^2}\left[\ln\frac{(M'^{\dagger}M')_{ii}}{\mu^2(t)} - \frac{3}{2}\right] - \frac{((M'M'^{\dagger})_{jj})^2}{32\pi^2}\left[\ln\frac{(M'M'^{\dagger})_{jj}}{\mu^2(t)} - \frac{3}{2}\right]. \tag{5.6}$$

Here $M' \;=\; \frac{Y_\nu}{\sqrt{2}}h$ for inverse seesaw and $M' \;=\; (\frac{Y_\nu}{\sqrt{2}}h \;\; \frac{Y_s}{\sqrt{2}}h\,)$ for linear seesaw. Also, j and i run over the light and heavy neutrinos respectively. In our analysis, we have taken two-loop (one-loop) contributions to the effective potential from the SM particles (extra singlet scalar and fermions). For $h(t) \;>>\; v$, the effective potential could be approximated as,

$$V_{eff}^{SM+S+\nu} \;=\; \lambda_{eff}(h)\frac{h^4}{4} \tag{5.7}$$

with

$$\lambda_{eff}(h) \;=\; \lambda_{eff}^{SM}(h) \;+\; \lambda_{eff}^{S}(h) \;+\; \lambda_{eff}^{\nu}(h). \tag{5.8}$$

where $\lambda_{eff}^{SM}(h)$ is the SM contribution. The contributions due to the extra scalar and the neutrinos are given by

$$\lambda_{eff}^{S}(h) \;=\; e^{4\Gamma(h)}\left[\frac{\kappa^2}{64\pi^2}\left(\ln\frac{\kappa}{2} - \frac{3}{2}\right)\right] \tag{5.9}$$

and

$$\lambda^{\nu}_{eff}(h) = -\frac{e^{4\Gamma(h)}}{32\pi^2}\Bigg[((Y'^{\dagger}_{\nu}Y'_{\nu})_{ii})^2\Bigg(\ln\frac{(Y'^{\dagger}_{\nu}Y'_{\nu})_{ii}}{2} - \frac{3}{2}\Bigg) + ((Y'_{\nu}Y'^{\dagger}_{\nu})_{jj})^2\Bigg(\ln\frac{(Y'_{\nu}Y'^{\dagger}_{\nu})_{jj}}{2} - \frac{3}{2}\Bigg)\Bigg] \tag{5.10}$$

where,

$$\Gamma(h) = \int_{M_t}^{h}\gamma(\mu)\, d\ln\mu. \tag{5.11}$$

Here $\gamma(\mu)$ is the anomalous dimension of the Higgs field and in eqn.(5.10), $Y'_{\nu} = Y_{\nu}$ for inverse seesaw and $Y'_{\nu} = (Y_{\nu}\ \ Y_s)$ for linear seesaw. The contribution of the singlet scalar to the anomalous dimension is zero [279] and the contribution from the right handed neutrinos at one loop is given in eqn.(5.16).

5.3.2 Renormalization Group evolution of the couplings from M_t to M_{Planck}

As we had done for the type-III model in the previous chapter, here also we have evaluated the SM coupling constants at the the top quark mass scale and then run them using the RGEs from M_t to M_{Planck} where we have taken into account the various threshold corrections at M_t [245, 248, 291]. To evaluate the couplings from M_t to M_{Planck}, we have used three-loop RGEs for the SM couplings [139, 252, 253, 255, 292], two-loop RGEs for the extra scalar couplings [282, 284, 293] and one-loop RGEs for the extra neutrino Yukawa couplings [294] [1]. The one loop RGEs for the scalar quartic couplings and the neutrino Yukawa coupling in our model are given below:

$$\beta_{\lambda} = \frac{1}{16\pi^2}\Big(\frac{27}{100}g_1^4 + \frac{9}{10}g_1^2g_2^2 + \frac{9}{4}g_2^4 - \frac{9}{5}g_1^2\lambda - 9g_2^2\lambda + 12\lambda^2 + \kappa^2 + 4T\lambda - 4Y\Big) \tag{5.12}$$

$$\beta_{\kappa} = \frac{1}{16\pi^2}\Big(- \frac{9}{10}g_1^2\kappa - \frac{9}{2}g_2^2\kappa + 6\lambda\kappa + \lambda_S\kappa + 4\kappa^2 + 2T\kappa\Big) \tag{5.13}$$

$$\beta_{\lambda_S} = \frac{1}{16\pi^2}\Big(3\lambda_S^2 + 12\kappa^2\Big) \tag{5.14}$$

[1]Our results do not change with the inclusion of two loop RGEs of Neutrino Yukawa couplings which has been checked using SARAH [295].

$$\beta_{Y_\nu} = \frac{1}{16\pi^2}\Big(Y_\nu\Big(\frac{3}{2}Y_\nu^\dagger Y_\nu - \frac{3}{2}Y_l^\dagger Y_l + T - \frac{9}{20}g_1^2 - \frac{9}{4}g_2^2\Big)\Big) \tag{5.15}$$

where,

$$\begin{aligned} T &= \text{Tr}(3Y_u^\dagger Y_u + 3Y_d^\dagger Y_d + Y_l^\dagger Y_l + Y_\nu^\dagger Y_\nu) \\ Y &= \text{Tr}(3(Y_u^\dagger Y_u)^2 + 3(Y_d^\dagger Y_d)^2 + (Y_l^\dagger Y_l)^2 + (Y_\nu^\dagger Y_\nu)^2). \end{aligned} \tag{5.16}$$

The effect of β- functions of new particles enters into the SM RGEs at their effective masses.

5.4 Existing bounds on the fermionic and the scalar sectors

For the vacuum stability analysis, we need to find the Yukawa and scalar couplings that satisfy the existing experimental and theoretical constraints. These bounds are discussed below.

5.4.1 Bounds on the fermionic Sector

- **Cosmological constraint on the sum of light neutrino masses** As already mentioned in section 1.2, the Planck 2018 results put an upper limit on the sum of active light neutrino masses to be [57]

$$\Sigma = m_1 + m_2 + m_3 < 0.12\,\text{eV}. \tag{5.17}$$

- **Constraints from Oscillation data** We use the standard parametrization of the PMNS matrix and the 3σ ranges of the oscillation parameters as discussed in section 1.2.

- **Constraints on the non-unitarity of U_{PMNS} = U_L** The analysis of the electroweak precision observables along with various other low energy precision observables put bound on the non-unitarity of light neutrino mixing matrix U_L [296]. At 90% confidence level,

$$|U_L U_L^\dagger| = \begin{pmatrix} 0.9979 - 0.9998 & < 10^{-5} & < 0.0021 \\ < 10^{-5} & 0.9996 - 1.0 & < 0.0008 \\ < 0.0021 & < 0.0008 & 0.9947 - 1.0 \end{pmatrix}, \tag{5.18}$$

where U_L is defined in Eqn.2.17 which can be extended for the case of inverse/linear seesaw models. The constraints on the unitarity also takes care of the constraints coming from various charged LFV decays.

- **Bounds on the heavy neutrino masses** The search for heavy singlet neutrinos at LEP by the L3 collaboration in the decay channel $N \to eW$ showed no evidence of a singlet neutrino in the mass range between $80\,\text{GeV}\,(|V_{\alpha i}|^2 \leq 2\times 10^{-5})$ and $205\,\text{GeV}\,(|V_{\alpha i}|^2 \leq 1)$ [297], $V_{\alpha i}$ being the mixing matrix elements between the heavy and light neutrinos. Heavy singlet neutrinos in the mass range from 3 GeV up to the Z-boson mass (m_Z) has also been excluded by LEP experiments from Z-boson decay up to $|V_{\alpha i}|^2 \approx 10^{-5}$ [298–300]. The recent search for the trilepton events in proton-proton collisions at $\sqrt{s} = 13$ TeV conducted by the CMS collaboration gives a bound of $|V_{\alpha i}|^2 < 0.01$ for $M_N \sim 200$ GeV [301]. These constraints are taken care of in our analysis and we have taken the mass of the lightest heavy neutrino to be greater than or equal to 200 GeV.

5.4.2 Bounds on the Scalar Sector

- **Constraints on scalar potential couplings from perturbative unitarity** Constraints on the scalar sector couplings in the singlet scalar model from perturbative unitarity has been discussed in [302]. At very high field values, one can obtain the scattering matrix a_0 for the $J=0$ partial wave [303] by considering the various scalar-scalar scattering amplitudes. Using the equivalence theorem [304–306], we have reproduced the perturbative unitarity bounds on the eigenvalues of the scattering matrix for this model. These are given by [302]

$$|\kappa(\Lambda)| \leq 8\pi, \quad \text{and} \quad \left|6\lambda + \lambda_S \pm \sqrt{4\kappa^2 + (6\lambda - \lambda_S)^2}\right| \leq 16\pi. \tag{5.19}$$

- **Dark matter constraints** The parameter space for the scalar sector should also satisfy dark matter relic density constraint given by Eqn.1.29. In addition, the invisible Higgs decay width and the recent direct detection experiments, in particular, the LUX-2016 [80] data and the indirect Fermi-LAT data[307] restrict the arbitrary Higgs portal coupling and the dark matter mass [144, 278].

Since the extra fermions are heavy ($\gtrsim$ 200 GeV), for low dark matter mass (around 60 GeV), the dominant (more than 75 %) contributions to the relic density is from the $SS \to b\bar{b}$ channel. The channels $SS \to V, V^*$ also contribute to the relic density where V stands for the vector bosons W and Z, V^* indicates the virtual particle which can decay into the SM fermions. In this mass region, the value of the Higgs portal coupling κ is $\mathcal{O}(10^{-2})$ to get the relic density in the right ballpark and simultaneously satisfying the other experimental bounds. However, this region is not of much interest to us since such a small coupling will not contribute much to the running of λ and hence will not affect the stability of the EW vacuum much. The LUX-2016 data [80] has ruled out the dark matter mass region $\sim 70 - 500$ GeV.

If we consider $M_{DM} >> M_t$, the annihilation cross-section is proportional to $\dfrac{\kappa^2}{M_{DM}^2}$, which ensures that the relic density band in $\kappa - M_{DM}$ [144] plane is a straight line. In this region, one can get the right relic density if the ratio of dark matter mass to the Higgs portal coupling κ is $\sim$ 3300 GeV. In this case, the dominant contributions to the dark matter annihilation channel are $SS \to hh, t\bar{t}$, VV.

We use FeynRules [308] along with micrOMEGAs [309, 310] to compute the relic density of the scalar dark matter. We have checked that the contribution from annihilation into extra fermions is very small. However this could be significant for dark matter mass $\gtrsim$ 2.5 TeV, provided the Yukawa couplings are large enough. But, in the stability analysis discussed in section 5.5.1, we will see that the dark matter mass $\gtrsim$ 2.5 TeV requires the value of $\kappa \gtrsim 0.65$ which violates the perturbativity bounds before M_{Planck}. Thus, we consider the dark matter mass in the range $\sim$ 500 GeV - 2.5 TeV with κ in the range $\sim$ 0.15 to 0.65. It is to be noted that in the presence of the singlet fermions the value of $\kappa(M_Z)$ and hence M_{DM} for which the perturbativity is not obeyed will also depend upon the value of Tr $[Y_\nu^\dagger Y_\nu]$. This will be discussed in the next section.

5.5 Results

In this section, we present our results of the stability analysis of the electroweak vacuum in the two seesaw scenarios. We confine ourselves to the normal hierarchy. The results for the inverted hierarchy are not expected to be very different [146]. We have used the package SARAH[295] to do the RG analysis in our work.

5.5.1 Inverse Seesaw Model

For the inverse seesaw model, the input parameters are the entries of the matrices Y_ν, M_S and M_μ. Here Y_ν is a complex 3×3 matrix. M_S is a real 3×3 matrix and M_μ is a 3×3 diagonal matrix with real entries. We vary the entries of various mass matrices in the range $10^{-2} < M_\mu < 1$ keV and $0 < M_R < 5 \times 10^4$ GeV. This implies a heavy neutrino mass of maximum up to a few TeV. With these input parameters, we search for parameter sets consistent with the low energy data using the downhill simplex method [311]. We present in table 5.1, some representative outputs consistent with data for two benchmark points. In this table, $Tr[Y_\nu Y_\nu^\dagger]$ is an input. As a consistency check, we also give the value of $Br(\mu \to e\,\gamma)$.

Vacuum Stability

In this section, we will discuss how the presence of the new fermionic and scalar couplings affect the running of the Higgs quartic coupling and thereby alter the stability of the EW vacuum. In Fig. 5.1, we display the running of the couplings for various benchmark points in the ISM. In Fig. 5.1(a), we have shown the variation in the running of the Higgs quartic coupling λ for different values of Tr $[Y_\nu^\dagger Y_\nu]$ (0, 0.15 and 0.30) for a fixed value of the Higgs portal coupling $\kappa = 0.304$. We have chosen the dark matter mass $M_{DM} = 1000$ GeV to get the relic density in the right ballpark. As λ_S doesn't alter the relic density, we have fixed its value at 0.1 for all the plots given in this chapter. We can see that for Tr $[Y_\nu^\dagger Y_\nu] = 0$, i.e., without the right handed neutrinos, the EW vacuum remains absolutely stable up to M_{Planck} (green line) and for large values of Tr $[Y_\nu^\dagger Y_\nu]$, the EW vacuum goes towards the instability (Higgs quartic coupling becomes negative around $\Lambda_I \sim 10^{10}$ GeV (red line) and $\Lambda_I \sim 10^{8}$ GeV (black line)) region.

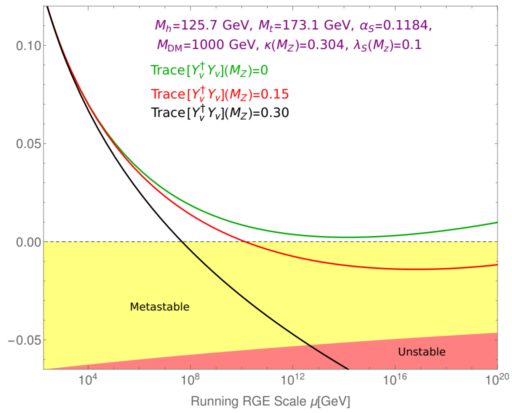

(a) Different Y_ν and fixed κ.

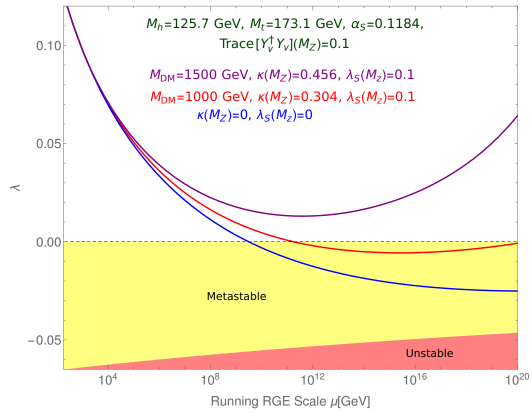

(b) Fixed Y_ν and different κ.

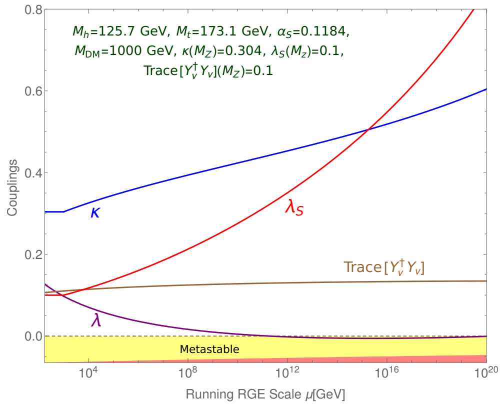

(c) Running of the couplings with energy for dark matter mass of 1000 GeV.

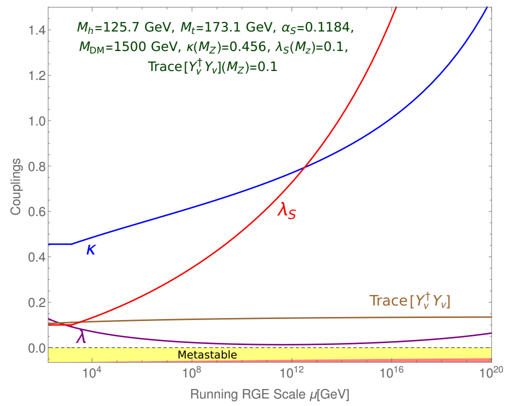

(d) Running of the couplings with energy for dark matter mass of 1500 GeV.

Figure 5.1: Running of the couplings with the energy scale in the Inverse seesaw model.

Parameter	$BM-I$	$BM-II$
$\Delta m^2_{21}/10^{-5}eV^2$	8.0891	7.8228
$\Delta m^2_{31}/10^{-3}eV^2$	2.4391	2.5046
$\sin^2\theta^L_{12}$	0.2710	0.3429
$\sin^2\theta^L_{23}$	0.3850	0.3850
$\sin^2\theta^L_{13}$	0.0239	0.0229
δ_{PMNS}	1.1173	1.4273
ϕ_1, ϕ_2	$2.5187, 2.9377$	$2.9384, 3.1379$
$m_i/10^{-1}\ eV$	$0.10, 0.13, 0.511$	$0.23, 0.25, 0.558$
$M_j\ GeV$	$200.77, 200.77, 461.159,$	$210.01, 210.01, 487.284,$
	$461.16, 1744.67, 1744.669$	$487.28, 1451.34, 1451.344$
$Tr[Y_\nu Y_\nu^\dagger]$	0.1	0.2
$Br(\mu \to e\,\gamma)$	0.731×10^{-16}	0.1×10^{-16}

Table 5.1: Output values for two different benchmark points for inverse seesaw model satisfying all the low energy constraints

In Fig. 5.1(b), we plot the running of λ for a fixed value of Tr $[Y_\nu^\dagger Y_\nu]$ = 0.1 and different sets of κ and M_{DM}. It is seen that for a larger value of $\kappa = 0.45$ with M_{DM} = 1500 GeV, the EW vacuum remains stable up to M_{Planck} (purple line). For $\kappa = 0.304$ with $M_{DM} = 1000$ GeV, the quartic coupling λ (red line) becomes negative around $\Lambda_I \sim 10^{11}$ GeV and in the absence of the singlet scalar field, i.e., for $\kappa = 0$, $\lambda_S = 0$ (blue line), λ becomes negative around $\Lambda_I \sim 10^9$ GeV and the vacuum goes to the metastability region.

In Figs. 5.1(c) and 5.1(d), we have shown the running of all the three scalar quartic couplings, λ, κ and λ_S and Tr$[Y_\nu^\dagger Y_\nu]$ for $(M_{DM},\ \kappa)$ = (1000 GeV, 0.304) and (1500 GeV, 0.456) respectively. It can be seen that the values of λ_s and κ increases considerably with the energy scale and can reach the perturbativity bound at M_{Planck} depending upon the initial values of κ and λ_S at M_Z. Here for λ_S = 0.1, the maximum allowed value of κ will be 0.58 from perturbativity. The value of Tr$[Y_\nu^\dagger Y_\nu]$ increases only slightly with the energy scale and the value of λ_S increases faster for larger value of κ.

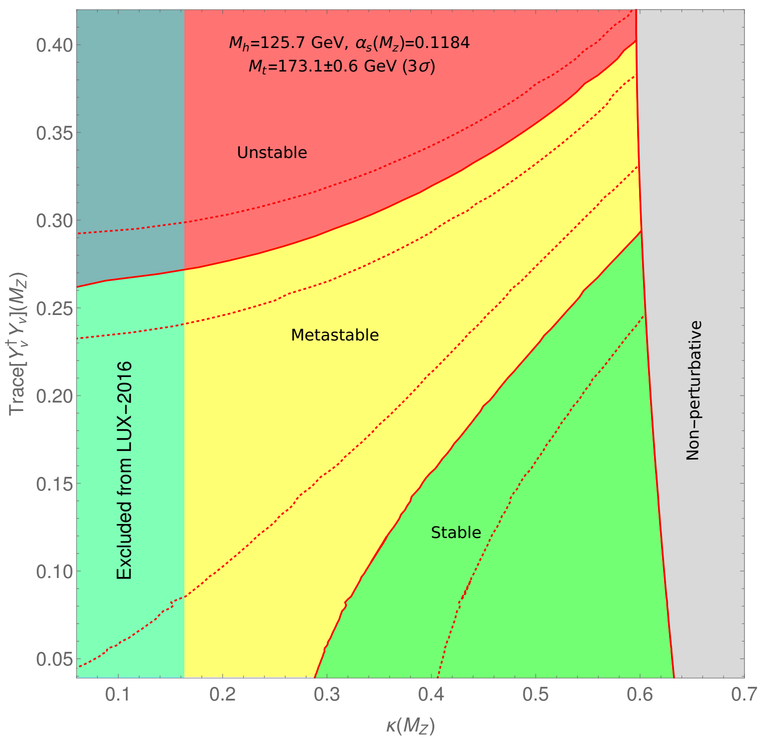

Figure 5.2: Phase diagram in the Tr$[Y_\nu^\dagger Y_\nu]$ - κ plane. We have fixed all the entries of Y_ν except for $(Y_\nu)_{33}$. The three boundary lines (two dotted and a solid) correspond to $M_t = 173.1 \pm 0.6$ GeV (3σ) and we have taken $\lambda_S(M_Z) = 0.1$. The dark matter mass is dictated by $\kappa(M_z)$ to give the correct relic density. See text for details.

Tunneling Probability and Phase Diagrams

In our model, the EW vacuum shifts towards stability/instability depending upon the new physics parameter space for the central values of $M_h = 125.7$ GeV, $M_t = 173.1$ GeV and $\alpha_s = 0.1184$ and there might be an extra minima around 10^{12-17} GeV. In Fig. 5.2, we have given the phase diagram in the Tr $[Y_\nu^\dagger Y_\nu] - \kappa$ plane. The line separating the stable region and the metastable region is obtained when the two vacuua are at the same depth, i.e., $\lambda(\mu) = \beta_\lambda(\mu) = 0$. The unstable and the metastable regions are separated by the boundary line where $\beta_\lambda(\mu) = 0$ along with $\lambda(\mu) = \lambda_{min}(\Lambda_B)$, as defined in Eqn.2.65. For simplicity, we have plotted Fig. 5.2 (also Fig. 5.1) by fixing all the eight entries of the 3×3 complex matrix Y_ν, but varying only the $(Y_\nu)_{33}$ element to get a smooth phase diagram. From Fig. 5.2, it could be seen that the values of κ beyond ~ 0.58 are disallowed by perturbativity bounds and those below ~ 0.16 are disallowed by the direct detection bounds from LUX-2016 [80]. The value of the dark matter mass in this allowed range is thus $\sim$ 530 $-$ 2100 GeV. Note that the vacuum stability analysis of the inverse seesaw model done in reference [152] had found that the parameter space with Tr $[Y_\nu^\dagger Y_\nu] > 0.4$ were excluded by vacuum metastability constraints. Whereas, in our case, Fig. 5.2 shows that the parameter space with Tr $[Y_\nu^\dagger Y_\nu] \gtrsim 0.25$ are excluded for the case when there is no extra scalar. The possible reasons could be that we have kept the maximum value of the heavy neutrino mass to be around a few TeV, whereas the authors of [152] had considered heavy neutrinos as heavy as 100 TeV. Obviously, considering larger thresholds would allow us to consider large value of Tr$[Y_\nu^\dagger Y_\nu]$ as the corresponding couplings will enter into RG running only at a higher scale. Another difference with the analysis of [152] is that we have fixed 8 of the 9 entries of the Yukawa coupling matrix Y_ν. Also, varying all the 9 Yukawa couplings will give us more freedom and the result is expected to change. The main result that we deduce from this plot is the effect of κ on the maximum allowed value of Tr $[Y_\nu^\dagger Y_\nu]$, which increases from 0.26 to 0.4 for a value of κ as large as 0.6. In addition, we see that the upper bound on $\kappa(M_Z)$ from perturbativity at M_{Planck} decreases from 0.64 to 0.58 as the value of Tr$[Y_\nu^\dagger Y_\nu]$ changes from 0 to 0.44. This can be explained from the expression of the β_κ in eqn.(5.16) which shows that $[Y_\nu^\dagger Y_\nu]$ affect the running κ positively through the quantity T. Since $M_{DM} \sim$ 3300 κ GeV for $M_{DM} >> M_t$, the mass of dark matter for which perturbativity is valid, decreases with increase in the value of the Yukawa coupling.

Confidence level of vacuum stability

Following the discussion in the last chapter, in Fig. 5.3, we graphically show how the confidence level at which stability of electroweak vacuum is allowed/excluded depends on new Yukawa couplings of the heavy fermions for the inverse seesaw model in the presence of the extra scalar (dark matter) field. We have plotted the dependence of confidence level against the trace of the Yukawa coupling, Tr$[Y_\nu^\dagger Y_\nu]$ for fixed values of Higgs portal coupling $\kappa = 0.304$ in Fig. 5.3(a). Here, the dark matter mass $M_{DM} =$ 1000 GeV is dictated by κ to obtain the correct relic density. Similar plot with a higher value of $\kappa = 0.455$ with dark matter mass $M_{DM} = 1500$ GeV is shown in Fig. 5.3(b). In this case the electroweak vacuum is absolutely stable for a larger parameter

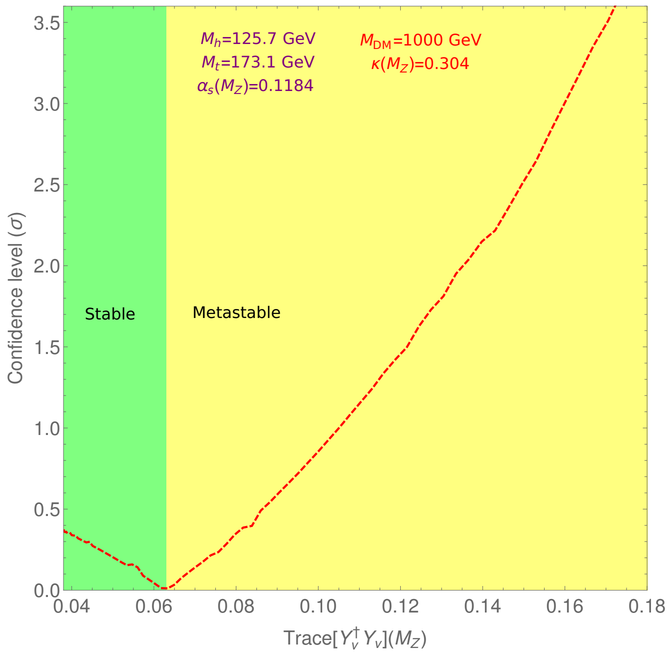

(a) (κ, M_{DM}) = (0.304, 1000 GeV)

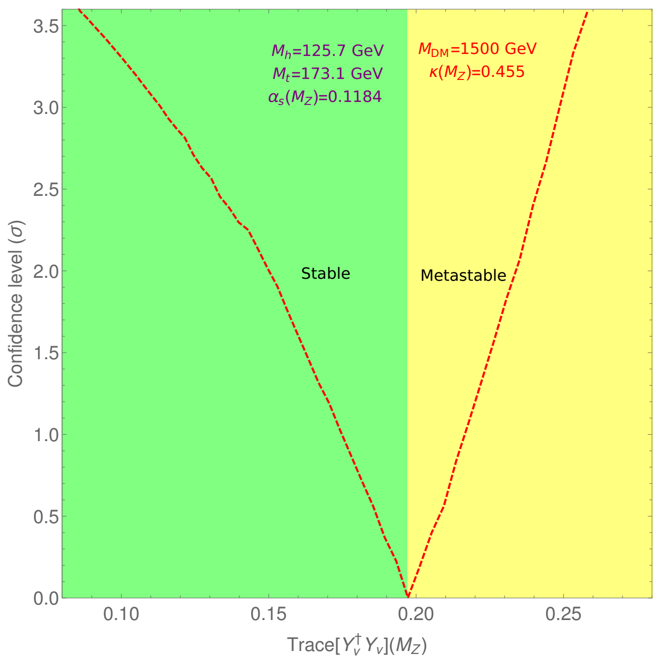

(b) (κ, M_{DM}) = (0.455, 1500 GeV)

Figure 5.3: Dependence of confidence level at which the EW vacuum stability is excluded/allowed on Tr$[Y_\nu^\dagger Y_\nu]$ for two different values of κ and M_{DM}. We have taken $\lambda_S(M_Z) = 0.1$.

space. For a particular set of values of the model parameters $M_h = 125.7$ GeV, $M_t = 173.1$ GeV, $\alpha_s(M_z) = 0.1184$ and κ, the confidence level (one-sided) at which the electroweak vacuum is absolutely stable (green region) decreases with the increase of Tr$[Y_\nu^\dagger Y_\nu]$ and becomes zero for Tr$[Y_\nu^\dagger Y_\nu] = 0.06$ in Fig. 5.3(a) and Tr$[Y_\nu^\dagger Y_\nu] = 0.20$ in Fig. 5.3(b). The confidence level at which the absolute stability of electroweak vacuum is excluded (one-sided) increases with the trace of the Yukawa coupling in the yellow region.

5.5.2 Minimal Linear Seesaw Model

In the minimal linear seesaw case, the Yukawa coupling matrices Y_ν and Y_s can be completely determined in terms of the oscillation parameters apart from the overall coupling constant y_ν and y_s respectively [288]. For normal hierarchy, in MLSM, the Yukawa coupling matrices Y_ν and Y_s can be parametrized as,

$$Y_\nu = \frac{y_\nu}{\sqrt{2}}\left(\sqrt{1+\rho}\,U_3^\dagger + \mathrm{e}^{i\frac{\pi}{2}}\sqrt{1-\rho}\,U_2^\dagger\right) \tag{5.20}$$

$$Y_s = \frac{y_s}{\sqrt{2}}\left(\sqrt{1+\rho}\,U_3^\dagger + \mathrm{e}^{i\frac{\pi}{2}}\sqrt{1-\rho}\,U_2^\dagger\right) \tag{5.21}$$

where

$$\rho = \frac{\sqrt{1+r}-\sqrt{r}}{\sqrt{1+r}+\sqrt{r}}. \tag{5.22}$$

Here, U_i's are the columns of the unitary PMNS matrix U_ν and r is the ratio of the solar and the atmospheric mass squared differences. This parametrization makes the vacuum stability analysis in the minimal linear seesaw model easier since there are only two independent parameters y_ν and M_N in the fermion sector, where M_N is the degenerate mass of the two heavy neutrinos (the value of y_s being very small $\mathcal{O}(10^{-11})$). A detailed analysis has already been performed in reference [146]. Here, we are interested in the interplay between the Z_2 odd singlet scalar and singlet fermions in the vacuum stability analysis.

In Fig. 5.4, we have plotted the running of the Higgs quartic coupling λ with the energy scale μ up to M_{Planck}. The Figs. 5.4(a) and 5.4(b) show the running of λ for different values of k (0.0, 0.304, 0.456) and M_{DM} (0,1000 GeV, 1500 GeV), for M_N = 200 GeV and M_N = 10^4 GeV respectively for a fixed value of y_ν^2 = 0.1. Comparing these two plots, we can see that λ tends to go to the instability region faster for smaller values of the heavy neutrino mass. So, the EW vacuum is more stable for larger values of M_N, because the effect of extra singlet fermion in the running of λ enters at a higher value. We also find that as the value of κ increases from 0 to 0.304, the electroweak vacuum becomes metastable at a higher value of the energy scale. For κ = 0.456 the electroweak vacuum becomes stable up to M_{Planck} even in the presence of the singlet fermions.

Figs. 5.4(c) and 5.4(d) display the running of λ for different values of y_ν^2 (0.0, 0.15, 0.3) and for fixed values of k = 0.304 and M_{DM} = 1000 GeV, for M_N = 200 GeV and for M_N = 10^4 GeV respectively. It could be seen from these plots that larger the value of y_ν, earlier λ becomes negative and more is the tendency for the EW vacuum to be unstable as expected. We note from these two figures that for κ = 0.304, absolute stability is attained only for y_ν = 0 even in the presence of the singlet scalar.

In Fig. 5.5, we have shown the phase diagram in the $y_\nu - M_N$ plane. The stable (green), unstable (red) and the metastable (yellow) regions are shown and it could be seen that higher the value of M_N, larger the allowed values of y_ν by vacuum stability as we have discussed earlier. The unstable and the metastable regions are separated by solid red line for the central values of the SM parameters, M_h = 125.7 GeV, M_t = 173.1 GeV and α_s = 0.1184. The red dashed lines represent the 3σ variation of the top quark mass. However, we get significant stable region for M_h = 125.7 GeV, M_t = 171.3 GeV and α_s = 0.1191 which corresponds to the solid line separating the stable and the metastable region. The region in the left side of the blue dotted line is disallowed by LFV constraints for the normal hierarchy of light neutrino masses. Fig. 5.5(a) is drawn in the absence of the extra scalar and Fig. 5.5(b) is drawn for (κ, M_{DM}) = (0.304, 1000 GeV). Clearly, there is more stable region in the presence of the extra scalar and the boundary line separating the metastable and the unstable regions also shifts upwards in this case.

In Fig. 5.6, we have shown the phase diagrams in the y_ν - κ plane for two different values of the heavy neutrino masses : Fig. 5.6(a) for $M_N = 200$ GeV and Fig. 5.6(b) for $M_N = 10^4$ GeV. Here also, the red dashed lines represent the 3σ variation of top quark mass. It could clearly be seen that as the value of the heavy neutrino mass is

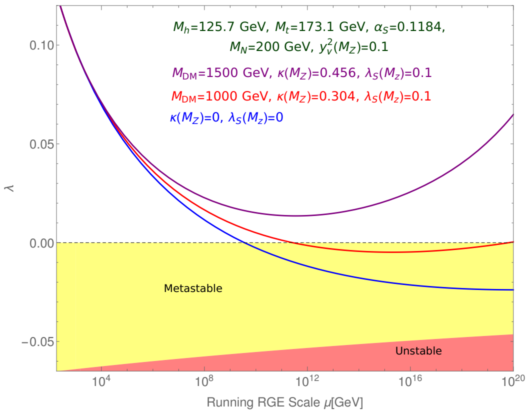

(a)

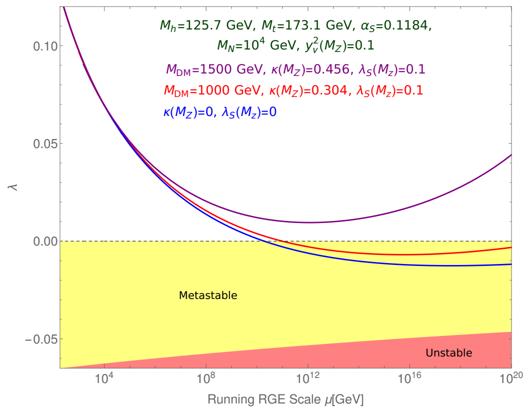

(b)

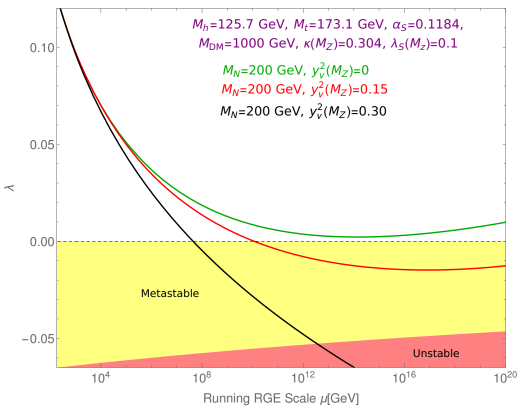

(c)

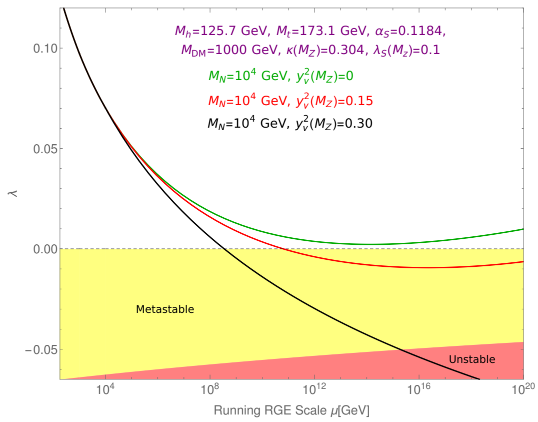

(d)

Figure 5.4: Running of the quartic coupling λ in MLSM with extra scalar for two different values of M_N. In the upper panel, the three lines are for different values of M_{DM} and κ whereas in the lower panel, they are for different values of y_ν and fixed values of M_{DM} and κ.

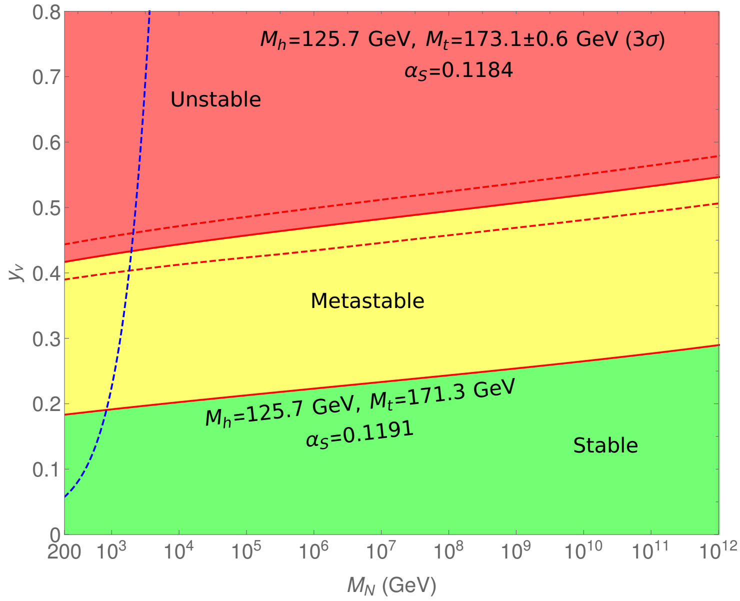

(a) Without the extra scalar

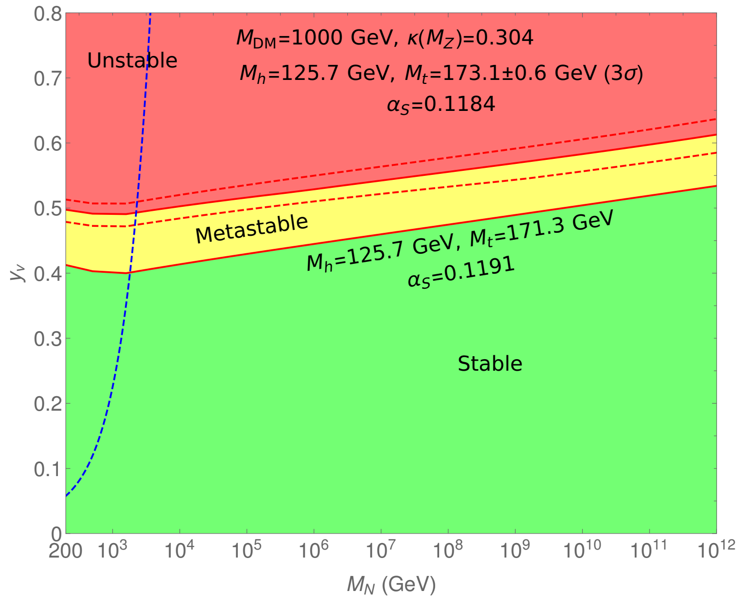

(b) With scalar, (κ, M_{DM}) = (0.304, 1000 GeV)

Figure 5.5: Phase diagrams in the y_ν - M_N plane in the presence and the absence of the extra scalar. Region in the left side of the blue dotted line is disallowed by constraint from BR($\mu \to e\gamma$). The three boundary lines (two dotted and a solid) correspond to $M_t = 173.1 \pm 0.6$ GeV (3σ) and we have taken $\lambda_S(M_Z) = 0.1$ in the second plot.

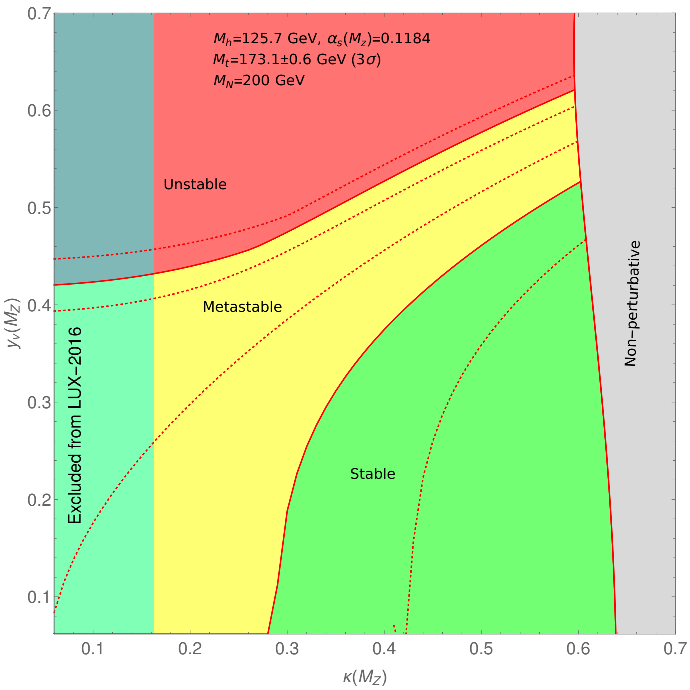

(a)

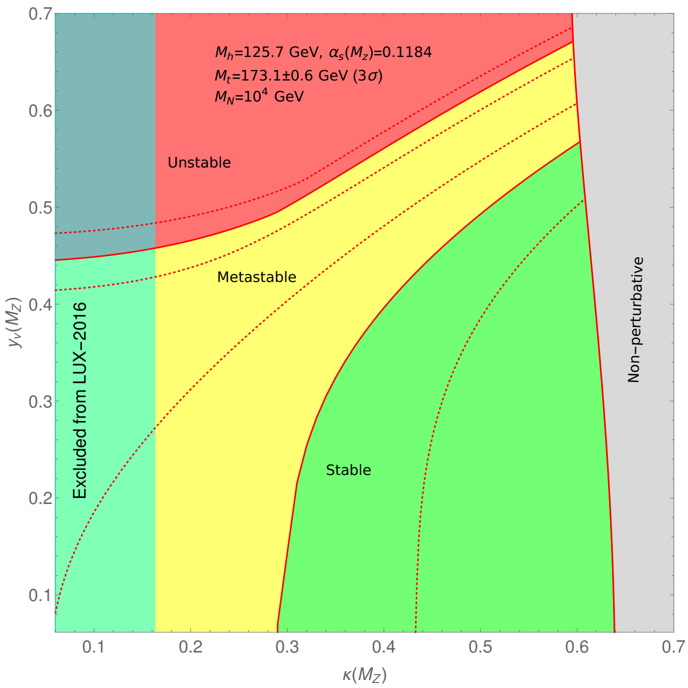

(b)

Figure 5.6: Phase Diagrams in the y_ν - κ plane for two different values of M_N. Here, $\lambda_S(M_Z) = 0.1$ and the dark matter mass is dictated by $\kappa(M_z)$ to give the correct relic density.

higher, the unstable region shifts towards the large values of y_ν. This is a result that should be expected from Fig. 5.5. In this model, the theory becomes non-perturbative (grey) for κ = 0.64 for y_ν = 0.05. The maximum allowed value of κ by perturbativity at M_{Planck} decreases with increase in y_ν as we have also seen for the inverse seesaw case. The region $\kappa \lesssim 0.16$ is excluded from the recent direct detection experiment at LUX.

5.6 Neutrino-less Double Beta Decay

The heavy neutral fermions may give rise to additional contributions to $0\nu\beta\beta$ through their mixing with the light neutrinos. Analogous to Eqn.4.18, the half life for $0\nu\beta\beta$ in this case is given by,

$$\frac{\Gamma_{0\nu\beta\beta}}{\ln 2} = G^{0\nu}(Q,Z)\,\frac{|M_\nu{}^2|}{m_e^2}\left|\Sigma\, U_{ei}^2\, m_i + \langle p^2\rangle \frac{V_{ei}^2}{M_i}\right|^2, \tag{5.23}$$

where V is the light-heavy mixing. From the fact that the lepton number violating parameters in both the inverse as well as the linear seesaw models are very small, we can predict that the heavy neutrino contribution to $0\nu\beta\beta$ will be very small. To see this explicitly in the case of the inverse seesaw model, consider the second term,

$$\frac{V_{ei}^2}{M_i} = \frac{V_{e1}^2}{M_1} + \frac{V_{e2}^2}{M_2} + \frac{V_{e3}^2}{M_3} + \frac{V_{e4}^2}{M_4} + \frac{V_{e5}^2}{M_5} + \frac{V_{e6}^2}{M_6,}. \tag{5.24}$$

In the limit $\mu = 0$, we have, $M_1 = M_2$, $M_3 = M_4$, $M_5 = M_6$, $V_{e1}^2 = -V_{e2}^2$, $V_{e3}^2 = -V_{e4}^2$ and $V_{e5}^2 = -V_{e6}^2$. Thus, the above term vanishes. Even if we consider the limit $\mu \neq 0$, one can see that the additional contribution is negligibly small compared to the active light neutrino contribution. One can reach similar conclusion in the case of the linear seesaw model as well and this has been discussed in [146].

5.7 Summary

In this chapter we have analysed the stability of the electroweak vacuum in the context of TeV scale inverse seesaw and minimal linear seesaw models extended with a scalar singlet dark matter. We have studied the interplay between the contribution of the extra singlet scalar and the singlet fermions to the EW vacuum stability. We have shown that the coupling constants in these two seemingly disconnected sectors can be correlated at high energy by the vacuum stability/metastability and perturbativity constraints.

In the inverse seesaw scenario, the EW vacuum stability analysis is done after fitting the model parameters with the neutrino oscillation data and non-unitarity constraints on U_{PMNS} (including the LFV constraints from $\mu \to e\gamma$). For the minimal linear seesaw model, the Yukawa matrix Y_ν can be fully parameterized in terms of the oscillation parameters excepting an overall coupling constant y_ν which can be constrained from vacuum stability and LFV. We have taken the heavy neutrino masses of order up to a few TeV for both the seesaw models. An extra Z_2 symmetry is imposed to ensure that the scalar particle serves as a viable dark matter candidate. We include all the experimental and theoretical bounds coming from the constraints on relic density and dark matter searches as well as unitarity and perturbativity up to M_{Planck}. For the masses of new fermions from 200 GeV to a few TeV, the annihilation cross section to the extra fermions is very small for dark matter mass $\mathcal{O}(1-2)$ TeV. We have also checked that the theory violates perturbativity before M_{Planck} for dark matter mass $\gtrsim 2.5$ TeV. In addition we find that the value of the Higgs portal coupling κ (M_Z) for which perturbativity is violated at M_{Planck} decreases with increase in the value of the Yukawa couplings of the new fermions. For $M_{DM} >> M_t$, one can approximately write $M_{DM} \sim 3300\,\kappa$ GeV. This implies that with the increasing Yukawa coupling, the mass of dark matter for which the perturbativity is maintained also decreases. Thus the RGE running induces a correlation between the couplings of the two sectors from the perturbativity constraints.

The presence of the fermionic Yukawa couplings in the context of TeV scale seesaw models drives the vacuum more towards instability while the singlet scalar tries to arrest this tendency. Overall, we find that it is possible to find parameter spaces for which the electroweak vacuum remains absolutely stable for both inverse and linear seesaw models in the presence of the extra scalar particle. We find an upper bound from metastability on Tr$[Y_\nu^\dagger Y_\nu]$ as 0.25 for κ = 0 which increases to 0.4 for κ = 0.6 in inverse seesaw model. We have also seen that in the absence of the extra scalar, the values of the Yukawa coupling y_ν greater than 0.42 are disallowed in the minimal linear seesaw model. But, in the presence of the extra scalar the values of y_ν up to ~ 0.6 are allowed for dark matter mass ~ 1 TeV. The correlations between the Yukawa couplings (Tr$[Y_\nu^\dagger Y_\nu]$ or y_ν) and κ are presented in terms of phase diagrams.

Inverse and linear seesaw models can be explored at LHC through trilepton signatures [186–194]. A higher value of Yukawa couplings, as can be achieved in the presence of the Higgs portal dark matter, can facilitate observing such signals at colliders.

Chapter 6

Inverse Seesaw and Fermionic Dark Matter in a Class of gauged $U(1)$ Extensions of the SM

6.1 Introduction

In the last two chapters, we have explored some low scale seesaw models in which the SM was extended by new particles without altering the gauge group structure. In this chapter, we study a class of models in which the SM gauge group is extended by an additional $U(1)$ gauge group. The models with an extra $U(1)$ gauge group naturally contain three right handed neutrinos as a result of the conditions for the gauge anomaly cancellation. Thus, the active light neutrino masses can be generated via the canonical type-I seesaw mechanism [89–92]. However, as we have already discussed, the canonical type-I seesaw model is not testable and this leads us to consider low scale seesaw models like inverse seesaw with sizable Yukawa couplings. An inverse seesaw mechanism in the context of a $U(1)_{B-L}$ extension of the SM has been studied in reference [149]. In these models, the presence of extra singlet fermions (in addition to the right handed neutrinos) helps us to bring down the seesaw scale (which is the $U(1)$ breaking scale) to $\sim O(\text{TeV})$, simultaneously allowing for large Yukawa couplings, $Y_\nu \sim O(0.1)$.

The implications for the stability of the electroweak (EW) vacuum in the context of $U(1)$ extended models have been studied in [150, 232, 312–315]. In such models, the behavior of the EW vacuum depends also on the $U(1)$ quantum numbers chosen, since the renormalization group equations (RGEs) depend on these quantum numbers. The conformal symmetric versions of such models have been considered in references [232, 315]. In addition, these models can accommodate a dark matter candidate even in the minimal version (with type-I seesaw), by adding an additional Z_2 symmetry [316, 317], where the third generation of the right handed neutrinos act as the dark matter candidate. Other versions of the $U(1)_{B-L}$ extension with scalar dark matter have been studied in [318–320]. Also, there are various realizations of the grand unified theories (GUTs) that predict the existence of extra Z' boson [321, 322]. The presence of the extra Z' boson that couples to the quarks and the leptons also gives rise to a rich collider phenomenology in the $U(1)$ models[232, 314, 323, 324]. Searches for such Z' boson through its decay to the dileptons have been conducted by the ATLAS and the CMS collaborations and lower limits on the Z' mass have been obtained [5, 325, 326].

In this chapter, we consider a class of gauged $U(1)$ extensions of the SM, where active light neutrino masses are generated by an inverse seesaw mechanism. This is based on the work that has been done in [327]. In addition to the three right handed neutrinos, we add three singlet fermions and demand an extra Z_2 symmetry under which, the third generations of both the neutral fermions are odd, which in turn gives us a stable fermionic dark matter candidate. This allows us to consider large neutrino Yukawa couplings and at the same time, keeping the $U(1)'$ symmetry breaking scale to be of the order of $\sim\ O(1)$ TeV. The main difference of this inverse seesaw model from that considered in [149] is that the extra neutral fermions are singlets under the gauge group and hence we do not have to worry about anomaly cancellation. Also, instead of considering one particular model, we express the $U(1)$ charges of all the fermions in terms of the U(1) charges of the SM Higgs and the new complex scalar. We perform a comprehensive study of the bounds on the model parameters from low energy neutrino data, vacuum stability, perturbative unitarity and dark matter as well as collider constraints.

The rest of the chapter is organized as follows. In sections 6.2 and 6.3, we introduce the class of the $U(1)$ models under consideration and discuss the fermionic and the scalar sectors. We discuss the fitting of the neutral fermion mass matrix in section 6.4, by taking all the experimental constraints into account. In section 6.5, we discuss the RG evolution of the couplings and present the parameter space allowed by vacuum stability and perturbative unitarity in various planes. This is followed by a discussion on the dark matter scenario in these models, where we present the parameter space giving the correct relic density and satisfying the direct detection bounds at the same time. In section 6.7, we discuss the combined bounds from vacuum stability, unitarity, dark matter relic density and the collider constraints and finally, we summarize in section 6.8.

6.2 Model and Neutrino Mass at the tree level

The model considered is based on the gauge group $SU(3)_c \times SU(2)_L \times U(1)_Y \times U(1)'$. In addition to the SM particles, we have three right handed neutrinos N_{Ri}, a complex scalar Φ required to break the $U(1)'$ symmetry and three gauge singlet Majorana fermions S_i. An extra Z_2 symmetry is imposed to have a stable fermionic dark matter. The matter and Higgs sector field content along with their transformation properties under $SU(3)_c \times SU(2)_L \times U(1)_Y \times U(1)'$ are given below.

$$Q_L = \begin{bmatrix} u_L \\ d_L \end{bmatrix} \sim (3,\ 2,\ \frac{1}{6},\ x_q)\ ;\ d_R \sim (3,\ 1,\ -\frac{1}{3},\ x_d)\ ;\ u_R \sim (3,\ 1,\ \frac{2}{3},\ x_u), \tag{6.1}$$

$$l_L = \begin{bmatrix} \nu_L \\ e_L \end{bmatrix} \sim (1,\ 2,\ -\frac{1}{2},\ x_l)\ ;\ e_R \sim (1,\ 1,\ -1,\ x_e)\ ;\ N_R \sim (1,\ 1,\ 0,\ x_\nu), \tag{6.2}$$

$$H = \frac{1}{\sqrt{2}} \begin{pmatrix} G^+ \\ v + h + iG^0 \end{pmatrix} \sim (1,\ 2,\ \frac{1}{2},\ \frac{x_H}{2})\ ;\ \Phi = \frac{1}{\sqrt{2}}(\phi + u + i\chi) \sim (1,\ 1,\ 0,\ -x_\Phi), \tag{6.3}$$

$$\nu_s \sim (1,\ 1,\ 0,\ 0). \tag{6.4}$$

Note that the generation indices have been suppressed here. Under Z_2, the third generation of N_R and ν_s, i.e., N_{R3} and ν_{s3} are odd whereas all the other particles are even and we assume that this Z_2 is not broken.

The $U(1)'$ charges of the fermions are defined to satisfy the gauge and gravitational anomaly-free conditions:

$$
\begin{aligned}
U(1)' \times [SU(3)_c]^2 &\quad : \quad 2x_q - x_u - x_d = 0, \\
U(1)' \times [SU(2)_L]^2 &\quad : \quad 3x_q + x_l = 0, \\
U(1)' \times [U(1)_Y]^2 &\quad : \quad x_q - 8x_u - 2x_d + 3x_l - 6x_e = 0, \\
[U(1)']^2 \times U(1)_Y &\quad : \quad x_q^2 - 2x_u^2 + x_d^2 - x_l^2 + x_e^2 = 0, \\
[U(1)']^3 &\quad : \quad 6x_q^3 - 3x_u^3 - 3x_d^3 + 2x_l^3 - x_\nu^3 - x_e^3 = 0, \\
U(1)' \times [\text{grav}]^2 &\quad : \quad 6x_q - 3x_u - 3x_d + 2x_l - x_\nu - x_e = 0.
\end{aligned} \tag{6.5}
$$

The most general Yukawa Lagrangian (along with the Majorana mass for ν_s) invariant under $SU(3)_c \times SU(2)_L \times U(1)_Y \times U(1)'$ that can be written using the fields given above is,

$$
-\mathcal{L}_{\text{Yukawa}} = Y_e \bar{l}_L H e_R + Y_\nu \bar{l}_L \tilde{H} N_R + Y_u \overline{Q}_L \tilde{H} u_R + Y_d \overline{Q}_L H d_R \; + \; y_{NS} \overline{N}_R \Phi \nu_s + \frac{1}{2} \overline{\nu_s{}^c} M_\mu \nu_s \; + \; \text{h.c.}, \tag{6.6}
$$

where $\tilde{H} = i\sigma_2 H^*$. The invariance of this Yukawa Lagrangian under the $U(1)'$ symmetry gives us the following conditions :

$$
\frac{x_H}{2} = -x_q + x_u = x_q - x_d = -x_l + x_\nu = x_l - x_e \;\; ; \;\; -x_\Phi = x_\nu. \tag{6.7}
$$

Using these conditions and the anomaly-free conditions, the $U(1)'$ charges of all the fermions could be determined in terms of x_H and x_Φ as,

$$
\begin{aligned}
x_\nu = -x_\Phi \;\; ; \;\; x_l = -x_\Phi - \frac{x_H}{2} \;\; ; \;\; x_e = -x_\Phi - x_H, \\
x_q = \frac{1}{6}(2x_\Phi + x_H) \;\; ; \;\; x_u = \frac{1}{3}(2x_H + x_\Phi) \;\; ; \;\; x_d = \frac{1}{3}(x_\Phi - x_H),
\end{aligned} \tag{6.8}
$$

Note that the choice $x_\Phi = 1$ and $x_H = 0$ correspond to the well known $U(1)_{B-L}$ model. From eqn.(6.6), after symmetry breaking, the terms relevant for neutrino mass are,

$$
-L_{mass} = \overline{\nu}_L M_D N_R + \overline{N_R}\, M_R S \; + \; \frac{1}{2} \overline{\nu_s{}^c} M_\mu \nu_s \; + \; \text{h.c.}, \tag{6.9}
$$

where, $M_D = Y_\nu \langle H \rangle$ and $M_R = y_{NS} \langle \Phi \rangle$. The neutral fermion mass matrix M_ν can be defined as,

$$-L_{mass} = \frac{1}{2}(\overline{\nu_L^c}\ \overline{N}_R\ \overline{\nu_s{}^c}) \begin{pmatrix} 0 & M_D^* & 0 \\ M_D^\dagger & 0 & M_R \\ 0 & M_R^T & M_\mu \end{pmatrix} \begin{pmatrix} \nu_L \\ N_R^c \\ \nu_s \end{pmatrix} + \text{ h.c..} \tag{6.10}$$

The mass scales of the three sub-matrices of M_ν may naturally have a hierarchy $M_R >> M_D >> M_\mu$. Then, the effective light neutrino mass matrix in the seesaw approximation is given by,

$$M_{light} = M_D^* (M_R^T)^{-1} M_\mu M_R^{-1} M_D^\dagger. \tag{6.11}$$

Thus, we have an inverse seesaw mechanism in which the smallness of M_{light} is naturally attributed to the smallness of both M_μ and $\dfrac{M_D}{M_R}$. Because of the extra Z_2 symmetry, the Yukawa coupling matrices Y_ν and y_{NS} and hence the mass matrices M_D and M_R will have the following textures,

$$M_R = y_{NS}\langle \Phi \rangle \sim \begin{pmatrix} \times & \times & 0 \\ \times & \times & 0 \\ 0 & 0 & \times \end{pmatrix} \quad \text{and} \quad M_D = Y_\nu \langle H \rangle \sim \begin{pmatrix} \times & \times & 0 \\ \times & \times & 0 \\ \times & \times & 0 \end{pmatrix}. \tag{6.12}$$

In addition, we will choose M_μ to be diagonal without loss of generality. Since N_{R3} and S_3 do not mix with other neutral fermions, they will not contribute to the seesaw mechanism and we will have a minimal inverse seesaw mechanism (3 ν_L + 2 N_R + 2 ν_s case) in which the lightest active neutrino will be massless. The two fermions N_{R3} and ν_{s3} mix among themselves and the lightest mass eigenstate could be a stable dark matter candidate. In the heavy sector, we will have two pairs of degenerate pseudo-Dirac neutrinos of masses of the order $\sim M_R \pm M_\mu$ that mix with the active light neutrinos.

6.3 Scalar Potential of the Model and Symmetry Breaking

The scalar potential of the model is given by,

$$V(\Phi, H) = m_1^2 H^\dagger H + \lambda_1 (H^\dagger H)^2 + \lambda_3 H^\dagger H\, \Phi^\dagger \Phi + m_2^2 \Phi^\dagger \Phi + \lambda_2 (\Phi^\dagger \Phi)^2 . \tag{6.13}$$

The trivial conditions that give a stable potential are,

$$\lambda_1 > 0 \quad ; \quad \lambda_2 > 0 \quad \text{and} \quad \lambda_3 > 0, \tag{6.14}$$

and if $\lambda_3 < 0$, the stability of the potential can still be achieved by satisfying the following conditions :

$$\lambda_1 > 0, \quad \lambda_2 > 0, \quad 4\lambda_1\lambda_2 - \lambda_3^2 > 0. \tag{6.15}$$

The above conditions are obtained by demanding the Hessian matrix corresponding to the potential to be positive definite at large field values [150, 328].

The two scalar fields acquire vacuum expectation values(vevs) given by,

$$\langle H \rangle = \frac{1}{\sqrt{2}} \begin{pmatrix} 0 \\ v \end{pmatrix} \quad ; \quad \langle \Phi \rangle = \frac{u}{\sqrt{2}}. \tag{6.16}$$

The values of v and u are determined by the minimization conditions and are given by,

$$v^2 = \frac{m_2^2\lambda_3/2 - m_1^2\lambda_2}{\lambda_1\lambda_2 - \lambda_3^2/4} \quad ; \quad u^2 = \frac{m_1^2\lambda_3/2 - m_2^2\lambda_1}{\lambda_1\lambda_2 - \lambda_3^2/4}. \tag{6.17}$$

After symmetry breaking, the mixing between the fields h and ϕ could be rotated away by an orthogonal transformation to get the physical mass eigenstates as, The values of v and u are determined by the minimization conditions and are given by,

$$v^2 = \frac{m_2^2\lambda_3/2 - m_1^2\lambda_2}{\lambda_1\lambda_2 - \lambda_3^2/4} \quad ; \quad u^2 = \frac{m_1^2\lambda_3/2 - m_2^2\lambda_1}{\lambda_1\lambda_2 - \lambda_3^2/4}. \tag{6.18}$$

After symmetry breaking, the mixing between the fields h and ϕ could be rotated away by an orthogonal transformation to get the physical mass eigenstates as, The values of v and u are determined by the minimization conditions and are given by,

$$v^2 = \frac{m_2^2\lambda_3/2 - m_1^2\lambda_2}{\lambda_1\lambda_2 - \lambda_3^2/4} \quad ; \quad u^2 = \frac{m_1^2\lambda_3/2 - m_2^2\lambda_1}{\lambda_1\lambda_2 - \lambda_3^2/4}. \tag{6.19}$$

After symmetry breaking, the mixing between the fields h and ϕ could be rotated away by an orthogonal transformation to get the physical mass eigenstates as,

$$\begin{pmatrix} h_1 \\ h_2 \end{pmatrix} = \begin{pmatrix} \cos\theta & -\sin\theta \\ \sin\theta & \cos\theta \end{pmatrix} \begin{pmatrix} h \\ \phi \end{pmatrix}, \tag{6.20}$$

The masses of the scalar eigenstates are,

$$m_{h_{1,2}}^2 = \lambda_1 v^2 + \lambda_2 u^2 \mp \sqrt{(\lambda_1 v^2 - \lambda_2 u^2)^2 + (\lambda_3 uv)^2}. \tag{6.21}$$

From these, one can get the relations,

$$\lambda_1 = \frac{m_{h_1}^2}{4v^2}(1+\cos 2\theta) + \frac{m_{h_2}^2}{4v^2}(1-\cos 2\theta),$$

$$\lambda_2 = \frac{m_{h_1}^2}{4u^2}(1-\cos 2\theta) + \frac{m_{h_2}^2}{4u^2}(1+\cos 2\theta),$$

$$\lambda_3 = \sin 2\theta\Big(\frac{m_{h_2}^2 - m_{h_1}^2}{2uv}\Big). \tag{6.22}$$

We use these equations to set the initial conditions on the scalar couplings λ_1, λ_2 and λ_3 while running the renormalization group equations. Also, from the above equations, one can get,

$$\tan 2\theta = \frac{\lambda_3 uv}{\lambda_1 v^2 - \lambda_2 u^2}. \tag{6.23}$$

6.3.1 Perturbative Unitarity

In addition to the vacuum stability conditions, the constraints from the perturbative unitarity conditions also put bounds on the model parameters. As we discussed in the previous chapter, by considering the $hh \to hh$ and $\phi\phi \to \phi\phi$ processes, one can derive combined constraints on the three couplings appearing in the scalar potential[329, 330] :

$$|\lambda_3| \leq 8\pi \quad ; \quad 3(\lambda_1+\lambda_2) \pm \sqrt{\lambda_3^2 + 9(\lambda_1-\lambda_2)^2} \leq 8\pi \tag{6.24}$$

Demanding the running gauge couplings to remain in the perturbative regime gives us,

$$g_i \leq \sqrt{4\pi}, \tag{6.25}$$

where g_i stands for SM gauge couplings. For the $U(1)$ gauge coupling g', we require,

$$(x_{q,d,u,l,e,\nu,\Phi})g', \ (x_H/2)g' < \sqrt{4\pi}. \tag{6.26}$$

6.4 Numerical Analysis and Parameter Scanning in the Neutrino Sector

To study the parameter space allowed by vacuum stability as well as perturbativity bounds upto M_{Planck} using the RGEs, we have to first fix the initial values for all the couplings. While setting the initial values for the neutrino Yukawa couplings Y_ν and y_{NS}, we have to make sure that they reproduce the correct oscillation parameters and satisfy all the experimental constraints. For this, we find sample benchmark points for Y_ν, y_{NS} and M_μ and the vev of the extra scalar Φ (u) by fitting them with all the constraints using the downhill simplex method [311] like we did in the case of the inverse seesaw model in the previous chapter. Note that here, Y_ν is a complex 3×2 matrix, y_{NS} is a complex 2×2 matrix and M_μ is a 2×2 diagonal matrix with real entries. The various constraints we have taken include the bounds on oscillation parameters (mass squared differences and mixing angles), cosmological constraint on the sum of light neutrino masses and the constraints on the non-unitarity of $U_{PMNS} = U_L$ and these are discussed in sections 1.2 and 5.4. In table (6.1), we give two benchmark points consistent with all the experimental data discussed above. As a consistency check, we also give the value of $Br(\mu \to e\,\gamma)$ obtained at the two benchmark points.

6.5 RG Evolution

We have evaluated the SM coupling constants at the the top quark mass scale and then run them using the RGEs from M_t to M_{planck}. For this, we have taken into account the various threshold corrections at M_t [245, 248, 291]. Then the SM RGEs are used to run all the couplings upto the vev of the new scalar, after which, the new couplings enter. Then we use the modified RGEs for the $SU(3)_c \times SU(2)_L \times U(1)_Y \times U(1)'$ and these have been generated using SARAH [295]. We have used two-loop RGEs for all the SM parameters and g' and the new scalar couplings λ_2 and λ_3, whereas for the neutrino Yukawa couplings, we have used the one-loop RGEs. The one-loop RGEs of the model are given in appendix-B. Throughout this paper, we have fixed the standard model parameters as $m_h = 125.7$ GeV, $M_t = 173.4$ GeV and $\alpha_s = 0.1184$. Also, we

Parameter	$BM-I$	$BM-II$
$Tr[Y_\nu Y_\nu^\dagger]$	0.089	0.222
$[Y_\nu]_{3\times2}$	$\begin{pmatrix} 0.119-i\,0.065 & 0-i\,0.026 \\ 0.001-i\,0.009 & 0.062+i\,0.01 \\ -i\,0.249 & -0.001-i\,0.063 \end{pmatrix}$	$\begin{pmatrix} -0.003-i\,0.002 & 0.129 \\ 0.191-i\,0.226 & 0.004-i\,0.014 \\ 0.008-i\,0.231 & 0.252+i\,0.024 \end{pmatrix}$
$Tr[y_{NS}y_{NS}^\dagger]$	0.010	0.110
$[y_{NS}]_{2\times2}$	$\begin{pmatrix} 0.003-i\,0.011 & 0.043-i\,0.026 \\ 0.082+i\,0.025 & -i\,0.007 \end{pmatrix}$	$\begin{pmatrix} 0.028+i\,0.013 & 0.288+i\,0.099 \\ 0.13-i\,0.005 & 0.001+i\,0.001 \end{pmatrix}$
$[M_\mu]_{2\times2}\ GeV$	$\begin{pmatrix} 2.303\times10^{-6} & 0 \\ 0 & -1.636\times10^{-8} \end{pmatrix}$	$\begin{pmatrix} -6.4735\times10^{-9} & 0 \\ 0 & -6.9781\times10^{-8} \end{pmatrix}$
$M_j\ GeV$	$1773.43,\ 1773.43,\ 3058.59,\ 3058.59$	$1095.88,\ 1095.88,\ 2598.39,\ 2598.39$
$Br(\mu\to e\,\gamma)$	1.069×10^{-14}	1.811×10^{-14}
$u\ (TeV)$	50	12

Table 6.1: Two sample benchmark points for the neutrino sector. The above parameters give the correct mixing angles and satisfies the non-unitarity constraints on U_{PMNS}. The value of $Br(\mu \to e\,\gamma)$ is given as a check.

have kept the $U(1)$ gauge mixing to be 0 at the scale u throughout this paper.

Fig. 6.1 displays the allowed region in the $m_{h_2} - \theta$ plane for the model with $x_H = x_\Phi = 1$, keeping all the other parameters fixed. For the neutrino Yukawa couplings, we have used BM-I from the Table 6.1 and we have fixed $g' = 0.1$ and $y_{NS}^{33} = 0.5$. From the figure, one can see that for higher values of θ, only smaller values of m_{h_2} are allowed whereas for smaller values of θ, larger values of m_{h_2} over a wider range are allowed. Also it can be seen that for this model with the considered set of parameters, the values of $m_{h_2} > 33$ TeV and $\theta > 0.013$ are disallowed.

In Fig. 6.2, we have plotted the running of λ_1, λ_2 and λ_3 for the model with $x_H = x_\Phi = 1$ for two different values of m_{h_2} and θ. The figure in the left side is for $m_{h_2} = 15$ TeV and $\theta = 0.004$ whereas the one in the right side is for $m_{h_2} = 20$ TeV and $\theta = 0.003$. For the neutrino Yukawa couplings, we have used BM-I from the Table 6.1 and we have fixed $g' = 0.1$ and $y_{NS}^{33} = 0.5$. We can see that all the three

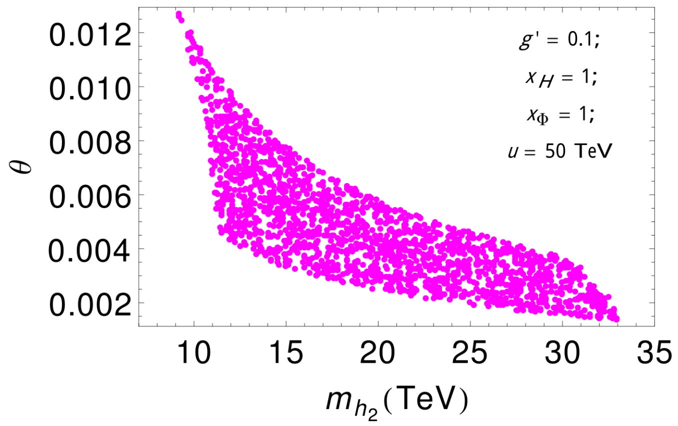

Figure 6.1: Region in the $m_{h_2} - \theta$ plane allowed by both vacuum stability and perturbativity bounds upto M_{Planck} for the model with $x_H = x_\Phi = 1$. For the neutrino Yukawa couplings, we have used BM-I from the Table 6.1 and we have fixed $g' = 0.1$ and $y^{33}_{NS} = 0.5$.

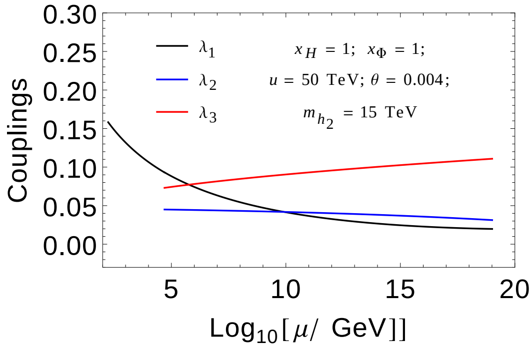

(a) $m_{h_2} = 15$ TeV, $\theta = 0.004$

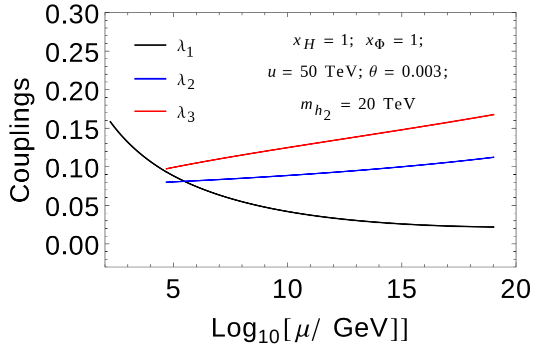

(b) $m_{h_2} = 20$ TeV, $\theta = 0.003$

Figure 6.2: Running of λ_1, λ_2, λ_3 and $4\lambda_1\lambda_2 - \lambda_3^2$ for the model with $x_H = x_\Phi = 1$ for two different values of m_{h_2} and θ. For the neutrino Yukawa couplings, we have used BM-I from the Table 6.1 and we have fixed $g' = 0.1$ and $y^{33}_{NS} = 0.5$.

quartic couplings remain positive up to M_{Planck} for both the cases implying that the electroweak vacuum is absolutely stable. This can be seen from Fig. 6.1 as well where the above mentioned points fall in the stable region. Here, the presence of the extra scalar coupling helps in stabilizing the vacuum.

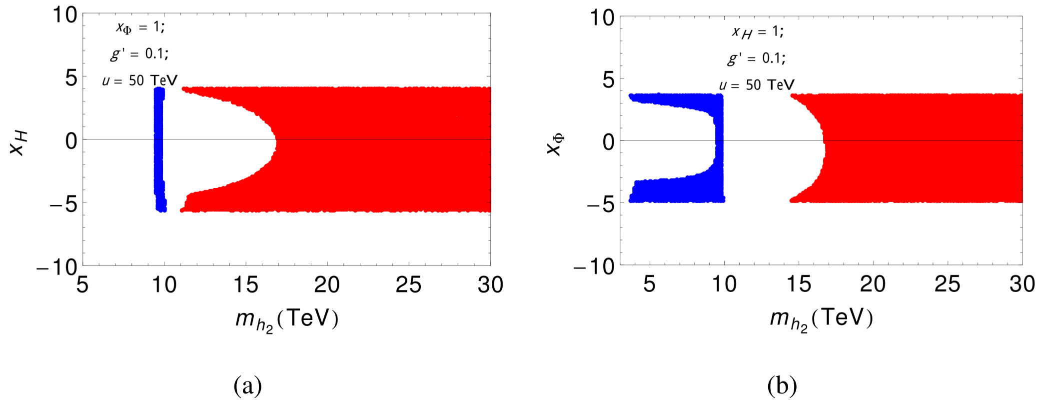

Figure 6.3: Regions in the $m_{h_2} - x_H$ and $m_{h_2} - x_\Phi$ planes allowed by both vacuum stability and perturbativity bounds upto M_{Planck} for two different values of θ. For the left panel, we have fixed $x_\Phi = 1$ and for the right panel, we have fixed $x_H = 1$. For the neutrino Yukawa couplings, we have used BM-I from the Table 6.1 and we have fixed $g' = 0.1$ and $y_{NS}^{33} = 0.5$. The red region is for $\theta = 0.003$ and the blue region is for $\theta = 0.01$.

In Fig. 6.3, we have plotted the regions allowed by both vacuum stability and perturbativity bounds upto M_{Planck} in the $m_{h_2} - x_H$ and $m_{h_2} - x_\Phi$ planes, for two different values of θ. The red regions are for $\theta = 0.003$ and the blue regions are for $\theta = 0.01$. The left panel of Fig. 6.3 shows the allowed regions in the $m_{h_2} - x_H$ plane keeping all the other parameters fixed. For the neutrino Yukawa couplings, we have used BM-I from the Table 6.1 and we have fixed $x_\Phi = 1$, $g' = 0.1$ and and $y_{NS}^{33} = 0.5$. It can be seen that for $\theta = 0.01$, a very narrow region of m_{h_2} in the range $\approx 9 - 10$ TeV is allowed by the stability and perturbativity constraints and the corresponding allowed range of x_H is $\approx -5.7 - 4.1$. Here, the higher values of m_{h_2} are disfavored by the perturbativity constraints whereas the lower values of m_{h_2} are disfavored by the constraints from vacuum stability. At the same time, for $\theta = 0.003$, $m_{h_2} \approx 11 - 30$ TeV is allowed depending on the value of x_H.

Similarly, in the right panel of Fig. 6.3, we have shown the allowed region in the

$m_{h_2} - x_\Phi$ plane keeping $x_H = 1$ and all the other parameters fixed for two different values of θ. Here also, for $\theta = 0.01$, the values of m_{h_2} greater than 10 TeV are disfavored by unitarity constraints. The lower values of m_{h_2} are disfavored by the stability constraints depending on the value of x_Φ. For $-3 \le x_\Phi \le 3$, values of m_{h_2} less than $\sim$ 9 TeV are disallowed, whereas for $-5.5 \le x_\Phi \le -3$ and $3 \le x_\Phi \le 4$, values of m_{h_2} as low as $\sim$ 3 TeV are allowed. For $\theta = 0.003$, values of $m_{h_2} < 14-15.5$ TeV are disallowed depending on the values of x_H, but values as high as 30 TeV are allowed for $-5 \le x_H \le 4$. These results are consistent with the observations from Fig. 6.1 where we have seen that for $x_H = x_\Phi = 1$, larger(smaller) values of m_{h_2} are disfavored for larger(smaller) values of θ.

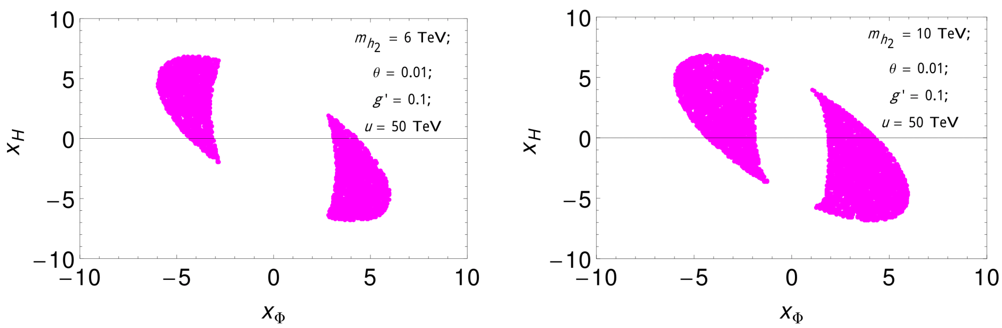

(a) Running of λ for different values of M_t keeping α_S and M_h fixed.

(b) Running of λ for different values of α_s keeping M_t and M_h fixed.

Figure 6.4: Regions in the $x_\Phi - x_H$ plane allowed by both vacuum stability and perturbativity upto M_{Planck}. We have taken the mass of the extra scalar to be 6 TeV (10 TeV) in the left (right) panel. For the neutrino Yukawa couplings, we have used BM-I from the Table 6.1 and we have fixed $\theta = 0.01$, $g' = 0.1$ and $y_{NS}^{33} = 0.5$ for both the plots.

In Fig.6.4, we have presented the regions in the $x_\Phi - x_H$ plane allowed by both vacuum stability (absolute stability) and perturbativity upto M_{Planck} for fixed values of m_{h_2}, θ and g'. For the neutrino Yukawa couplings, we have used the BM-I in Table 6.1 and we have taken and $y_{NS}^{33} = 0.5$. The mass of the extra scalar have been taken to be 6 TeV (10 TeV) in the left (right) panel and the values of θ and g' are taken to be 0.01 and 0.1 respectively for both the plots. From these two figures, we can see that increasing the scalar mass will allow more values of x_Φ for a given value of x_H. In fact, one can see that the allowed values for x_Φ lie in the ranges $\approx \pm 3$ to ± 6 and $\approx \pm 1$ to ± 6 for the figures in the left and the right panels respectively. Also, x_H lies in the range ≈ -7 to 7 for both the cases with the considered values of the parameters. This can be understood from eqn.6.22 which shows that higher value of m_{h_2} implies higher value of the scalar couplings which in turn favors stability.

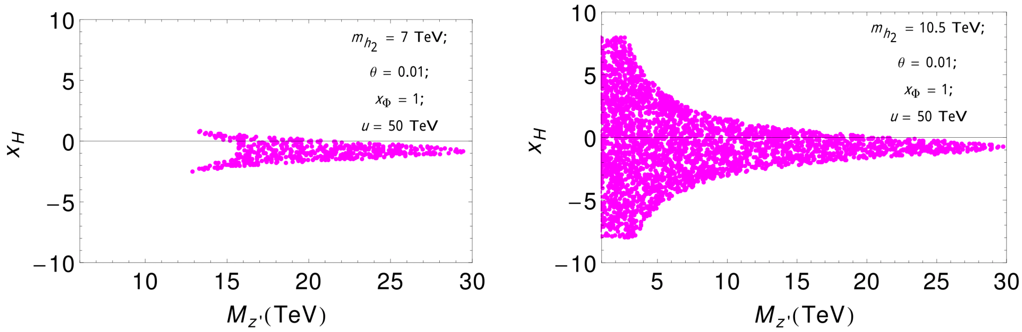

(a) Running of λ for different values of M_t keeping α_S and M_h fixed.

(b) Running of λ for different values of α_s keeping M_t and M_h fixed.

Figure 6.5: Regions in the $M_Z' - x_H$ plane allowed by both vacuum stability and perturbativity bounds up to M_{Planck}. We have taken the mass of the extra scalar to be 7 TeV (10.5 TeV) in the left (right) panel. For the neutrino Yukawa couplings, we have used BM-I from the Table 6.1 and we have fixed $\theta = 0.01$, $x_\Phi = 1$ and and $y_{NS}^{33} = 0.5$ for both the plots.

Fig.6.5, displays the regions allowed by both vacuum stability and perturbativity up to M_{Planck} in the $M_Z' - x_H$ plane for fixed values of m_{h_2}, θ and x_Φ. Here also, we have used the BM-I in Table 6.1 for the neutrino Yukawa couplings and we have taken and $y_{NS}^{33} = 0.5$. The mass of the extra scalar have been taken to be 7 and 10.5 TeV in the left and the right panels respectively and the values of θ and x_Φ are taken to be 0.01 and 1 for both the plots. Also, we have varied g' from 0 to 1 keeping u fixed at 50 TeV and x_H in the range -8 to 8. The corresponding values of M_Z' have been calculated using,

$$M_Z' = \sqrt{(x_\Phi g' u)^2 + (\frac{x_H}{2} g' v_{\rm SM})^2}. \tag{6.27}$$

From these figures, we can see that lower values of M_Z' allow large values of x_H. From these figures, one can see that for a lower scalar mass, the lower values of M_Z' (or equivalently, lower values of g') are disfavored. For $m_{h_2} = 7$ TeV, values of M_Z'

less than 12 TeV are disallowed and a very small range of x_H is allowed whereas for $m_{h_2} = 10.5$ TeV, values of M_Z' as low as 1 TeV are allowed and correspondingly, x_H is allowed from -8 to 8.

6.6 Dark matter scenario

In this section we discuss dark matter physics in our model with respect to the constraints from relic density and direct detection experiments. As mentioned earlier, the third generations of N_R and S_L (N_{R3}, ν_{s3}) are odd under the Z_2 parity in the general $U(1)'$ inverse seesaw model that we consider. This ensures the stability of N_{R3} and ν_{s3} which is required for these to be potential dark matter candidates. As a result the relevant interactions in the Lagrangian can be written as

$$-\mathcal{L}^2_{mass} \supset y^{33}_{NS}\overline{N_{R3}}\nu_{s3}\Phi + M^{33}_S\overline{\nu^c_{s3}}\nu_{s3}. \tag{6.28}$$

Note that N_{R3} can not couple to the SM Higgs and lepton doublets due to the Z_2 symmetry. After the symmetry breaking we have $\langle\Phi\rangle = \dfrac{u}{\sqrt{2}}$ and the mass matrix can be written as,

$$M_{N^3S^3} = \begin{pmatrix} 0 & M^{33}_{NS} \\ M^{33}_{NS} & M^{33}_S \end{pmatrix} \tag{6.29}$$

where $M^{33}_{NS} = \dfrac{y^{33}_{NS}u}{\sqrt{2}}$. Now rotating the basis we can write the physical eigenstates as

$$\begin{pmatrix} N^c_{R3} \\ \nu_{s3} \end{pmatrix} = \begin{pmatrix} \cos\overline{\theta} & \sin\overline{\theta} \\ -\sin\overline{\theta} & \cos\overline{\theta} \end{pmatrix} \begin{pmatrix} \psi_1 \\ \psi_2 \end{pmatrix} \tag{6.30}$$

where $\tan 2\overline{\theta} = \left|\dfrac{2M^{33}_{NS}}{-M^{33}_S}\right| = \sqrt{2}\dfrac{y^{33}_{NS}u}{M^{33}_S}$. Note that ψ_1 and ψ_2 are Majorana fermions. The mass eigenvalues are obtained as,

$$m_{\psi_1,\psi_2} = \frac{1}{2}\sqrt{(M^{33}_S)^2 + 4(M^{33}_{NS})^2} \mp \frac{1}{2}M^{33}_S, \tag{6.31}$$

where we take $m_{\psi_1} < m_{\psi_2}$. Thus ψ_1 is the lightest Z_2 odd particle and our dark matter candidate. Putting ψ_1 and ψ_2 back into Eq. 6.28 along with the physical mass eigenstates of h and ϕ we write the interaction among Z_2 odd fermion and scalars as,

$$-\mathcal{L} \supset y^{33}_{NS}\Big(-\sin\theta\cos\overline{\theta}\cos\overline{\theta}\; h_1 + \cos\theta\sin\overline{\theta}\sin\overline{\theta}\; h_2\Big)\Big(-\overline{\psi^c_1}\psi_1 + \overline{\psi^c_2}\psi_2\Big). \tag{6.32}$$

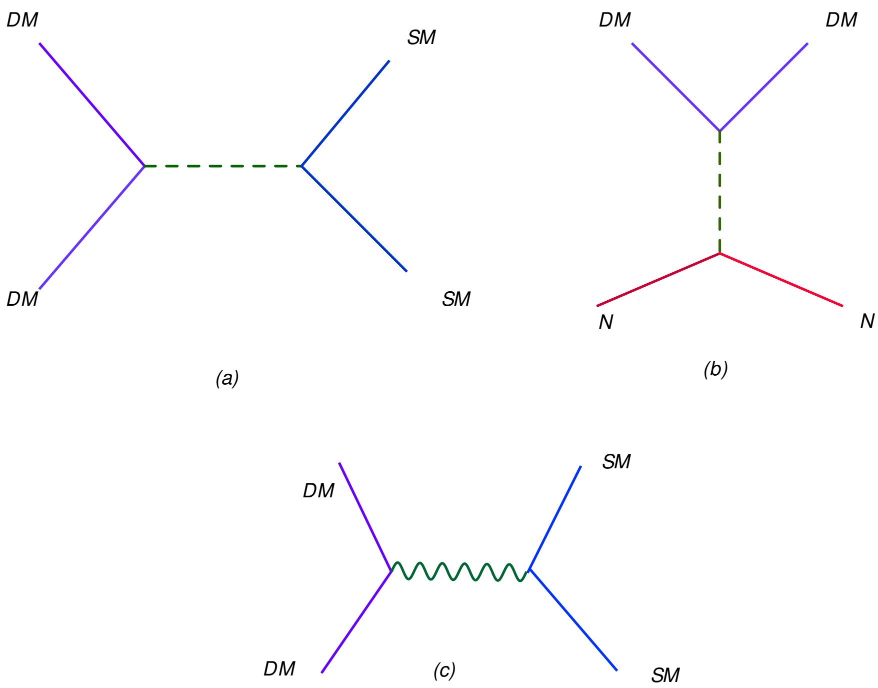

Figure 6.6: (a) Scalar mediated dark matter annihilation (b) Direct detection and (c) Z' mediated dark matter annihilation.

Then the dark matter candidate can annihilate through the scalar portal (Fig. 6.6a), where interactions between h_2 and SM particles are induced by scalar mixing (See Eqn.6.20) and these couplings are equal to the SM Higgs couplings times $\sin\theta$. In addition, the dark matter can annihilate to the SM particles via Z' exchange (Fig. 6.6c) where the gauge interactions are given by,

$$\mathcal{L} \supset -\frac{x_\Phi g'}{2} Z'_\mu \left(\cos^2\bar{\theta}\bar{\psi}_1\gamma^\mu\gamma_5\psi_1 + \sin^2\bar{\theta}\bar{\psi}_2\gamma^\mu\gamma_5\psi_2 - 2\cos\bar{\theta}\sin\bar{\theta}\bar{\psi}_1\gamma^\mu\gamma_5\psi_2\right). \quad (6.33)$$

Furthermore, dark matter can annihilate into $Z'Z'$ mode via scalar portal where the relevant scalar-$Z'Z'$ interaction is given by

$$\mathcal{L} \supset \frac{{M'_Z}^2}{u}\cos\theta\, h_2 Z'Z' - \frac{{M'_Z}^2}{u}\sin\theta\, h_1 Z'Z'. \quad (6.34)$$

6.6.1 Relic density

Here we analyze the relic density of our dark matter candidate. The dark matter candidate ψ_1 annihilate into the SM particles via processes induced by Z' and scalar boson interactions as shown in Fig. 6.6. Then we estimate the relic density using *micrOMEGAs 4.3.5* [331] implementing the relevant interactions. Firstly we focus on the parameter space where the Z' mediated process dominates for dark matter annihilation. For illustration, in Fig. 6.7, we show the relic density as a function of the dark matter mass ($M_{DM} \equiv m_{\psi_1}$) for $M'_Z = 4$ TeV, fixing the other parameters as indicated in the plot. The plot indicates that the required gauge coupling is $g' \gtrsim 0.5$ but it is excluded by the LHC data as we will see later. Note that in this case, the value of g' that gives the correct relic density depends on the choice of x_H and x_Φ since the interaction strength of Z' with the other particles is a product of g' and a linear combination of x_H and x_Φ. If we increase x_H and x_Φ, then the value of g' that can give the correct relic density can be lowered. However, for smaller values of g', the LHC constraints imply much lower values of M'_Z where the Z' exchange is not a dominant process. We also find that the Z' mediated process cannot provide sufficient annihilation cross section to explain the observed relic density if dark matter is heavier than ~ 3 TeV, complying with the requirement that the gauge coupling satisfy $(x_{q,d,u,l,e,\nu,\Phi})g',\ (x_H/2)g' < \sqrt{4\pi}$ for perturbativity. This tendency comes from the fact that the annihilation cross section is P-wave suppressed since our dark matter particle is Majorana fermion.

We will now focus on the contribution of h_2 exchange process to the relic density of dark matter. For illustrating the effect of this process, we show the relic density as a function of dark matter mass for different values of y^{33}_{NS} and m_{h_2} in Fig. 6.8. In the left panel, we have fixed $y^{33}_{NS} = 2.5$ and plotted the relic density as a function of M_{DM} for three different values of m_{h_2}, keeping all the other parameters fixed. Similarly, we have taken $m_{h_2} = 13$ TeV in the right plot and plotted the relic density for three different values of y^{33}_{NS}. We find that the observed relic density can be realized for $y^{33}_{NS} \gtrsim 2$ when $m_{h_2} = 13$ TeV. In addition, $m_{h_2} \sim 2M_{DM}$ is preferred to enhance the annihilation cross section which implies that m_{h_2} mass is around $\mathcal{O}(10)$ TeV in our model. Note that such a heavy mass scale for h_2 is also preferred in stabilizing the scalar potential as we already discussed in the previous section.

We perform a parameter scan and search for the allowed regions which can give the correct relic density of dark matter. Firstly, we perform parameter scan in the following ranges focusing on the scalar exchange process,

$$M_{DM} \in [1.0, 10.0]\ \text{TeV}, \quad m_{h_2} \in [1.8M_{DM}, 2.2M_{DM}], \quad y^{33}_{NS} \in [0.2, 3.0], \quad \sin\theta \in [0.001, 0.02],$$

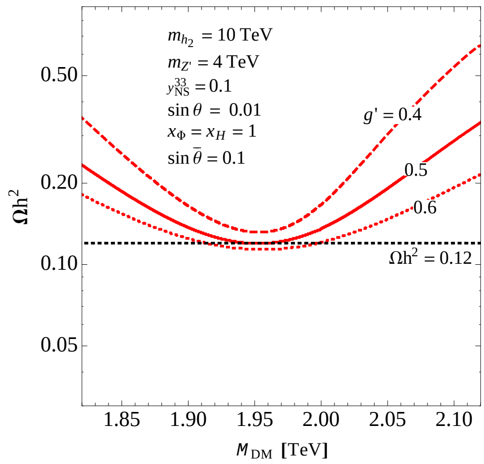

Figure 6.7: Relic abundance as a function of dark matter mass for different values of g'. All the other parameters have been fixed as given in the plot.

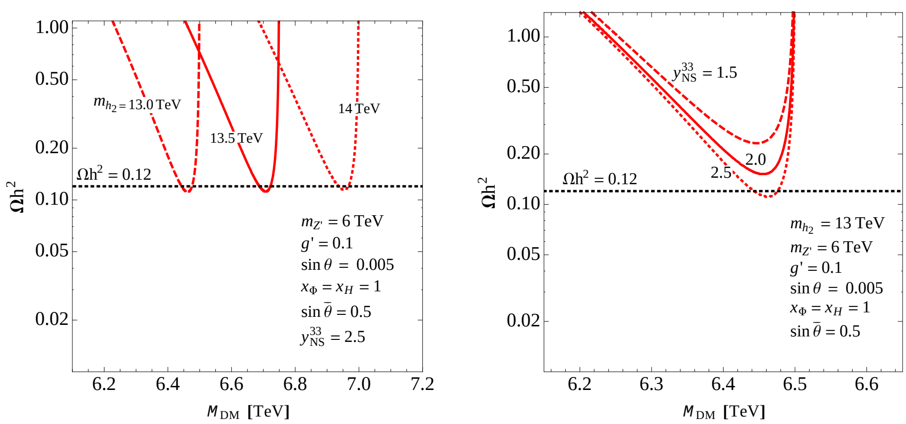

Figure 6.8: Relic abundance as a function of dark matter mass : (a) For different values of m_{h_2} and fixed $y^{33}_{NS} = 2.5$; (b) For different values of y^{33}_{NS} and fixed $m_{h_2} = 13$ TeV.

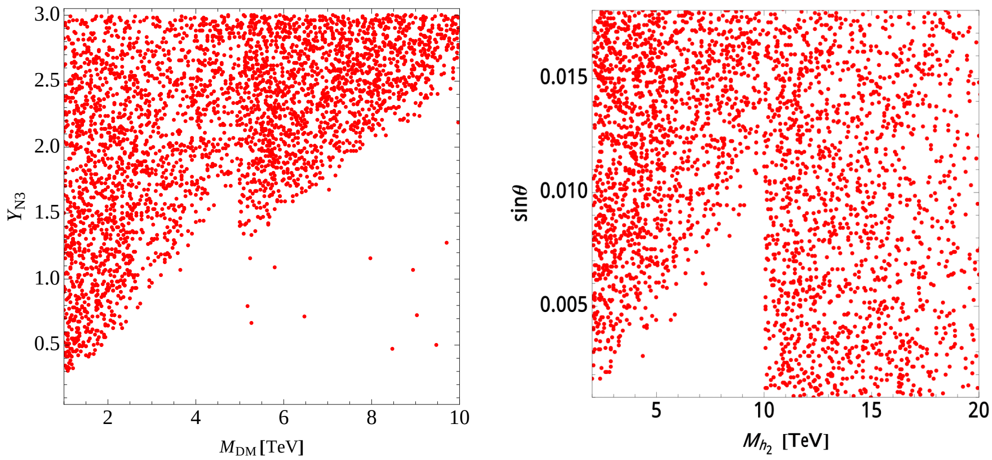

Figure 6.9: Parameter regions that give the correct relic density of dark matter in M_{DM}-Y_{N3} and M_{h_2}-$\sin\theta$ planes for scanning done in the ranges of parameters as given by Eq. (6.35).

$$x_H \in [-5, 5], \quad x_\Phi \in [-5, 5], \quad \sin\overline{\theta} \in [0.2, 0.7], \quad M_Z' = 5 \text{ TeV}, \quad g' = 0.01. \tag{6.35}$$

We fixed Z' mass and g' for simplicity. Note that we chose $m_{h_2} \sim 2M_{DM}$ since we can obtain the observed relic density in this region via h_2 exchange process as discussed above. In Fig. 6.9, we show the allowed parameter space in $M_{DM} - y_{NS}^{33}$ and $m_{h_2} - \sin\theta$ planes that give the correct relic density of dark matter, $0.11 < \Omega h^2 < 0.13$, adopting the approximate range around the best fit value [57]. From the left panel of Fig. 6.9, we can see that in general, for larger values of M_{DM}, the allowed values of y_{NS}^{33} are large. But, a few points with smaller values of y_{NS}^{33} are also obtained for $M_{DM} > M_Z'$ since $\psi_1\psi_1 \to h_2 \to Z'Z'$ process is kinematically allowed there. In the right panel of Fig. 6.9, we have shown the allowed parameter space in the $m_{h_2} - \sin\theta$ plane. From this plot, we can see that $\sin\theta$ can be small for $M_{DM} > M_Z'$ ($m_{h_2} \sim 2M_{DM}$) since $h_2Z'Z'$ coupling is not suppressed by $\sin\theta$ as we can see from Eqn. (6.34). However, we have some lower limit of $\sin\theta$ for $M_{DM} < M_Z'$ since here, $\psi_1\psi_1 \to h_2 \to Z'Z'$ process is kinematically disallowed and the coupling of h_2 to the SM particles is suppressed by $\sin\ \theta$.

6.6.2 Direct detection

Here we briefly discuss the constraints from the direct detection experiments by estimating the dark matter-nucleon (N) scattering cross section in our model. Firstly note that the Z' exchange process between dark matter and nucleon will not get stringent constraint since dark matter-Z' interaction is via axial vector current due to the Majorana property of dark matter and provides spin-dependent operator for dark mater-nucleon interaction. We thus focus on the scalar mediated processes for dark matter-nucleon scattering where the corresponding Feynman diagram is given in Fig 6.6b. In our case, the dark matter interacts with the nucleon through the scalar boson exchange (h_1, h_2). The relevant interaction Lagrangian with the mixing effect is given by,

$$\mathcal{L} \supset C_{\psi_1\psi_1 h_1} h_1 \overline{\psi_1^c}\psi_1 + C_{\psi_1\psi_1 h_1} h_2 \overline{\psi_1^c}\psi_1 + C_{NNh_1} h_1 \overline{N} N + C_{NNh_2} h_2 \overline{N} N, \quad (6.36)$$

where the effective couplings are,

$$C_{\psi_1\psi_1 h_1} = \sin\overline{\theta}\cos\overline{\theta}\cos\theta \frac{Y_N^3}{\sqrt{2}}, \quad C_{\psi_1\psi_1 h_2} = -\sin\overline{\theta}\cos\overline{\theta}\sin\theta \frac{Y_N^3}{\sqrt{2}}, \quad (6.37)$$

$$C_{NNh_1} = \sin\theta g_{hNN}, \quad C_{NNh_2} = \cos\theta g_{hNN}. \quad (6.38)$$

Hence the effective Lagrangian can be written as,

$$\mathcal{L}_{eff} = G_h \overline{\psi_1}\psi_1 \overline{N} N, \quad (6.39)$$

$$G_h = \left[\frac{C_{\psi_1\psi_1 h_1} C_{h_1 NN}}{m_{h_1}^2} + \frac{C_{\psi_2\psi_2 h_2} C_{h_2 NN}}{m_{h_2}^2} \right] \quad (6.40)$$

where m_{h_1} and m_{h_2} are the SM and BSM Higgs masses. The corresponding cross section of Fig. 6.6b in the non-relativistic limit can be calculated as,

$$\sigma = g_{hNN}^2 \frac{M_{DM}^2 M_N^2}{16\pi (M_{DM}^2 + M_N^2)^2} (Y_N^3 \sin 2\overline{\theta} \sin 2\theta)^2 \left(\frac{1}{m_{h_1}^2} - \frac{1}{m_{h_2}^2} \right)^2, \quad (6.41)$$

where, M_{DM} and M_N are the dark matter and nucleon masses respectively. The effective coupling can be written as $g_{hNN} = \dfrac{f_N M_N}{v\sqrt{2}}$ where we apply $f_N = 0.287$ for neutron [310] [1] and $v = 246$ GeV. We then estimate the cross sections applying allowed parameter sets obtained in previous subsection and the results are shown in Fig. 6.10. The black dotted and dashed lines show the current upper bounds from

[1] f_N for proton has similar value and we here just use f_N in estimating the cross section.

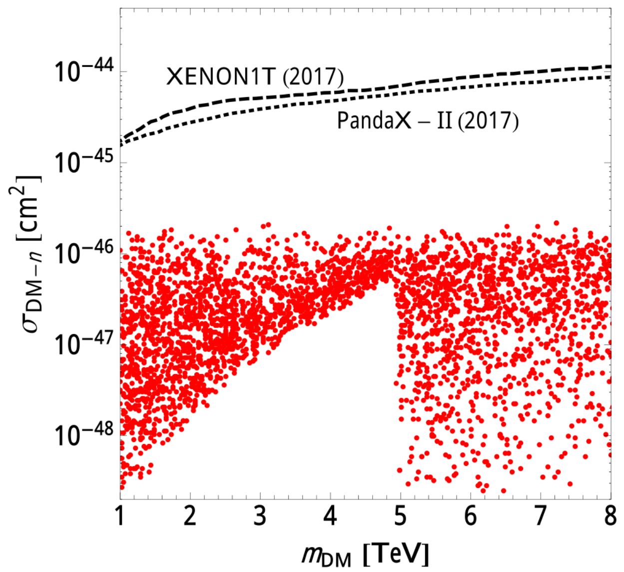

Figure 6.10: Nucleon-dark matter scattering cross section as a function of dark matter mass for parameters that give the correct relic density. The current upper bounds from PANDAX-II [3] (black dotted line) and XENON-1t [4] (back dashed line) are also shown.

PANDAX-II [3] and XENON-1t [4] respectively. We find that our parameter region is allowed by the direct detection constraints since the cross section is suppressed by small $\sin\theta$ which is also preferred by the constraints from vacuum stability. The cross section will be further explored by the future direct detection experiments.

6.7 Bounds on the $M_Z' - g'$ plane

In this section, we consider the production of Z' from the proton proton collision at the LHC and its decay into different types of leptons. We first calculate the Z' production cross section at the LHC from protons followed by the decay into lepton, $pp \to Z' \to \ell^+\ell^-$ with $\ell = e,\ \mu$. In our analysis we calculate the cross section combining the electron and muon final states. We compare our cross section with the latest ATLAS search [5] for the heavy Z' resonance. Since we are considering $U(1)'$ models with extra Z', the ATLAS results can be compared directly with our results. Atlas analysis has considered different models like SSM and Z'_ψ [332] where the Z' decays into e and

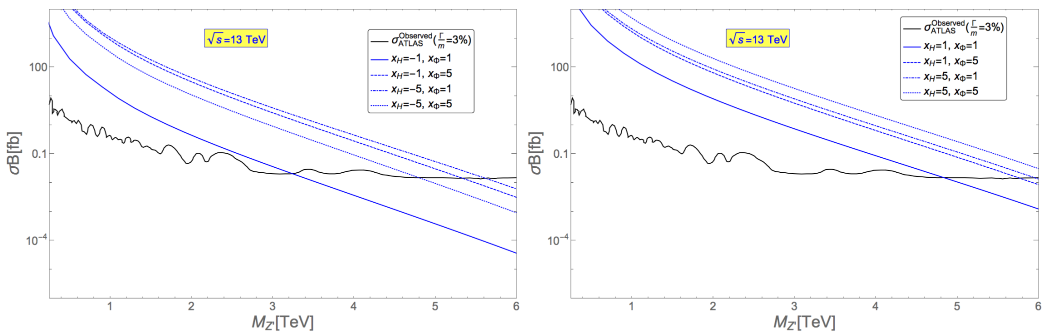

Figure 6.11: Comparison between the ATLAS [5] (black solid line) result and model cross sections (blue lines) for the different values of x_H and x_Φ. The model cross sections are produced with $g_{\text{Model}} = 0.05$. The left and right panels correspond to $x_H < 0$ and $x_H > 0$ respectively and we have considered $x_\Phi > 0$ for both the cases.

μ. Conservatively considering these limits for our case we first produce the Z' (300 GeV $\leq M'_Z \leq 6$ TeV) at the 13 TeV LHC followed by the decay into dilepton mode and finally compare with the cross sections in our model. To calculate the bounds on the g', we calculate the model cross section, σ_{Model}, for the process $pp \to Z' \to 2e,\ 2\mu$, with a $U(1)'$ coupling constant g_{Model} at the LHC at the 13TeV center of mass energy. Then we compare this with the observed ATLAS bound ($\sigma_{\text{ATLAS}}^{\text{Observed}}$) for $\dfrac{\Gamma}{m} = 3\%$ which has been studied for the SSM. The corresponding cross sections are plotted in Fig. 6.11 for different choices of x_H and x_Φ. Thus, the value of g' corresponding to a given M'_Z is given as,

$$g' = \sqrt{\frac{\sigma_{\text{ATLAS}}^{\text{Observed}}}{\left(\frac{\sigma_{\text{Model}}}{g^2_{\text{Model}}}\right)}}, \tag{6.42}$$

since the cross section varies with the square of the $U(1)'$ coupling (g^2_{Model}).

In this analysis we consider several choices of the x_H and x_Φ to calculate the bounds in the $M'_Z - g'$ plane. These correspond to two scenarios : (1) x_H is negative and x_Φ is positive for which the results are shown in Fig. 6.12 and (2) both x_H and x_Φ are positive and the corresponding constraints in the $M'_Z - g'$ plane are shown in Fig. 6.13. The interaction of the Z' with the fermions via the covariant derivative will depend on the x_H and x_ϕ values and is given by the Lagrangian,

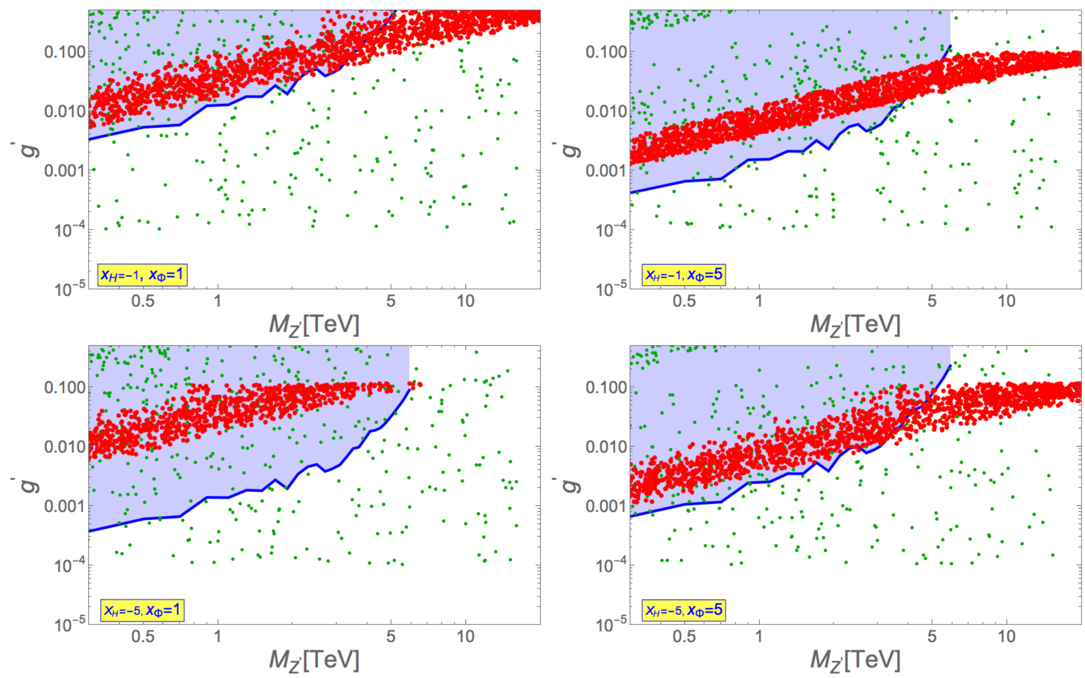

Figure 6.12: Allowed parameter space combining the bounds obtained on g' as a function of M'_Z from vacuum stability and perturbativity (red dots), dark matter constraints (green dots) and collider (region below the blue solid line). The blue shaded regions are ruled out by the recent ATLAS search [5] at 139 fb $^{-1}$ luminosity.

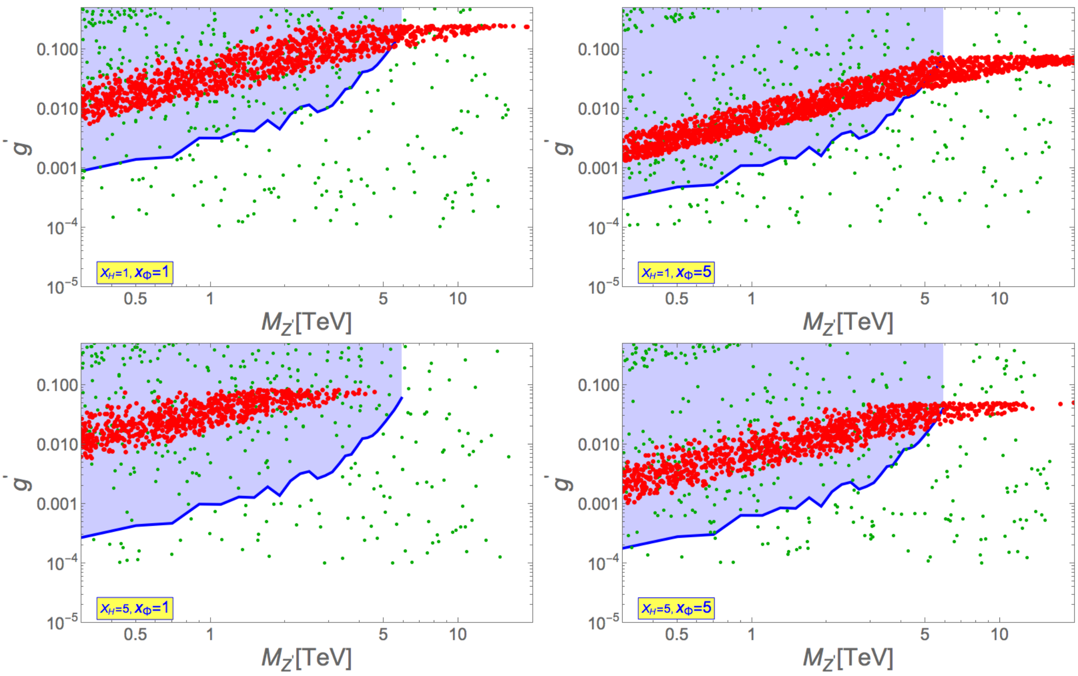

Figure 6.13: Allowed parameter space combining the bounds obtained on g' as a function of M_Z' from vacuum stability and perturbativity (red dots), dark matter constraints (green dots) and collider (region below the blue solid line). The blue shaded regions are ruled out by the recent ATLAS search [5] at 139 fb^{-1} luminosity.

$$-\mathcal{L}_{int} \supset \overline{f_L}\gamma^\mu g' Q_x Z'_\mu f_L + \overline{f_R}\gamma^\mu g' Q'_x Z'_\mu f_R. \tag{6.43}$$

Here, f_L and f_R are the left handed and right handed fermions and Q_x and Q'_x are the corresponding charges under the $U(1)'$ gauge group. These charges are linear combinations of x_H and x_Φ and will appear in the C_V and C_A coefficients of the Z' interactions. The Z' interaction with the colored fermions will contain the color factor $N_c = 3$ in the interaction whereas $N_c = 1$ for the uncolored fermions. The bounds from the collider for various models are shown by the blue solid lines in Figs. 6.12 and 6.13. The blue shaded regions in these figures are ruled out by the current LHC data obtained from the ATLAS experiment [5] at 139 fb^{-1} luminosity.

In these figures, we have also given the bounds from vacuum stability, perturbativity and relic density for purposes of comparison. For finding the regions that are allowed by vacuum stability and perturbativity, we have done a scanning in the following ranges of parameters,

$$g' \in [0.0001, 1.0], \quad u \in [0.3, 100] \text{ TeV} \quad m_{h_2} \in [2.0, 16] \text{ TeV}, \quad y_{NS}^{33} \in [0.2, 2.5], \tag{6.44}$$

with $\theta = 0.01$. For Y_ν and $(y_{NS})_{2\times 2}$, we have used BM-I from the Table 6.1 and we have scaled y_{NS} according to the variation in u. The values of M_Z' have been calculated using Eq.6.27 and the allowed regions are shown by the red points in Figs. 6.12 and 6.13. It can be seen from these figures that the bulk of the parameter space allowed by vacuum stability lies in the region disfavoured by the ATLAS results. Regions beyond $M_Z' > 5TeV$ that is not explored by ATLAS are seen to be allowed by vacuum stability and perturbativity constraints. Future ATLAS results will be able to explore this region.

Similarly, to find out the points that can give the correct dark matter relic density, we have performed a scanning of parameters in the ranges,

$$\begin{aligned} g' \in [0.0001, 1.0], \quad M_Z' \in [0.1, 16] \text{ TeV} \quad m_{h_2} \in [2.0, 16] \text{ TeV}, \\ y_{NS}^{33} \in [0.2, 2.5], M_{DM} \in [1.0, 10.0]\text{TeV}. \end{aligned} \tag{6.45}$$

Here also, we have fixed $\theta = 0.01$. The green dots in Figs. 6.12 and 6.13 correspond to the values that give the correct dark matter relic density. The constraints coming from this is seen to be less stringent than the combined constraints from vacuum stability, perturbativity and ATLAS analysis.

6.8 Summary

In this chapter, we have studied the inverse seesaw model in a class of general $U(1)$ extensions of the SM. We have studied the parameter spaces in various planes that are allowed by vacuum stability and perturbativity as well as consistent with the low energy neutrino data. In addition, this model can have a prospective dark matter candidate by demanding the third generations of the $SU(2)_L$ singlet neutral fermions to be odd odd under a discrete Z_2 symmetry. Comparing the Z' production and its decay into the dilepton mode at the LHC with the current ATLAS results, we find the bounds on the $U(1)'$ coupling constant with respect to the Z' mass. Finally, combining all the constraints, we obtain the resultant allowed parameter space which can be probed in the future experiments.

Chapter 7

Summary and Conclusions

The SM has been higly successful in explaining a wide range of experimental observations and the the discovery of the Higgs boson at the Large Hadron Collider experiment in 2012 has completed the hunt for its last missing piece. The Higgs boson holds a special status in the SM as it gives mass to all the other particles whereas the neutrinos are predicted to be massless in the SM due to the absence of right handed neutrinos. However, observation of neutrino oscillation from solar, atmospheric, reactor and accelerator experiments necessitates the extension of the SM to incorporate small neutrino masses. In addition, there are several astrophysical evidences that have established the existence of dark matter. These are the two major experimental indications that motivate us to consider theories beyond SM and a successful theory of particle physics should be able to address these two issues.

The seesaw mechanism is considered to be the most elegant way to generate small neutrino masses. The philosophy of the seesaw mechanism is that the neutrinos are Majorana particles and lepton number is violated at high energy. According to this, the tree level exchange of some heavy particle at high energy will give rise to the dimension-five Weinberg operator at low energy, which in turn will give rise to small Majorana masses to the neutrinos once the electroweak symmetry is broken. Depending on whether the exchange particle is a fermionic singlet, scalar triplet or fermionic triplet, the corresponding scenarios are called as type-I, type-II and type-III seesaw models respectively. However, in order to get a neutrino mass of the sub-eV scale, one has to take the new particles to be extremely heavy or else take the new couplings to be extremely small. This spoils the testability of the theory which motivates one to consider the low scale seesaw models. One can reduce the scale of new physics to TeV by decoupling the new physics scale from the scale of lepton number violation. The smallness of the neutrino mass can then be attributed to small lepton number violating terms. Tiny values of the latter are deemed natural in accordance with t Hoofts naturalness criteria, since when these parameters are set to zero, the global U(1) lepton number symmetry is restored and neutrinos become massless. Such models can have various phenomenological as well as theoretical consequences. For example, the heavy seesaw particles can lead to enhanced rates of various charged lepton flavor violating decays and the new couplings associated with the seesaw can alter the stability/metastability of the electroweak vacuum. In addition, these heavy particles can have interesting signatures in the collider experiments. In this thesis, we have studied various phenomenological and theoretical implications of massive neutrinos in the context of different low scale seesaw models. We have also explored the possibility of having a plausible candidate for dark matter in the context of seesaw models.

We yet do not know whether neutrinos are lepton number violating Majorana particles or Dirac particles even though the seesaw mechanism implies that they are Majorana particles. This can be tested in the experiments searching for the lepton number violating neutrino-less double beta decay. No positive result has been observed in any of the experiments so far and this has put an upper bound on the effective mass governing $0\nu\beta\beta$. The predictions for the effective mass for IH and NH are separated by a "desert region" if we assume that the light Majorana neutrino exchange is the sole mechanism for $0\nu\beta\beta$. The current upper bound is just above the IH region (~ 0.1 eV) and several future experiments with sensitivity reach ~ 0.015 eV are expected to probe the IH parameter space completely. However if no positive signal is found in these searches then the projected sensitivity reach of these experiments are in the ballpark of of 0.005 eV which can explore only a small part of the NH region for lightest neutrino mass $\geq$ 0.005 eV. The next frontier that is envisaged is $\sim 10^{-3}$ eV. In this thesis, we have explored the implications of the DLMA solution to the solar neutrino problem for neutrino-less double beta decay ($0\nu\beta\beta$). The standard LMA solution corresponds to standard neutrino oscillations with $\Delta m^2_{21} \simeq 7.5 \times 10^{-5}$ eV^2 and $\sin^2\theta_{12} \simeq 0.3$, and satisfies the solar neutrino data at high significance. The DLMA solution appears as a nearly-degenerate solution to the solar neutrino problem for $\Delta m^2_{21} \simeq 7.5 \times 10^{-5}$ eV^2 and sin$^2\theta_{12} \simeq 0.7$, in the presence of large NSIs. We have seen that if we take the Dark-LMA solution, the effective mass for NH shifts into the intermediate "desert zone" between NH and IH whereas the predictions for IH remain the same. Therefore, in an incremental advancement, a new goal for the $0\nu\beta\beta$ experiments can be to first explore this region $\sim 0.004 - 0.0075$ eV, which is possible even for very low values of the lightest neutrino mass. In addition to defining a new sensitivity goal for future $0\nu\beta\beta$ experimental program, this also can provide an independent confirmation/refutal of the DLMA solution to the solar neutrino problem in presence of NSI.

We have also studied a minimal type-III seesaw model where we have extended the SM by adding two degenerate $SU(2)_L$ triplet fermions with zero hypercharge. In this case, the lightest active neutrino is massless and the minimality of the model allows us to express the yukawa couplings (Y_Σ) in terms of just three free parameters (a complex number z and the degenerate mass of the triplet fermion, M_Σ) using the Casas-Ibarra parametrization. We have analyzed the implications of naturalness and the stability of the electroweak vacuum in this context. We have found that the lighter masses of the fermionic triplets, $M_\Sigma \simeq 400$ GeV are disallowed for all values of Y_Σ by the constraints coming from $\mu \to e$ conversion in the atomic nucleus. At the same time, the heavier triplet masses are disfavored by naturalness depending on the naturalness condition that we impose. For instance, if we demand the correction to the Higgs mass to be less than 200 GeV, it will put an upper bound of $\sim 10^5$ GeV on the masses of the triplets. Also, the maximum value of Tr$[Y_\Sigma^\dagger Y_\Sigma]^{\frac{1}{2}}$ that is allowed in this case by the compbined bounds from LFV and naturalness is 0.1, corresponding to $M_\Sigma \sim 10^4$ GeV. Another important result is that in the parameter space which is allowed by both LFV as well as naturalness constraints, the EW vacuum is stable/metastable depending on the values of Tr$[Y_\Sigma^\dagger Y_\Sigma]^{\frac{1}{2}}$ and the standard model parameters used. Hence, one does not really have to worry about the instability of the vacuum in this model.

In the next chapter, we have analyzed the stability of the electroweak vacuum in the context of TeV scale inverse seesaw and minimal linear seesaw models extended with a scalar singlet dark matter. We have studied the interplay between the contribution of the extra singlet scalar and the singlet fermions to the EW vacuum stability. We have shown that the coupling constants in these two seemingly disconnected sectors can be correlated at high energy by the vacuum stability/metastability and perturbativity constraints. In the inverse seesaw scenario, the EW vacuum stability analysis is done after fitting the model parameters with the neutrino oscillation data and the non-unitarity constraints on U_{PMNS}. For the minimal linear seesaw model, the Yukawa matrix Y_ν can be fully parameterized in terms of the oscillation parameters excepting an overall coupling constant y_ν which can be constrained from vacuum stability and LFV. We have taken the heavy neutrino masses of order up to a few TeV for both the seesaw models. An extra Z_2 symmetry is imposed to ensure that the scalar particle serves as a viable dark matter candidate. We include all the experimental and theoretical bounds coming from the constraints on relic density and dark matter searches as well as unitarity and perturbativity up to M_{Planck}. For the masses of new fermions from 200 GeV to a few TeV, the annihilation cross section to the extra fermions is very small for dark matter mass $\mathcal{O}(1-2)$ TeV. We have also checked that the theory violates perturbativity before M_{Planck} for DM mass $\gtrsim 2.5$ TeV. In addition we find that the value of the Higgs portal coupling κ (M_Z) for which perturbativity is violated at M_{Planck} decreases with increase in the value of the Yukawa couplings of the new fermions. For $M_{DM} >> M_t$, one can approximately write $M_{DM} \sim 3300\ \kappa$ GeV. This implies that with the increasing Yukawa coupling, the mass of dark matter for which the perturbativity is maintained also decreases. Thus the RGE running induces a correlation between the couplings of the two sectors from the perturbativity constraints. The presence of the fermionic Yukawa couplings in the context of TeV scale seesaw models drives the vacuum more towards instability while the singlet scalar tries to arrest this tendency. Overall, we have found that it is possible to find parameter spaces for which the electroweak vacuum remains absolutely stable for both inverse and linear seesaw models in the presence of the extra scalar particle. We have hot an upper bound from metastability on Tr$[Y_\nu^\dagger Y_\nu]$ as 0.25 for $\kappa = 0$ which increases to 0.4 for $\kappa = 0.6$ in inverse seesaw model. We have also seen that in the absence of the extra scalar, the values of the Yukawa coupling y_ν greater than 0.42 are disallowed in the minimal linear seesaw model. But, in the presence of the extra scalar the values of y_ν up to ~ 0.6 are allowed for dark matter mass ~ 1 TeV. The correlations between the Yukawa couplings (Tr$[Y_\nu^\dagger Y_\nu]$ or y_ν) and κ are presented in terms of phase diagrams.

In addition to the simple particle extensions, we have also studied a class of gauged $U(1)$ extensions of the SM, where active light neutrino masses are generated by the inverse seesaw mechanism. In addition to the three right handed neutrinos needed for the anomaly cancellation, we have added three extra neutral fermions. We have kept the third generations of the $SU(2)_L$ singlet neutral fermions as odd under a discrete Z_2 symmetry and the lightest of this can be a stable dark matter candidate. Using the conditions from anomaly cancellation and gauge invariance, we have expressed the $U(1)$ charges of all the fermions in terms of the $U(1)$ charges of the SM Higgs (x_H) and the new complex scalar (x_Φ). We have studied the parameter spaces in various planes that are consistent with the low energy neutrino data a well as allowed by absolute stability of the EW vacuum and perturbativity and at the same time giving the correct relic density. We have seen that these bounds depends strongly on the model under consideration since the corresponding RGEs depend on the values of x_H and x_Φ. Also, comparing the Z' production and its decay into the dilepton mode at the LHC with the current ATLAS results, we have found the bounds on the $U(1)'$ coupling constant with respect to the Z' mass for different models.

Also, we have found that the extra contributions to the neutrino-less double beta decay process due to the extra heavy particles in these low scale seesaw models that we have considered are negligibly small in comparison to the standard light Majorana neutrino contributions.

As a general conclusion of the thesis, we have studied various theoretical and phenomenological implications of seesaw models with special emphasis on low scale variants. We also considered the possibilities of inclusion of a viable dark matter candidate in models that can generate neutrino masses suggested by the oscillation data. We have stressed on constraining the parameter spaces of these models using the bounds from vacuum stability, perturbativity and low energy neutrino oscillation data as well as dark matter and collider constraints in some cases. Analysis of future data from various experiments can further test these models.

Appendix A

Effective Potential

A.1 Calculating the Effective Potential in a Simple ϕ^4 Theory

In this section, we will derive the expression for the for a simple ϕ^4 theory [333, 334]. Consider a scalar field theory defined by the Lagrangian,

$$\mathcal{L} = \frac{1}{2}(\partial\phi)^2 - \frac{1}{2}\mu^2\phi^2 - \frac{1}{4!}\lambda\phi^4. \tag{A.1}$$

The generating function is defined as,

$$Z = e^{iW(J)} = \int D\phi e^{i[S(\phi)+J\phi]}, \tag{A.2}$$

where for convenience, we define $J\phi = \int d^4xJ(x)\phi(x)$. Here $W(J)$ is the generating functional and $J(x)$ is the external source. Now, the classical expectation value of the field ϕ is given by,

$$\phi_c \equiv \frac{\delta W}{\delta J(x)} = \frac{1}{Z}\int D\phi e^{i[S(\phi)+J\phi]}\phi(x). \tag{A.3}$$

The above relation determines $\phi_c(x)$ as a functional of J. Given a functional W of J, a Legendre transform can be performed to obtain a functional Γ of ϕ_c,

$$\Gamma(\phi_c) = W(J) - \int d^4xJ(x)\phi_c(x). \tag{A.4}$$

J is to be eliminated in favor of ϕ_c on the right-hand side of Eqn.A.4 by solving Eqn.A.3. We expand $\Gamma(\phi_c)$ in the form,

$$\Gamma(\phi_c) = \int d^4(x)[-V_{eff}(\phi_c) + Z(\phi_c)(\partial\phi_c)^2) + ...]. \tag{A.5}$$

Also, the functional derivative of Γ is given by,

$$\frac{\delta\Gamma(\phi_c)}{\delta\phi_C(y)} = \int d^4x \frac{\delta J(x)}{\delta\phi_c(y)} \frac{\delta W(J)}{\delta J(x)} - \int d^4x \frac{\delta J(x)}{\delta\phi_c(y)} \phi_c(x) - J(y) = -J(y). \quad \text{(A.6)}$$

The above relation can be thought of as the dual of $\delta W(J)/\delta J(x) = \phi_c(x)$. If J and ϕ_c are independent of x, using Eqn.A.5, the condition given by Eqn.A.6 becomes,

$$V'_{eff}(\phi_c) = J. \quad \text{(A.7)}$$

If there is no external source,

$$V'_{eff}(\phi_c) = 0. \quad \text{(A.8)}$$

Thus, the vacuum expectation value of ϕ in the absence of an external source is obtained by minimizing $V_{eff}(\phi_c)$.

Now, $e^{iW(J)} = \int D\phi e^{i[S(\phi)+J\phi]}$ can be evaluated in the steepest descent approximation, and the steepest descent point, $\phi_s(x)$ is obtained as the solution of,

$$\frac{\delta[S(\phi) + \int d^4y J(y)\phi(y)]}{\delta\phi(x)}|_{\phi_s} = 0. \quad \text{(A.9)}$$

That is,

$$\partial^2\phi_s(x) + V'[\phi_s(x)] = J(x). \quad \text{(A.10)}$$

Writing the dummy integration variable in EqnA.2 as $\phi = \phi_s + \tilde{\phi}$ and expanding to quadratic order in $\tilde{\phi}$,

$$\begin{aligned} Z = e^{iW(J)} &= \int D\phi e^{i[S(\phi)+J\phi]} \\ &\simeq e^{i[S(\phi_s)+J\phi_s]} \int D\tilde{\phi} e^{i\int d^4x \frac{1}{2}[(\partial\tilde{\phi})^2 - V''(\phi_s)\tilde{\phi}^2]}, \\ &= e^{i[S(\phi_s)+J\phi_s] - \frac{1}{2}\text{Tr ln}[\partial^2 + V''(\phi_s)]} \end{aligned} \quad \text{(A.11)}$$

where, ϕ_s, being a solution of Eqn.A.10, is a function of J. Thus,

$$W(J) = [S(\phi_s) + J\phi_s] + \frac{1}{2}\text{Tr ln}[\partial^2 + V''(\phi_s)] + ... \quad \text{(A.12)}$$

where ... stands for the higher order terms, and hence using Eqn.A.3,

$$\phi_c = \frac{\delta W}{\delta J} = \frac{\delta[S(\phi_s) + J\phi_s]}{\delta\phi_s} \frac{\delta\phi_s}{\delta J} + \phi_s + ... = \phi_s + ... \quad \text{(A.13)}$$

That is, to leading order, ϕ_c is equal to ϕ_s. Thus from Eqn.A.4,

$$\Gamma(\phi) = S(\phi) + \frac{i}{2}\text{Tr ln}[\partial^2 + V''(\phi)] + ... \tag{A.14}$$

Restricting to the case where ϕ is independent of x and hence $V''(\phi)$ is a constant and the operator $\partial^2 + V''(\phi)$ is translational invariant, one gets,

$$\begin{aligned}\text{Tr ln}\,[\partial^2 + V''(\phi)] &= \int d^4x \langle x| \text{ ln}\,[\partial^2 + V''(\phi)]|x\rangle \\ &= \int d^4x \int \frac{d^4k}{2\pi^4} \langle x|k\rangle\langle k|\text{ln}\,[\partial^2 + V''(\phi)]|k\rangle\langle k|x\rangle \\ &= \int d^4x \int \frac{d^4k}{2\pi^4} \text{ln}\,[-k^2 + V''(\phi)].\end{aligned} \tag{A.15}$$

Using the above two equations and Eqn.A.5,

$$V_{eff}(\phi) = V(\phi) - \frac{i}{2}\int \frac{d^4k}{2\pi^4}\text{ln}\,[-k^2 + V''(\phi)]. \tag{A.16}$$

This is known as the Coleman-Weinberg effective potential [333].

Now, consider adding a fermion field, ψ to the this simple ϕ^4 theory and the corresponding Lagrangian is,

$$\mathcal{L}_\psi = \bar{\psi}(i\gamma_\mu\partial^\mu - m - f\phi)\psi. \tag{A.17}$$

In the path integral,

$$Z = \int D\phi\ D\bar{\psi}\ D\psi e^{i\int d^4x[\frac{1}{2}(\partial\phi)^2 - V(\phi) + \bar{\psi}(i\gamma_\mu\partial^\mu - m - f\phi)\psi]}. \tag{A.18}$$

After performing the integration over ψ,

$$Z = \int D\phi\ D\bar{\psi}\ D\psi e^{i\int d^4x[\frac{1}{2}(\partial\phi)^2 - V(\phi) + \text{Tr ln }(i\gamma_\mu\partial^\mu - m - f\phi)]}. \tag{A.19}$$

Repeating the same steps as in Eqn.A.15, we can find the fermion contribution to the effective potential as,

$$V_F(\phi) = i\int \frac{d^4k}{(2\pi)^4}\text{Tr ln }(i\gamma_\mu\partial^\mu - m - f\phi). \tag{A.20}$$

The same procedure can be extended to calculate the contribution to the effective potential due to the scalars, fermions and gauge bosons in the case of SM.

A.2 Correction to the SM Effective Potential due to a Singlet Scalar

For SM extended by a singlet scalar, the new scalar potential is given by,

$$V(S,H) \;=\; -m^2 H^\dagger H \;+\; \lambda (H^\dagger H)^2 \;+\; \frac{\kappa}{2} H^\dagger H\, S^2 \;+\; \frac{m_S^2}{2} S^2 \;+\; \frac{\lambda_S}{24} S^4\,. \tag{A.21}$$

Substituting for the SM scalar doublet H and expanding around the classical value $h(t)$, the mass term for the scalar S is given by,

$$M_S^2(h) \;=\; \frac{\partial^2 V}{\partial S^2} \;=\; m_S^2 \;+\; \kappa h^2/2. \tag{A.22}$$

Thus, from Eqn.A.16, the contribution to the effective potential due to S is given by [289, 290],

$$\begin{aligned} V_{eff}^S(h) &= -\frac{i}{2}\int \frac{d^4k}{2\pi^4} \ln\left[-k^2 + M_S^2\right] \\ &= \frac{1}{2}\int \frac{d^4k_E}{2\pi^4} \ln\left[k_E^2 + M_S^2\right] \\ &= -\frac{1}{4}\left(\frac{M_S^2}{4\pi}\right)^2 \left[\frac{2}{\epsilon} - \gamma_E + \ln 4\pi + \frac{3}{2} - \ln M_S^2\right], \end{aligned} \tag{A.23}$$

where we have used dimensional regularization.

In the $\overline{\text{MS}}$ scheme,

$$V_{eff}^S(h) = \frac{1}{64\pi^2} M_S^4(h) \left[\ln \frac{M_S^2(h)}{\mu^2} \;-\; \frac{3}{2}\right], \tag{A.24}$$

where μ is the renormalization scale. This is what we used in Eqn.5.5.

A.3 Neutrino Correction to the SM Effective Potential

In the case of SM extended by type-I seesaw, the fermions come in multiple generations and the expression for the effective potential given in Eqn.A.20 can be generalized as,

$$V_{eff}(h) = i \int \frac{d^4k}{(2\pi)^4} \text{Tr} \ln(k^\mu \gamma_\mu \delta_{ij} - |M|_{ij}). \tag{A.25}$$

Here, i and j are the generation indices.

The relevant part of the Lagrangian in this case is,

$$\begin{aligned}\mathcal{L}_{N_R} =& \frac{1}{2}(\,\bar{\nu}_L \;\; \bar{N}_R^c\,)\begin{pmatrix} 0 & Y_\nu \frac{h}{\sqrt{2}} \\ Y_\nu^T \frac{h}{\sqrt{2}} & M_N \end{pmatrix}\begin{pmatrix} \nu_L^c \\ N_R \end{pmatrix} \;+\; \text{h.c.} \\ =& -\frac{1}{2}\bar{\psi}^c \mathcal{M} P_R \psi - \frac{1}{2}\bar{\psi}\mathcal{M}^\dagger P_L \psi \end{aligned} \quad (A.26)$$

Thus, the mass term relevant for Eqn.A.25 is given by,

$$M_{ij} \;=\; \frac{\partial^2 V}{\partial\psi_j \partial\psi_i} \;=\; (\mathcal{M}P_L + \mathcal{M}^\dagger \mathcal{P_R})_{ij}. \quad (A.27)$$

In the limit $h >> M_N$, the matrix $M^\dagger M$ will take the form,

$$M^\dagger M = \begin{pmatrix} (Y_\nu Y_\nu^\dagger P_L + Y_\nu^* Y_\nu^T P_R)\frac{h^2}{2} & 0 \\ 0 & (Y_\nu^\dagger Y_\nu P_R + Y_\nu^T Y_\nu^* P_L)\frac{h^2}{2} \end{pmatrix} \quad (A.28)$$

Now, the trace in Eqn.A.25 can be simplified as,

$$\begin{aligned}\text{Tr}\ \ln(k^\mu\gamma_\mu\delta_{ij} - |M|_{ij}) &= \frac{1}{2}[\text{Tr}\ \ln(k^\mu\gamma_\mu\delta_{ij} - |M|_{ij}) + \text{Tr}\ \ln(k^\mu\gamma_\mu\delta_{ij} - |M|_{ij})] \\ &= \frac{1}{2}[\text{Tr}\ \ln(k^\mu\gamma_\mu\delta_{ij} - |M|_{ij}) + \text{Tr}\ \ln\gamma_5(k^\mu\gamma_\mu\delta_{ij} - |M|_{ij})\gamma_5] \\ &= \frac{1}{2}[\text{Tr}\ \ln(k^\mu\gamma_\mu\delta_{ij} - |M|_{ij}) + \text{Tr}\ \ln(-k^\mu\gamma_\mu\delta_{ij} - |M|_{ij})] \\ &= \frac{1}{2}\text{Tr}\ \ln(-k^2\delta_{ii} + (M^\dagger M)_{ii}) \end{aligned} \quad (A.29)$$

Thus, after using dimensional regularization, the fermionic contribution to the effective potential in the $\overline{\text{MS}}$ scheme becomes,

$$V_{eff}(h) = -\frac{(M^\dagger M)^2_{ii}}{16\pi^2}\left[\ln\left(\frac{(M^\dagger M)_{ii}}{\mu^2}\right) - \frac{3}{2}\right]. \quad (A.30)$$

Here, we are working in a basis in which $M^\dagger M$ is diagonal. In the case of neutrinos, using Eqn.A.28 and noting that there will be an additional factor of half since both the neutrinos have only one handedness each, the effective potential becomes [145, 146],

$$V_1^\nu(h) = -\frac{(\frac{1}{2}h^2(Y_\nu^\dagger Y_\nu)_{ii})^2}{32\pi^2}\left[\ln\frac{(\frac{1}{2}h^2(Y_\nu^\dagger Y_\nu)_{ii})}{\mu^2(t)} - \frac{3}{2}\right] - \frac{(\frac{1}{2}h^2(Y_\nu Y_\nu^\dagger)_{jj})^2}{32\pi^2}\left[\ln\frac{(\frac{1}{2}h^2(Y_\nu Y_\nu^\dagger)_{jj})}{\mu^2(t)} - \frac{3}{2}\right]. \quad (A.31)$$

In the case of type-III seesaw model, one can get the expression for the effective potential in the same way as outlined above and the final answer will differ only by a multiplicative factor of 3, as can be seen in Eqn.4.10.

Appendix B

Renormalization Group Equations, Effective Quartic Coupling and Matching Conditions at M_t

B.1 Standard Model RGEs

Beta function of the standard model coupling constants and the mass term up to three loop are presented here for completeness [139, 252–255, 292],

$$
\begin{aligned}
\beta_{g_1} &= g_1^3\Bigg[\frac{1}{16\pi^2}\Big(\frac{41}{6}\Big) + \frac{1}{(16\pi^2)^2}\Bigg\{\frac{1}{18}\big(199g_1^2 + 81g_2^2 + 264g_3^2 - 51y_t^2\big)\Bigg\} \\
&\quad + \frac{1}{(16\pi^2)^3}\Bigg\{-\frac{388613g_1^4}{5184} + \frac{1315g_2^4}{64} + 99g_3^4 - 3\lambda^2 - \frac{29g_3^2y_t^2}{3} \\
&\quad + \frac{315y_t^4}{16} + \frac{1}{864}g_1^2(1845g_2^2 - 4384g_3^2 + 1296\lambda - 8481y_t^2) \\
&\quad + g_2^2\Big(-g_3^2 + \frac{3\lambda}{2} - \frac{785y_t^2}{32}\Big)\Bigg\}\Bigg] \qquad \text{(B.1)} \\
\beta_{g_2} &= g_2^3\Bigg[\frac{1}{16\pi^2}\Big(-\frac{19}{6}\Big) + \frac{1}{(16\pi^2)^2}\Bigg\{\frac{1}{6}\big(9g_1^2 + 35g_2^2 + 72g_3^2 - 9y_t^2\big)\Bigg\} \\
&\quad + \frac{1}{(16\pi^2)^3}\Bigg\{-\frac{5597g_1^4}{576} + \frac{324953g_2^4}{1728} + 81g_3^4 - 3\lambda^2 - 7g_3^2y_t^2 \\
&\quad + \frac{147y_t^4}{16} + \frac{1}{96}g_1^2(873g_2^2 - 32g_3^2 + 48\lambda - 593y_t^2)
\end{aligned}
$$

$$
+g_2^2\big(39g_3^2+\frac{3\lambda}{2}-\frac{729y_t^2}{32}\big)\Big\}\Big] \tag{B.2}
$$

$$
\begin{aligned}
\beta_{g_3} &= g_3^3\Bigg[\frac{1}{16\pi^2}\Big(-7\Big)+\frac{1}{(16\pi^2)^2}\Bigg\{\frac{11g_1^2}{6}+\frac{9g_2^2}{2}-2(13g_3^2+y_t^2)\Bigg\}\\
&+\frac{1}{(16\pi^2)^3}\Bigg\{-\frac{2615g_1^4}{216}+\frac{109g_2^4}{8}+\frac{65g_3^4}{2}-40g_3^2y_t^2+15y_t^4\\
&+g_2^2\Bigg(21g_3^2-\frac{93y_t^2}{8}\Bigg)-\frac{1}{72}g_1^2\big(9g_2^2-616g_3^2+303y_t^2\big)\Bigg\}\Bigg]
\end{aligned} \tag{B.3}
$$

$$
\begin{aligned}
\beta_{y_t} &= y_t\Bigg[\frac{1}{16\pi^2}\Big\{\frac{1}{12}\big(-17g_1^2-27g_2^2-96g_3^2+54yt^2\big)\Bigg\}+\frac{1}{(16\pi^2)^2}\Big\{\frac{1187g_1^4}{216}-\frac{23g_2^4}{4}\\
&+g_1^2\Bigg(-\frac{3g_2^2}{4}+\frac{19g_3^2}{9}+\frac{131y_t^2}{16}\Bigg)+g_2^2\Bigg(9g_3^2+\frac{225y_t^2}{16}\Bigg)\\
&-6(18g_3^4-\lambda^2-6g_3^2y_t^2+2\lambda y_t^2+2y_t^4)\Bigg\}\\
&+\frac{1}{(16\pi^2)^3}\frac{1}{24}\Big\{24g_3^2(16\lambda y_t^2-157y_t^4)\\
&+4g_3^4y_t^2(3827-1368\zeta(3))+16g_3^6(-2083+960\zeta(3))\\
&+9\big(-96\lambda^3+10\lambda^2y_t^2+528\lambda y_t^4+y_t^6(113+36\zeta(3))\big)\Big\}\Bigg]
\end{aligned} \tag{B.4}
$$

$$
\begin{aligned}
\beta_\lambda &= \Bigg[\frac{1}{16\pi^2}\Bigg\{\frac{3}{8}(2g_2^4+(g_1^2+g_2^2)^2)+24\lambda^2-6y_t^4-3\lambda(g_1^2+3g_2^2-4y_t^2)\Bigg\}\\
&+\frac{1}{(16\pi^2)^2}\frac{1}{48}\Bigg\{-379g_1^6-559g_1^4g_2^2-289g_1^2g_2^4+915g_2^6\\
&+48\lambda\Bigg(\frac{629g_1^4}{24}-\frac{73g_2^4}{8}+108g_2^2\lambda-312\lambda^2+g_1^2\Bigg(\frac{39g_2^2}{4}+36\lambda\Bigg)\Bigg)\\
&-4\big(57g_1^4-2g_1^2(63g_2^2+85\lambda)+3(9g_2^4-90g_2^2\lambda+64\lambda(-5g_3^2+9\lambda))\big)y_t^2\\
&-16(8g_1^2+96g_3^2+9\lambda)y_t^4+1440y_t^6\Bigg\}+\frac{1}{(16\pi^2)^3}\frac{1}{12}\Bigg\{20952\lambda^3y_t^2\\
&+288\lambda^4(299+168\zeta(3))\\
&-y_t^4\big(g_3^4(2128-768\zeta(3))+48g_3^2y_t^2(19-120\zeta(3))+9y_t^4(533+96\zeta(3))\big)\\
&+108\lambda^2y_t^2\big(16g_3^2(-17+16\zeta(3))+y_t^2(191+168\zeta(3))\big)\\
&+\lambda y_t^2\big(27y_t^4(13-176\zeta(3))-32g_3^4(-311+36\zeta(3))\\
&-24g_3^2y_t^2(-895+1296\zeta(3))\big)\Bigg\}+0.0000133607g_3^6y_t^4\Bigg]
\end{aligned} \tag{B.5}
$$

$$\begin{aligned}
\beta_{m^2} &= m^2\Bigg[\frac{1}{(16\pi^2)}\left\{6\lambda+3y_t^2-\frac{9g_2^2}{4}-\frac{3g_1^2}{4}\right\}+\frac{1}{(16\pi^2)^2}\Bigg\{\lambda(-30\lambda-36y_t^2+36g_2^2+12g_1^2)\\
&+y_t^2\left(-\frac{27y_t^2}{4}+20g_3^2+\frac{45g_2^2}{8}+\frac{85g_1^2}{24}\right)+-\frac{145}{32}g_2^4+\frac{557}{96}g_1^4+\frac{15g_2^2g_1^2}{16}\Bigg\}\\
&+\frac{1}{(16\pi^2)^3}\Big\{\lambda^2(1026\lambda+148.5y_t^2-192.822g_2^2-64.273g_1^2)+\lambda y_t^2(347.394y_t^2\\
&+80.385g_3^2-318.591g_2^2-99.498g_1^2)+\lambda(-64.5145g_2^4-182.79g_1^4\\
&-63.0385g_2^2g_1^2)+y_t^4(154.405y_t^2-209.24g_3^2-3.82928g_2^2-12.5128g_1^2)\\
&+y_t^2(178.484g_3^4-102.627g_2^4-77.0028g_1^4+7.572g_3^2g_2^2+14.545g_3^2g_1^2\\
&+19.1167g_2^2g_1^2)+g_2^4(-28.572g_3^2+301.724g_2^2+16.552g_1^2)+g_1^4(-11.642g_3^2\\
&+27.161g_2^2+38.786g_1^2)\Big\}\Bigg]
\end{aligned} \tag{B.6}$$

B.1.1 Matching Conditions at M_t

To calculate the couplings at the scale M_t, we have included the QCD corrections up to three loops [248], electroweak corrections up to one-loop [249, 250] and the $O(\alpha\alpha_s)$ corrections to the matching of top Yukawa and top pole mass [246, 251].

$$g_1(\mu=M_t) = 0.358725+0.000007\left(\frac{M_t\,[\mathrm{GeV}]-173.1}{0.6}\right) \tag{B.7}$$

$$g_2(\mu=M_t) = 0.64818-0.00002\left(\frac{M_t\,[\mathrm{GeV}]-173.1}{0.6}\right) \tag{B.8}$$

$$\begin{aligned}
g_3(\mu=M_t) &= 1.16449-0.0003\left(\frac{M_t\,[\mathrm{GeV}]-173.1}{0.6}\right)\\
&+0.0031\left(\frac{\alpha_S(M_Z)-0.1184}{0.0007}\right)
\end{aligned} \tag{B.9}$$

$$\begin{aligned}
y_t(\mu=M_t) &= 0.935643+0.0033\left(\frac{M_t\,[\mathrm{GeV}]-173.1}{0.6}\right)-0.0004\left(\frac{\alpha_S(M_Z)-0.1184}{0.0007}\right)\\
&-0.00001\left(\frac{M_h\,[\mathrm{GeV}]-125.7}{0.3}\right)
\end{aligned} \tag{B.10}$$

$$\begin{aligned}
\lambda(\mu=M_t) &= 0.127054-0.00003\left(\frac{M_t\,[\mathrm{GeV}]-173.1}{0.6}\right)\\
&-0.00001\left(\frac{\alpha_S(M_Z)-0.1184}{0.0007}\right)+0.00061\left(\frac{M_h[\mathrm{GeV}]-125.7}{0.3}\right)
\end{aligned} \tag{B.11}$$

B.1.2 Effective Higgs quartic coupling for SM

The Higgs effective quartic coupling including the one- and two-loop radiative corrections is given as[139],

$$\lambda_{\text{eff}}^{\text{SM}}(\phi) \;=\; e^{4\Gamma(\phi)}[\lambda(\mu=\phi)+\lambda_{\text{eff}}^{(1)}(\mu=\phi)+\lambda_{\text{eff}}^{(2)}(\mu=\phi)]. \tag{B.12}$$

Here,

$$\begin{aligned}(16\pi^2)\,\lambda_{\text{eff}}^{(1)} \;=\;& \frac{3}{8}g_2^4\left(\ln\frac{g_2^2}{4}-\frac{5}{6}+2\Gamma\right)+\frac{3}{16}(g_1^2+g_2^2)^2\left(\ln\frac{g_1^2+g_2^2}{4}-\frac{5}{6}+2\Gamma\right)\\ &-3y_t^4\left(\ln\frac{y_t^2}{2}-\frac{3}{2}+2\Gamma\right)+3\lambda^2\left(4\ln\lambda-6+3\ln 3+8\Gamma\right)\end{aligned} \tag{B.13}$$

and

$$\begin{aligned}(16\pi^2)^2\lambda_{\text{eff}}^{(2)} \;=\;& \frac{1}{576}g_1^4g_2^2\Bigg\{4359+218\pi^2-36\Big(2\Gamma+\ln\frac{g_2^2}{4}\Big)-153\Big(2\Gamma+\ln\frac{g_2^2}{4}\Big)^2\\ &-4080\Big(2\Gamma+\ln\frac{g_1^2+g_2^2}{4}\Big)+306\Big(2\Gamma+\ln\frac{g_2^2}{4}\Big)\Big(2\Gamma+\ln\frac{g_1^2+g_2^2}{4}\Big)\\ &+924\Big(2\Gamma+\ln\frac{g_1^2+g_2^2}{4}\Big)^2+132\Big(2\Gamma+\ln\frac{g_1^2+g_2^2}{4}\Big)\Big(2\Gamma+\ln\frac{y_t^2}{2}\Big)\\ &-66\Big(2\Gamma+\ln\frac{y_t^2}{2}\Big)^2\Bigg\}+\frac{1}{192}g_1^2g_2^4\Bigg\{817+46\pi^2+213\Big(2\Gamma+\ln\frac{g_2^2}{4}\Big)^2\\ &-6\Big(2\Gamma+\ln\frac{g_2^2}{4}\Big)(50+53\Big(2\Gamma+\ln\frac{g_1^2+g_2^2}{4}\Big)\\ &+4\Big(2\Gamma+\ln\frac{g_1^2+g_2^2}{4}\Big)\Big(-91+57(2\Gamma+\ln\frac{g_1^2+g_2^2}{4}\Big)\\ &+12\Big(2\Gamma+\ln\frac{g_1^2+g_2^2}{4}\Big)\Big(2\Gamma+\ln\frac{y_t^2}{2}\Big)-6\Big(2\Gamma+\ln\frac{y_t^2}{2}\Big)^2\Bigg\}\\ &+8g_3^2y_t^4\Bigg\{9-8\Big(2\Gamma+\ln\frac{y_t^2}{2}\Big)+3\Big(2\Gamma+\ln\frac{y_t^2}{2}\Big)^2\Bigg\}\\ &+\frac{1}{8}g_1^2g_2^2y_t^2\Bigg\{-57+44\Big(2\Gamma+\ln\frac{g_1^2+g_2^2}{4}\Big)+4\Big(2\Gamma+\ln\frac{y_t^2}{2}\Big)\\ &-18\Big(2\Gamma+\ln\frac{g_1^2+g_2^2}{4}\Big)\Big(2\Gamma+\ln\frac{y_t^2}{2}\Big)+9\Big(2\Gamma+\ln\frac{y_t^2}{2}\Big)^2\Bigg\}\\ &+\frac{1}{48}g_1^4y_t^2\Bigg\{189-28\Big(2\Gamma+\ln\frac{g_1^2+g_2^2}{4}\Big)-68\Big(2\Gamma+\ln\frac{y_t^2}{2}\Big)\\ &-54\Big(2\Gamma+\ln\frac{g_1^2+g_2^2}{4}\Big)\Big(2\Gamma+\ln\frac{y_t^2}{2}\Big)+27\Big(2\Gamma+\ln\frac{y_t^2}{2}\Big)^2\Bigg\}\end{aligned}$$

$$
\begin{aligned}
&+\frac{1}{576}g_1^6\Bigg\{2883+206\pi^2-9\left(2\Gamma+\ln\frac{g_2^2}{4}\right)^2+708\left(2\Gamma+\ln\frac{g_1^2+g_2^2}{4}\right)^2\\
&-102\left(2\Gamma+\ln\frac{y_t^2}{2}\right)^2+6\left(2\Gamma+\ln\frac{g_1^2+g_2^2}{4}\right)\Bigg(-470+3\left(2\Gamma+\ln\frac{g_2^2}{4}\right)\\
&+34\left(2\Gamma+\ln\frac{y_t^2}{2}\right)\Bigg)\Bigg\}+\frac{1}{6}y_t^6\Bigg\{-9g_2^2\left(1-\ln\frac{g_2^2}{4}+\ln\frac{y_t^2}{2}\right)+4g_1^2\Bigg(9-8\Bigg(2\Gamma\\
&+\ln\frac{y_t^2}{2}\Bigg)+3\left(2\Gamma+\ln\frac{y_t^2}{2}\right)^2\Bigg)\Bigg\}+\frac{1}{192}g_2^6\Bigg\{-2067+90\pi^2+1264\Bigg(2\Gamma\\
&+\ln\frac{g_2^2}{4}\Bigg)+69\left(2\Gamma+\ln\frac{g_2^2}{4}\right)^2+632\left(2\Gamma+\ln\frac{g_1^2+g_2^2}{4}\right)-414\left(2\Gamma+\ln\frac{g_2^2}{4}\right)\Bigg(2\Gamma\\
&+\ln\frac{g_1^2+g_2^2}{4}\Bigg)+156\left(2\Gamma+\ln\frac{g_1^2+g_2^2}{4}\right)^2+36\left(2\Gamma+\ln\frac{g_1^2+g_2^2}{4}\right)\left(2\Gamma+\ln\frac{y_t^2}{2}\right)\\
&54\left(2\Gamma+\ln\frac{y_t^2}{2}\right)^2-144\left(-\ln\frac{g_2^2}{4}+\ln\frac{y_t^2}{2}\right)\left(2\Gamma+\ln\frac{g_2^2y_t^2}{4}\right)\Bigg\}\\
&+\frac{1}{2}y_t^6\Bigg\{-69-\pi^2+48\left(2\Gamma+\ln\frac{y_t^2}{2}\right)-6\left(2\Gamma+\ln\frac{g_2^2}{4}\right)\left(2\Gamma+\ln\frac{y_t^2}{2}\right)\\
&-3\left(2\Gamma+\ln\frac{y_t^2}{2}\right)^2-6\left(-\ln\frac{g_2^2}{4}+\ln\frac{y_t^2}{2}\right)\left(2\Gamma+\ln\frac{g_2^2y_t^2}{4}\right)\Bigg\}\\
&+\frac{3}{16}g_2^4y_t^2\Bigg\{15+2\pi^2+8\left(2\Gamma+\ln\frac{g_2^2}{4}\right)+4\left(2\Gamma+\ln\frac{g_1^2+g_2^2}{4}\right)-12\left(2\Gamma+\ln\frac{y_t^2}{2}\right)\\
&-6\left(2\Gamma+\ln\frac{g_1^2+g_2^2}{4}\right)\left(2\Gamma+\ln\frac{y_t^2}{2}\right)-3\left(2\Gamma+\ln\frac{y_t^2}{2}\right)^2\\
&+12\left(-\ln\frac{g_2^2}{4}+\ln\frac{y_t^2}{2}\right)\left(2\Gamma+\ln\frac{g_2^2y_t^2}{4}\right)\Bigg\}+\frac{3}{4}\left(g_2^6-3g_2^4y_t^2+4y_t^6\right)\text{Polylog}_2\left[\frac{g_2^2}{2y_t^2}\right]\\
&+\frac{1}{64}g_2^2\left(g_1^4+18g_1^2g_2^2-51g_2^4-\frac{48g_2^6}{g_1^2+g_2^2}\right)\sqrt{-\frac{4(g_1^2+g_2^2)}{g_2^2}+\frac{(g_1^2+g_2^2)^2}{g_2^4}}\Bigg\{\frac{\pi^2}{3}\\
&-\ln\left[\frac{g_1^2+g_2^2}{g_2^2}\right]^2+2\ln\left[\frac{1}{2}-\frac{1}{2}\sqrt{-3+\frac{4g_1^2}{g_1^2+g_2^2}}\right]^2\\
&-4\text{Polylog}_2\left[\frac{1}{2}-\frac{1}{2}\sqrt{-3+\frac{4g_1^2}{g_1^2+g_2^2}}\right]\Bigg\}+\frac{1}{96}\sqrt{(g_1^2+g_2^2)(g_1^2+g_2^2-8y_t^2)}\;\Bigg(17g_1^4\\
&-6g_1^2g_2^2+9g_2^4+2\left(7g_1^2-73g_2^2+\frac{64g_2^2}{g_1^2+g_2^2}\right)y_t^2\Bigg)\Bigg\{\frac{\pi^2}{3}-\ln\left[\frac{g_1^2+g_2^2}{2y_t^2}\right]^2\\
&+2\ln\left[\frac{1}{2}\left(1-\sqrt{1-\frac{8y_t^2}{g_1^2+g_2^2}}\right)\right]^2-4\text{Polylog}_2\left[\frac{1}{2}\left(1-\sqrt{1-\frac{8y_t^2}{g_1^2+g_2^2}}\right)\right]\Bigg\},
\end{aligned}
\tag{B.14}
$$

where,

$$\Gamma(\phi) \;=\; \int_{M_t}^{\phi} \gamma(\mu)\, d\, \ln \mu\, .$$

Here, $\gamma(\mu)$ is the anomalous dimensions of the Higgs field and is given as,

$$\begin{aligned}
\gamma \;=\; & \frac{1}{16\pi^2}\left\{\frac{3g_1^2}{4}+\frac{9g_2^2}{4}-3y_t^2\right\}+\frac{1}{(16\pi^2)^2}\left\{-\frac{431g_1^4}{96}-\frac{9g_1^2g_2^2}{16}+\frac{271g_2^4}{32}-6\lambda^2\right. \\
& \left.+y_t^2\left(-\frac{85g_1^2}{24}-\frac{45g_2^2}{8}-20g_3^2+\frac{27y_t^2}{4}\right)\right\}+\frac{1}{(16\pi^2)^3}\left\{-\frac{1315g_1^6}{54}+\frac{193g_1^4g_2^2}{36}+\frac{181g_1^2g_2^4}{60}\right. \\
& -\frac{15851g_2^6}{100}+\frac{419g_1^4g_3^2}{36}+\frac{2857g_2^4g_3^2}{100}+\frac{107g_1^4\lambda}{36}+\frac{119}{20}g_1^2g_2^2\lambda+\frac{223g_2^4\lambda}{25} \\
& -15g_1^2\lambda^2-45g_2^2\lambda_1^2+36\lambda^3+\frac{1499g_1^4y_t^2}{36}-\frac{1321}{60}g_1^2g_2^2y_t^2+\frac{117g_2^4y_t^2}{5} \\
& -\frac{291}{20}g_1^2g_3^2y_t^2-\frac{757}{100}g_2^2g_3^2y_t^2-\frac{4462g_3^4y_t^2}{25}+\frac{135\lambda^2y_t^2}{2}+\frac{471g_1^2y_t^4}{20}+\frac{4011g_2^2y_t^4}{100} \\
& \left.+\frac{1581g_3^2y_t^4}{20}-45\lambda y_t^4-\frac{6013y_t^6}{13}\right\}
\end{aligned}$$

B.2 One-loop RGEs in General $U(1)$ Extended Models with Inverse Seesaw Mechanism

Here, we give the one-loop RGEs for the $SU(3)_c \times SU(2)_L \times U(1)_Y \times U(1)'$ model that we have considered in chapter 6 and these have been generated using SARAH [295].

$$\begin{aligned}
\beta_{g_1} = \frac{1}{16\pi^2}\frac{1}{6}\Big(& 41g_1^3+g_1^2g_{1p1}(78x_H+64x_\Phi)+g_{11p}g_{1p1}(39g_{11p}x_H+41g'x_H^2+32g_{11p}x_\Phi \\
& +64g'x_Hx_\Phi+66g'x_\Phi^2)+g_1(41g_{11p}^2+g_{11p}g'(39x_H+32x_\Phi) \\
& +g_{1p1}^2(41x_H^2+64x_Hx_\Phi+66x_\Phi^2))\Big)
\end{aligned} \tag{B.15}$$

$$\beta_{g_2} = \frac{1}{16\pi^2}\frac{(-19g_2^3)}{6} \tag{B.16}$$

$$\beta g_3 = \frac{1}{16\pi^2}(-7g_3^3) \tag{B.17}$$

$$\beta_{g'} = \frac{1}{16\pi^2}\frac{1}{6}\Big(41g_{11p}^2 g' + g_{11p}(41g1g_{1p1} + (2g'^2 + g_{1p1}^2)(39x_H + 32x_\Phi)) + g'(g1g_{1p1}(39x_H + 32x_\Phi) + (g'^2 + g_{1p1}^2)(41x_H^2 + 64x_H x_\Phi + 66x_\Phi^2))\Big) \tag{B.18}$$

$$\beta_{g_{1p1}} = \frac{1}{16\pi^2}\frac{1}{6}\Big(41g_1^2 g_{1p1} + g1(41g_{11p}g' + (g'^2 + 2g_{1p1}^2)(39x_H + 32x_\Phi)) + g_{1p1}(g_{11p}g'(39x_H + 32x_\Phi) + (g'^2 + g_{1p1}^2)(41x_H^2 + 64x_H x_\Phi + 66x_\Phi^2))\Big) \tag{B.19}$$

$$\beta_{g_{11p}} = \frac{1}{16\pi^2}\frac{1}{6}\Big(g_1^2(41g_{11p} + 39g'x_H + 32g'x_\Phi) + g1g_{1p1}(39g_{11p}x_H + 41g'x_H^2 + 32g_{11p}x_\Phi + 64g'x_H x_\Phi + 66g'x_\Phi^2) + g_{11p}(41g_{11p}^2 + g_{11p}g'(78x_H + 64x_\Phi) + g'^2(41x_H^2 + 64x_H x_\Phi + 66x_\Phi^2))\Big) \tag{B.20}$$

$$\begin{aligned}\beta_{\lambda_1} = \frac{1}{16\pi^2}\frac{1}{8}\Big(&3g_1^4 + 6g_1^2 g_{11p}^2 + 3g_{11p}^4 + 6g_1^2 g_2^2 + 6g_{11p}^2 g_2^2 + 9g_2^4 - 24g_1^2\lambda_1 - 24g_{11p}^2\lambda_1 - 72g_2^2\lambda_1 \\ &+ 192\lambda_1^2 + 8\lambda_3^2 - 12g_1^2 g_{11p}g'x_H - 12g_{11p}^3 g'x_H - 12g_1^3 g_{1p1}x_H - 12g_1 g_{11p}^2 g_{1p1}x_H \\ &- 12g_{11p}g'g_2^2 x_H - 12g_1 g_{1p1}g_2^2 x_H + 48g_{11p}g'\lambda_1 x_H + 48g_1 g_{1p1}\lambda_1 x_H + 6g_1^2 g'^2 x_H^2 \\ &+ 18g_{11p}^2 g'^2 x_H^2 + 24g_1 g_{11p}g'g_{1p1}x_H^2 + 18g_1^2 g_{1p1}^2 x_H^2 + 6g_{11p}^2 g_{1p1}^2 x_H^2 + 6g'^2 g_2^2 x_H^2 \\ &+ 6g_{1p1}^2 g_2^2 x_H^2 - 24g'^2\lambda_1 x_H^2 - 24g_{1p1}^2\lambda_1 x_H^2 - 12g_{11p}g'^3 x_H^3 - 12g_1 g'^2 g_{1p1}x_H^3 \\ &- 12g_{11p}g'g_{1p1}^2 x_H^3 - 12g_1 g_{1p1}^3 x_H^3 + 3g'^4 x_H^4 + 6g'^2 g_{1p1}^2 x_H^4 + 3g_{1p1}^4 x_H^4 + 96\lambda_1 y_t^2 \\ &+ 32\lambda_1 \mathrm{Tr}[Y_\nu Y_\nu^\dagger] - 48y_t^4 - 16\mathrm{Tr}[Y_\nu Y_\nu^\dagger Y_\nu Y_\nu^\dagger]\Big)\end{aligned} \tag{B.21}$$

$$\beta_{\lambda_2} = \frac{1}{16\pi^2}\Big(10\lambda_2^2 + \lambda_3^2 - 6g'^2\lambda_2 x_\Phi^2 - 6g_{1p1}^2\lambda_2 x_\Phi^2 + 3g'^4 x_\Phi^4 + 2\lambda_2\mathrm{Tr}[y_{NS}y_{NS}^\dagger] - \mathrm{Tr}[y_{NS}y_{NS}^\dagger y_{NS}y_{NS}^\dagger]\Big) \tag{B.22}$$

$$\beta_{\lambda_3} = \frac{1}{16\pi^2}\frac{1}{2}\Big(- 3g_1^2\lambda_3 - 3g_{11p}^2\lambda_3 - 9g_2^2\lambda_3 + 24\lambda_1\lambda_3 + 16\lambda_2\lambda_3 + 8\lambda_3^2 + 6g_{11p}g'\lambda_3 x_H + 6g1g_{1p1}\lambda_3 x_H - 3g'^2\lambda_3 x_H^2 - 3g_{1p1}^2\lambda_3 x_H^2 + 6g_{11p}^2 g'^2 x_\Phi^2 - 12g'^2\lambda_3 x_\Phi^2 - 12g_{1p1}^2\lambda_3 x_\Phi^2 - 12g_{11p}g'^3 x_H x_\Phi^2 + 6g'^4 x_H^2 x_\Phi^2 + 12\lambda_3 y_t^2 + 4\lambda_3 \mathrm{Tr}[Y_\nu Y_\nu^\dagger] + 4\lambda_3 \mathrm{Tr}[y_{NS}y_{NS}^\dagger] - 8\mathrm{Tr}[y_{NS}y_{NS}^\dagger Y_\nu Y_\nu^\dagger]\Big) \tag{B.23}$$

$$\beta_{y_t} = \frac{1}{16\pi^2}\frac{1}{12}\Big(- (\Big(17g_1^2 + 17g_{11p}^2 + 27g_2^2 + 96g_3^2 + 34g_{11p}g'x_H + 34g1g_{1p1}x_H + 17g'^2x_H^2 + 17g_{1p1}^2x_H^2 + 20g_{11p}g'x_\Phi + 20g1g_{1p1}x_\Phi + 20g'^2x_Hx_\Phi + 20g_{1p1}^2x_Hx_\Phi + 8g'^2x_\Phi^2 + 8g_{1p1}^2x_\Phi^2 - 36y_t^2 - 12\mathrm{Tr}[Y_\nu Y_\nu^\dagger]\Big)y_t) + 18(y_t^3)\Big) \tag{B.24}$$

$$\beta_{y_{NS}} = \frac{1}{16\pi^2}\Big(\Big(- 3(g'^2 + g_{1p1}^2)x_\Phi^2 + \mathrm{Tr}[y_{NS}y_{NS}^\dagger]\Big)y_{NS} + y_{NS}y_{NS}^\dagger y_{NS} + Y_\nu^T Y_\nu^* y_{NS}\Big) \tag{B.25}$$

$$\beta_{Y_\nu} = \frac{1}{16\pi^2}\frac{1}{4}\Big(- (\Big(3g_1^2 + 3g_{11p}^2 + 9g_2^2 + 6g_{11p}g'x_H + 6g1g_{1p1}x_H + 3g'^2x_H^2 + 3g_{1p1}^2x_H^2 + 12g_{11p}g'x_\Phi + 12g1g_{1p1}x_\Phi + 12g'^2x_Hx_\Phi + 12g_{1p1}^2x_Hx_\Phi + 24g'^2x_\Phi^2 + 24g_{1p1}^2x_\Phi^2 - 12y_t^2 - 4\mathrm{Tr}[Y_\nu Y_\nu^\dagger]\Big)Y\nu) + 2(3Y\nu Y_\nu^\dagger Y_\nu + Y_\nu y_{NS}^* y_{NS}^T)\Big) \tag{B.26}$$

Bibliography

[1] Wikipedia, *Standard Model — Wikipedia, the free encyclopedia,* http://en.wikipedia.org/w/index.php?title=Standard%20Model&oldid=916336382 (2019). [Online; accessed 22-September-2019].

[2] Wikipedia, *Dark matter — Wikipedia, the free encyclopedia,* http://en.wikipedia.org/w/index.php?title=Dark%20matter&oldid=916765182 (2019). [Online; accessed 22-September-2019].

[3] X. Cui *et al.*, *Dark Matter Results From 54-Ton-Day Exposure of PandaX-II Experiment,* Phys. Rev. Lett. **119**, 181302 (2017).

[4] E. Aprile *et al.*, *First Dark Matter Search Results from the XENON1T Experiment,* Phys. Rev. Lett. **119**, 181301 (2017).

[5] G. Aad *et al.*, *Search for high-mass dilepton resonances using 139 fb^{-1} of pp collision data collected at $\sqrt{s}$ =13 TeV with the ATLAS detector,* (2019).

[6] S. L. Glashow, *Partial Symmetries of Weak Interactions,* Nucl. Phys. **22**, 579–588 (1961).

[7] S. Weinberg, *A Model of Leptons,* Phys. Rev. Lett. **19**, 1264–1266 (1967).

[8] A. Salam, *Weak and Electromagnetic Interactions,* Conf. Proc. **C680519**, 367–377 (1968).

[9] S. Chatrchyan *et al.*, *Observation of a new boson at a mass of 125 GeV with the CMS experiment at the LHC,* Phys. Lett. **B716**, 30–61 (2012).

[10] G. Aad *et al.*, *Observation of a new particle in the search for the Standard Model Higgs boson with the ATLAS detector at the LHC,* Phys. Lett. **B716**, 1–29 (2012).

[11] P. W. Higgs, *Broken symmetries, massless particles and gauge fields,* Phys. Lett. **12**, 132–133 (1964).

[12] P. W. Higgs, *Broken Symmetries and the Masses of Gauge Bosons,* Phys. Rev. Lett. **13**, 508–509 (1964). [,160(1964)].

[13] F. Englert and R. Brout, *Broken Symmetry and the Mass of Gauge Vector Mesons,* Phys. Rev. Lett. **13**, 321–323 (1964). [,157(1964)].

[14] G. S. Guralnik, C. R. Hagen, and T. W. B. Kibble, *Global Conservation Laws and Massless Particles,* Phys. Rev. Lett. **13**, 585–587 (1964). [,162(1964)].

[15] M. Gell-Mann, *Isotopic Spin and New Unstable Particles,* Phys. Rev. **92**, 833–834 (1953).

[16] K. Nishijima, *Charge Independence Theory of V Particles,* Prog. Theor. Phys. **13**, 285–304 (1955).

[17] Y. Nambu, *Axial vector current conservation in weak interactions,* Phys. Rev. Lett. **4**, 380–382 (1960). [,107(1960)].

[18] Y. Nambu and G. Jona-Lasinio, *Dynamical Model of Elementary Particles Based on an Analogy with Superconductivity. 1.* Phys. Rev. **122**, 345–358 (1961). [,127(1961)].

[19] J. Goldstone, *Field Theories with Superconductor Solutions,* Nuovo Cim. **19**, 154–164 (1961).

[20] J. Goldstone, A. Salam, and S. Weinberg, *Broken Symmetries,* Phys. Rev. **127**, 965–970 (1962).

[21] C. Wu, E. Ambler, R. Hayward, D. Hoppes, and R. Hudson, *EXPERIMENTAL TEST OF PARITY CONSERVATION IN BETA DECAY,* Phys.Rev. **105**, 1413–1414 (1957).

[22] B. Pontecorvo, *Mesonium and anti-mesonium,* Sov. Phys. JETP **6**, 429 (1957). [Zh. Eksp. Teor. Fiz.33,549(1957)].

[23] B. Pontecorvo, *Inverse beta processes and nonconservation of lepton charge,* Sov. Phys. JETP **7**, 172–173 (1958). [Zh. Eksp. Teor. Fiz.34,247(1957)].

[24] Z. Maki, M. Nakagawa, and S. Sakata, *Remarks on the unified model of elementary particles,* Prog. Theor. Phys. **28**, 870–880 (1962). [,34(1962)].

[25] L. Wolfenstein, *Neutrino Oscillations in Matter,* Phys. Rev. **D17**, 2369–2374 (1978). [,294(1977)].

[26] S. P. Mikheyev and A. Yu. Smirnov, *Resonance Amplification of Oscillations in Matter and Spectroscopy of Solar Neutrinos,* Sov. J. Nucl. Phys. **42**, 913–917 (1985). [,305(1986)].

[27] S. P. Mikheev and A. Yu. Smirnov, *Resonant amplification of neutrino oscillations in matter and solar neutrino spectroscopy,* Nuovo Cim. **C9**, 17–26 (1986).

[28] B. T. Cleveland, T. Daily, R. Davis, Jr., J. R. Distel, K. Lande, C. K. Lee, P. S. Wildenhain, and J. Ullman, *Measurement of the solar electron neutrino flux with the Homestake chlorine detector,* Astrophys. J. **496**, 505–526 (1998).

[29] P. Anselmann *et al.*, *Solar neutrinos observed by GALLEX at Gran Sasso.* Phys. Lett. **B285**, 376–389 (1992).

[30] J. N. Abdurashitov *et al.*, *Results from SAGE,* Phys. Lett. **B328**, 234–248 (1994).

[31] M. Altmann *et al.*, *Complete results for five years of GNO solar neutrino observations,* Phys. Lett. **B616**, 174–190 (2005).

[32] Y. Fukuda *et al.*, *Solar neutrino data covering solar cycle 22,* Phys. Rev. Lett. **77**, 1683–1686 (1996).

[33] Y. Fukuda *et al.*, *Evidence for oscillation of atmospheric neutrinos,* Phys.Rev.Lett. **81**, 1562–1567 (1998).

[34] Y. Ashie *et al.*, *Evidence for an oscillatory signature in atmospheric neutrino oscillation,* Phys.Rev.Lett. **93**, 101801 (2004).

[35] Q. Ahmad *et al.*, *Direct evidence for neutrino flavor transformation from neutral current interactions in the Sudbury Neutrino Observatory,* Phys.Rev.Lett. **89**, 011301 (2002).

[36] B. Aharmim *et al.*, *Electron energy spectra, fluxes, and day-night asymmetries of B-8 solar neutrinos from measurements with NaCl dissolved in the heavy-water detector at the Sudbury Neutrino Observatory,* Phys. Rev. **C72**, 055502 (2005).

[37] J. N. Bahcall and M. H. Pinsonneault, *What do we (not) know theoretically about solar neutrino fluxes?* Phys. Rev. Lett. **92**, 121301 (2004).

[38] K. Eguchi *et al.*, *First results from KamLAND: Evidence for reactor anti-neutrino disappearance,* Phys.Rev.Lett. **90**, 021802 (2003).

[39] T. Araki *et al.*, *Measurement of neutrino oscillation with KamLAND: Evidence of spectral distortion,* Phys. Rev. Lett. **94**, 081801 (2005).

[40] D. Casper *et al.*, *Measurement of atmospheric neutrino composition with IMB-3,* Phys. Rev. Lett. **66**, 2561–2564 (1991).

[41] R. Becker-Szendy *et al.*, *The Electron-neutrino and muon-neutrino content of the atmospheric flux,* Phys. Rev. **D46**, 3720–3724 (1992).

[42] M. H. Ahn *et al.*, *Measurement of Neutrino Oscillation by the K2K Experiment,* Phys. Rev. **D74**, 072003 (2006).

[43] D. Michael *et al.*, *Observation of muon neutrino disappearance with the MINOS detectors and the NuMI neutrino beam,* Phys.Rev.Lett. **97**, 191801 (2006).

[44] P. Adamson *et al.*, *Measurement of Neutrino Oscillations with the MINOS Detectors in the NuMI Beam,* Phys.Rev.Lett. **101**, 131802 (2008).

[45] P. Adamson *et al.*, *Measurement of the Neutrino Mass Splitting and Flavor Mixing by MINOS,* Phys. Rev. Lett. **106**, 181801 (2011).

[46] K. Abe *et al.*, *First Muon-Neutrino Disappearance Study with an Off-Axis Beam,* Phys.Rev. **D85**, 031103 (2012).

[47] K. Abe *et al.*, *Measurement of Neutrino Oscillation Parameters from Muon Neutrino Disappearance with an Off-axis Beam,* Phys. Rev. Lett. **111**, 211803 (2013).

[48] I. Esteban, M. C. Gonzalez-Garcia, A. Hernandez-Cabezudo, M. Maltoni, and T. Schwetz, *Global analysis of three-flavour neutrino oscillations: synergies and tensions in the determination of $\theta_2 3, \delta_C P$, and the mass ordering,* JHEP **01**, 106 (2019).

[49] P. F. de Salas, D. V. Forero, C. A. Ternes, M. Tortola, and J. W. F. Valle, *Status of neutrino oscillations 2018: 3σ hint for normal mass ordering and improved CP sensitivity,* Phys. Lett. **B782**, 633–640 (2018).

[50] F. Capozzi, E. Di Valentino, E. Lisi, A. Marrone, A. Melchiorri, and A. Palazzo, *Global constraints on absolute neutrino masses and their ordering,* Phys. Rev. **D95**, 096014 (2017).

[51] M. Tanabashi *et al.*, *Review of Particle Physics,* Phys. Rev. **D98**, 030001 (2018).

[52] W. Furry, *On transition probabilities in double beta-disintegration,* Phys.Rev. **56**, 1184–1193 (1939).

[53] V. N. Aseev *et al.*, *An upper limit on electron antineutrino mass from Troitsk experiment,* Phys. Rev. **D84**, 112003 (2011).

[54] C. Kraus *et al.*, *Final results from phase II of the Mainz neutrino mass search in tritium beta decay,* Eur. Phys. J. **C40**, 447–468 (2005).

[55] A. Osipowicz *et al.*, *KATRIN: A Next generation tritium beta decay experiment with sub-eV sensitivity for the electron neutrino mass. Letter of intent,* (2001).

[56] F. Frankle, *KATRIN: An experiment to determine the neutrino mass,* PoS **EPS-HEP2009**, 271 (2009).

[57] N. Aghanim *et al.*, *Planck 2018 results. VI. Cosmological parameters,* (2018).

[58] K. Garrett and G. Duda, *Dark Matter: A Primer,* Adv. Astron. **2011**, 968283 (2011).

[59] M. Lisanti, *Lectures on Dark Matter Physics,* in "Proceedings, Theoretical Advanced Study Institute in Elementary Particle Physics: New Frontiers in Fields and Strings (TASI 2015): Boulder, CO, USA, June 1-26, 2015," (2017), pp. 399–446.

[60] M. Bauer and T. Plehn, *Yet Another Introduction to Dark Matter,* (2017).

[61] I. Tkachev, *Cosmology and Dark Matter,* in "Proceedings, 2016 European School of High-Energy Physics (ESHEP2016): Skeikampen, Norway, June 15-28 2016," , vol. 5 (2017), vol. 5, pp. 259–294.

[62] J. H. Oort, *The force exerted by the stellar system in the direction perpendicular to the galactic plane and some related problems,* Bull. Astron. Inst. Netherlands **6**, 249–287 (1932).

[63] F. Zwicky, *On the Masses of Nebulae and of Clusters of Nebulae,* Astrophysical Journal **86**, 217 (1937).

[64] V. C. Rubin, *On the Masses of Nebulae and of Clusters of Nebulae,* Scientific American (ISSN 0036-8733) **248**, 96–106 (1983).

[65] D. Clowe, M. Bradac, A. H. Gonzalez, M. Markevitch, S. W. Randall, C. Jones, and D. Zaritsky, *A direct empirical proof of the existence of dark matter,* Astrophys. J. **648**, L109–L113 (2006).

[66] V. Silveira and A. Zee, *SCALAR PHANTOMS,* Phys. Lett. **B161**, 136–140 (1985).

[67] J. McDonald, *Gauge singlet scalars as cold dark matter,* Phys. Rev. **D50**, 3637–3649 (1994).

[68] C. P. Burgess, M. Pospelov, and T. ter Veldhuis, *The Minimal model of nonbaryonic dark matter: A Singlet scalar,* Nucl. Phys. **B619**, 709–728 (2001).

[69] G. Jungman, M. Kamionkowski, and K. Griest, *Supersymmetric dark matter,* Phys. Rept. **267**, 195–373 (1996).

[70] L. Delle Rose, S. Khalil, S. J. D. King, S. Kulkarni, C. Marzo, S. Moretti, and C. S. Un, *Sneutrino Dark Matter, Constraints and Perspectives,* (2018).

[71] W. Buchmuller, *Gravitino Dark Matter,* AIP Conf. Proc. **1200**, 155–164 (2010).

[72] J. L. Feng, *Dark Matter Candidates from Particle Physics and Methods of Detection,* Ann. Rev. Astron. Astrophys. **48**, 495–545 (2010).

[73] Y. Hochberg, E. Kuflik, T. Volansky, and J. G. Wacker, *Mechanism for Thermal Relic Dark Matter of Strongly Interacting Massive Particles,* Phys. Rev. Lett. **113**, 171301 (2014).

[74] L. D. Duffy and K. van Bibber, *Axions as Dark Matter Particles,* New J. Phys. **11**, 105008 (2009).

[75] T. D. Brandt, *Constraints on MACHO Dark Matter from Compact Stellar Systems in Ultra-Faint Dwarf Galaxies,* Astrophys. J. **824**, L31 (2016).

[76] H.-C. Cheng, J. L. Feng, and K. T. Matchev, *Kaluza-Klein dark matter,* Phys. Rev. Lett. **89**, 211301 (2002).

[77] V. A. Mitsou, *Dark matter: experimental and observational status,* in "15th Marcel Grossmann Meeting on Recent Developments in Theoretical and Experimental General Relativity, Astrophysics, and Relativistic Field Theories (MG15) Rome, Italy, July 1-7, 2018," (2019).

[78] J. Liu, X. Chen, and X. Ji, *Current status of direct dark matter detection experiments,* Nature Phys. **13**, 212–216 (2017).

[79] M. Schumann, *Direct Detection of WIMP Dark Matter: Concepts and Status,* (2019).

[80] D. S. Akerib *et al.*, *Results from a search for dark matter in the complete LUX exposure,* Phys. Rev. Lett. **118**, 021303 (2017).

[81] R. Bernabei *et al.*, *First results from DAMA/LIBRA and the combined results with DAMA/NaI,* Eur. Phys. J. **C56**, 333–355 (2008).

[82] J. M. Gaskins, *A review of indirect searches for particle dark matter,* Contemp. Phys. **57**, 496–525 (2016).

[83] W. B. Atwood *et al.*, *The large area telescope on the fermi gamma-ray space telescope mission,* .

[84] M. G. Aartsen *et al.*, *Search for neutrinos from decaying dark matter with Ice-Cube,* Eur. Phys. J. **C78**, 831 (2018).

[85] J. D. Bowman, A. E. E. Rogers, R. A. Monsalve, T. J. Mozdzen, and N. Mahesh, *An absorption profile centred at 78 megahertz in the sky-averaged spectrum,* Nature **555**, 67–70 (2018).

[86] V. A. Mitsou, *Shedding Light on Dark Matter at Colliders,* Int. J. Mod. Phys. **A28**, 1330052 (2013).

[87] V. A. Mitsou, *Overview of searches for dark matter at the LHC,* J. Phys. Conf. Ser. **651**, 012023 (2015).

[88] S. Weinberg, *Baryon- and lepton-nonconserving processes,* Phys. Rev. Lett. **43**, 1566–1570 (1979).

[89] P. Minkowski, *mu $\to$ e gamma at a Rate of One Out of 1-Billion Muon Decays?* Phys.Lett. **B67**, 421 (1977).

[90] M. Gell-Mann, P. Ramond, and R. Slansky, Proc.Supergravity Workshop pp. 315–318 (1979).

[91] T. Yanagida, Workshop on Unified Theory and Baryon Number in the Universe pp. 95–98 (1979).

[92] R. N. Mohapatra and G. Senjanovic, *Neutrino Mass and Spontaneous Parity Violation,* Phys.Rev.Lett. **44**, 912 (1980).

[93] J. Schechter and J. Valle, *Neutrino Masses in SU(2) x U(1) Theories,* Phys.Rev. **D22**, 2227 (1980).

[94] J. Schechter and J. Valle, *Neutrino Decay and Spontaneous Violation of Lepton Number,* Phys.Rev. **D25**, 774 (1982).

[95] G. Lazarides, Q. Shafi, and C. Wetterich, *Proton Lifetime and Fermion Masses in an SO(10) Model,* Nucl.Phys. **B181**, 287 (1981).

[96] R. N. Mohapatra and G. Senjanovic, *Neutrino Masses and Mixings in Gauge Models with Spontaneous Parity Violation,* Phys.Rev. **D23**, 165 (1981).

[97] R. Foot, H. Lew, X. He, and G. C. Joshi, *SEESAW NEUTRINO MASSES INDUCED BY A TRIPLET OF LEPTONS,* Z.Phys. **C44**, 441 (1989).

[98] G. Senjanovic, *Neutrino mass: From LHC to grand unification,* Riv. Nuovo Cim. **34**, 1–68 (2011).

[99] A. Broncano, M. Gavela, and E. E. Jenkins, *The Effective Lagrangian for the seesaw model of neutrino mass and leptogenesis,* Phys.Lett. **B552**, 177–184 (2003).

[100] Z.-z. Xing and S. Zhou, *Why is the 3 x 3 neutrino mixing matrix almost unitary in realistic seesaw models?* HEPNP **30**, 828–832 (2006).

[101] W. Grimus and L. Lavoura, *The Seesaw mechanism at arbitrary order: Disentangling the small scale from the large scale,* JHEP **0011**, 042 (2000).

[102] F. F. Freitas, C. A. de S. Pires, and P. S. Rodrigues da Silva, *Inverse type II seesaw mechanism and its signature at the LHC and ILC,* Phys. Lett. **B769**, 48–56 (2017).

[103] A. Abada, C. Biggio, F. Bonnet, M. B. Gavela, and T. Hambye, *mu —¿ e gamma and tau —¿ l gamma decays in the fermion triplet seesaw model,* Phys. Rev. **D78**, 033007 (2008).

[104] G. 't Hooft, C. Itzykson, A. Jaffe, H. Lehmann, P. K. Mitter, I. M. Singer, and R. Stora, *Recent Developments in Gauge Theories. Proceedings, Nato Advanced Study Institute, Cargese, France, August 26 - September 8, 1979,* NATO Sci. Ser. B **59**, pp.1–438 (1980).

[105] R. Mohapatra and J. Valle, *Neutrino Mass and Baryon Number Nonconservation in Superstring Models,* Phys.Rev. **D34**, 1642 (1986).

[106] P.-H. Gu and U. Sarkar, *Leptogenesis with Linear, Inverse or Double Seesaw,* Phys.Lett. **B694**, 226–232 (2010).

[107] H. Zhang and S. Zhou, *The Minimal Seesaw Model at the TeV Scale,* Phys.Lett. **B685**, 297–301 (2010).

[108] M. Hirsch, S. Morisi, and J. Valle, *A4-based tri-bimaximal mixing within inverse and linear seesaw schemes,* Phys.Lett. **B679**, 454–459 (2009).

[109] R. N. Mohapatra, *Mechanism for Understanding Small Neutrino Mass in Superstring Theories,* Phys. Rev. Lett. **56**, 561–563 (1986).

[110] S. K. Kang and C. Kim, *Extended double seesaw model for neutrino mass spectrum and low scale leptogenesis,* Phys.Lett. **B646**, 248–252 (2007).

[111] L.-J. Hu, S. Dulat, and A. Ablat, *Neutrino masses and flavor mixing in the Extended Double Seesaw Model with two texture zeros,* Eur.Phys.J. **C71**, 1772 (2011).

[112] P. B. Dev and A. Pilaftsis, *Minimal Radiative Neutrino Mass Mechanism for Inverse Seesaw Models,* Phys.Rev. **D86**, 113001 (2012).

[113] M. Goeppert-Mayer, *Double beta-disintegration,* Phys. Rev. **48**, 512–516 (1935).

[114] S. R. Elliott, A. A. Hahn, and M. K. Moe, *Direct Evidence for Two Neutrino Double Beta Decay in* ^{82}Se*,* Phys. Rev. Lett. **59**, 2020–2023 (1987). [,989(1987)].

[115] M. Doi, T. Kotani, and E. Takasugi, *Double beta Decay and Majorana Neutrino,* Prog. Theor. Phys. Suppl. **83**, 1 (1985).

[116] W. C. Haxton and G. J. Stephenson, *Double beta Decay,* Prog. Part. Nucl. Phys. **12**, 409–479 (1984).

[117] A. Gando *et al.*, *Search for Majorana Neutrinos near the Inverted Mass Hierarchy Region with KamLAND-Zen,* Phys. Rev. Lett. **117**, 082503 (2016). [Addendum: Phys. Rev. Lett.117,no.10,109903(2016)].

[118] S. T. Petcov, H. Sugiyama, and Y. Takanishi, *Neutrinoless Double Beta Decay and H+- +- —¿ l-prime+- l+- Decays in the Higgs Triplet Model,* Phys. Rev. **D80**, 015005 (2009).

[119] A. Ibarra, E. Molinaro, and S. Petcov, *TeV Scale See-Saw Mechanisms of Neutrino Mass Generation, the Majorana Nature of the Heavy Singlet Neutrinos and* $(\beta\beta)_{0\nu}$*-Decay,* JHEP **1009**, 108 (2010).

[120] M. Blennow, E. Fernandez-Martinez, J. Lopez-Pavon, and J. Menendez, *Neutrinoless double beta decay in seesaw models,* JHEP **07**, 096 (2010).

[121] S. M. Bilenky, A. Faessler, W. Potzel, and F. Simkovic, *Neutrinoless double-beta decay and seesaw mechanism,* Eur. Phys. J. **C71**, 1754 (2011).

[122] M. Mitra, G. Senjanovic, and F. Vissani, *Neutrinoless Double Beta Decay and Heavy Sterile Neutrinos,* Nucl.Phys. **B856**, 26–73 (2012).

[123] J. Lopez-Pavon, E. Molinaro, and S. T. Petcov, *Radiative Corrections to Light Neutrino Masses in Low Scale Type I Seesaw Scenarios and Neutrinoless Double Beta Decay,* JHEP **11**, 030 (2015).

[124] V. Tello, M. Nemevsek, F. Nesti, G. Senjanovic, and F. Vissani, *Left-Right Symmetry: from LHC to Neutrinoless Double Beta Decay,* Phys.Rev.Lett. **106**, 151801 (2011).

[125] J. Chakrabortty, H. Z. Devi, S. Goswami, and S. Patra, *Neutrinoless double-*β *decay in TeV scale Left-Right symmetric models,* JHEP **1208**, 008 (2012).

[126] J. Barry and W. Rodejohann, *Lepton number and flavour violation in TeV-scale left-right symmetric theories with large left-right mixing,* JHEP **09**, 153 (2013).

[127] P. S. Bhupal Dev, S. Goswami, and M. Mitra, *TeV Scale Left-Right Symmetry and Large Mixing Effects in Neutrinoless Double Beta Decay,* Phys. Rev. **D91**, 113004 (2015).

[128] R. L. Awasthi, P. S. B. Dev, and M. Mitra, *Implications of the Diboson Excess for Neutrinoless Double Beta Decay and Lepton Flavor Violation in TeV Scale Left Right Symmetric Model,* Phys. Rev. **D93**, 011701 (2016).

[129] G. Bambhaniya, P. S. B. Dev, S. Goswami, and M. Mitra, *The Scalar Triplet Contribution to Lepton Flavour Violation and Neutrinoless Double Beta Decay in Left-Right Symmetric Model,* JHEP **04**, 046 (2016).

[130] L. Calibbi and G. Signorelli, *Charged Lepton Flavour Violation: An Experimental and Theoretical Introduction,* Riv. Nuovo Cim. **41**, 71–174 (2018).

[131] R. Coy and M. Frigerio, *Effective approach to lepton observables: the seesaw case,* (2018).

[132] A. M. Baldini *et al.*, *Search for the Lepton Flavour Violating Decay $\mu^+ \to e^+\gamma$ with the Full Dataset of the MEG Experiment,* (2016).

[133] W. H. Bertl *et al.*, *Search for the Decay $\mu^+ \to e^+e^+e^-$,* Nucl. Phys. **B260**, 1–31 (1985).

[134] C. Dohmen *et al.*, *Test of lepton flavor conservation in mu —¿ e conversion on titanium,* Phys. Lett. **B317**, 631–636 (1993).

[135] W. H. Bertl *et al.*, *A Search for muon to electron conversion in muonic gold,* Eur. Phys. J. **C47**, 337–346 (2006).

[136] J. Casas, J. Espinosa, and M. Quiros, *Improved Higgs mass stability bound in the standard model and implications for supersymmetry,* Phys.Lett. **B342**, 171–179 (1995).

[137] J. Casas, J. Espinosa, and M. Quiros, *Standard model stability bounds for new physics within LHC reach,* Phys.Lett. **B382**, 374–382 (1996).

[138] S. Alekhin, A. Djouadi, and S. Moch, *The top quark and Higgs boson masses and the stability of the electroweak vacuum,* Phys.Lett. **B716**, 214–219 (2012).

[139] D. Buttazzo, G. Degrassi, P. P. Giardino, G. F. Giudice, F. Sala, A. Salvio, and A. Strumia, *Investigating the near-criticality of the Higgs boson,* JHEP **12**, 089 (2013).

[140] G. Isidori, G. Ridolfi, and A. Strumia, *On the metastability of the standard model vacuum,* Nucl.Phys. **B609**, 387–409 (2001).

[141] J. Espinosa, G. Giudice, and A. Riotto, *Cosmological implications of the Higgs mass measurement,* JCAP **0805**, 002 (2008).

[142] P. A. R. Ade *et al.*, *Planck 2015 results. XIII. Cosmological parameters,* Astron. Astrophys. **594**, A13 (2016).

[143] G. Isidori, V. S. Rychkov, A. Strumia, and N. Tetradis, *Gravitational corrections to standard model vacuum decay,* Phys. Rev. **D77**, 025034 (2008).

[144] N. Khan and S. Rakshit, *Study of electroweak vacuum metastability with a singlet scalar dark matter,* Phys. Rev. **D90**, 113008 (2014).

[145] J. A. Casas, V. Di Clemente, A. Ibarra, and M. Quiros, *Massive neutrinos and the Higgs mass window,* Phys. Rev. **D62**, 053005 (2000).

[146] S. Khan, S. Goswami, and S. Roy, *Vacuum Stability constraints on the minimal singlet TeV Seesaw Model,* Phys.Rev. **D89**, 073021 (2014).

[147] W. Rodejohann and H. Zhang, *Impact of massive neutrinos on the higgs self-coupling and electroweak vacuum stability,* Journal of High Energy Physics **2012**, 22 (2012).

[148] J. Chakrabortty, M. Das, and S. Mohanty, *Constraints on TeV scale Majorana neutrino phenomenology from the Vacuum Stability of the Higgs,* Mod. Phys. Lett. **A28**, 1350032 (2013).

[149] A. Datta, A. Elsayed, S. Khalil, and A. Moursy, *Higgs vacuum stability in the $B-L$ extended standard model,* Phys. Rev. **D88**, 053011 (2013).

[150] J. Chakrabortty, P. Konar, and T. Mondal, *Constraining a class of BL extended models from vacuum stability and perturbativity,* Phys. Rev. **D89**, 056014 (2014).

[151] A. Kobakhidze and A. Spencer-Smith, *Neutrino Masses and Higgs Vacuum Stability,* JHEP **08**, 036 (2013).

[152] L. Delle Rose, C. Marzo, and A. Urbano, *On the stability of the electroweak vacuum in the presence of low-scale seesaw models,* (2015).

[153] G. Bambhaniya, P. S. Bhupal Dev, S. Goswami, S. Khan, and W. Rodejohann, *Naturalness, Vacuum Stability and Leptogenesis in the Minimal Seesaw Model,* Phys. Rev. **D95**, 095016 (2017).

[154] G. Bambhaniya, S. Khan, P. Konar, and T. Mondal, *Constraints on a seesaw model leading to quasidegenerate neutrinos and signatures at the LHC,* Phys. Rev. **D91**, 095007 (2015).

[155] M. Lindner, H. H. Patel, and B. Radovi, *Electroweak Absolute, Meta-, and Thermal Stability in Neutrino Mass Models,* (2015).

[156] F. F. Deppisch, P. S. Bhupal Dev, and A. Pilaftsis, *Neutrinos and Collider Physics,* New J. Phys. **17**, 075019 (2015).

[157] A. Pilaftsis, *Radiatively induced neutrino masses and large Higgs neutrino couplings in the standard model with Majorana fields,* Z.Phys. **C55**, 275–282 (1992).

[158] S. Bray, J. S. Lee, and A. Pilaftsis, *Resonant CP violation due to heavy neutrinos at the LHC,* Nucl.Phys. **B786**, 95–118 (2007).

[159] A. Atre, T. Han, S. Pascoli, and B. Zhang, *The Search for Heavy Majorana Neutrinos,* JHEP **0905**, 030 (2009).

[160] W.-Y. Keung and G. Senjanovic, *Majorana Neutrinos and the Production of the Right-handed Charged Gauge Boson,* Phys.Rev.Lett. **50**, 1427 (1983).

[161] A. Datta, M. Guchait, and A. Pilaftsis, *Probing lepton number violation via majorana neutrinos at hadron supercolliders,* Phys. Rev. **D50**, 3195–3203 (1994).

[162] F. M. L. Almeida, Jr., Y. do Amaral Coutinho, J. A. Martins Simoes, and M. A. B. do Vale, *On a signature for heavy Majorana neutrinos in hadronic collisions,* Phys. Rev. **D62**, 075004 (2000).

[163] O. Panella, M. Cannoni, C. Carimalo, and Y. N. Srivastava, *Signals of heavy Majorana neutrinos at hadron colliders,* Phys. Rev. **D65**, 035005 (2002).

[164] T. Han and B. Zhang, *Signatures for Majorana neutrinos at hadron colliders,* Phys.Rev.Lett. **97**, 171804 (2006).

[165] F. del Aguila, J. Aguilar-Saavedra, and R. Pittau, *Heavy neutrino signals at large hadron colliders,* JHEP **0710**, 047 (2007).

[166] F. del Aguila and J. Aguilar-Saavedra, *Distinguishing seesaw models at LHC with multi-lepton signals,* Nucl.Phys. **B813**, 22–90 (2009).

[167] A. Akeroyd and M. Aoki, *Single and pair production of doubly charged Higgs bosons at hadron colliders,* Phys.Rev. **D72**, 035011 (2005).

[168] T. Han, B. Mukhopadhyaya, Z. Si, and K. Wang, *Pair production of doubly-charged scalars: Neutrino mass constraints and signals at the LHC,* Phys.Rev. **D76**, 075013 (2007).

[169] A. Akeroyd, M. Aoki, and H. Sugiyama, *Probing Majorana Phases and Neutrino Mass Spectrum in the Higgs Triplet Model at the CERN LHC,* Phys.Rev. **D77**, 075010 (2008).

[170] P. Fileviez Perez, T. Han, G.-y. Huang, T. Li, and K. Wang, *Neutrino Masses and the CERN LHC: Testing Type II Seesaw,* Phys.Rev. **D78**, 015018 (2008).

[171] A. G. Akeroyd and C.-W. Chiang, *Doubly charged Higgs bosons and three-lepton signatures in the Higgs Triplet Model,* Phys. Rev. **D80**, 113010 (2009).

[172] A. G. Akeroyd, C.-W. Chiang, and N. Gaur, *Leptonic signatures of doubly charged Higgs boson production at the LHC,* JHEP **11**, 005 (2010).

[173] A. Melfo, M. Nemevsek, F. Nesti, G. Senjanovic, and Y. Zhang, *Type II Seesaw at LHC: The Roadmap,* Phys.Rev. **D85**, 055018 (2012).

[174] H. Sugiyama, K. Tsumura, and H. Yokoya, *Discrimination of models including doubly charged scalar bosons by using tau lepton decay distributions,* Phys. Lett. **B717**, 229–234 (2012).

[175] F. del guila and M. Chala, *LHC bounds on Lepton Number Violation mediated by doubly and singly-charged scalars,* JHEP **03**, 027 (2014).

[176] C.-H. Chen and T. Nomura, *Search for $\delta^{\pm\pm}$ with new decay patterns at the LHC,* Phys. Rev. **D91**, 035023 (2015).

[177] Z.-L. Han, R. Ding, and Y. Liao, *LHC Phenomenology of Type II Seesaw: Non-degenerate Case,* Phys. Rev. **D91**, 093006 (2015).

[178] B. Bajc and G. Senjanovic, *Seesaw at LHC,* JHEP **0708**, 014 (2007).

[179] B. Bajc, M. Nemevsek, and G. Senjanovic, *Probing seesaw at LHC,* Phys.Rev. **D76**, 055011 (2007).

[180] R. Franceschini, T. Hambye, and A. Strumia, *Type-III see-saw at LHC,* Phys.Rev. **D78**, 033002 (2008).

[181] T. Li and X.-G. He, *Neutrino Masses and Heavy Triplet Leptons at the LHC: Testability of Type III Seesaw,* Phys. Rev. **D80**, 093003 (2009).

[182] P. Bandyopadhyay, S. Choi, E. J. Chun, and K. Min, *Probing Higgs bosons via the type III seesaw mechanism at the LHC,* Phys. Rev. **D85**, 073013 (2012).

[183] O. J. P. Eboli, J. Gonzalez-Fraile, and M. C. Gonzalez-Garcia, *Neutrino Masses at LHC: Minimal Lepton Flavour Violation in Type-III See-saw,* JHEP **12**, 009 (2011).

[184] F. von der Pahlen, G. Palacio, D. Restrepo, and O. Zapata, *Radiative Type III Seesaw Model and its collider phenomenology,* Phys. Rev. **D94**, 033005 (2016).

[185] R. Ruiz, *QCD Corrections to Pair Production of Type III Seesaw Leptons at Hadron Colliders,* JHEP **12**, 165 (2015).

[186] G. Bambhaniya, S. Goswami, S. Khan, P. Konar, and T. Mondal, *Looking for hints of a reconstructible seesaw model at the Large Hadron Collider,* Phys.Rev. **D91**, 075007 (2015).

[187] N. Haba, S. Matsumoto, and K. Yoshioka, *Observable Seesaw and its Collider Signatures,* Phys. Lett. **B677**, 291–295 (2009).

[188] C.-Y. Chen and P. S. B. Dev, *Multi-Lepton Collider Signatures of Heavy Dirac and Majorana Neutrinos,* Phys. Rev. **D85**, 093018 (2012).

[189] A. Das and N. Okada, *Inverse seesaw neutrino signatures at the LHC and ILC,* Phys. Rev. **D88**, 113001 (2013).

[190] P. Bandyopadhyay, E. J. Chun, H. Okada, and J.-C. Park, *Higgs Signatures in Inverse Seesaw Model at the LHC,* JHEP **01**, 079 (2013).

[191] A. Das, P. S. Bhupal Dev, and N. Okada, *Direct bounds on electroweak scale pseudo-Dirac neutrinos from* $\sqrt{s} = 8$ *TeV LHC data,* Phys. Lett. **B735**, 364–370 (2014).

[192] A. Das and N. Okada, *Improved bounds on the heavy neutrino productions at the LHC,* Phys. Rev. **D93**, 033003 (2016).

[193] S. Mondal and S. K. Rai, *Probing the Heavy Neutrinos of Inverse Seesaw Model at the LHeC,* Phys. Rev. **D94**, 033008 (2016).

[194] A. Das, P. Konar, and S. Majhi, *Production of Heavy neutrino in next-to-leading order QCD at the LHC and beyond,* JHEP **06**, 019 (2016).

[195] A. S. Barabash, *Double Beta Decay: Historical Review of 75 Years of Research,* Phys. Atom. Nucl. **74**, 603–613 (2011).

[196] O. G. Miranda, M. A. Tortola, and J. W. F. Valle, *Are solar neutrino oscillations robust?* JHEP **10**, 008 (2006).

[197] F. J. Escrihuela, O. G. Miranda, M. A. Tortola, and J. W. F. Valle, *Constraining nonstandard neutrino-quark interactions with solar, reactor and accelerator data,* Phys. Rev. **D80**, 105009 (2009). [Erratum: Phys. Rev.D80,129908(2009)].

[198] Y. Farzan and M. Tortola, *Neutrino oscillations and Non-Standard Interactions,* Front.in Phys. **6**, 10 (2018).

[199] P. Bakhti and Y. Farzan, *Shedding light on LMA-Dark solar neutrino solution by medium baseline reactor experiments: JUNO and RENO-50,* JHEP **07**, 064 (2014).

[200] P. Coloma and T. Schwetz, *Generalized mass ordering degeneracy in neutrino oscillation experiments,* Phys. Rev. **D94**, 055005 (2016).

[201] K. N. Deepthi, S. Goswami, and N. Nath, *Can nonstandard interactions jeopardize the hierarchy sensitivity of DUNE?* Phys. Rev. **D96**, 075023 (2017).

[202] M. C. Gonzalez-Garcia and M. Maltoni, *Determination of matter potential from global analysis of neutrino oscillation data,* JHEP **09**, 152 (2013).

[203] P. Coloma, P. B. Denton, M. C. Gonzalez-Garcia, M. Maltoni, and T. Schwetz, *Curtailing the Dark Side in Non-Standard Neutrino Interactions,* JHEP **04**, 116 (2017).

[204] P. Coloma, M. C. Gonzalez-Garcia, M. Maltoni, and T. Schwetz, *COHERENT Enlightenment of the Neutrino Dark Side,* Phys. Rev. **D96**, 115007 (2017).

[205] P. B. Denton, Y. Farzan, and I. M. Shoemaker, *Testing large non-standard neutrino interactions with arbitrary mediator mass after COHERENT data,* JHEP **07**, 037 (2018).

[206] I. Esteban, M. C. Gonzalez-Garcia, M. Maltoni, I. Martinez-Soler, and J. Salvado, *Updated Constraints on Non-Standard Interactions from Global Analysis of Oscillation Data,* JHEP **08**, 180 (2018).

[207] L. Cardani, *Neutrinoless Double Beta Decay Overview,* SciPost Phys. Proc. **1**, 024 (2019).

[208] M. Agostini *et al.*, *Improved Limit on Neutrinoless Double-β Decay of ^{76}Ge from GERDA Phase II,* Phys. Rev. Lett. **120**, 132503 (2018).

[209] S. A. Kharusi *et al.*, *nEXO Pre-Conceptual Design Report,* (2018).

[210] C. Alduino *et al.*, *First Results from CUORE: A Search for Lepton Number Violation via $0\nu\beta\beta$ Decay of ^{130}Te,* Phys. Rev. Lett. **120**, 132501 (2018).

[211] R. Arnold *et al.*, *Probing New Physics Models of Neutrinoless Double Beta Decay with SuperNEMO,* Eur. Phys. J. **C70**, 927–943 (2010).

[212] P. P. Povinec, *Background constrains of the SuperNEMO experiment for neutrinoless double beta-decay searches,* Nucl. Instrum. Meth. **A845**, 398–403 (2017).

[213] M. Agostini, G. Benato, and J. Detwiler, *Discovery probability of next-generation neutrinoless double- decay experiments,* Phys. Rev. **D96**, 053001 (2017).

[214] J. Engel and J. Menndez, *Status and Future of Nuclear Matrix Elements for Neutrinoless Double-Beta Decay: A Review,* Rept. Prog. Phys. **80**, 046301 (2017).

[215] J. Kotila and F. Iachello, *Phase space factors for double-β decay,* Phys. Rev. **C85**, 034316 (2012).

[216] S. Pascoli and S. T. Petcov, *The SNO solar neutrino data, neutrinoless double beta decay and neutrino mass spectrum,* Phys. Lett. **B544**, 239–250 (2002).

[217] S. Goswami and W. Rodejohann, *Constraining mass spectra with sterile neutrinos from neutrinoless double beta decay, tritium beta decay and cosmology,* Phys. Rev. **D73**, 113003 (2006).

[218] J. Barry, W. Rodejohann, and H. Zhang, *Light Sterile Neutrinos: Models and Phenomenology,* JHEP **07**, 091 (2011).

[219] J. T. Penedo and S. T. Petcov, *The 10^3 eV frontier in neutrinoless double beta decay,* Phys. Lett. **B786**, 410–417 (2018).

[220] F. Vissani, *Do experiments suggest a hierarchy problem?* Phys. Rev. **D57**, 7027–7030 (1998).

[221] J. A. Casas, J. R. Espinosa, and I. Hidalgo, *Implications for new physics from fine-tuning arguments. 1. Application to SUSY and seesaw cases,* JHEP **11**, 057 (2004).

[222] A. Abada, C. Biggio, F. Bonnet, M. Gavela, and T. Hambye, *Low energy effects of neutrino masses,* JHEP **0712**, 061 (2007).

[223] M. Farina, D. Pappadopulo, and A. Strumia, *A modified naturalness principle and its experimental tests,* JHEP **08**, 022 (2013).

[224] J. D. Clarke, R. Foot, and R. R. Volkas, *Electroweak naturalness in the three-flavor type I seesaw model and implications for leptogenesis,* Phys.Rev. **D91**, 073009 (2015).

[225] M. Fabbrichesi and A. Urbano, *Naturalness redux: The case of the neutrino seesaw mechanism,* Phys. Rev. **D92**, 015028 (2015).

[226] J. D. Clarke, R. Foot, and R. R. Volkas, *Natural leptogenesis and neutrino masses with two Higgs doublets,* Phys. Rev. **D92**, 033006 (2015).

[227] M. Chabab, M. C. Peyranre, and L. Rahili, *Naturalness in a type II seesaw model and implications for physical scalars,* Phys. Rev. **D93**, 115021 (2016).

[228] N. Haba, H. Ishida, N. Okada, and Y. Yamaguchi, *Vacuum stability and naturalness in type-II seesaw,* Eur. Phys. J. **C76**, 333 (2016).

[229] P. S. B. Dev, C. M. Vila, and W. Rodejohann, *Naturalness in testable type II seesaw scenarios,* Nucl. Phys. **B921**, 436–453 (2017).

[230] J. N. Ng and A. de la Puente, *Electroweak Vacuum Stability and the Seesaw Mechanism Revisited,* Eur. Phys. J. **C76**, 122 (2016).

[231] A. Das, N. Okada, and N. Papapietro, *Electroweak vacuum stability in classically conformal B-L extension of the Standard Model,* Eur. Phys. J. **C77**, 122 (2017).

[232] A. Das, S. Oda, N. Okada, and D.-s. Takahashi, *Classically conformal U(1) extended standard model, electroweak vacuum stability, and LHC Run-2 bounds,* Phys. Rev. **D93**, 115038 (2016).

[233] S. Bhattacharya, P. Ghosh, T. N. Maity, and T. S. Ray, *Mitigating Direct Detection Bounds in Non-minimal Higgs Portal Scalar Dark Matter Models,* (2017).

[234] I. Garg, S. Goswami, V. K. N., and N. Khan, *Electroweak vacuum stability in presence of singlet scalar dark matter in TeV scale seesaw models,* Phys. Rev. **D96**, 055020 (2017).

[235] B. He, N. Okada, and Q. Shafi, *125 GeV Higgs, type III seesaw and gaugeHiggs unification,* Phys. Lett. **B716**, 197–202 (2012).

[236] S. Goswami, K. N. Vishnudath, and N. Khan, *Constraining the minimal type-III seesaw model with naturalness, lepton flavor violation, and electroweak vacuum stability,* Phys. Rev. **D99**, 075012 (2019).

[237] J. Casas and A. Ibarra, *Oscillating neutrinos and muon —¿ e, gamma,* Nucl.Phys. **B618**, 171–204 (2001).

[238] A. Ibarra and G. G. Ross, *Neutrino phenomenology: The Case of two right-handed neutrinos,* Phys.Lett. **B591**, 285–296 (2004).

[239] C. Collaboration, *Search for Type-III Seesaw Heavy Fermions with Multilepton Final States using 2.3/fb of 13 TeV proton-proton Collision Data,* (2016).

[240] G. Aad *et al.*, *Search for type-III Seesaw heavy leptons in pp collisions at $\sqrt{s} = 8$ TeV with the ATLAS Detector,* Phys. Rev. **D92**, 032001 (2015).

[241] G. Altarelli and G. Isidori, *Lower limit on the Higgs mass in the standard model: An Update,* Phys. Lett. **B337**, 141–144 (1994).

[242] J. A. Casas, J. R. Espinosa, M. Quiros, and A. Riotto, *The Lightest Higgs boson mass in the minimal supersymmetric standard model,* Nucl. Phys. **B436**, 3–29 (1995). [Erratum: Nucl. Phys.B439,466(1995)].

[243] M. Quiros, *Constraints on the Higgs boson properties from the effective potential,* (1997).

[244] C. Ford, D. Jones, P. Stephenson, and M. Einhorn, *The Effective potential and the renormalization group,* Nucl.Phys. **B395**, 17–34 (1993).

[245] A. Sirlin and R. Zucchini, *Dependence of the Quartic Coupling H(m) on M(H) and the Possible Onset of New Physics in the Higgs Sector of the Standard Model,* Nucl.Phys. **B266**, 389 (1986).

[246] F. Bezrukov, M. Y. Kalmykov, B. A. Kniehl, and M. Shaposhnikov, *Higgs Boson Mass and New Physics,* JHEP **1210**, 140 (2012).

[247] G. Degrassi, S. Di Vita, J. Elias-Miro, J. R. Espinosa, G. F. Giudice *et al.*, *Higgs mass and vacuum stability in the Standard Model at NNLO,* JHEP **1208**, 098 (2012).

[248] K. Melnikov and T. v. Ritbergen, *The Three loop relation between the MS-bar and the pole quark masses,* Phys.Lett. **B482**, 99–108 (2000).

[249] R. Hempfling and B. A. Kniehl, *On the relation between the fermion pole mass and MS Yukawa coupling in the standard model,* Phys.Rev. **D51**, 1386–1394 (1995).

[250] B. Schrempp and M. Wimmer, *Top quark and Higgs boson masses: Interplay between infrared and ultraviolet physics,* Prog.Part.Nucl.Phys. **37**, 1–90 (1996).

[251] F. Jegerlehner and M. Y. Kalmykov, *O(alpha alpha(s)) correction to the pole mass of the t quark within the standard model,* Nucl.Phys. **B676**, 365–389 (2004).

[252] K. Chetyrkin and M. Zoller, *Three-loop β-functions for top-Yukawa and the Higgs self-interaction in the Standard Model,* JHEP **1206**, 033 (2012).

[253] M. F. Zoller, *Vacuum stability in the SM and the three-loop β-function for the Higgs self-interaction,* Subnucl. Ser. **50**, 557–566 (2014).

[254] K. G. Chetyrkin and M. F. Zoller, *β-function for the Higgs self-interaction in the Standard Model at three-loop level,* JHEP **04**, 091 (2013). [Erratum: JHEP09,155(2013)].

[255] M. Zoller, *Beta-function for the Higgs self-interaction in the Standard Model at three-loop level,* PoS **EPS-HEP2013**, 322 (2013).

[256] J. Chakrabortty, A. Dighe, S. Goswami, and S. Ray, *Renormalization group evolution of neutrino masses and mixing in the Type-III seesaw mechanism,* Nucl.Phys. **B820**, 116–147 (2009).

[257] N. Khan and S. Rakshit, *Constraints on inert dark matter from the metastability of the electroweak vacuum,* Phys. Rev. **D92**, 055006 (2015).

[258] N. Khan, *Exploring Hyperchargeless Higgs Triplet Model up to the Planck Scale,* (2016).

[259] G. Belanger, B. Dumont, U. Ellwanger, J. F. Gunion, and S. Kraml, *Global fit to Higgs signal strengths and couplings and implications for extended Higgs sectors,* Phys. Rev. **D88**, 075008 (2013).

[260] G. Aad *et al.*, *Constraints on new phenomena via Higgs boson couplings and invisible decays with the ATLAS detector,* JHEP **11**, 206 (2015).

[261] V. Khachatryan *et al.*, *Searches for invisible decays of the Higgs boson in pp collisions at sqrt(s) = 7, 8, and 13 TeV,* JHEP **02**, 135 (2017).

[262] R. Dick, R. B. Mann, and K. E. Wunderle, *Cosmic rays through the Higgs portal,* Nucl. Phys. **B805**, 207–230 (2008).

[263] C. E. Yaguna, *Gamma rays from the annihilation of singlet scalar dark matter,* JCAP **0903**, 003 (2009).

[264] Y. Cai, X.-G. He, and B. Ren, *Low Mass Dark Matter and Invisible Higgs Width In Darkon Models,* Phys. Rev. **D83**, 083524 (2011).

[265] A. Urbano and W. Xue, *Constraining the Higgs portal with antiprotons,* JHEP **03**, 133 (2015).

[266] A. Cuoco, B. Eiteneuer, J. Heisig, and M. Krmer, *A global fit of the γ-ray galactic center excess within the scalar singlet Higgs portal model,* JCAP **1606**, 050 (2016).

[267] V. Barger, P. Langacker, M. McCaskey, M. J. Ramsey-Musolf, and G. Shaughnessy, *LHC Phenomenology of an Extended Standard Model with a Real Scalar Singlet,* Phys. Rev. **D77**, 035005 (2008).

[268] K. Cheung, P. Ko, J. S. Lee, and P.-Y. Tseng, *Bounds on Higgs-Portal models from the LHC Higgs data,* JHEP **10**, 057 (2015).

[269] A. Djouadi, O. Lebedev, Y. Mambrini, and J. Quevillon, *Implications of LHC searches for Higgs–portal dark matter,* Phys. Lett. **B709**, 65–69 (2012).

[270] M. Endo and Y. Takaesu, *Heavy WIMP through Higgs portal at the LHC,* Phys. Lett. **B743**, 228–234 (2015).

[271] H. Han, J. M. Yang, Y. Zhang, and S. Zheng, *Collider Signatures of Higgs-portal Scalar Dark Matter,* Phys. Lett. **B756**, 109–112 (2016).

[272] P. Ko and H. Yokoya, *Search for Higgs portal DM at the ILC,* JHEP **08**, 109 (2016).

[273] Y. Mambrini, *Higgs searches and singlet scalar dark matter: Combined constraints from XENON 100 and the LHC,* Phys. Rev. **D84**, 115017 (2011).

[274] K. Cheung, Y.-L. S. Tsai, P.-Y. Tseng, T.-C. Yuan, and A. Zee, *Global Study of the Simplest Scalar Phantom Dark Matter Model,* JCAP **1210**, 042 (2012).

[275] J. M. Cline, K. Kainulainen, P. Scott, and C. Weniger, *Update on scalar singlet dark matter,* Phys. Rev. **D88**, 055025 (2013). [Erratum: Phys. Rev.D92,no.3,039906(2015)].

[276] F. S. Queiroz, K. Sinha, and A. Strumia, *Leptoquarks, Dark Matter, and Anomalous LHC Events,* Phys. Rev. **D91**, 035006 (2015).

[277] F. S. Queiroz and K. Sinha, *The Poker Face of the Majoron Dark Matter Model: LUX to keV Line,* Phys. Lett. **B735**, 69–74 (2014).

[278] P. Athron *et al.*, *Status of the scalar singlet dark matter model,* (2017).

[279] M. Gonderinger, Y. Li, H. Patel, and M. J. Ramsey-Musolf, *Vacuum Stability, Perturbativity, and Scalar Singlet Dark Matter,* JHEP **01**, 053 (2010).

[280] J. Elias-Miro, J. R. Espinosa, G. F. Giudice, H. M. Lee, and A. Strumia, *Stabilization of the Electroweak Vacuum by a Scalar Threshold Effect,* JHEP **06**, 031 (2012).

[281] C.-S. Chen and Y. Tang, *Vacuum stability, neutrinos, and dark matter,* JHEP **04**, 019 (2012).

[282] N. Haba, K. Kaneta, and R. Takahashi, *Planck scale boundary conditions in the standard model with singlet scalar dark matter,* JHEP **04**, 029 (2014).

[283] S. Ghosh, A. Kundu, and S. Ray, *Potential of a singlet scalar enhanced Standard Model,* Phys. Rev. **D93**, 115034 (2016).

[284] H. Davoudiasl, R. Kitano, T. Li, and H. Murayama, *The New minimal standard model,* Phys. Lett. **B609**, 117–123 (2005).

[285] W. Chao, M. Gonderinger, and M. J. Ramsey-Musolf, *Higgs Vacuum Stability, Neutrino Mass, and Dark Matter,* Phys. Rev. **D86**, 113017 (2012).

[286] S. Bhattacharya, S. Jana, and S. Nandi, *Neutrino Masses and Scalar Singlet Dark Matter,* Phys. Rev. **D95**, 055003 (2017).

[287] P. Ghosh, A. K. Saha, and A. Sil, *Study of Electroweak Vacuum Stability from Extended Higgs Portal of Dark Matter and Neutrinos,* (2017).

[288] M. Gavela, T. Hambye, D. Hernandez, and P. Hernandez, *Minimal Flavour Seesaw Models,* JHEP **0909**, 038 (2009).

[289] R. N. Lerner and J. McDonald, *Gauge singlet scalar as inflaton and thermal relic dark matter,* Phys. Rev. **D80**, 123507 (2009).

[290] M. Gonderinger, H. Lim, and M. J. Ramsey-Musolf, *Complex Scalar Singlet Dark Matter: Vacuum Stability and Phenomenology,* Phys. Rev. **D86**, 043511 (2012).

[291] M. Holthausen, K. S. Lim, and M. Lindner, *Planck scale Boundary Conditions and the Higgs Mass,* JHEP **1202**, 037 (2012).

[292] L. N. Mihaila, J. Salomon, and M. Steinhauser, *Gauge Coupling Beta Functions in the Standard Model to Three Loops,* Phys.Rev.Lett. **108**, 151602 (2012).

[293] T. E. Clark, B. Liu, S. T. Love, and T. ter Veldhuis, *The Standard Model Higgs Boson-Inflaton and Dark Matter,* Phys. Rev. **D80**, 075019 (2009).

[294] S. Antusch, J. Kersten, M. Lindner, and M. Ratz, *Neutrino mass matrix running for nondegenerate seesaw scales,* Phys.Lett. **B538**, 87–95 (2002).

[295] F. Staub, *SARAH 4 : A tool for (not only SUSY) model builders,* Comput. Phys. Commun. **185**, 1773–1790 (2014).

[296] S. Antusch and O. Fischer, *Probing the nonunitarity of the leptonic mixing matrix at the CEPC,* Int. J. Mod. Phys. **A31**, 1644006 (2016).

[297] P. Achard *et al.*, *Search for heavy isosinglet neutrino in e^+e^- annihilation at LEP,* Phys.Lett. **B517**, 67–74 (2001).

[298] O. Adriani *et al.*, *Search for isosinglet neutral heavy leptons in Z0 decays,* Phys.Lett. **B295**, 371–382 (1992).

[299] P. Abreu *et al.*, *Search for neutral heavy leptons produced in Z decays,* Z.Phys. **C74**, 57–71 (1997).

[300] M. Z. Akrawy *et al.*, *Limits on neutral heavy lepton production from Z0 decay,* Phys. Lett. **B247**, 448–457 (1990).

[301] A. M. Sirunyan *et al.*, *Search for heavy neutral leptons in events with three charged leptons in proton-proton collisions at $\sqrt{s} = 13$ TeV,* Phys. Rev. Lett. **120**, 221801 (2018).

[302] G. Cynolter, E. Lendvai, and G. Pocsik, *Note on unitarity constraints in a model for a singlet scalar dark matter candidate,* Acta Phys. Polon. **B36**, 827–832 (2005).

[303] B. W. Lee, C. Quigg, and H. B. Thacker, *Weak Interactions at Very High-Energies: The Role of the Higgs Boson Mass,* Phys. Rev. **D16**, 1519 (1977).

[304] Y. Y. P. and Y. C. P., *Modification of the Equivalence Theorem Due to Loop Corrections,* Phys. Rev. **D38**, 2237 (1988).

[305] V. H. G. J., *The Equivalence Theorem,* Phys. Rev. **D41**, 2294 (1990).

[306] H. H. J., *On the precise formulation of equivalence theorem,* Phys. Rev. **D69**, 2619 (1992).

[307] M. Ajello *et al.*, *Fermi-LAT Observations of High-Energy γ-Ray Emission Toward the Galactic Center,* Astrophys. J. **819**, 44 (2016).

[308] A. Alloul, N. D. Christensen, C. Degrande, C. Duhr, and B. Fuks, *FeynRules 2.0 - A complete toolbox for tree-level phenomenology,* Comput. Phys. Commun. **185**, 2250–2300 (2014).

[309] G. Belanger, F. Boudjema, P. Brun, A. Pukhov, S. Rosier-Lees, P. Salati, and A. Semenov, *Indirect search for dark matter with micrOMEGAs2.4,* Comput. Phys. Commun. **182**, 842–856 (2011).

[310] G. Belanger, F. Boudjema, A. Pukhov, and A. Semenov, *$micrOMEGAs_3$: A program for calculating dark matter observables,* Comput. Phys. Commun. **185**, 960–985 (2014).

[311] W. T. V. W. H. Press, S. A. Teukolsky and B. P. Flannery, *Numerical Recipes in Fortran 90, Second Edition* (Cambridge Univ, 1996).

[312] C. Coriano, L. Delle Rose, and C. Marzo, *Vacuum Stability in U(1)-Prime Extensions of the Standard Model with TeV Scale Right Handed Neutrinos,* Phys. Lett. **B738**, 13–19 (2014).

[313] C. Coriano, L. Delle Rose, and C. Marzo, *Constraints on abelian extensions of the Standard Model from two-loop vacuum stability and $U(1)_{B-L}$,* JHEP **02**, 135 (2016).

[314] E. Accomando, C. Coriano, L. Delle Rose, J. Fiaschi, C. Marzo, and S. Moretti, *Z, Higgses and heavy neutrinos in U(1) models: from the LHC to the GUT scale,* JHEP **07**, 086 (2016).

[315] S. Oda, N. Okada, and D.-s. Takahashi, *Classically conformal U(1) extended standard model and Higgs vacuum stability,* Phys. Rev. **D92**, 015026 (2015).

[316] T. Basak and T. Mondal, *Constraining Minimal $U(1)_{B-L}$ model from Dark Matter Observations,* Phys. Rev. **D89**, 063527 (2014).

[317] S. Oda, N. Okada, and D.-s. Takahashi, *Right-handed neutrino dark matter in the classically conformal U(1) extended standard model,* Phys. Rev. **D96**, 095032 (2017).

[318] W. Rodejohann and C. E. Yaguna, *Scalar dark matter in the BL model,* JCAP **1512**, 032 (2015).

[319] J. Cao, L. Feng, X. Guo, L. Shang, F. Wang, and P. Wu, *Scalar dark matter interpretation of the DAMPE data with U(1) gauge interactions,* Phys. Rev. **D97**, 095011 (2018).

[320] S. Singirala, R. Mohanta, and S. Patra, *Singlet scalar Dark matter in $U(1)_{B-L}$ models without right-handed neutrinos,* Eur. Phys. J. Plus **133**, 477 (2018).

[321] P. Langacker, *Grand Unified Theories and Proton Decay,* Phys.Rept. **72**, 185 (1981).

[322] J. L. Hewett and T. G. Rizzo, *Low-Energy Phenomenology of Superstring Inspired E(6) Models,* Phys. Rept. **183**, 193 (1989).

[323] L. Basso, A. Belyaev, S. Moretti, and C. H. Shepherd-Themistocleous, *Phenomenology of the minimal B-L extension of the Standard model: Z' and neutrinos,* Phys. Rev. **D80**, 055030 (2009).

[324] E. Accomando, L. Delle Rose, S. Moretti, E. Olaiya, and C. H. Shepherd-Themistocleous, *Extra Higgs boson and Z as portals to signatures of heavy neutrinos at the LHC,* JHEP **02**, 109 (2018).

[325] M. Aaboud *et al.*, *Search for high-mass new phenomena in the dilepton final state using proton-proton collisions at $\sqrt{s} = 13$ TeV with the ATLAS detector,* Phys. Lett. **B761**, 372–392 (2016).

[326] V. Khachatryan *et al.*, *Search for narrow resonances in dilepton mass spectra in proton-proton collisions at $\sqrt{s}$ = 13 TeV and combination with 8 TeV data,* Phys. Lett. **B768**, 57–80 (2017).

[327] A. Das, S. Goswami, V. K. N., and T. Nomura, *Constraining a general U(1)$'$ inverse seesaw model from vacuum stability, dark matter and collider,* (2019).

[328] J. Chakrabortty, P. Konar, and T. Mondal, *Copositive Criteria and Boundedness of the Scalar Potential,* Phys. Rev. **D89**, 095008 (2014).

[329] H. Huffel and G. Pocsik, *Unitarity Bounds on Higgs Boson Masses in the Weinberg-Salam Model With Two Higgs Doublets,* Z. Phys. **C8**, 13 (1981).

[330] M. Duerr, F. Kahlhoefer, K. Schmidt-Hoberg, T. Schwetz, and S. Vogl, *How to save the WIMP: global analysis of a dark matter model with two s-channel mediators,* JHEP **09**, 042 (2016).

[331] G. Blanger, F. Boudjema, A. Pukhov, and A. Semenov, *micrOMEGAs4.1: two dark matter candidates,* Comput. Phys. Commun. **192**, 322–329 (2015).

[332] P. Langacker, *The Physics of Heavy Z' Gauge Bosons,* Rev. Mod. Phys. **81**, 1199–1228 (2009).

[333] S. R. Coleman and E. J. Weinberg, *Radiative Corrections as the Origin of Spontaneous Symmetry Breaking,* Phys. Rev. **D7**, 1888–1910 (1973).

[334] A. Zee, *Quantum field theory in a nutshell* (2003).

List of Publications

Thesis related Publications

1. I. Garg, S. Goswami,**Vishnudath K. N.** and N. Khan,
   Electroweak vacuum stability in presence of singlet scalar dark matter in TeV scale seesaw models
   Phys. Rev. D **96**, 055020 (2017). arXiv:1706.08851

2. S. Goswami,**Vishnudath K. N.** and N. Khan,
   Constraining the minimal type-III seesaw model with naturalness, lepton flavor violation, and electroweak vacuum stability
   Phys. Rev. D **99**, 075012 (2019). arXiv:1810.11687

3. **Vishnudath K. N.**, S. Choubey and S. Goswami,
   A New Sensitivity Goal for Neutrino-less Double Beta Decay Experiments
   arXiv:1901.04313 (Accepted for publication in Phys. Rev. D)

4. Arindam Das, Srubabati Goswami, **Vishnudath K. N.** and Takaaki Nomura,
   Constraining a general $U(1)$ inverse seesaw model from vacuum stability, dark matter and collider
   arXiv:1905.00201 (Submitted to Phys. Rev. D)

Publication attached with thesis

1. I. Garg, S. Goswami,**Vishnudath K. N.**, and N. Khan,
   Electroweak vacuum stability in presence of singlet scalar dark matter in TeV scale seesaw models
   Phys. Rev. D **96**, 055020 (2017). arXiv:1706.08851

PHYSICAL REVIEW D **96,** 055020 (2017)

Electroweak vacuum stability in presence of singlet scalar dark matter in TeV scale seesaw models

Ila Garg,[1,2,*] Srubabati Goswami,[2,†] K. N. Vishnudath,[2,3,‡] and Najimuddin Khan[2,§]

[1]*Department of Physics, Indian Institute of Technology Bombay, Powai, Mumbai 400 076, India*
[2]*Theoretical Physics Division, Physical Research Laboratory, Ahmedabad 380009, India*
[3]*Discipline of Physics, Indian Institute of Technology, Gandhinagar 382355, India*

(Received 5 July 2017; published 15 September 2017)

We consider singlet extensions of the standard model, both in the fermion and in the scalar sector, to account for the generation of neutrino mass at the TeV scale and the existence of dark matter, respectively. For the neutrino sector we consider models with extra singlet fermions that can generate neutrino mass via the so-called inverse or linear seesaw mechanism, whereas a singlet scalar is introduced as the candidate for dark matter. We show that although these two sectors are disconnected at low energy, the coupling constants of both the sectors get correlated at the high-energy scale by the constraints coming from the perturbativity and stability/metastability of the electroweak vacuum. The singlet fermions try to destabilize the electroweak vacuum while the singlet scalar aids the stability. As an upshot, the electroweak vacuum may attain absolute stability even up to the Planck scale for suitable values of the parameters. We delineate the parameter space for the singlet fermion and the scalar couplings for which the electroweak vacuum remains stable/metastable and at the same time gives the correct relic density and neutrino masses and mixing angles as observed.

DOI: 10.1103/PhysRevD.96.055020

I. INTRODUCTION

The Large Hadron Collider (LHC) experiment has completed the hunt for the last missing piece of the Standard Model (SM) with the discovery of the Higgs boson [1,2]. The Higgs boson holds a special status in the SM as it gives mass to all the other particles, with the exception of the neutrino. However, observation of neutrino oscillation from solar, atmospheric, reactor, and accelerator experiments necessitates the extension of the SM to incorporate small neutrino masses. The seesaw mechanism is considered to be the most elegant way to generate small neutrino masses. The origin of the seesaw is from the dimension-five effective operator $\kappa LLHH$, proposed by Weinberg in [3]. Here, L and H are the SM lepton and Higgs fields, respectively. κ is a coupling constant with inverse mass dimension. This term violates the lepton number by two units and implies that neutrinos are Majorana particles. The generation of the effective dimension-five operator needs extension of the SM by new particles. The most minimal scenario in this respect is the canonical type-1 seesaw model, in which the SM is extended by heavy right-handed Majorana neutrinos for ultraviolet completion of the theory [4–7]. The essence of the seesaw mechanism lies in the fact that the lepton number is explicitly violated at a high-energy scale that defines the scale of the new physics. However, to get an observed neutrino mass of the order of $m_\nu \sim 0.01$ eV one needs the Majorana neutrinos to be very heavy ($\sim 10^{15}$ GeV), close to the scale of grand unification. However, since such high scales are not accessible to colliders, in the context of the LHC, there have been a proliferation of studies involving TeV scale seesaw models. For recent reviews see, for instance, [8,9]. For an ordinary seesaw mechanism, lowering the scale of new physics to TeV requires small Yukawa couplings $\mathcal{O}(10^{-6})$,[1] and for such values, the light-heavy mixing is small and no interesting collider signals can be studied. One of the ways to reduce the scale of new physics to TeV is to decouple the new physics scale from the scale of lepton number violation. The smallness of the neutrino mass can then be attributed to small lepton number violating terms. A tiny value of the latter is deemed natural, since when this parameter is zero, the global U(1) lepton number symmetry is reinstated and neutrinos are massless. One of the most popular TeV scale seesaw models based on the above idea is the inverse seesaw model [13]. This contains additional singlet states (ν_s), along with the right-handed neutrinos (N_R), having opposite lepton numbers. The lepton number is broken softly by introducing a small Majorana mass term for the singlets. This parameter is responsible for the smallness of the neutrino mass, and one does not require small Yukawa couplings to get observed neutrino masses;

*ila.garg@iitb.ac.in
†sruba@prl.res.in
‡vishnudath@prl.res.in
§najimuddin@prl.res.in

[1]Unless very special textures leading to cancellations are invoked [10–12].

at the same time the scale of new physics can be at TeV. Another possibility of a TeV scale singlet seesaw model is the linear seesaw model [14–16]. In this case, a small lepton number violating term is generated by the coupling between the left-handed neutrinos and the singlet states. Thus, the inverse seesaw and the linear seesaw differ from each other in the way lepton number violation is introduced in the model, as we will see in the next section. Also, the particle content of the minimal models that agree with the oscillation data for these two are different. For the linear seesaw, we need only one N_R and one ν_s [17–19], whereas in the inverse seesaw case, we need two N_R and two ν_s [20]. Note that the minimal linear seesaw model is the simplest reconstructable TeV scale seesaw model having a minimum number of independent parameters.

Apart from the neutrino mass, another issue that requires extension of the SM is the existence of dark matter (DM). Measurements by Planck and WMAP demonstrate that nearly 85% of the Universe's matter density is dark [21]. Among the various models of dark matter that are proposed in the literature, the most minimal renormalizable extension of the SM is the so-called Higgs portal models [22–24]. These models include a scalar singlet that couples only to the Higgs. An additional Z_2 symmetry is imposed to prevent the decay of the DM and safeguard its stability. The coupling of the singlet with the Higgs provides the only portal for its interaction with the SM. Nevertheless, there can be testable consequences of this scenario that can put constraints on its coupling and mass. These include constraints from searches of invisible decay of Higgs at the LHC [25–27], direct and indirect detections of DM as well as compliance with the observed relic density [28–33]. Implications for the LHC [34–38] and ILC [39] have also been studied. Combined constraints from all these have been discussed in [40–44] and most recently in [45].

The singlet Higgs can also affect the stability of the electroweak (EW) vacuum [46–51]. It is well known that the electroweak vacuum in the standard model is metastable and the Higgs quartic coupling λ is pulled down to negative value by renormalization group running, at an energy of about 10^9–10^{10} GeV, depending on the value of α_s and the top quark mass m_t, as the dominant contribution comes from the top-Yukawa coupling, y_t [52,53]. This indicates the existence of another low lying vacuum. If the quartic coupling $\lambda(\mu)$ becomes negative at large renormalization scale μ, it implies that in the early universe the Higgs potential would be unbounded from below and the vacuum would be unstable in that era. But it does not pose any threat to the standard model as it has been shown that the decay time is greater than the age of the universe [54]. In the context of the standard model extended with neutrino masses via the canonical type-1 seesaw mechanism, the Yukawa coupling of the RH neutrinos also contributes to the RG running, just as y_t, and thereby we expect it to affect the electroweak vacuum stability negatively. But this effect is not so much because, as discussed before, in order to get the light neutrino masses, either one has to resort to extremely small Yukawa couplings or one needs a very large Majorana mass scale ($\approx 10^{15}$ GeV) and the contribution to the running of λ is much smaller in both cases compared to that from y_t. However, for the TeV scale seesaw models with sizable Yukawa couplings, the stability of the vacuum can be altered considerably by the contribution from the neutrinos [18,55–63]. On the other hand, the singlet scalar can help in stabilizing the electroweak vacuum by adding a positive contribution that prevents the Higgs quartic coupling from becoming negative. The stability of the electroweak vacuum in the context of the singlet scalar extended SM with an unbroken Z_2 symmetry has been explored in [46,48–50].

In this paper, we extend the SM by adding extra fermion as well as scalar singlets to explain the origin of neutrino mass as well as the existence of dark matter.[2] The candidate for dark matter is a real singlet scalar added to SM with an additional Z_2 symmetry that ensures its stability. For generation of neutrino mass at the TeV scale we consider two models. The first one is the general inverse seesaw model with three right-handed neutrinos and three additional singlets. The second one is the minimal linear seesaw model. These two sectors are disconnected at low energy. However, the consideration of the stability of the electroweak vacuum and perturbativity induces a correlation between the two sectors. We study the stability of the electroweak vacuum in this model and explore the effect of the two opposing trends—singlet fermions trying to destabilize the vacuum further and singlet Higgs trying to oppose this. We find the parameter space, which is consistent with the constraints of relic density and neutrino oscillation data and at the same time can cure the instability of the electroweak vacuum. We present some benchmark points for which the electroweak vacuum is stable up to Planck's scale. In addition to absolute stability, we also explore the parameter region that gives metastability in the context of this model. We investigate the combined effect of these two sectors and obtain the allowed parameter space consistent with observations and vacuum stability/metastability and perturbativity.

The plan of the paper is as follows. In the next section we discuss the TeV scale singlet seesaw models, in particular, the inverse seesaw and linear seesaw mechanism. We also outline the diagonalization procedure to give the low-energy neutrino mass matrix. In Sec. III we discuss the potential in the presence of a singlet scalar. Section IV presents the effective Higgs potential and the renormalization group (RG) evolution of the different couplings. In particular, we include the contribution from both fermion

[2]For other studies including neutrino mass, dark matter, and/or vacuum stability analysis using scalar singlets see, for instance, [64–67].

and scalar singlets in the effective potential. In Sec. V we discuss the existing constraints on the fermion and the scalar sector couplings from experimental observations and also from perturbativity. We present the results in Sec. VI and the conclusions in Sec. VII.

II. TEV SCALE SINGLET SEESAW MODELS

The most general low scale singlet seesaw scenario consists of adding m right-handed neutrinos N_R and n gauge-singlet sterile neutrinos ν_s to the standard model. The lepton number for ν_s is chosen to be -1 and that for N_R is $+1$. For simplicity, we will work in a basis where the charged leptons are identified with their mass eigenstates. We can write the most general Yukawa part of the Lagrangian responsible for neutrino masses, before spontaneous symmetry breaking as

$$-L_\nu = \bar{l}_L Y_\nu H^c N_R + \bar{l}_L Y_s H^c \nu_s + \overline{N_R^c} M_R \nu_s + \frac{1}{2}\overline{\nu_s^c} M_\mu \nu_s + \frac{1}{2}\overline{N_R^c} M_N N_R + \text{H.c.}, \tag{2.1}$$

where l_L and H are the lepton and the Higgs doublets, respectively; Y_ν and Y_s are the Yukawa coupling matrices; M_N and M_μ are the symmetric Majorana mass matrices for N_R and ν_s, respectively; and Y_ν, Y_s, M_N, and M_μ are of dimensions $3\times m$, $3\times n$, $m\times m$, and $n\times n$, respectively.

Now, after symmetry breaking, the above equation gives

$$-L_{\text{mass}} = \bar{\nu}_L M_D N_R + \bar{\nu}_L M_s \nu_s + \overline{N_R^c} M_R \nu_s + \frac{1}{2}\overline{\nu_s^c} M_\mu \nu_s + \frac{1}{2}\overline{N_R^c} M_N N_R + \text{H.c.}, \tag{2.2}$$

where $M_D = Y_\nu\langle H\rangle$ and $M_s = Y_s\langle H\rangle$. The neutral fermion mass matrix M can be defined as

$$-L_{\text{mass}} = \frac{1}{2}(\bar{\nu}_L \overline{N_R^c}\,\overline{\nu_s^c}) \begin{pmatrix} 0 & M_D & M_s \\ M_D^T & M_N & M_R \\ M_s^T & M_R^T & M_\mu \end{pmatrix} \begin{pmatrix} \nu_L^c \\ N_R \\ \nu_s \end{pmatrix} + \text{H.c.} \tag{2.3}$$

From this equation, we can get the variants of the singlet seesaw scenarios by setting certain terms to be zero.

A. Inverse seesaw model

In the inverse seesaw model (ISM), M_s and M_N are taken to be zero [13]. The mass scales of the three submatrices of M may naturally have a hierarchy $M_R \gg M_D \gg M_\mu$, because the mass term M_R is not subject to the $SU(2)_L$ symmetry breaking and the mass term M_μ violates the lepton number. Thus we can take M_μ to be naturally small by 't Hooft's naturalness criteria since the expected degree of lepton number violation in nature is very small. In this paper, we consider a $(3+3+3)$ scenario for the inverse seesaw model for generality, and hence all the three submatrices M_R, M_D, and M_μ are 3×3 matrices. The effective light neutrino mass matrix in the seesaw approximation is given by

$$M_{\text{light}} = M_D (M_R^T)^{-1} M_\mu M_R^{-1} M_D^T, \tag{2.4}$$

and in the heavy sector, we will have three pairs of degenerate pseudo-Dirac neutrinos of masses of the order $\sim M_R \pm M_\mu$. Note that the smallness of M_{light} is naturally attributed to the smallness of both M_μ and $\frac{M_D}{M_R}$. For instance, $M_{\text{light}} \sim \mathcal{O}(0.1)$ eV can easily be achieved for $\frac{M_D}{M_R} \sim 10^{-2}$ and $M_\mu \sim \mathcal{O}(1)$ keV. Thus, the seesaw scale can be lowered considerably assuming $Y_\nu \sim \mathcal{O}(0.1)$, such that $M_D \sim 10$ GeV and $M_R \sim 1$ TeV.

B. Minimal linear seesaw model

In Eq. (2.3), if we put M_N and M_μ to be zero and choose the hierarchy $M_R \gg M_D \gg M_s$, we will get the linear seesaw model [14–16]. In this paper, we consider the minimal linear seesaw model (MLSM) in which we add only one right-handed neutrino N_R and one gauge-singlet sterile neutrino ν_s [17–19]. In such a case, the lightest neutrino mass is zero. The source of lepton number violation is through the coupling Y_s, which is assumed to be very small. Here, Y_ν and Y_s are the (3×1) Yukawa coupling matrices, and the overall neutrino mass matrix is a symmetric matrix of dimensions 5×5. The light neutrino mass matrix to the leading order is given by

$$M_{\text{light}} = M_D (M_R^T)^{-1} M_S^T + M_S (M_R^T)^{-1} M_D^T. \tag{2.5}$$

Assuming $M_D \sim 100$ GeV and $M_R \sim 1$ TeV, one needs $Y_s \sim 10^{-11}$ to get light neutrino mass $m_\nu \sim 0.1$ eV. The heavy neutrino sector will consist of a pair of degenerate neutrinos.

C. Diagonalization of the seesaw matrix and nonunitary PMNS matrix

The diagonalization procedure is the same for both cases. Here we illustrate it for the inverse seesaw case. The 9×9 inverse seesaw mass matrix can be rewritten as

$$M_\nu = \begin{pmatrix} 0 & \hat{M}_D \\ \hat{M}_D^T & \hat{M}_R \end{pmatrix}, \tag{2.6}$$

where $\hat{M}_D = (M_D \quad 0)$ and $\hat{M}_R = \left(\begin{smallmatrix} 0 & M_R \\ M_R^T & M_\mu \end{smallmatrix}\right)$. We can diagonalize the neutrino mass matrix using a 9×9 unitary matrix [68,69],

$$U_0^T M_\nu U = M_\nu^{\text{diag}}, \tag{2.7}$$

where $M_\nu^{\rm diag} = {\rm diag}(m_1, m_2, m_3, M_1, \ldots, M_6)$ with mass eigenvalues $m_i (i = 1, 2, 3)$ and $M_j (j = 1, \ldots, 6)$ for three light neutrinos and six heavy neutrinos, respectively. Following the two-step diagonalization procedure, U_0 could be expressed as [by keeping terms up to order $\mathcal{O}(\hat{M}_D^2/\hat{M}_R^2)$] [69]

$$U_0 = WT = \begin{pmatrix} U_L & V \\ S & U_H \end{pmatrix} = \begin{pmatrix} (1 - \frac{1}{2}\epsilon)U_\nu & \hat{M}_D^*(\hat{M}_R^{-1})^* U_R \\ -\hat{M}_R^{-1}\hat{M}_D^T U_\nu & (1 - \frac{1}{2}\epsilon')U_R \end{pmatrix}. \tag{2.8}$$

Here, U_L, V, S, and U_H are 3×3, 3×6, 6×3, and 6×6 matrices, respectively, which are not unitary. W is the matrix that brings the full 9×9 neutrino matrix, in the block diagonal form,

$$W^T \begin{pmatrix} 0 & \hat{M}_D \\ \hat{M}_D^T & \hat{M}_R \end{pmatrix} W = \begin{pmatrix} M_{\rm light} & 0 \\ 0 & M_{\rm heavy} \end{pmatrix}, \tag{2.9}$$

$T = {\rm diag}(U_\nu, U_R)$ diagonalizes the mass matrices in the light and heavy sectors appearing in the upper and lower blocks of the block diagonal matrix, respectively. In the seesaw limit, $M_{\rm light}$ is given by Eq. (2.4) and $M_{\rm heavy} = \hat{M}_R$. In Eq. (2.8), U_L corresponds to the Pontecorvo–Maki–Nakagawa–Sakata (PMNS) matrix that acquires a nonunitary correction $(1 - \frac{\epsilon}{2})$. The parameters ϵ and ϵ' characterize the nonunitarity and are given by

$$\epsilon = \hat{M}_D^* \hat{M}_R^{-1*} \hat{M}_R^{-1} \hat{M}_D^T, \tag{2.10}$$

$$\epsilon' = \hat{M}_R^{-1} \hat{M}_D^T \hat{M}_D^* \hat{M}_R^{-1*}. \tag{2.11}$$

III. SCALAR POTENTIAL OF THE MODEL

As mentioned earlier, in addition to the extra fermions, we also add an extra real scalar singlet S to the standard model. The potential for the scalar sector with an extra Z_2 symmetry under $S \to -S$ is given by

$$V(S, H) = -m^2 H^\dagger H + \lambda (H^\dagger H)^2 + \frac{\kappa}{2} H^\dagger H S^2 + \frac{m_S^2}{2} S^2 + \frac{\lambda_S}{24} S^4. \tag{3.1}$$

In this model, we take the vacuum expectation value (VEV) of S as 0, so that Z_2 symmetry is not broken. The standard model scalar doublet H could be written as

$$H = \frac{1}{\sqrt{2}} \begin{pmatrix} G^+ \\ v + h + iG^0 \end{pmatrix}, \tag{3.2}$$

where the VEV $v = 246$ GeV.

Thus, the scalar sector consists of two particles h and S, where h is the standard model Higgs boson with a mass of $\sim$126 GeV, and the mass of the extra scalar is given by

$$M_{\rm DM}^2 = {m_S}^2 + \frac{\kappa}{2} v^2. \tag{3.3}$$

As the Z_2 symmetry is unbroken up to the Planck scale $M_{pl} = 1.22 \times 10^{19}$ GeV, the potential can have minima only along the Higgs field direction, and also this symmetry prevents the extra scalar from acquiring a vacuum expectation value. This extra scalar field does not mix with the SM Higgs. Also an *odd* number of this extra scalar does not couple to the standard model particles and the new fermions. As a result, this scalar is stable and serves as a viable weakly interacting massive dark matter particle. The scalar field S can annihilate to the SM particles as well as to the new fermions only via the Higgs exchange. So it is called a Higgs portal dark matter.

IV. EFFECTIVE HIGGS POTENTIAL AND RG EVOLUTION OF THE COUPLINGS

The effective Higgs potential and the renormalization group equations are the same for both the linear and the inverse seesaw models. The two models differ only by the way in which a small lepton number violation is introduced in them, whose effect could be neglected in the RG evolution. So, effectively, the renormalization group equations (RGEs) are the same in both the models, the only difference being the dimensions of the Yukawa coupling matrices and the number of heavy neutrinos present in the model.

A. Effective Higgs potential

The tree level Higgs potential in the standard model is given by

$$V(H) = -m^2 H^\dagger H + \lambda (H^\dagger H)^2. \tag{4.1}$$

This will get corrections from higher order loop diagrams of SM particles. In the presence of the extra singlets, the effective potential will get additional contributions from the extra scalar and the fermions. Thus, we have the one-loop effective Higgs potential $[V_1(h)]$ in our model as

$$V_1^{{\rm SM}+S+\nu}(h) = V_1^{\rm SM}(h) + V_1^S(h) + V_1^\nu(h), \tag{4.2}$$

where the one-loop contribution to the effective potential due to the standard model particles is given by [70,71]

$$V_1^{\rm SM}(h) = \sum_i \frac{n_i}{64\pi^2} M_i^4(h) \left[\ln \frac{M_i^2(h)}{\mu^2(t)} - c_i \right]. \tag{4.3}$$

Here, the index i is summed over all SM particles and $c_{H,G,f} = 3/2$ and $c_{W,Z} = 5/6$, where H, G, f, W, and Z

stand for the Higgs boson, the Goldstone boson, fermions, and W and Z bosons, respectively; $M_i(h)$ can be expressed as

$$M_i^2(h) = \kappa_i(t)h^2(t) - \kappa_i'(t).$$

The values of n_i, κ_i, and κ_i' are given in Eq. (4) in [70]. Here $h = h(t)$ denotes the classical value of the Higgs field, t being the dimensionless parameter related to the running energy scale μ as $t = \log(\mu/M_Z)$.

The one-loop contribution due to the extra scalar is given by [72,73]

$$V_1^S(h) = \frac{1}{64\pi^2} M_S^4(h)\left[\ln\frac{M_S^2(h)}{\mu^2(t)} - \frac{3}{2}\right], \tag{4.4}$$

where

$$M_S^2(h) = m_S^2(t) + \kappa(t)h^2(t)/2.$$

The contribution of the extra neutrino Yukawa coupling to the one-loop effective potential can be written as [18,74]

$$V_1^\nu(h) = -\frac{((M'^\dagger M')_{ii})^2}{32\pi^2}\left[\ln\frac{(M'^\dagger M')_{ii}}{\mu^2(t)} - \frac{3}{2}\right] - \frac{((M'M'^\dagger)_{jj})^2}{32\pi^2}\left[\ln\frac{(M'M'^\dagger)_{jj}}{\mu^2(t)} - \frac{3}{2}\right]. \tag{4.5}$$

Here $M' = \frac{Y_\nu}{\sqrt{2}}h$ for inverse seesaw and $M' = (\frac{Y_\nu}{\sqrt{2}}h \frac{Y_s}{\sqrt{2}}h)$ for linear seesaw. Also, i and j run over three light neutrinos and m heavy neutrinos, respectively. In our analysis, we have taken two-loop (one-loop) contributions to the effective potential from the standard model particles (extra singlet scalar and fermions). For $h(t) \gg v$, the effective potential could be approximated as

$$V_{\rm eff}^{\rm SM+S+\nu} = \lambda_{\rm eff}(h)\frac{h^4}{4} \tag{4.6}$$

with

$$\lambda_{\rm eff}(h) = \lambda_{\rm eff}^{\rm SM}(h) + \lambda_{\rm eff}^{S}(h) + \lambda_{\rm eff}^{\nu}(h), \tag{4.7}$$

where the standard model contribution is

$$\lambda_{\rm eff}^{\rm SM}(h) = e^{4\Gamma(h)}[\lambda(\mu = h) + \lambda_{\rm eff}^{(1)}(\mu = h) + \lambda_{\rm eff}^{(2)}(\mu = h)]. \tag{4.8}$$

$\lambda_{\rm eff}^{(1)}$ and $\lambda_{\rm eff}^{(2)}$ are the one- and two-loop contributions, respectively, and their expressions can be found in [53]. The contributions due to the extra scalar and the neutrinos are given by

$$\lambda_{\rm eff}^{S}(h) = e^{4\Gamma(h)}\left[\frac{\kappa^2}{64\pi^2}\left(\ln\frac{\kappa}{2} - \frac{3}{2}\right)\right] \tag{4.9}$$

and

$$\lambda_{\rm eff}^{\nu}(h) = -\frac{e^{4\Gamma(h)}}{32\pi^2}\left[((Y'^\dagger_\nu Y'_\nu)_{ii})^2\left(\ln\frac{(Y'^\dagger_\nu Y'_\nu)_{ii}}{2} - \frac{3}{2}\right) + ((Y'_\nu Y'^\dagger_\nu)_{jj})^2\left(\ln\frac{(Y'_\nu Y'^\dagger_\nu)_{jj}}{2} - \frac{3}{2}\right)\right], \tag{4.10}$$

where

$$\Gamma(h) = \int_{M_t}^{h} \gamma(\mu)d\ln\mu. \tag{4.11}$$

Here $\gamma(\mu)$ is the anomalous dimension of the Higgs field, and in Eq. (4.10), $Y'_\nu = Y_\nu$ for the inverse seesaw and $Y'_\nu = (Y_\nu Y_s)$ for the linear seesaw. The contribution of the singlet scalar to the anomalous dimension is zero [46], and the contribution from the right-handed neutrinos at one loop is given in Eq. (4.19).

B. Renormalization group evolution of the couplings from M_t to $M_{\rm planck}$

We know that the couplings in a quantum field theory get corrections from higher-order loop diagrams and as a result, the couplings run with the renormalization scale. For a coupling C, we have the RGE,

$$\mu\frac{dC}{d\mu} = \sum_i \frac{\beta_C^{(i)}}{(16\pi^2)^i}, \tag{4.12}$$

where i stands for the ith loop.

We have evaluated the SM coupling constants at the top quark mass scale and then run them using the RGEs from m_t to $M_{\rm planck}$. For this, we have taken into account the various threshold corrections at M_t [75–77]. All couplings are expressed in terms of the pole masses [78]. We have used one-loop RGEs to calculate $g_1(M_t)$ and $g_2(M_t)$.[3] For $g_3(M_t)$, we use the three-loop RGE running of α_s where we have neglected the sixth quark contribution and the effect of the top quark has been included using an effective field theory approach. We have also taken the leading term in the four-loop RGE for α_s. The mismatch between the top pole mass and the $\overline{\rm MS}$ renormalized coupling has been included. This is given by

$$y_t(M_t) = \frac{\sqrt{2}M_t}{v}(1 + \delta_t(M_t)), \tag{4.13}$$

where $\delta_t(M_t)$ is the matching correction for y_t at the top pole mass, and similarly for $\lambda(M_t)$ we have

[3]Our results are not changed even if we use the two-loop RGEs for g_1 and g_2.

$$\lambda(M_t) = \frac{M_H^2}{2v^2}(1+\delta_H(M_t)). \tag{4.14}$$

We have included the QCD corrections up to three loops [76], electroweak corrections up to one loop [79,80], and the $O(\alpha\alpha_s)$ corrections to the matching of the top Yukawa and the top pole mass [78,81]. Using these corrections, we have reproduced the couplings at M_t as in Refs. [49,53].

Now to evaluate the couplings from M_t to M_{planck}, we have used three-loop RGEs for standard model couplings [53,82–85], two-loop RGEs for the extra scalar couplings [50,64,86], and one-loop RGEs for the extra neutrino Yukawa couplings [87].[4] The one-loop RGEs for the scalar quartic couplings and the neutrino Yukawa coupling in our model are given as

$$\beta_\lambda = \frac{27}{100}g_1^4 + \frac{9}{10}g_1^2g_2^2 + \frac{9}{4}g_2^4 - \frac{9}{5}g_1^2\lambda - 9g_2^2\lambda + 12\lambda^2 + \kappa^2 + 4T\lambda - 4Y, \tag{4.15}$$

$$\beta_\kappa = -\frac{9}{10}g_1^2\kappa - \frac{9}{2}g_2^2\kappa + 6\lambda\kappa + \lambda_S\kappa + 4\kappa^2 + 2T\kappa, \tag{4.16}$$

$$\beta_{\lambda_S} = 3\lambda_S^2 + 12\kappa^2, \tag{4.17}$$

$$\beta_{Y_\nu} = Y_\nu\left(\frac{3}{2}Y_\nu^\dagger Y_\nu - \frac{3}{2}Y_l^\dagger Y_l + T - \frac{9}{20}g_1^2 - \frac{9}{4}g_2^2\right), \tag{4.18}$$

where

$$T = \mathrm{Tr}(3Y_u^\dagger Y_u + 3Y_d^\dagger Y_d + Y_l^\dagger Y_l + Y_\nu^\dagger Y_\nu),$$
$$Y = \mathrm{Tr}(3(Y_u^\dagger Y_u)^2 + 3(Y_d^\dagger Y_d)^2 + (Y_l^\dagger Y_l)^2 + (Y_\nu^\dagger Y_\nu)^2). \tag{4.19}$$

The effect of β functions of new particles enters into the SM RGEs at their effective masses.

V. EXISTING BOUNDS ON THE FERMIONIC AND THE SCALAR SECTORS

For the vacuum stability analysis, we need to find the Yukawa and scalar couplings that satisfy the existing experimental and theoretical constraints. These bounds are discussed below.

A. Bounds on the fermionic sector

(i) *Cosmological constraint on the sum of light neutrino masses*: The Planck 2015 results put an upper limit on the sum of active light neutrino masses to be [21]

$$\Sigma = m_1 + m_2 + m_3 < 0.23 \text{ eV}. \tag{5.1}$$

(ii) *Constraints from oscillation data*: We use the standard parametrization of the PMNS matrix in which

$$U_\nu = \begin{pmatrix} c_{12}c_{13} & s_{12}c_{13} & s13e^{-i\delta} \\ -c_{23}s_{12} - s_{23}s_{13}c_{12}e^{i\delta} & c_{23}c_{12} - s_{23}s_{13}s_{12}e^{i\delta} & s_{23}c_{13} \\ s_{23}s_{12} - c_{23}s_{13}c_{12}e^{i\delta} & -s_{23}c_{12} - c_{23}s_{13}s_{12}e^{i\delta} & c_{23}c_{13} \end{pmatrix} P, \tag{5.2}$$

where $c_{ij} = \cos\theta_{ij}$, $s_{ij} = \sin\theta_{ij}$, and the phase matrix $P = \mathrm{diag}(1, e^{i\alpha_2}, e^{i(\alpha_3+\delta)})$ contains the Majorana phases. The global analysis [89,90] of neutrino oscillation measurements with three light active neutrinos give the oscillation parameters in their 3σ range, for both normal hierarchy (NH) for which $m_3 > m_2 > m_1$ and inverted hierarchy (IH) for which $m_2 > m_1 > m_3$, as follows:

(a) Mass squared differences

$$\Delta m_{21}^2/10^{-5}\ \text{eV}^2 = (7.03 \to 8.09); \begin{cases} \Delta m_{31}^2/10^{-3}\ \text{eV}^2 = (2.407 \to 2.643) & \text{NH} \\ \Delta m_{31}^2/10^{-3}\ \text{eV}^2 = (-2.635 \to -2.399) & \text{IH} \end{cases}. \tag{5.3}$$

(b) *Mixing angles*

$$\sin^2\theta_{12} = (0.271 \to 0.345); \tag{5.4}$$

$$\sin^2\theta_{23} = \begin{cases} (0.385 \to 0.635) \\ (0.393 \to 0.640) \end{cases}; \qquad \sin^2\theta_{13} = \begin{cases} (0.01934 \to 0.02392) & \text{NH} \\ (0.01953 \to 0.02408) & \text{IH} \end{cases}. \tag{5.5}$$

[4] Our results do not change with the inclusion of two-loop RGEs of neutrino Yukawa couplings, which have been checked using SARAH [88].

(iii) *Constraints on the nonunitarity of $U_{\rm PMNS} = U_L$*: The analysis of electroweak precision observables along with various other low-energy precision observables put bound on the nonunitarity of light neutrino mixing matrix U_L [91]. At 90% confidence level,

$$|U_L U_L^\dagger| = \begin{pmatrix} 0.9979-0.9998 & <10^{-5} & <0.0021 \\ <10^{-5} & 0.9996\text{–}1.0 & <0.0008 \\ <0.0021 & <0.0008 & 0.9947\text{–}1.0 \end{pmatrix}. \tag{5.6}$$

This also takes care of the constraints coming from various charged lepton flavor violating (LFV) decays such as $l_i \to l_j\gamma$, among which $\mu \to e\gamma$ is the one that gives the most severe bound [92],

$$\mathrm{Br}(\mu \to e\gamma) < 4.2 \times 10^{-13}. \tag{5.7}$$

(iv) *Bounds on the heavy neutrino masses*: The search for heavy singlet neutrinos at LEP by the L3 Collaboration in the decay channel $N \to eW$ showed no evidence of a singlet neutrino in the mass range between 80 GeV($|V_{\alpha i}|^2 \le 2 \times 10^{-5}$) and 205 GeV($|V_{\alpha i}|^2 \le 1$) [93], $V_{\alpha i}$ being the mixing matrix elements between the heavy and light neutrinos. Heavy singlet neutrinos in the mass range from 3 GeV up to the Z-boson mass (m_Z) has also been excluded by LEP experiments from Z-boson decay up to $|V_{\alpha i}|^2 \approx 10^{-5}$ [94–96]. These constraints are taken care of in our analysis by keeping the mass of the lightest heavy neutrino to be greater than or equal to 200 GeV.

B. Bounds on the scalar sector

(i) *Constraints on scalar potential couplings from perturbative unitarity*: Constraints on the scalar sector couplings in the singlet scalar model from perturbative unitarity has been discussed in [97]. At very high field values, one can obtain the scattering matrix a_0 for the $J = 0$ partial wave [98] by considering the various scalar-scalar scattering amplitudes. Using the equivalence theorem [99–104], we have reproduced the perturbative unitarity bounds on the eigenvalues of the scattering matrix for this model. These are given by [97]

$$|\kappa(\Lambda)| \le 8\pi \quad \text{and}$$
$$\left|6\lambda + \lambda_S \pm \sqrt{4\kappa^2 + (6\lambda - \lambda_S)^2}\right| \le 16\pi. \tag{5.8}$$

(ii) *Dark matter constraints*: The parameter space for the scalar sector should also satisfy the Planck and WMAP imposed dark matter relic density constraint [21],

$$\Omega_{\rm DM} h^2 = 0.1198 \pm 0.0026. \tag{5.9}$$

In addition, the invisible Higgs decay width and the recent direct detection experiments, in particular, the LUX-2016 [105] data and the indirect Fermi-LAT data [106], restrict the arbitrary Higgs portal coupling and the dark matter mass [45,49].

Since the extra fermions are heavy ($\gtrsim$200 GeV), for low dark matter mass (around 60 GeV), the dominant (more than 75%) contribution to the relic density is from the $SS \to b\bar{b}$ channel. The channels $SS \to V, V^*$ also contribute to the relic density where V stands for the vector bosons W and Z, and V^* indicates the virtual particle that can decay into the SM fermions. In this mass region, the value of the Higgs portal coupling κ is $\mathcal{O}(10^{-2})$ to get the relic density in the right ballpark and simultaneously satisfy the other experimental bounds. However, this region is not of much interest to us since such a small coupling will not contribute much to the running of λ and hence will not affect the stability of the EW vacuum much. The LUX-2016 data [105] have ruled out the dark matter mass region ~70–500 GeV.

If we consider $M_{\rm DM} \gg M_t$, the annihilation cross section is proportional to $\frac{\kappa^2}{M_{\rm DM}^2}$, which ensures that the relic density band in the $\kappa - M_{\rm DM}$ [49] plane is a straight line. In this region, one can get the right relic density if the ratio of dark matter mass to the Higgs portal coupling κ is ~3300 GeV. In this case, the dominant contributions to the dark matter annihilation channel are $SS \to hh, t\bar{t}, VV$.

We use FeynRules [107] along with micrOMEGAs [108,109] to compute the relic density of the scalar DM. We have checked that the contribution from annihilation into extra fermions is very small. However, this could be significant for dark matter mass $\gtrsim$2.5 TeV, provided the Yukawa couplings are large enough. But, in the stability analysis discussed in Sec. VI A 2, we will see that the dark matter mass $\gtrsim$2.5 TeV requires the value of $\kappa \gtrsim 0.65$, which violates the perturbativity bounds before the Planck scale. Thus, we consider the dark matter mass in the range ~500 GeV–2.5 TeV with κ in the range ~0.15–0.65. It is to be noted that in the presence of the singlet fermions the value of $\kappa(M_Z)$ and hence $M_{\rm DM}$ for which the perturbativity is not obeyed will also depend upon the value of Tr $[Y_\nu^\dagger Y_\nu]$. This will be discussed in the next section.

VI. RESULTS

In this section, we present our results of the stability analysis of the electroweak vacuum in the two seesaw scenarios. We confine ourselves to the normal hierarchy. The results for the inverted hierarchy are not expected to be

TABLE I. Output values for three different benchmark points for the inverse seesaw model satisfying all the low-energy constraints

Parameter	BM-I	BM-II	BM-III
$\Delta m^2_{21}/10^{-5}$ eV^2	8.0891	7.8228	7.6277
$\Delta m^2_{31}/10^{-3}$ eV^2	2.4391	2.5046	2.4078
$\sin^2\theta^L_{12}$	0.2710	0.3429	0.3449
$\sin^2\theta^L_{23}$	0.3850	0.3850	0.4102
$\sin^2\theta^L_{13}$	0.0239	0.0229	0.0238
δ_{PMNS}	1.1173	1.4273	1.1715
ϕ_1, ϕ_2	2.5187, 2.9377	2.9384, 3.1379	0.4264, 0.7426
$m_i/10^{-1}$ eV	0.10, 0.13, 0.511	0.23, 0.25, 0.558	0.10, 0.13, 0.507
M_j GeV	200.77, 200.77, 461.159, 461.16, 1744.67, 1744.669	210.01, 210.01, 487.284, 487.28, 1451.34, 1451.344	200.00, 200.00, 332.993, 332.99, 3568.87, 3568.869
$\mathrm{Tr}[Y_\nu Y_\nu^\dagger]$	0.1	0.2	0.3
$\mathrm{Br}(\mu \to e\gamma)$	0.731×10^{-16}	0.1×10^{-16}	0.13×10^{-15}

very different [18]. We have used the package SARAH [88] to do the RG analysis in our work.

A. Inverse seesaw model

For the inverse seesaw model, the input parameters are the entries of the matrices Y_ν, M_S, and M_μ. Here Y_ν is a complex 3×3 matrix. M_S is a real 3×3 matrix, and M_μ is a 3×3 diagonal matrix with real entries. We vary the entries of various mass matrices in the range $10^{-2} < M_\mu <$ 1 keV and $0 < M_R < 5 \times 10^4$ GeV. This implies a heavy neutrino mass of maximum up to a few TeV. With these input parameters, we search for parameter sets consistent with the low-energy data using the downhill simplex method [110]. We present in Table I, some representative outputs consistent with data for three benchmark points. In this table, $\mathrm{Tr}[Y_\nu Y_\nu^\dagger]$ is an input. As a consistency check, we also give the value of $\mathrm{Br}(\mu \to e\gamma)$.

1. Vacuum stability

In Fig. 1, we display the running of the couplings for various benchmark points in the ISM. In Fig. 1(a), we have shown the variation in the running of the Higgs quartic coupling λ for different values of Tr $[Y_\nu^\dagger Y_\nu]$ (0, 0.15, and 0.30) for a fixed value of the Higgs portal coupling $\kappa = 0.304$. We have chosen the DM mass $M_{\mathrm{DM}} =$ 1000 GeV to get the relic density in the right ballpark. As λ_S does not alter the relic density, we have fixed its value at 0.1 for all the plots in this paper. We can see that for Tr $[Y_\nu^\dagger Y_\nu] = 0$; i.e., without the right-handed neutrinos, the EW vacuum remains absolutely stable up to the Planck scale (green line) and for large values of Tr $[Y_\nu^\dagger Y_\nu]$, the EW vacuum goes toward the instability [Higgs quartic coupling becomes negative around $\Lambda_I \sim 10^{10}$ GeV (red line) and $\Lambda_I \sim 10^8$ GeV (black line)] region.

In Fig. 1(b), we plot the running of λ for a fixed value of Tr $[Y_\nu^\dagger Y_\nu] = 0.1$ and different sets of κ and M_{DM}. It is seen that for a larger value of $\kappa = 0.45$ with $M_{\mathrm{DM}} = 1500$ GeV, the EW vacuum remains stable up to the Planck scale (purple line). For $\kappa = 0.304$ with $M_{\mathrm{DM}} = 1000$ GeV, the quartic coupling λ (red line) becomes negative around $\Lambda_I \sim 10^{11}$ GeV, and in the absence of the singlet scalar field, i.e., for $\kappa = 0$, $\lambda_S = 0$ (blue line), λ becomes negative around $\Lambda_I \sim 10^9$ GeV and the vacuum goes to the metastability region.

In Figs. (1c)and (1d), we have shown the running of all three scalar quartic couplings, λ, κ, and λ_S and $\mathrm{Tr}[Y_\nu^\dagger Y_\nu]$ for $(M_{\mathrm{DM}}, \kappa) = (1000\ \mathrm{GeV}, 0.304)$ and (1500 GeV, 0.456), respectively. It can be seen that the values of λ_s and κ increase considerably with the energy scale and can reach the perturbativity bound at the Planck scale depending upon the initial values of κ and λ_S at M_Z. Here for $\lambda_S = 0.1$, the maximum allowed value of κ will be 0.58 from perturbativity. The value of $\mathrm{Tr}[Y_\nu^\dagger Y_\nu]$ increases only slightly with the energy scale, and the value of λ_S increases faster for a larger value of κ.

2. Tunneling probability and phase diagrams

The present central values of the SM parameters, especially the top Yukawa coupling y_t and strong coupling constant α_s with Higgs mass $M_h \approx 125.7$ GeV, suggest that the beta function of the Higgs quartic coupling $\beta_\lambda (\equiv dV(h)/dh)$ goes from negative to positive around 10^{15} GeV [52,53]. This implies that there is an extra deeper minima situated at that scale. So there is a finite probability that the electroweak vacuum might tunnel into that true (deeper) vacuum. But this tunneling probability is not large enough, and hence the lifetime of the EW vacuum remains larger than the age of the universe. This implies that the EW vacuum is metastable in the SM. The expression for the tunneling probability at zero temperature is given by [54,111]

$$\mathcal{P}_0 = V_U \Lambda_B^4 \exp\left(-\frac{8\pi^2}{3|\lambda(\Lambda_B)|}\right), \tag{6.1}$$

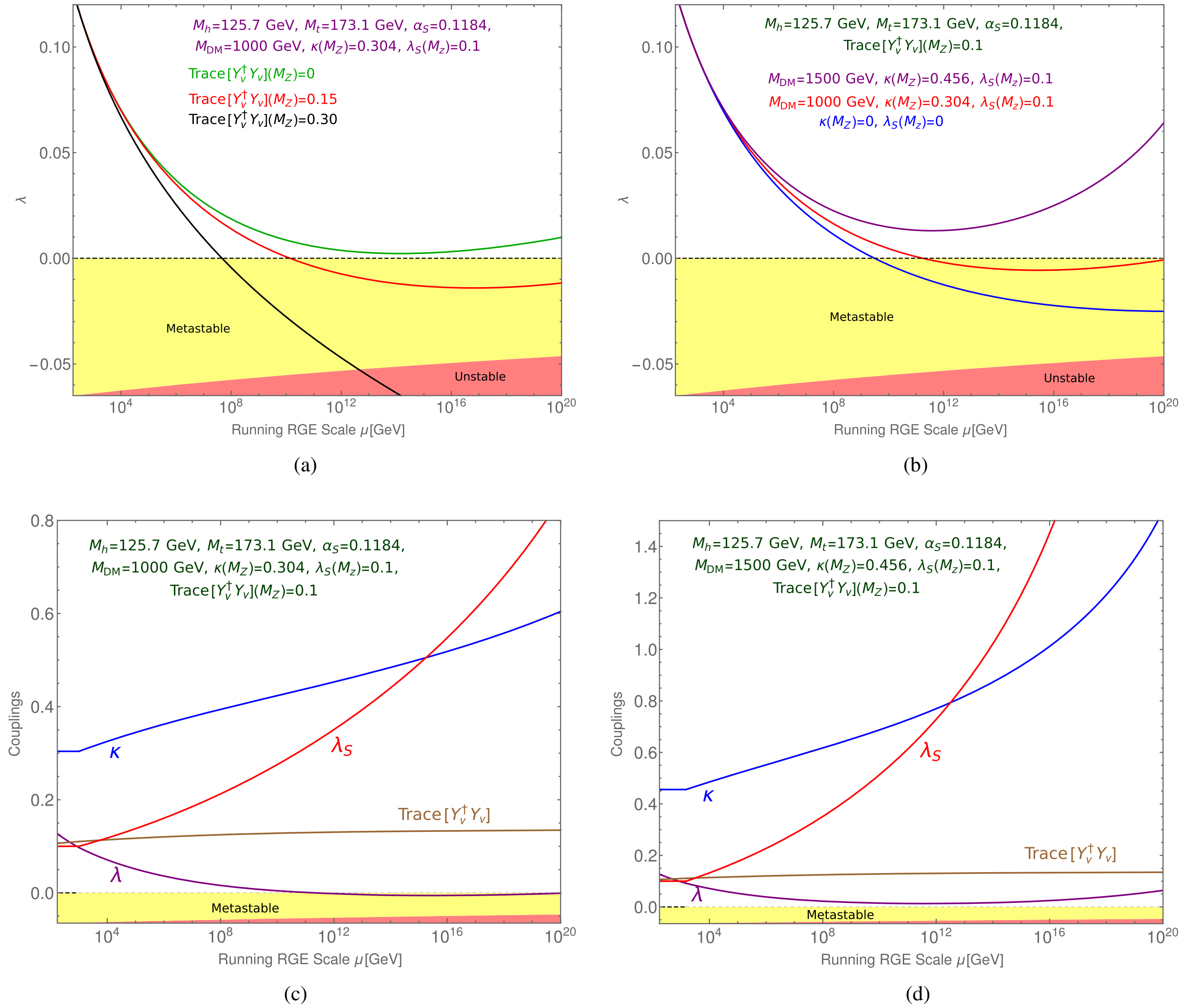

FIG. 1. Running of the couplings with the energy scale in the inverse seesaw model. (a) Running of λ for dierent values of $\mathrm{Tr}[Y_\nu^\dagger Y_\nu]$ and a fixed value of κ. (b) Running of λ for a fixed value of $\mathrm{Tr}[Y_\nu^\dagger Y_\nu]$ and dierent values of κ. (c) Running of the couplings with energy for dark matter mass of 1000 GeV. (d) Running of the couplings with energy for dark matter mass of 1500 GeV.

where Λ_B is the energy scale at which the action of the Higgs potential is minimum. V_U is the volume of the past light cone taken as τ_U^4, where τ_U is the age of the universe ($\tau_U = 4.35 \times 10^{17}$ s) [21]. In this work we have neglected the loop corrections and gravitational correction to the action of the Higgs potential [112]. For the vacuum to be metastable, we should have $\mathcal{P}_0 < 1$, which implies that [49]

$$0 > \lambda(\mu) > \lambda_{\min}(\Lambda_B) = \frac{-0.06488}{1 - 0.00986 \ln(v/\Lambda_B)}, \quad (6.2)$$

whereas the situation $\lambda(\mu) < \lambda_{\min}(\Lambda_B)$ leads to the unstable EW vacuum. In these regions, κ and λ_S should always be positive to get the scalar potential bounded from below [49]. In our model, the EW vacuum shifts toward stability/instability depending upon the new physics parameter space for the central values of $M_h = 125.7$ GeV, $M_t = 173.1$ GeV, and $\alpha_s = 0.1184$, and there might be extra minima around 10^{12-17} GeV.

In Fig. 2, we have given the phase diagram in the $\mathrm{Tr}[Y_\nu^\dagger Y_\nu] - \kappa$ plane. The line separating the stable region and the metastable region is obtained when the two vacuua are at the same depth, i.e., $\lambda(\mu) = \beta_\lambda(\mu) = 0$. The unstable and the metastable regions are separated by the boundary line where $\beta_\lambda(\mu) = 0$ along with $\lambda(\mu) = \lambda_{\min}(\Lambda_B)$, as defined in Eq. (6.2). For simplicity, we have plotted Fig. 2 (also Fig. 1) by fixing all the eight entries of the 3×3 complex matrix Y_ν, but varying only the $(Y_\nu)_{33}$ element to get a smooth phase diagram. From Fig. 2, it

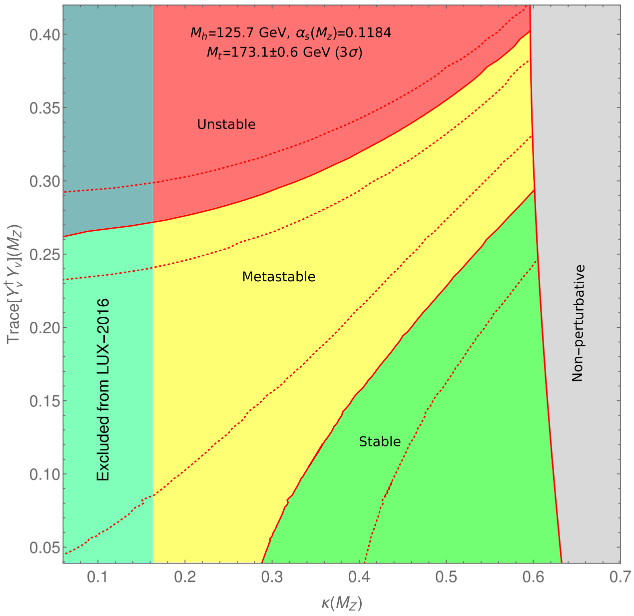

FIG. 2. Phase diagram in the $\mathrm{Tr}[Y_\nu^\dagger Y_\nu] - \kappa$ plane. We have fixed all the entries of Y_ν except for $(Y_\nu)_{33}$. The three boundary lines (two dotted and a solid) correspond to $M_t = 173.1 \pm 0.6$ GeV (3σ), and we have taken $\lambda_S(M_Z) = 0.1$. The dark matter mass is dictated by $\kappa(M_z)$ to give the correct relic density. See text for details.

could be seen that the values of κ beyond ~0.58 are disallowed by perturbativity bounds, and those below ~0.16 are disallowed by the direct detection bounds from LUX-2016 [105]. The value of the dark matter mass in this allowed range is thus ~530–2100 GeV. Note that the vacuum stability analysis of the inverse seesaw model done in Ref. [60] had found that the parameter space with $\mathrm{Tr}[Y_\nu^\dagger Y_\nu] > 0.4$ was excluded by vacuum metastability constraints. Whereas, in our case, Fig. 2 shows that the parameter space with $\mathrm{Tr}[Y_\nu^\dagger Y_\nu] \gtrsim 0.25$ is excluded for the case when there is no extra scalar. The possible reasons could be that we have kept the maximum value of the heavy neutrino mass to be around a few TeV, whereas the authors of [60] had considered heavy neutrinos as heavy as 100 TeV. Obviously, considering larger thresholds would allow us to consider large values of $\mathrm{Tr}[Y_\nu^\dagger Y_\nu]$ as the corresponding couplings will enter into RG running only at a higher scale. Another difference with the analysis of [60] is that we have fixed eight of the nine entries of the Yukawa coupling matrix Y_ν. Also, varying all the nine Yukawa couplings will give us more freedom and the result is expected to change. The main result that we deduce from this plot is the effect of κ on the maximum allowed value of Tr $[Y_\nu^\dagger Y_\nu]$, which increases from 0.26 to 0.4 for a value of κ as large as 0.6. In addition, we see that the upper bound on $\kappa(M_Z)$ from perturbativity at the Planck scale decreases from 0.64 to 0.58 as the value of $\mathrm{Tr}[Y_\nu^\dagger Y_\nu]$ changes from 0 to 0.44. This can be explained from the expression of the β_κ in Eq. (4.19), which shows that $[Y_\nu^\dagger Y_\nu]$ affect the running κ positively through the quantity T. Since $M_{\mathrm{DM}} \sim 3300\kappa$ GeV for $M_{\mathrm{DM}} \gg M_t$, the mass of dark matter for which perturbativity is valid decreases with the increase in the value of the Yukawa coupling.

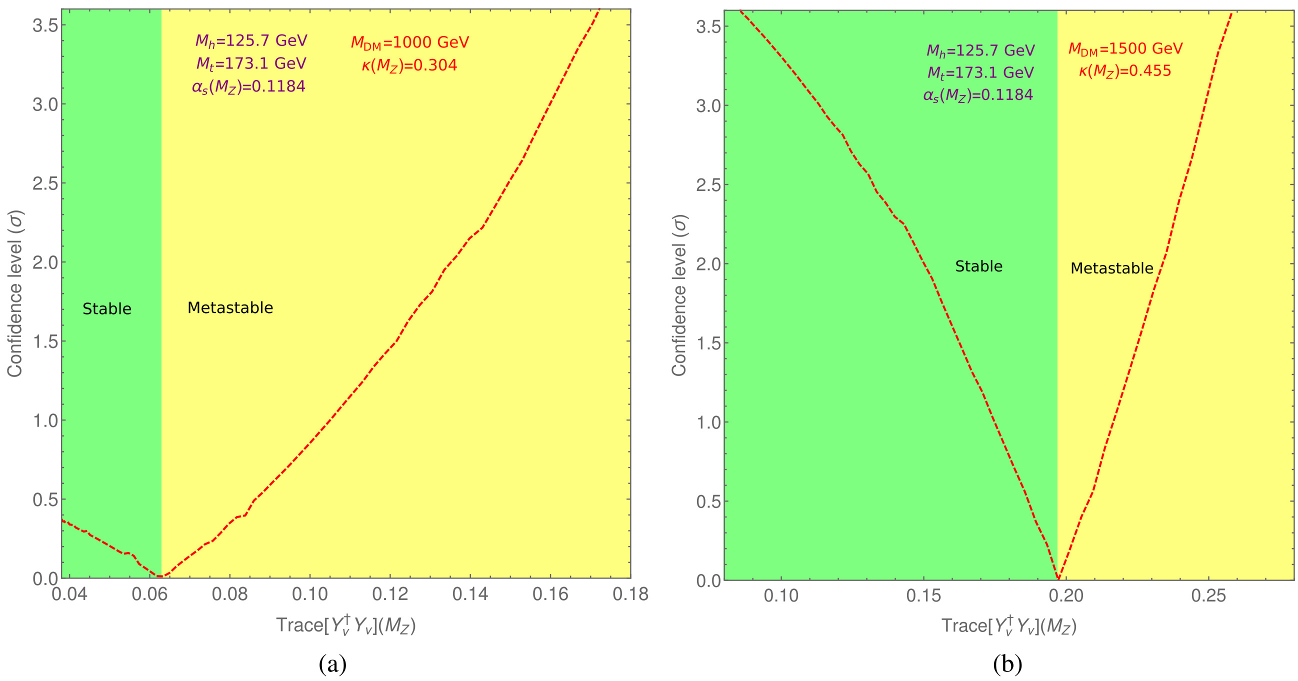

FIG. 3. Dependence of confidence level at which the EW vacuum stability is excluded/allowed on $\mathrm{Tr}[Y_\nu^\dagger Y_\nu]$ for two different values of κ and M_{DM}. We have taken $\lambda_S(M_Z) = 0.1$. (a) $(\kappa, M_{DM}) = (0.304, 1000$ GeV). (b) $(\kappa, M_{DM}) = (0.455, 1500$ GeV).

3. Confidence level of vacuum stability

As we have seen, the stability of the electroweak vacuum changes due to the presence of new physics, and hence it becomes important to demonstrate the change in the confidence level at which stability is excluded or allowed (one sided) [49,113,114]. In particular, it will provide a quantitative measurement of (meta)stability in the presence of new physics. In Fig. 3, we graphically show how the confidence level at which stability of electroweak vacuum is allowed/excluded depends on new Yukawa couplings of the heavy fermions for the inverse seesaw model in the presence of the extra scalar (dark matter) field. We have plotted the dependence of the confidence level against the trace of the Yukawa coupling, $\mathrm{Tr}[Y_\nu^\dagger Y_\nu]$, for fixed values of Higgs portal coupling $\kappa = 0.304$ in Fig. 3(a). Here, the dark matter mass $M_{\rm DM} = 1000$ GeV is dictated by κ to obtain the correct relic density. A similar plot with a higher value of $\kappa = 0.455$ with dark matter mass $M_{\rm DM} = 1500$ GeV is shown in Fig. 3(b). In this case the electroweak vacuum is absolutely stable for a larger parameter space. For a particular set of values of the model parameters $M_h = 125.7$ GeV, $M_t = 173.1$ GeV, $\alpha_s(M_z) = 0.1184$, and κ, the confidence level (one sided) at which the electroweak vacuum is absolutely stable (green region) decreases with the increase of $\mathrm{Tr}[Y_\nu^\dagger Y_\nu]$ and becomes zero for $\mathrm{Tr}[Y_\nu^\dagger Y_\nu] = 0.06$ in Fig. 3(a) and $\mathrm{Tr}[Y_\nu^\dagger Y_\nu] = 0.20$ in Fig. 3(b). The

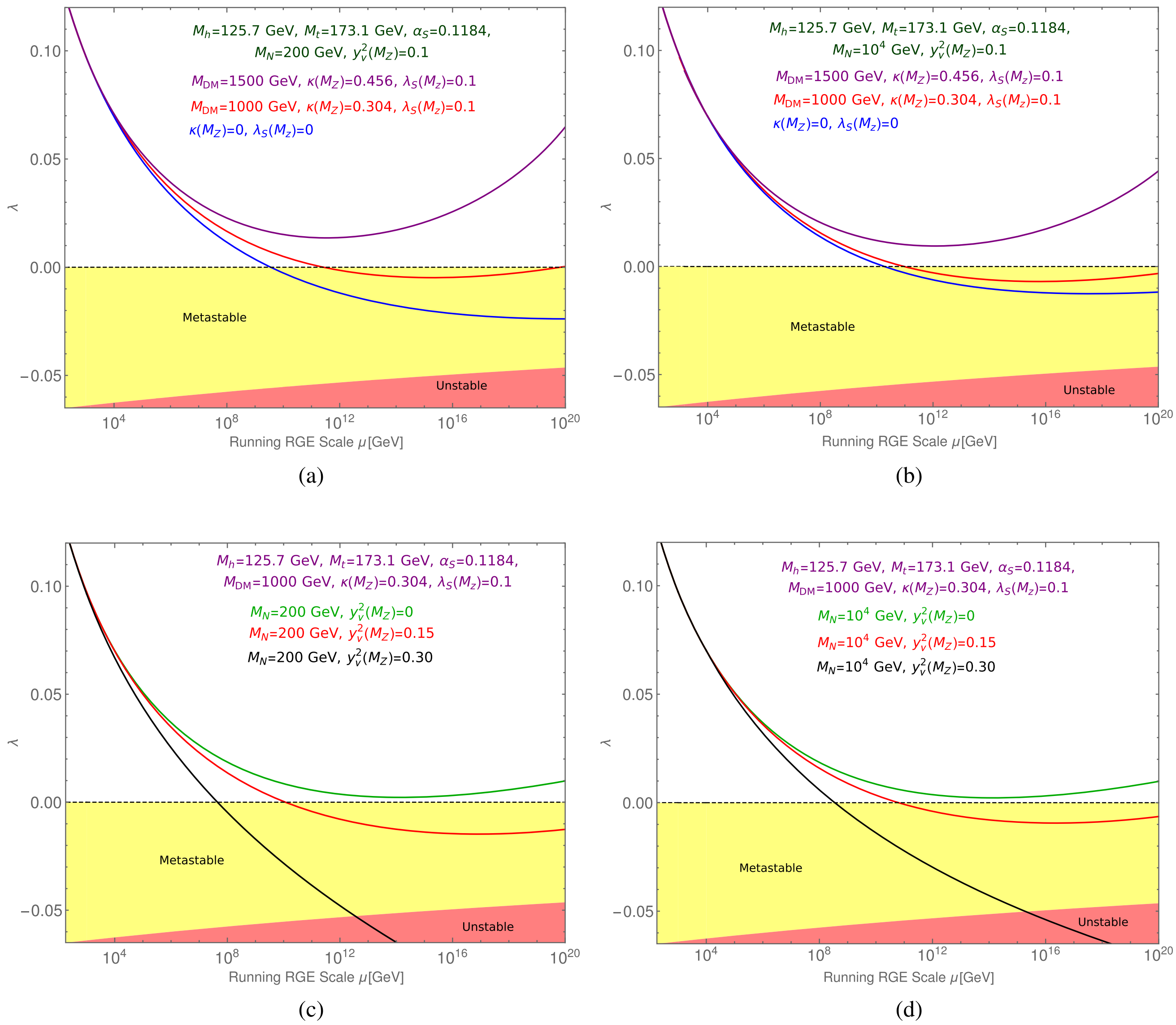

FIG. 4. Running of the quartic coupling λ in MLSM with extra scalar for two different values of M_N. In the upper panel, the three lines are for different values of $M_{\rm DM}$ and κ, whereas in the lower panel, they are for different values of y_ν and fixed values of $M_{\rm DM}$ and κ.

confidence level at which the absolute stability of the electroweak vacuum is excluded (one sided) increases with the trace of the Yukawa coupling in the yellow region.

B. Minimal linear seesaw model

In the minimal linear seesaw case, the Yukawa coupling matrices Y_ν and Y_s can be completely determined in terms of the oscillation parameters apart from the overall coupling constant y_ν and y_s, respectively [17]. For normal hierarchy, in MLSM, the Yukawa coupling matrices Y_ν and Y_s can be parametrized as

$$Y_\nu = \frac{y_\nu}{\sqrt{2}}\left(\sqrt{1+\rho}U_3^\dagger + e^{i\frac{\pi}{2}}\sqrt{1-\rho}U_2^\dagger\right), \quad (6.3)$$

$$Y_s = \frac{y_s}{\sqrt{2}}\left(\sqrt{1+\rho}U_3^\dagger + e^{i\frac{\pi}{2}}\sqrt{1-\rho}U_2^\dagger\right), \quad (6.4)$$

where

$$\rho = \frac{\sqrt{1+r}-\sqrt{r}}{\sqrt{1+r}+\sqrt{r}}. \quad (6.5)$$

Here, U_i's are the columns of the unitary PMNS matrix U_ν and r is the ratio of the solar and the atmospheric mass squared differences. This parametrization makes the vacuum stability analysis in the minimal linear seesaw model easier since there are only two independent parameters y_ν and M_N in the fermion sector, where M_N is the degenerate mass of the two heavy neutrinos [the value of y_s being very small $\mathcal{O}(10^{-11})$]. A detailed analysis has already been performed in Ref. [18]. Here, we are interested in the interplay between the Z_2 odd singlet scalar and singlet fermions in the vacuum stability analysis.

In Fig. 4, we have plotted the running of the Higgs quartic coupling λ with the energy scale μ up to the Planck scale. Figures 4(a) and 4(b) show the running of λ for different values of k (0.0, 0.304, 0.456) and $M_{\rm DM}$ (0, 1000 GeV, 1500 GeV), for $M_N = 200$ GeV and $M_N = 10^4$ GeV, respectively, for a fixed value of $y_\nu^2 = 0.1$. Comparing these two plots, we can see that λ tends to go to the instability region faster for smaller values of the heavy neutrino mass. So, the EW vacuum is more stable for larger values of M_N, because the effect of the extra singlet fermion in the running of λ enters at a higher value. We also find that as the value of κ increases from 0 to 0.304, the electroweak vacuum becomes metastable at a higher value of the energy scale. For $\kappa = 0.456$ the electroweak vacuum becomes stable up to the Planck scale even in the presence of the singlet fermions.

Figures 4(c) and 4(d) display the running of λ for different values of y_ν^2 (0.0, 0.15, 0.3) and for fixed values of $k = 0.304$ and $M_{\rm DM} = 1000$ GeV, for $M_N = 200$ GeV and for $M_N = 10^4$ GeV, respectively. It could be seen from these plots that the larger the value of y_ν, the earlier λ becomes negative and greater is the tendency for the EW vacuum to be unstable as expected. We note from these two figures that for $\kappa = 0.304$, absolute stability is attained only for $y_\nu = 0$ even in the presence of the singlet scalar.

In Fig. 5, we have shown the phase diagram in the y_ν-M_N plane. The stable (green), unstable (red), and the metastable

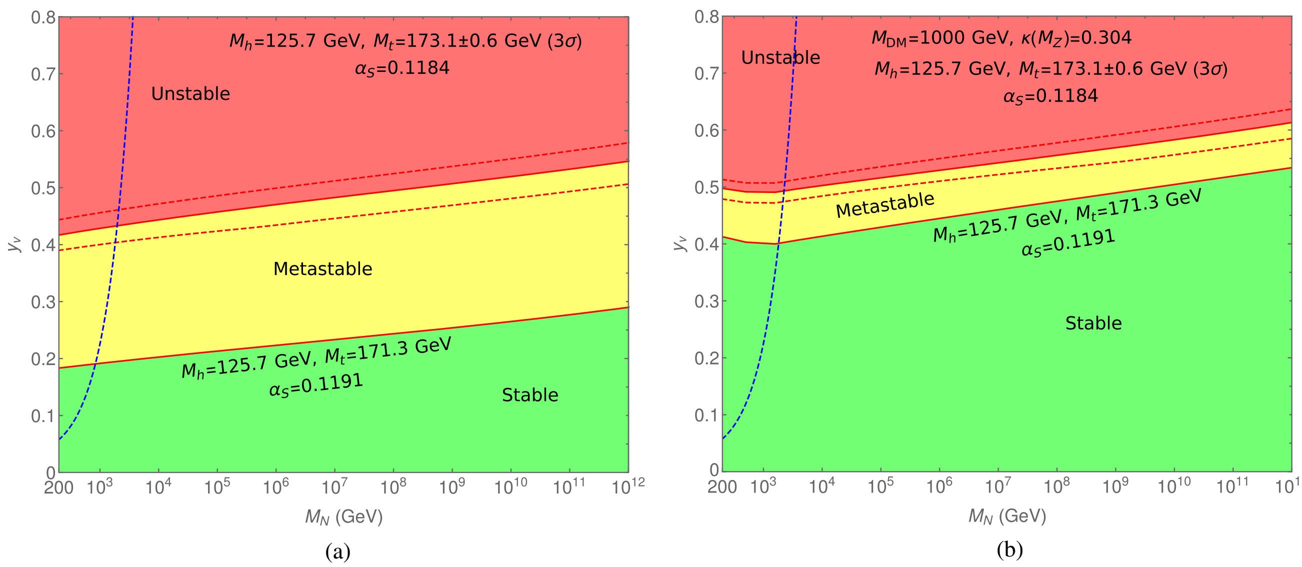

FIG. 5. Phase diagrams in the y_ν-M_N plane in the presence and the absence of the extra scalar. The region to the left side of the blue dotted line is disallowed by constraint from BR($\mu \to e\gamma$). The three boundary lines (two dotted and a solid) correspond to $M_t = 173.1 \pm 0.6$ GeV (3σ), and we have taken $\lambda_S(M_Z) = 0.1$ in the second plot. (a) Without the extra scalar. (b) With scalar, $(\kappa, M_{DM}) = (0.304, 1000$ GeV)

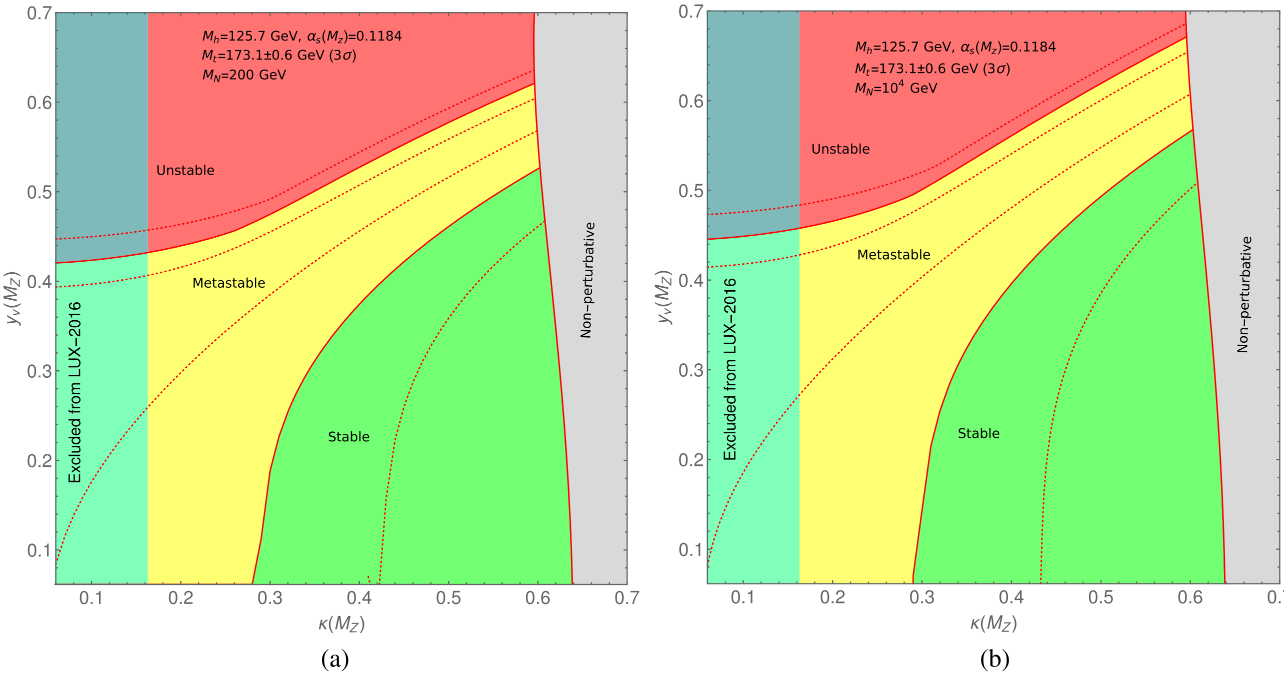

FIG. 6. Phase diagrams in the y_ν-κ plane for two different values of M_N. Here, $\lambda_S(M_Z) = 0.1$ and the dark matter mass is dictated by $\kappa(M_z)$ to give the correct relic density.

(yellow) regions are shown, and it could be seen that the higher the value of M_N, the larger the allowed values of y_ν by vacuum stability as we have discussed earlier. The unstable and the metastable regions are separated by solid red lines for the central values of the SM parameters, $M_h = 125.7$ GeV, $M_t = 173.1$ GeV, and $\alpha_s = 0.1184$. The red dashed lines represent the 3σ variation of the top quark mass. However, we get a significant stable region for $M_h = 125.7$ GeV, $M_t = 171.3$ GeV, and $\alpha_s = 0.1191$, which corresponds to the solid line separating the stable and the metastable regions. The region to the left side of the blue dotted line is disallowed by LFV constraints for the normal hierarchy of light neutrino masses. Figure 5(a) is drawn in the absence of the extra scalar and Fig. 5(b) is drawn for $(\kappa, M_{\rm DM}) = (0.304, 1000$ GeV$)$. Clearly, there is a more stable region in the presence of the extra scalar, and the boundary line separating the metastable and the unstable regions also shifts upwards in this case.

In Fig. 6, we have shown the phase diagrams in the y_ν-κ plane for two different values of the heavy neutrino masses: Fig. 6(a) for $M_N = 200$ GeV and Fig. 6(b) for $M_N = 10^4$ GeV. Here also, the red dashed lines represent the 3σ variation of top quark mass. It could clearly be seen that as the value of the heavy neutrino mass is higher, the unstable region shifts toward the large values of y_ν. This is a result that should be expected from Fig. 5. In this model, the theory becomes nonperturbative (grey) for $\kappa = 0.64$ for $y_\nu = 0.05$. The maximum allowed value of κ by perturbativity at the Planck scale decreases with an increase in y_ν as we have also seen for the inverse seesaw case. The region $\kappa \lesssim 0.16$ is excluded from the recent direct detection experiment at LUX.

VII. CONCLUSIONS

In this paper we have analyzed the stability of the electroweak vacuum in the context of the TeV scale inverse seesaw and minimal linear seesaw models extended with a scalar singlet dark matter. We have studied the interplay between the contribution of the extra singlet scalar and the singlet fermions to the EW vacuum stability. We have shown that the coupling constants in these two seemingly disconnected sectors can be correlated at high energy by the vacuum stability/metastability and perturbativity constraints.

In the inverse seesaw scenario, the EW vacuum stability analysis is done after fitting the model parameters with the neutrino oscillation data and nonunitarity constraints on $U_{\rm PMNS}$ (including the LFV constraints from $\mu \to e\gamma$). For the minimal linear seesaw model, the Yukawa matrix Y_ν can be fully parametrized in terms of the oscillation parameters excepting an overall coupling constant y_ν, which can be constrained from vacuum stability and LFV. We have taken the heavy neutrino masses of order up to a few TeV for both the seesaw models. An extra Z_2 symmetry is imposed to ensure that the scalar particle serves as a viable dark matter candidate. We include all the experimental and theoretical bounds coming from the constraints on relic density and dark matter searches as well as unitarity and perturbativity up to the Planck scale. For the masses of new fermions from 200 GeV to a few TeV, the annihilation cross section to the extra fermions is very small for dark matter mass $\mathcal{O}(1\text{–}2)$ TeV. We have also checked that the theory violates perturbativity before the Planck scale for DM mass $\gtrsim 2.5$ TeV. In addition, we find that the value of the Higgs portal coupling $\kappa\,(M_Z)$ for which perturbativity is violated at the Planck scale decreases with an increase in the value of the Yukawa couplings of the new fermions. For $M_{\mathrm{DM}} \gg M_t$, one can approximately write $M_{\mathrm{DM}} \sim 3300\kappa$ GeV. This implies that with the increasing Yukawa coupling, the mass of dark matter for which the perturbativity is maintained also decreases. Thus the RGE running induces a correlation between the couplings of the two sectors from the perturbativity constraints.

It is well known that the electroweak vacuum of SM is in the metastable region. The presence of the fermionic Yukawa couplings in the context of TeV scale seesaw models drives the vacuum more toward instability while the singlet scalar tries to arrest this tendency. Overall, we find that it is possible to find parameter spaces for which the electroweak vacuum remains absolutely stable for both inverse and linear seesaw models in the presence of the extra scalar particle. We find an upper bound from metastability on $\mathrm{Tr}[Y_\nu^\dagger Y_\nu]$ as 0.25 for $\kappa = 0$, which increases to 0.4 for $\kappa = 0.6$ in the inverse seesaw model. We have also seen that in the absence of the extra scalar, the values of the Yukawa coupling y_ν greater than 0.42 are disallowed in the minimal linear seesaw model. But, in the presence of the extra scalar the values of y_ν up to ~ 0.6 are allowed for dark matter mass ~ 1 TeV. The correlations between the Yukawa couplings ($\mathrm{Tr}[Y_\nu^\dagger Y_\nu]$ or y_ν) and κ are presented in terms of phase diagrams.

Inverse and linear seesaw models can be explored at LHC through trilepton signatures [19,115–123]. A higher value of Yukawa couplings, as can be achieved in the presence of the Higgs portal dark matter, can facilitate observing such signals at colliders.

[1] S. Chatrchyan *et al.* (CMS Collaboration), Observation of a new boson at a mass of 125 GeV with the CMS experiment at the LHC, Phys. Lett. B **716**, 30 (2012).

[2] G. Aad *et al.* (ATLAS Collaboration), Observation of a new particle in the search for the Standard Model Higgs boson with the ATLAS detector at the LHC, Phys. Lett. B **716**, 1 (2012).

[3] S. Weinberg, Baryon- and Lepton-Nonconserving Processes, Phys. Rev. Lett. **43**, 1566 (1979).

[4] P. Minkowski, $\mu \to e\gamma$ at a rate of one out of 1-billion muon decays?, Phys. Lett. **67B**, 421 (1977).

[5] M. Gell-Mann, P. Ramond, and R. Slansky, in *Proceedings of the Supergravity Workshop* (North-Holland, Amsterdam, 1979), pp. 315–318; www.scopus.com.

[6] T. Yanagida, in *Proceedings of the Workshop on Unified Theory and Baryon Number in the Universe* (KEK, Tsukuba, Japan, 1979), pp. 95–98; www.scopus.com.

[7] R. N. Mohapatra and G. Senjanovic, Neutrino Mass and Spontaneous Parity Violation, Phys. Rev. Lett. **44**, 912 (1980).

[8] S. M. Boucenna, S. Morisi, and J. W. F. Valle, The low-scale approach to neutrino masses, Adv. High Energy Phys. **2014**, 831598 (2014).

[9] F. F. Deppisch, P. S. Bhupal Dev, and A. Pilaftsis, Neutrinos and collider physics, New J. Phys. **17**, 075019 (2015).

[10] R. Adhikari and A. Raychaudhuri, Light neutrinos from massless texture and below TeV seesaw scale, Phys. Rev. D **84**, 033002 (2011).

[11] J. Kersten and A. Y. Smirnov, Right-handed neutrinos at CERN LHC and the mechanism of neutrino mass fenera-tion, Phys. Rev. D **76**, 073005 (2007).

[12] A. Pilaftsis, Radiatively induced neutrino masses and large Higgs neutrino couplings in the standard model with Majorana fields, Z. Phys. C **55**, 275 (1992).

[13] R. Mohapatra and J. Valle, Neutrino mass and baryon number nonconservation in superstring models, Phys. Rev. D **34**, 1642 (1986).

[14] P.-H. Gu and U. Sarkar, Leptogenesis with linear, inverse or double seesaw, Phys. Lett. B **694**, 226 (2010).

[15] H. Zhang and S. Zhou, The minimal seesaw model at the TeV scale, Phys. Lett. B **685**, 297 (2010).

[16] M. Hirsch, S. Morisi, and J. Valle, A4-based tri-bimaximal mixing within inverse and linear seesaw schemes, Phys. Lett. B **679**, 454 (2009).

[17] M. Gavela, T. Hambye, D. Hernandez, and P. Hernandez, Minimal flavour seesaw models, J. High Energy Phys. 09 (2009) 038.

[18] S. Khan, S. Goswami, and S. Roy, Vacuum stability constraints on the minimal singlet TeV seesaw model, Phys. Rev. D **89**, 073021 (2014).

[19] G. Bambhaniya, S. Goswami, S. Khan, P. Konar, and T. Mondal, Looking for hints of a reconstructible seesaw model at the Large Hadron Collider, Phys. Rev. D **91**, 075007 (2015).

[20] M. Malinsky, T. Ohlsson, Z.-z. Xing, and H. Zhang, Non-unitary neutrino mixing and *CP* violation in the minimal inverse seesaw model, Phys. Lett. B **679**, 242 (2009).

[21] P. A. R. Ade *et al.* (Planck Collaboration), Planck 2015 results. XIII. Cosmological parameters, Astron. Astrophys. **594**, A13 (2016).

[22] V. Silveira and A. Zee, Scalar phantoms, Phys. Lett. B **161**, 136 (1985).

[23] J. McDonald, Gauge singlet scalars as cold dark matter, Phys. Rev. D **50**, 3637 (1994).
[24] C. P. Burgess, M. Pospelov, and T. ter Veldhuis, The minimal model of nonbaryonic dark matter: A singlet scalar, Nucl. Phys. **B619**, 709 (2001).
[25] G. Belanger, B. Dumont, U. Ellwanger, J. F. Gunion, and S. Kraml, Global fit to Higgs signal strengths and couplings and implications for extended Higgs sectors, Phys. Rev. D **88**, 075008 (2013).
[26] G. Aad *et al.* (ATLAS Collaboration), Constraints on new phenomena via Higgs boson couplings and invisible decays with the ATLAS detector, J. High Energy Phys. 11 (2015) 206.
[27] V. Khachatryan *et al.* (CMS Collaboration), Searches for invisible decays of the Higgs boson in pp collisions at $\sqrt{(s)} = 7$, 8, and 13 TeV, J. High Energy Phys. 02 (2017) 135.
[28] R. Dick, R. B. Mann, and K. E. Wunderle, Cosmic rays through the Higgs portal, Nucl. Phys. **B805**, 207 (2008).
[29] C. E. Yaguna, Gamma rays from the annihilation of singlet scalar dark matter, J. Cosmol. Astropart. Phys. 03 (2009) 003.
[30] Y. Cai, X.-G. He, and B. Ren, Low mass dark matter and invisible Higgs width in darkon models, Phys. Rev. D **83**, 083524 (2011).
[31] A. Urbano and W. Xue, Constraining the Higgs portal with antiprotons, J. High Energy Phys. 03 (2015) 133.
[32] A. Cuoco, B. Eiteneuer, J. Heisig, and M. Krämer, A global fit of the γ-ray galactic center excess within the scalar singlet Higgs portal model, J. Cosmol. Astropart. Phys. 06 (2016) 050.
[33] S. Bhattacharya, P. Ghosh, T. N. Maity, and T. S. Ray, Mitigating direct detection bounds in non-minimal Higgs portal scalar dark matter models, arXiv:1706.04699.
[34] V. Barger, P. Langacker, M. McCaskey, M. J. Ramsey-Musolf, and G. Shaughnessy, LHC phenomenology of an extended standard model with a real scalar singlet, Phys. Rev. D **77**, 035005 (2008).
[35] K. Cheung, P. Ko, J. S. Lee, and P.-Y. Tseng, Bounds on Higgs-portal models from the LHC Higgs data, J. High Energy Phys. 10 (2015) 057.
[36] A. Djouadi, O. Lebedev, Y. Mambrini, and J. Quevillon, Implications of LHC searches for Higgs-portal dark matter, Phys. Lett. B **709**, 65 (2012).
[37] M. Endo and Y. Takaesu, Heavy WIMP through Higgs portal at the LHC, Phys. Lett. B **743**, 228 (2015).
[38] H. Han, J. M. Yang, Y. Zhang, and S. Zheng, Collider signatures of Higgs-portal scalar dark matter, Phys. Lett. B **756**, 109 (2016).
[39] P. Ko and H. Yokoya, Search for Higgs portal DM at the ILC, J. High Energy Phys. 08 (2016) 109.
[40] Y. Mambrini, Higgs searches and singlet scalar dark matter: Combined constraints from XENON 100 and the LHC, Phys. Rev. D **84**, 115017 (2011).
[41] K. Cheung, Y.-L. S. Tsai, P.-Y. Tseng, T.-C. Yuan, and A. Zee, Global study of the simplest scalar phantom dark matter model, J. Cosmol. Astropart. Phys. 10 (2012) 042.
[42] J. M. Cline, K. Kainulainen, P. Scott, and C. Weniger, Update on scalar singlet dark matter, Phys. Rev. D **88**, 055025 (2013); Erratum, Phys. Rev. D **92**, 039906 (2015).
[43] F. S. Queiroz, K. Sinha, and A. Strumia, Leptoquarks, dark matter, and anomalous LHC events, Phys. Rev. D **91**, 035006 (2015).
[44] F. S. Queiroz and K. Sinha, The poker face of the Majoron dark matter model: LUX to keV line, Phys. Lett. B **735**, 69 (2014).
[45] P. Athron *et al.* (GAMBIT Collaboration), Status of the scalar singlet dark matter model, arXiv:1705.07931.
[46] M. Gonderinger, Y. Li, H. Patel, and M. J. Ramsey-Musolf, Vacuum stability, perturbativity, and scalar singlet dark matter, J. High Energy Phys. 01 (2010) 053.
[47] J. Elias-Miro, J. R. Espinosa, G. F. Giudice, H. M. Lee, and A. Strumia, Stabilization of the electroweak vacuum by a scalar threshold effect, J. High Energy Phys. 06 (2012) 031.
[48] C.-S. Chen and Y. Tang, Vacuum stability, neutrinos, and dark matter, J. High Energy Phys. 04 (2012) 019.
[49] N. Khan and S. Rakshit, Study of electroweak vacuum metastability with a singlet scalar dark matter, Phys. Rev. D **90**, 113008 (2014).
[50] N. Haba, K. Kaneta, and R. Takahashi, Planck scale boundary conditions in the standard model with singlet scalar dark matter, J. High Energy Phys. 04 (2014) 029.
[51] S. Ghosh, A. Kundu, and S. Ray, Potential of a singlet scalar enhanced Standard Model, Phys. Rev. D **93**, 115034 (2016).
[52] S. Alekhin, A. Djouadi, and S. Moch, The top quark and Higgs boson masses and the stability of the electroweak vacuum, Phys. Lett. B **716**, 214 (2012).
[53] D. Buttazzo, G. Degrassi, P. P. Giardino, G. F. Giudice, F. Sala, A. Salvio, and A. Strumia, Investigating the near-criticality of the Higgs boson, J. High Energy Phys. 12 (2013) 089.
[54] G. Isidori, G. Ridolfi, and A. Strumia, On the metastability of the standard model vacuum, Nucl. Phys. **B609**, 387 (2001).
[55] W. Rodejohann and H. Zhang, Impact of massive neutrinos on the Higgs self-coupling and electroweak vacuum stability, J. High Energy Phys. 06 (2012) 22.
[56] J. Chakrabortty, M. Das, and S. Mohanty, Constraints on TeV scale Majorana neutrino phenomenology from the vacuum stability of the Higgs, Mod. Phys. Lett. A **28**, 1350032 (2013).
[57] A. Datta, A. Elsayed, S. Khalil, and A. Moursy, Higgs vacuum stability in the $B-L$ extended standard model, Phys. Rev. D **88**, 053011 (2013).
[58] J. Chakrabortty, P. Konar, and T. Mondal, Constraining a class of B-L extended models from vacuum stability and perturbativity, Phys. Rev. D **89**, 056014 (2014).
[59] A. Kobakhidze and A. Spencer-Smith, Neutrino masses and Higgs vacuum stability, J. High Energy Phys. 08 (2013) 036.
[60] L. Delle Rose, C. Marzo, and A. Urbano, On the stability of the electroweak vacuum in the presence of low-scale seesaw models, J. High Energy Phys. 12 (2015) 050.
[61] G. Bambhaniya, P. S. Bhupal Dev, S. Goswami, S. Khan, and W. Rodejohann, Naturalness, vacuum stability and leptogenesis in the minimal seesaw model, Phys. Rev. D **95**, 095016 (2017).

[62] G. Bambhaniya, S. Khan, P. Konar, and T. Mondal, Constraints on a seesaw model leading to quasidegenerate neutrinos and signatures at the LHC, Phys. Rev. D **91**, 095007 (2015).
[63] M. Lindner, H. H. Patel, and B. Radovi, Electroweak absolute, meta-, and thermal stability in neutrino mass models, Phys. Rev. D **93**, 073005 (2016).
[64] H. Davoudiasl, R. Kitano, T. Li, and H. Murayama, The new minimal standard model, Phys. Lett. B **609**, 117 (2005).
[65] W. Chao, M. Gonderinger, and M. J. Ramsey-Musolf, Higgs vacuum stability, neutrino mass, and dark matter, Phys. Rev. D **86**, 113017 (2012).
[66] S. Bhattacharya, S. Jana, and S. Nandi, Neutrino masses and scalar singlet dark matter, Phys. Rev. D **95**, 055003 (2017).
[67] P. Ghosh, A. K. Saha, and A. Sil, Study of electroweak vacuum stability from extended Higgs portal of dark matter and neutrinos, arXiv:1706.04931.
[68] Z.-z. Xing and S. Zhou, Why is the 3×3 neutrino mixing matrix almost unitary in realistic seesaw models?, High Energy Phys. Nucl. Phys. **30**, 828 (2006).
[69] W. Grimus and L. Lavoura, The seesaw mechanism at arbitrary order: Disentangling the small scale from the large scale, J. High Energy Phys. 11 (2000) 042.
[70] J. Casas, J. Espinosa, and M. Quiros, Improved Higgs mass stability bound in the standard model and implications for supersymmetry, Phys. Lett. B **342**, 171 (1995).
[71] J. Casas, J. Espinosa, and M. Quiros, Standard model stability bounds for new physics within LHC reach, Phys. Lett. B **382**, 374 (1996).
[72] R. N. Lerner and J. McDonald, Gauge singlet scalar as inflaton and thermal relic dark matter, Phys. Rev. D **80**, 123507 (2009).
[73] M. Gonderinger, H. Lim, and M. J. Ramsey-Musolf, Complex scalar singlet dark matter: Vacuum stability and phenomenology, Phys. Rev. D **86**, 043511 (2012).
[74] J. A. Casas, V. Di Clemente, A. Ibarra, and M. Quiros, Massive neutrinos and the Higgs mass window, Phys. Rev. D **62**, 053005 (2000).
[75] A. Sirlin and R. Zucchini, Dependence of the Higgs coupling $h_{MS}(M)$ on m_H and the possible onset of new physics, Nucl. Phys. **B266**, 389 (1986).
[76] K. Melnikov and T. v. Ritbergen, The three loop relation between the MS-bar and the pole quark masses, Phys. Lett. B **482**, 99 (2000).
[77] M. Holthausen, K. S. Lim, and M. Lindner, Planck scale boundary conditions and the Higgs mass, J. High Energy Phys. 02 (2012) 037.
[78] F. Bezrukov, M. Y. Kalmykov, B. A. Kniehl, and M. Shaposhnikov, Higgs boson mass and new physics, J. High Energy Phys. 10 (2012) 140.
[79] R. Hempfling and B. A. Kniehl, On the relation between the fermion pole mass and MS Yukawa coupling in the standard model, Phys. Rev. D **51**, 1386 (1995).
[80] B. Schrempp and M. Wimmer, Top quark and Higgs boson masses: Interplay between infrared and ultraviolet physics, Prog. Part. Nucl. Phys. **37**, 1 (1996).
[81] F. Jegerlehner and M. Y. Kalmykov, $O(\alpha\alpha_s)$ correction to the pole mass of the t quark within the standard model, Nucl. Phys. **B676**, 365 (2004).
[82] L. N. Mihaila, J. Salomon, and M. Steinhauser, Gauge Coupling Beta Functions in the Standard Model to Three Loops, Phys. Rev. Lett. **108**, 151602 (2012).
[83] K. Chetyrkin and M. Zoller, Three-loop β-functions for top-Yukawa and the Higgs self-interaction in the Standard Model, J. High Energy Phys. 06 (2012) 033.
[84] M. Zoller, Beta-function for the Higgs self-interaction in the Standard Model at three-loop level, *Proc. Sci.*, EPS-HEP2013 (2013) 322 [arXiv:1311.5085].
[85] M. F. Zoller, Vacuum stability in the SM and the three-loop β-function for the Higgs self-interaction, Subnuclear series **50**, 557 (2014).
[86] T. E. Clark, B. Liu, S. T. Love, and T. ter Veldhuis, The Standard Model Higgs boson-inflaton and dark matter, Phys. Rev. D **80**, 075019 (2009).
[87] S. Antusch, J. Kersten, M. Lindner, and M. Ratz, Neutrino mass matrix running for nondegenerate seesaw scales, Phys. Lett. B **538**, 87 (2002).
[88] F. Staub, SARAH 4: A tool for (not only SUSY) model builders, Comput. Phys. Commun. **185**, 1773 (2014).
[89] F. Capozzi, E. Lisi, A. Marrone, D. Montanino, and A. Palazzo, Neutrino masses and mixings: Status of known and unknown 3ν parameters, Nucl. Phys. **B908**, 218 (2016).
[90] I. Esteban, M. C. Gonzalez-Garcia, M. Maltoni, I. Martinez-Soler, and T. Schwetz, Updated fit to three neutrino mixing: exploring the accelerator-reactor complementarity, J. High Energy Phys. 01 (2017) 087.
[91] S. Antusch and O. Fischer, Probing the nonunitarity of the leptonic mixing matrix at the CEPC, Int. J. Mod. Phys. A **31**, 1644006 (2016).
[92] A. M. Baldini *et al.* (MEG Collaboration), Search for the lepton flavour violating decay $\mu^+ \to e^+\gamma$ with the full dataset of the MEG experiment, Eur. Phys. J. C **76**, 434 (2016).
[93] P. Achard *et al.* (L3 Collaboration), Search for heavy isosinglet neutrino in e^+e^- annihilation at LEP, Phys. Lett. B **517**, 67 (2001).
[94] O. Adriani *et al.* (L3 Collaboration), Search for isosinglet neutral heavy leptons in Z0 decays, Phys. Lett. B **295**, 371 (1992).
[95] P. Abreu *et al.* (DELPHI Collaboration), Search for neutral heavy leptons produced in Z decays, Z. Phys. C **74**, 57 (1997).
[96] M. Z. Akrawy *et al.* (OPAL Collaboration), Limits on neutral heavy lepton production from Z0 decay, Phys. Lett. B **247**, 448 (1990).
[97] G. Cynolter, E. Lendvai, and G. Pocsik, Note on unitarity constraints in a model for a singlet scalar dark matter candidate, Acta Phys. Pol. B **36**, 827 (2005).
[98] B. W. Lee, C. Quigg, and H. B. Thacker, Weak interactions at very high-energies: The role of the Higgs boson mass, Phys. Rev. D **16**, 1519 (1977).
[99] Y.-P. Yao and C.-P. Yuan, Modification of the equivalence theorem due to loop corrections, Phys. Rev. D **38**, 2237 (1988).
[100] H. G. J. Veltman, The equivalence theorem, Phys. Rev. D **41**, 2294 (1990).

[101] H.-J. He, Y.-P. Kuang, and X. Li, On the Precise Formulation of Equivalence Theorem, Phys. Rev. Lett. **69**, 2619 (1992).

[102] H.-J. He, Y. P. Kuang, and X. Li, Further investigation on the precise formulation of the equivalence theorem, Phys. Rev. D **49**, 4842 (1994).

[103] H.-J. He, Y.-P. Kuang, and C.-P. Yuan, Equivalence theorem and probing electroweak symmetry breaking sector, Phys. Rev. D **51**, 6463 (1995).

[104] H.-J. He and W. B. Kilgore, Equivalence theorem and its radiative- correction-free formulation for all R_ξ gauges, Phys. Rev. D **55**, 1515 (1997).

[105] D. S. Akerib *et al.* (LUX Collaboration), Results from a Search for Dark Matter in the Complete LUX Exposure, Phys. Rev. Lett. **118**, 021303 (2017).

[106] M. Ajello *et al.* (Fermi-LAT Collaboration), Fermi-LAT observations of high-energy γ-ray emission toward the Galactic Center, Astrophys. J. **819**, 44 (2016).

[107] A. Alloul, N. D. Christensen, C. Degrande, C. Duhr, and B. Fuks, FeynRules 2.0—A complete toolbox for tree-level phenomenology, Comput. Phys. Commun. **185**, 2250 (2014).

[108] G. Belanger, F. Boudjema, P. Brun, A. Pukhov, S. Rosier-Lees, P. Salati, and A. Semenov, Indirect search for dark matter with micrOMEGAs2.4, Comput. Phys. Commun. **182**, 842 (2011).

[109] G. Belanger, F. Boudjema, A. Pukhov, and A. Semenov, micrOMEGAs3: A program for calculating dark matter observables, Comput. Phys. Commun. **185**, 960 (2014).

[110] W. T. V. W. H. Press, S. A. Teukolsky, and B. P. Flannery, *Numerical Recipes in Fortran 90, Second Edition* (Cambridge University Press, Cambridge, UK, 1996).

[111] J. Espinosa, G. Giudice, and A. Riotto, Cosmological implications of the Higgs mass measurement, J. Cosmol. Astropart. Phys. 05 (2008) 002.

[112] G. Isidori, V. S. Rychkov, A. Strumia, and N. Tetradis, Gravitational corrections to standard model vacuum decay, Phys. Rev. D **77**, 025034 (2008).

[113] N. Khan and S. Rakshit, Constraints on inert dark matter from the metastability of the electroweak vacuum, Phys. Rev. D **92**, 055006 (2015).

[114] N. Khan, Exploring hyperchargeless Higgs triplet model up to the Planck scale, arXiv:1610.03178.

[115] F. del Aguila and J. Aguilar-Saavedra, Distinguishing seesaw models at LHC with multi-lepton signals, Nucl. Phys. **B813**, 22 (2009).

[116] N. Haba, S. Matsumoto, and K. Yoshioka, Observable seesaw and its collider signatures, Phys. Lett. B **677**, 291 (2009).

[117] C.-Y. Chen and P. S. B. Dev, Multi-lepton collider signatures of heavy dirac and Majorana neutrinos, Phys. Rev. D **85**, 093018 (2012).

[118] A. Das and N. Okada, Inverse seesaw neutrino signatures at the LHC and ILC, Phys. Rev. D **88**, 113001 (2013).

[119] P. Bandyopadhyay, E. J. Chun, H. Okada, and J.-C. Park, Higgs signatures in inverse seesaw model at the LHC, J. High Energy Phys. 01 (2013) 079.

[120] A. Das, P. S. Bhupal Dev, and N. Okada, Direct bounds on electroweak scale pseudo-Dirac neutrinos from $\sqrt{s} =$ 8 TeV LHC data, Phys. Lett. B **735**, 364 (2014).

[121] A. Das and N. Okada, Improved bounds on the heavy neutrino productions at the LHC, Phys. Rev. D **93** (2016) 033003.

[122] S. Mondal and S. K. Rai, Probing the heavy neutrinos of inverse seesaw model at the LHeC, Phys. Rev. D **94**, 033008 (2016).

[123] A. Das, P. Konar, and S. Majhi, Production of heavy neutrino in next-to-leading order QCD at the LHC and beyond, J. High Energy Phys. 06 (2016) 019.